University of Exeter
Department of Mathematics and Statistics

Jets and instabilities in forced magnetohydrodynamic flows

Azza Mohammed M Al Gatheem

Submitted by Azza Mohammed M Al Gatheem to the University of Exeter as a thesis for the degree of Doctor of Philosophy in Mathematics, October, 2023.

I certify that all material in this thesis which is not my own work has been identified and that any material that has previously been submitted and approved for the award of a degree by this or any other University has been acknowledged.

Signed: .....

Abstract

Magnetic fields are present in the solar system and astrophysical bodies (e.g. the Sun's field, the Earth's field, and the fields of giant planets, stars and galaxies). Our research examines the effect of magnetic fields on these systems, extending the work of Meshalkin and Sinai (1961) and Manfroi and Young (2002). The results will be useful for understanding the effects of the magnetic field in more turbulent regimes, although this study is concerned with the instabilities associated with classical laminar flow. We aim to investigate the role played by the magnetic field in modifying the stability properties of planar-forced fluid flows. In the absence of magnetic fields, the flow found by a body force, and nonlinear interactions with Rossby waves result in the generation of strong zonal flows. However, we find that the presence of a weak magnetic field suppresses the zonal jet generation.

Here we study the instabilities of the Kolmogorov flow. We consider $\boldsymbol{u_0} = (0, \sin x)$ as a 2D incompressible flow. In the presence of a mean magnetic field, the dynamics are governed by the Navier–Stokes equations and the induction equation. We perform a classical linear analysis, in which growth rate, stability criteria, and MHD effects are derived. Instabilities are investigated associated with two magnetic field orientations, which can be x-directed (*horizontal*) or y-directed (*vertical*) in our two-dimensional system to give an MHD version of Kolmogorov flow. In a basic equilibrium state magnetic field lines are straight for the case of vertical field and sinusoidal for horizontal field with an additional component of the external force balancing the resulting Lorentz force. As the basic state is independent of the y-coordinate we use Fourier analysis to study waves of wavenumber k in the y-direction, using the methods of classical stability theory and numerical solution of eigenvalue problems.

Instability can occur at a single Fourier mode in the y-direction, which can be identified as hydrodynamic instability for sufficiently small wavenumber k, while sometimes occurs at different Fourier modes by introducing Floquet wavenumber ℓ in the x-direction. The classic hydrodynamic instability is suppressed by increasing field strength B_0. The linear stability problem can be truncated to determine the eigenvalues of finite matrices numerically, by applying perturbation theory to the limit $k \to 0$ and $\ell \to 0$. For the vertical field case, there are strong-field branch destabilised Alfvén waves that occur when the magnetic Prandtl number $P < 1$ is less than unity, as found in recent work conducted by Fraser, Cresswell and Garaud (2022).

A significant influence of the magnetic field is that it can lead to enhanced instabilities in parameter regimes in the case of an imposed horizontal magnetic field. The basic state is formed by a steady solution of field and flow with the driving body force balancing both viscosity and the Lorentz force. Increasing the magnetic field from zero suppresses the purely hydrodynamic instability once again, however, stronger fields reveal a new branch of instabilities. Introducing a non-zero Floquet wavenumber ℓ allows a new branch of instability. A further point of interest is that the most unstable modes can occur for horizontal magnetic field $\gamma \to \pi/2$, whereas the system stabilizes when $\gamma \to 0$, where γ is the angle between the field and y-axis. We also present some results using analytical approximations of eigenvalue perturbation theory in the limit of $k, \ell \to 0$, for which the instability is large scale compared to the jets. Analytical approximations are provided to represent both weak field and strong field instabilities, as well as to determine the growth rates and thresholds that are in good agreement with the calculated values. Analytical approximations also provided the thresholds of instability with the combination of vertical and horizontal fields for a general magnetic field with variation in the angle γ.

Exploration of the nonlinear evolution of a Kolmogorov flow under MHD effects is an interesting subject that we address in the final chapters of the thesis. Fluid dynamics can be observed in a variety of ways through the nonlinear interactions between

Kolmogorov flow and Alfvén waves in the case of MHD instabilities. The onset of instability is characterised by the exponential growth in perturbation energy of flow and field specifically kinetic energy, enstrophy and magnetic energy. Perturbation quantities such as energy grow as a result of initial instability. In addition to this, we then justify the choice of magnetic field strength and magnetic Prandtl number and discuss the instability's behaviour during non-linear evolution. First, we focus on the nonlinear evolution parameterised by the inverse Reynolds number effects in hydrodynamic systems, before investigating the instability evolution of MHD effects.

Nonlinear simulation based on two systems is undertaken using the Dedalus framework; the hydrodynamic simulation demonstrated the effect of viscosity on instability, checking instability linear growth rate from simulations against the theory. We have found that a small viscosity has a destabilizing effect while increasing viscosity leads to stabilization. Introducing the magnetic field in our simulations exhibits different characteristics of instability, the presence of a weak vertical magnetic field can give hydrodynamic behaviour. While an oscillatory behaviour is obtained for a strong vertical magnetic field and a small magnetic Prandtl number. We also obtained an oscillatory behaviour for a large Prandtl number in the case of the horizontal magnetic field. Another phenomenon can be observed with the horizontal magnetic field; the system exhibits a tearing mode instability as B_0 increases. The Flouquet wavenumber $\ell \neq 0$ allows large scales in the x-direction and even with a weak horizontal magnetic field in some cases we observe an inverse cascade and the formation of jets governed by the nonlinear properties of the system.

Acknowledgements

Firstly, I would like to express my gratitude to my supervisor, Prof. Andrew Gilbert for his guidance during my PhD research and insightful feedback. I will be forever grateful for the chance to work with him, his support has been extremely meaningful to me over the past four years. It would have been extremely difficult to have completed the work presented in this Thesis without his precious support.

Secondly, I want to express my gratitude to Dr Andrew Hillier for his advice, and encouragement, which helped me through the development of this research. I would also like to thank the members of the Geophysical and Astrophysical Fluid Dynamics group of the University of Exeter for their guidance through the seminar series. My colleagues, Dr.Chen, Liam, William, Andrew Darlington, and Velizar, Manohar, all contributed to making this PhD experience even better. A special sense of gratitude goes to Dr. Giulia Murtas for her kind support and encouragement during my time at Exeter.

I would like to express my gratitude to my soulmate, my first and utmost supporter, and my dear husband. You kept taking my hands step by step through this journey to achieve my dream. Thank you. Finally, This work was supported by the Ministry of Education, Riyadh, Kingdom of Saudi Arabia. To whom I would like to also extend my thanks.

Dedication

To my little hero and angel, Firas whose unconditional love, hugs and smiles let me through the darkest moments. I am grateful for having you.

General nomenclature	
α	angle for β-effect
β	magnitude of β-effect
ρ	density
η	magnetic diffusion/ the inverse of magnetic Reynolds number
ν	viscosity / the inverse of Reynolds number
R_c	critical Reynolds number
g	gravitational acceleration
f	rotation rate
p	pressure / or (later) growth rate
Ω	rotation rate
γ	the angle of the magnetic field
B_0	magnetic field strength
Wave properties	
k	wavenumber in y-direction
n	wavenumber in x-direction
ℓ	Floquet wavenumber in x-direction
Operators and vectors	
$\nabla = (\frac{\partial}{\partial_x}, \frac{\partial}{\partial_y})$	vector gradient in two dimensions
$\boldsymbol{u}$	velocity (u, v), u is horizontal, v is vertical
$\boldsymbol{B}$	magnetic field
A	vector potential
$\boldsymbol{J}$	current of the magnetic field.
Ψ	stream function or ψ
ω	vorticity

Contents

List of Figures

List of Tables

1. Introduction

1.1 Geophysical and Astrophysical Fluid Dynamics

Many fundamental processes in the universe are governed by fluid dynamics, which plays an important role in the understanding of astrophysics and geophysics. In this introduction, we provide an overview of the fluid dynamics needed to understand some astronomical phenomena, starting with the physics of the solar interior (magnetohydrodynamic instability), to atmospheric dynamics applications (e.g. waves, hydrodynamic instability, and planetary dynamics). In the next sections, we present an overview of the stability and application of magnetic fields, in the atmosphere and solar system, which will provide context for the work described in subsequent chapters.

1.1.1 Solar interior structure

Kolmogorov flow stability can be used to model physical processes in the solar interior. As a general motivation, we have linked our findings to the solar atmosphere (e.g. the Sun's tachocline). In this section, we briefly describe the properties of the solar structure and discuss the tachocline, and convection zone as well as observations published in the literature. We can give another example of the Sun's corona which lies above the chromosphere and is dominated by the magnetic field described by MHD theory.

The centre of the Sun is where the energy of the Sun is produced. The Sun is a

source of heat and light and consists of fluid largely in hydrostatic equilibrium. A small change in the Sun's behaviour could change the mechanical equilibrium (Priest, 2014). It is natural to introduce a magnetic field and study the coupled MHD system; for example, the interaction between magnetic field, shear, and convection remains poorly understood in the solar tachocline as discussed in Hughes, Rosner and Weiss (2007).

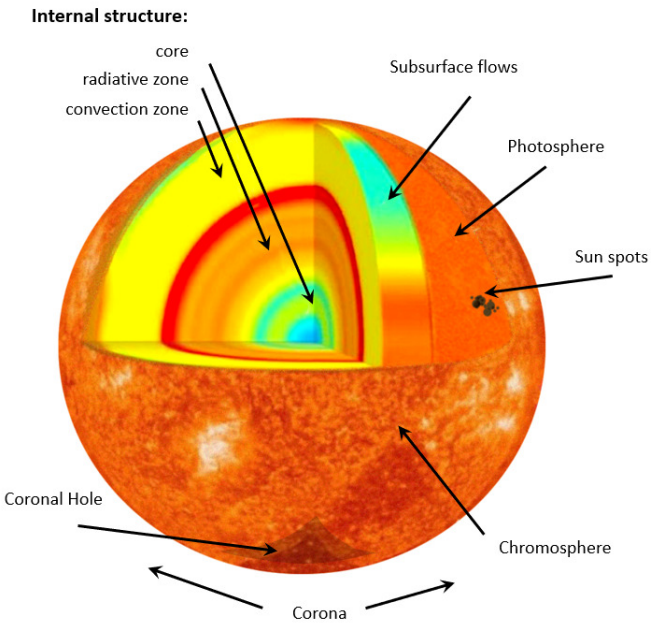

Figure 1.1: Internal structure of the Sun, The schematic is created by me and is similar to the image of the Center of Science Education.

The Sun is often viewed as a uniform or solid sphere, but the structure of the Sun is made up of distinct layers similar to the Earth. The layers of the Sun can be divided into two groups: the three inner layers and the three outer layers. Each layer has different characteristics. The layers of the Sun shown in figure 1.1 include a label for each of the six layers: The core, radiative zone, and convective zone are categorized as the inner layers. The photosphere, chromosphere, and corona are categorized as the outer layers. The photosphere is irregular and exhibits features, including sunspots.

In the solar system, there are a number of processes that generate magnetic fields. external effects observed from planetary magnetic fields include Venus's ionospheric

currents and Earth's magnetospheric currents. Jupiter's and Saturn's fields are extremely powerful and dipolar, while Mercury's is weak. In contrast, the fields of Uranus and Neptune do not show this dominance in their axial dipolar components, (Stanley, 2014). Even though most planets possess magnetic fields, scientists are unable to fully explain how they are generated. Future missions aim to study planetary magnetic fields, which provide insight into the interior makeup of planets as well as their history and formation. e.g. NASA's Juno mission is orbiting Jupiter with two sensor experiments to create the first global map of Jupiter's magnetic field. The book Childress and Gilbert (1995) is an example of MHD theory for explaining the time variation and persistence of magnetic fields produced by astrophysical objects.

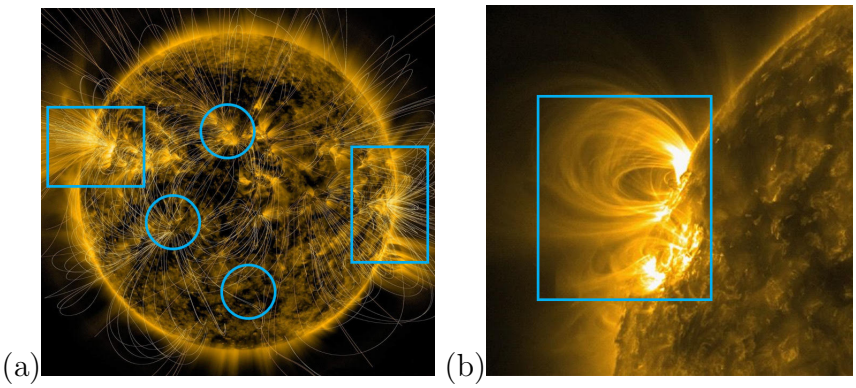

Figure 1.2: (a) Solar corona holes region of open magnetic field lines, the white light near solar maximum is the active region, (b) Coronal loops at the solar limb, taken from the NASA TRACE mission.

Over the years, the solar phenomena can be classified into two categories: quiet and active, (Priest, 2014). Figure 1.2 shows the solar corona is described with two regions. The *quiet Sun* is considered as a stationary, spherical symmetric ball of plasma as shown in panel (a) whose properties are determined by the radial distance from the centre and for which the magnetic field is negligible. The *active Sun* is characterized by transient phenomena, such as sunspots and prominences, which are present in the quiet atmosphere and originate from the magnetic field, as indicated by the blue squares in both panels. Generally, the corona consists of three parts: relatively dark coronal holes, indicated by the blue circles in panel (a), where plasma escapes along open magnetic fields to generate the fast solar wind. Brighter coronal loops are the

building blocks of the bright solar corona and are magnetically closed and connected to photospheric regions as indicated by the blue squares in panel (a). The X-ray bright points are composed of a set of small-scale loops distributed throughout the disc, as shown in panels (a,b).

Chromosphere and corona heating continue to be a prominent problem in solar physics, and two main mechanisms have been proposed to explain this phenomenon: Magnetic waves generated in convection zones propagate outwards and dump their energy. A second type of mechanism involves magnetic reconnection in various current sheets. In the corona, various types of waves have been observed, including Alfvén waves. Magnetic fields in the sun are forming flux tubes that can drive the formation of Alfvén waves, (Priest, 2014).

1.1.2 The Solar Tachocline

The solar tachocline, a thin region of a strong shear layer, is driven principally by differential rotation of the convection zone, (Gough, 2007). One of the most important aspects of the tachocline is the magnetorotational instability, which was first stressed by Steve Balbus and John Hawley, (Hughes, Rosner and Weiss, 2007).

The Sun's tachocline is an excellent and unique laboratory for astronomy research. The variations in temperature, density, pressure, β- effect, and magnetic field strength observed across the external layers of the Sun provide the opportunity to study the fundamental concept of instability in a wide range of conditions, and at a wide range of spatial and temporal scales. The solar dynamo is an important physical process that generates the solar magnetic field and drives the features we observe at the solar surface. The tachocline is primarily responsible for the generation of large-scale magnetic fields caused by the solar dynamo and may also play a critical role in mixing processes within the solar interior, contributing to the strengthening of the magnetic field via differential rotation (Tobias and Weiss, 2007). This differential rotation sits just below the base of the solar convection zone and forms a matching layer

known as a tachocline. A comprehensive review of current tachocline research problems is available in the book "The solar tachocline" (Hughes, Rosner and Weiss, 2007).

A variety of instabilities may also occur in the solar convection zone. A review of observations, theoretical studies, and computational investigations of global-scale dynamics in the solar interior was presented in Miesch (2005) and it was emphasized that high-resolution global simulations of solar convection could be improved. Bushby and Mason (2004) discussed how the sun's dynamo could operate and developed a physical theory that shows comparisons between dynamo models with α-effect dynamo, in which small-scale turbulent motion generates large-scale poloidal magnetic fields and found that localization of this process at the base of the convection zone is more effective. Soward et al. (2005) argue that the solar dynamo exists primarily in the tachocline.

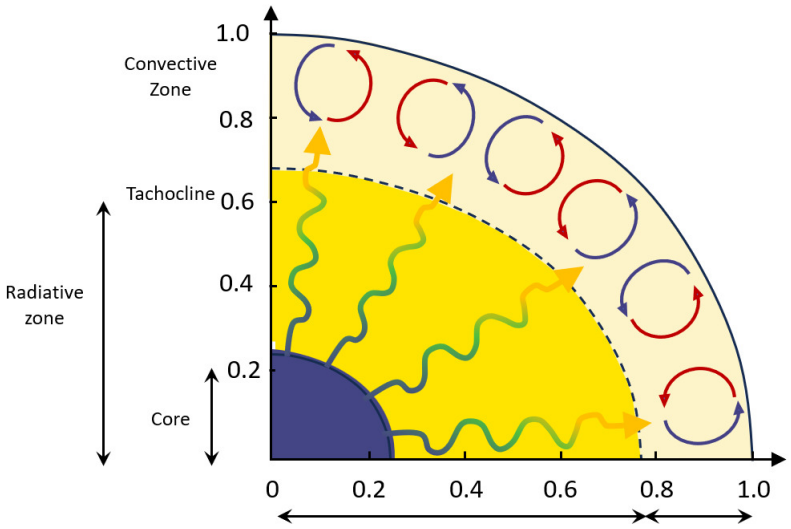

Figure 1.3: Schematic showing the internal structure of the Sun and the location of the tachocline. The base of the convection zone is marked by the black dashed line, (Priest, 2014).

Helioseismology provides the most crucial information for dynamo theory: known as a technique that measures oscillations of the Sun caused primarily by sound waves. Figure 1.3, shows a theoretical model of the Sun's interior. Qualitatively we describe the internal solar structure splits into three regions in figure 1.3: the core (blue region), the radiative zone (dark yellow), and the convective zone (light yellow). The central region of the Sun is the core: this region produces energy. This energy is

carried outwards towards the surface of the star initially by radiation about 90 % of the Sun's mass contained within 80 % of the Sun's radius. The convection zone becomes more important for energy transport and has 20 % of the Sun's radius, with low density. The radiative zone indicated by the yellow arrows extends out about 80% of the sun's radius, where the radiative transfer of energy in the radiative zone and convective transfer by fluid motions in the convection zone. The small-scale convection at the solar surface can be seen in the form of granulation.

1.1.3 Simulation of the sun

Numerical simulations of the Sun are complex. Solar processes generate both large-scale and small-scale magnetic structures associated with unique computational challenges at various spatial and temporal scales. It is known that the convective region is highly turbulent, which is an unsolved problem in fluid mechanics. A discussion of this can be found in Hughes, Rosner and Weiss (2007).

Parameters	values
Density ρ	0.2 g cm^{-3}
Pressure p	6.7×10^{13} $g\ cm^{-1}s^{-2}$
Temperature T	$2.3 \times 10^{6}K$
Kinematic viscosity ν	2.7×10^{1} $cm^{2}s^{-1}$
Magnetic diffusivity η	4.1×10^{2} $cm^{2}s^{-1}$
thermal diffusivity κ	1.4×10^{7} $cm^{2}s^{-1}$
Magnetic Prandtl number P	6.6×10^{-2}
Gravitational acceleration g	5.4×10^{4} $cm\ s^{-2}$

Table 1.1: Physical parameters in the table shows properties relevant to the tachocline at in $R = 0.7R_{sun}$, (Gough, 2007).

To gain a better understanding of the structure and dynamics of these regions, simulations of the Sun require improved numerical methods, and high resolutions to accurately predict the evolution of the solar interior. Table 1.1 presents estimates

of the parameter values within the convection zone base. We observed that the dimensionless magnetic Prandtl number is small and that agrees with other physical quantities in the sun's interior

$$P = \frac{\text{Kinematic viscosity}}{\text{Magnetic diffusivity}} = \frac{\nu}{\eta} = 6.6 \times 10^{-2} \tag{1.1}$$

A study conducted by Christensen-Dalsgaard and Thompson (2007) observed that magnetic diffusivity comes entirely from particle transport. They derived a Prandtl number based on these coefficients $\frac{\nu}{\kappa} \simeq 1.9 \times 10^{-6}$ and magnetic Prandtl number $\frac{\nu}{\eta} \simeq 6.6 \times 10^{-2}$ considered as a characteristic of the tachocline.

1.2 Fundamental concept of instabilities

To gain a more comprehensive understanding of instability, we refer to equilibrium as the "basic" state of the system, (Drazin and Reid, 2004; Chen et al., 2015). Before we dive into the main concepts in this thesis, it is necessary to have a physical sense of what instability means. A simple model was presented in Hillier (2020). To look at stability, think about a ball at rest in a valley or on the top of a hill.

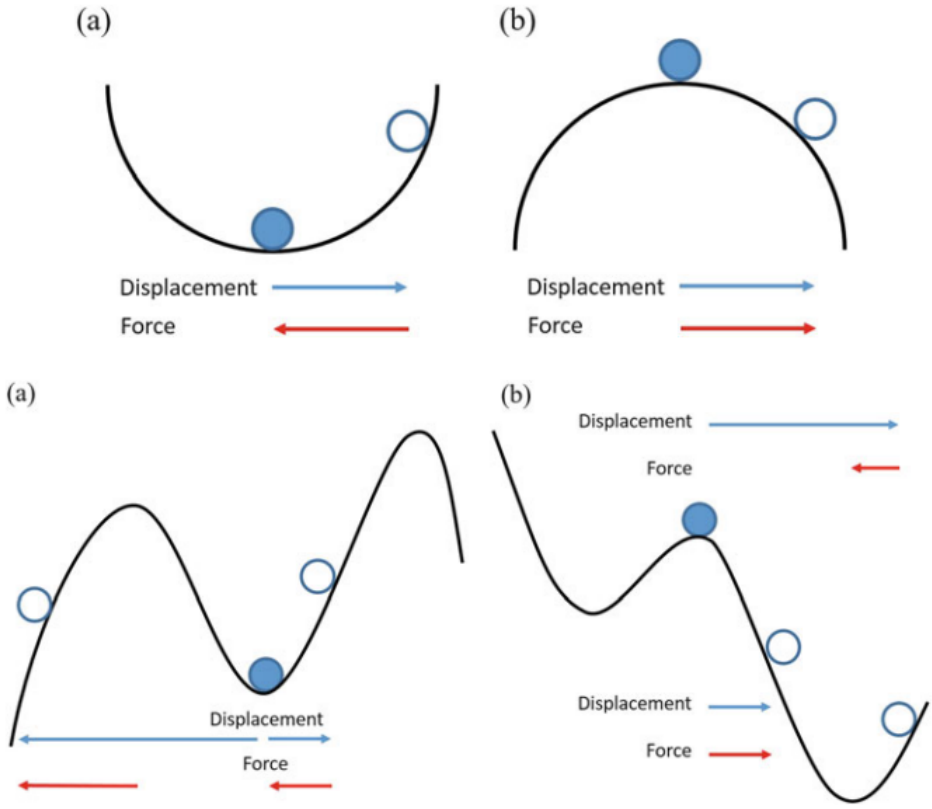

Figure 1.4: Schematic of the physical mechanism of instability. ***Top***: is the linear stability, (a) stable and (b) unstable. ***Bottom***: is the non-linear stability (a)linearly stable, non-linearly unstable, (b) linearly unstable, non-linearly stable. Figures are taken from (Hillier, 2020).

Figure 1.4 shows a concept of linear instability through a ball placed at the bottom of the valley and the top of the hill as shown in top panels (a,b). As a result of displacement, the ball will move sideways and upwards, creating a force in the opposite direction shown in panel (a). In addition, since the ball has kinetic energy when it returns to the base of the valley, it will continue past the central point and head up the other side of the valley, oscillating about the central point. Panel (b) depicts a ball placed at the top of a hill. Any sideways displacement will also move the ball downwards, resulting in a force in the same direction. The concept can also be understood by determining whether a displacement must add energy to a system or extract energy from it as shown in panel (b).

The concept can be understood in terms of energy change. An alternative way to view this concept is to consider whether displacement uses energy to put energy into the system or extracts energy from the system. For example, as shown in Figure

1.4(a). We must add more energy to the system in order to push the ball upwards. In panel (b), gravity performs the work for us. Therefore, the displacement results in the loss of more gravitational potential energy and accelerates, but conservation of energy dictates that all this energy must be expended at some point. As a result, it must be converted to kinetic energy in this case. The model can be viewed as a local statement regarding the stability of the system. Our study of linear stability in the following chapters of this thesis is based on this approach when we are only considering small perturbations.

Two potential nonlinear scenario examples are presented in the bottom panels (a,b) of figure 1.4. In (a) for a small displacement, the force works in the opposite direction to the small displacement leading to keeping the ball located in the local potential well, the displacement thereby giving stability. However, since the potential well is finite, a relatively large displacement can cause the ball to leave the potential well to a place where the force also acts in the same direction. As a result, the nonlinear instability leads to a large enough initial displacement. There is also the possibility of an initially unstable situation shown in panel (b). When the ball moves away from the hill (the peak of the gravitational potential), it passes through the base of a valley (basically a trough in the gravitational potential) and the force direction changes. Ultimately, the ball has passed through a point of local stability and oscillates around that point. This gives us a concept of nonlinear stability.

Theoretical and numerical techniques used in studying hydrodynamic stability can also be used in other fields like magnetohydrodynamics, the physics of plasma, as well as elasticity; even though the physics is different, the mathematics and techniques remain the same. Understanding the stability analytically was formulated by Liapounov. A definition of stability in the sense of Liapounov can be found in Drazin and Reid (2004) as follows: for any $\nu > 0$ there exists some positive number δ (depending on ν) such that at $t = 0$:

$$\|\boldsymbol{u}(x, y, t) - \boldsymbol{U}(x, y, t)\| < \delta, \tag{1.2}$$

then for all $t > 0$

$$\|\boldsymbol{u}(x, y, t) - \boldsymbol{U}(x, y, t)\| < \nu \tag{1.3}$$

where for example, we measure the distance between $\boldsymbol{u}$ & $\boldsymbol{U}$ with an L^2 or energy norm :

$$\|\boldsymbol{u}(x, y, t) - \boldsymbol{U}(x, y, t)\|^2 = \int\int \mid \boldsymbol{u}(x, y, t) - \boldsymbol{U}(x, y, t) \mid^2 dxdy, \tag{1.4}$$

Here $\boldsymbol{u}$ is the velocity field which satisfies the equations of motion. This definition means the flow $\boldsymbol{U}$ will be stable if the perturbation is small enough for all times provided it is small initially. The mathematical treatment of these small perturbations is based on linearisation for small initial disturbances of the basic flow .

Linear stability can be studied using this definition. Basically, we need to decompose all quantities into their background components and add a small perturbation; we have

$$\boldsymbol{\omega}(x, y, t) = \omega_0(x) + \omega_1(x, y, t), \tag{1.5}$$

$$\boldsymbol{\psi}(x, y, t) = \psi_0(x) + \psi_1(x, y, t), \tag{1.6}$$

where ω_0, ψ_0 represents the equilibrium solution and ω_1, ψ_1 is the perturbation of the flow. Using this decomposition, one can derive equations that do not include higher-order perturbation terms (in the case of our problem at hand, these equations will be deduced below under subsection 2.1). By solving the linearised equations, one can determine whether the system is stable, in which case the perturbations produce a decaying function over time, or unstable, in which case the perturbations produce a growing function.

In this thesis, we will derive the fundamental equations and convey an intuitive understanding of the subject matter by emphasizing fluid dynamical phenomena that can be observed. The essential problem is modelled by nonlinear partial differential equations and examines the stability of known steady solutions. Typically, Navier–Stokes

equations and continuity equations govern the majority of hydrodynamic stability problems (see section 1.2.1), which are often applied to geophysical and astrophysical systems.

1.2.1 Navier-Stokes Equations

The Navier-Stokes Equations (NSE) are partial differential equations Newtonian governing fluid motion. In 1823, Claude-Louis Navier first derived the formula, and George Gabriel Stokes refined it in Stokes (1849), Stokes (1880). The NSE incorporates several important physical principles: Newton's law of viscosity, which relates shear stress linearly to the distortion rate of elements, Mass conservation, in which the mass of each parcel of fluid remains constant over time, and Newton's second law. For incompressible flow, the Navier-Stokes equations are given by

$$\rho(\partial_t \boldsymbol{u} + (\boldsymbol{u}\cdot\nabla)\boldsymbol{u}) + \nabla p = \frac{1}{\mu_0}(\nabla\times\boldsymbol{B})\times\boldsymbol{B} + \rho\nu\nabla^2\boldsymbol{u} + \rho\boldsymbol{f} \tag{1.7}$$

$$\partial_t \boldsymbol{u} + (\boldsymbol{u}\cdot\nabla)\boldsymbol{u}) + \nabla\frac{p}{\rho} = \frac{1}{\mu_0\rho}(\nabla\times\boldsymbol{B})\times\boldsymbol{B} + \nu\nabla^2\boldsymbol{u} + \boldsymbol{f} \tag{1.8}$$

$$p' = \frac{p}{\rho}, \qquad \boldsymbol{B}' = \frac{\boldsymbol{B}}{\sqrt{\mu_0\rho}} \tag{1.9}$$

If we drop the prime then we get the most convenient form for further work, namely

$$\partial_t \boldsymbol{u} + (\boldsymbol{u}\cdot\nabla)\boldsymbol{u}) + \nabla p = (\nabla\times\boldsymbol{B})\times\boldsymbol{B} + \nu\nabla^2\boldsymbol{u} + \boldsymbol{f} \tag{1.10}$$

$$\nabla\cdot\boldsymbol{u} = 0, \tag{1.11}$$

$\boldsymbol{u}(x,t)$ is the fluid velocity, $p(x,t)$ the fluid pressure, and $\boldsymbol{f}(x,t)$ is the body force per unit of mass, ν the kinematic viscosity. $\frac{1}{\mu_0}(\nabla\times\boldsymbol{B})\times\boldsymbol{B}$ is the Lorentz force, which makes possible the interaction between the conducting fluid and the electromagnetic field. $\frac{1}{\mu_0}$ is the vacuum permeability. Equation (1.7) is also known as the momentum equation, which governs momentum transport, and equation (1.11) is known as the mass continuity equation, which describes the conservation of mass in

a continuous fluid, (Coleman, 2010). The NSE describes the motion of fluids, such as air and water, from laminar to turbulent flows. With increasing velocity, fluid flow changes from laminar, which flows in layers, to turbulent, which has random fluctuations. Therefore, fluid velocity is the key variable in NSE applications, along with density ρ, pressure p, and external forces $\boldsymbol{f}$, (Berselli, 2021). In our study, we use two-dimensional NSE for an incompressible flow, where the density is constant $\rho = \rho_0$.

1.2.2 Non-dimensionalized Equations

The dimensional Navier-Stokes equations in terms of the velocity field $\boldsymbol{u}$ are defined as:

$$\partial_{\tilde{t}}\tilde{\boldsymbol{u}} + \tilde{\boldsymbol{u}} \cdot \nabla\tilde{\boldsymbol{u}} + \nabla\tilde{p} = \tilde{\nu}\tilde{\nabla}^2\tilde{\boldsymbol{u}} + \tilde{\boldsymbol{f}}, \tag{1.12}$$

where ν is viscosity, p is the pressure, and $\boldsymbol{f}$ is the external body force per unit of mass and used to maintain the basic state of the system. We specified the Kolmogorov flow by

$$\tilde{\boldsymbol{u}_0} = (0, U\sin(x/L), 0), \quad \text{with} \quad \tilde{\boldsymbol{f}} = \tilde{\nu}UL^{-2}(0, \sin(x/L), 0) \tag{1.13}$$

We use the length L and velocity U as the basis for non-dimensionalisation and $T = L/U$ as an appropriate time scale

$$\tilde{x} = x/L, \qquad \tilde{\boldsymbol{u}} = \boldsymbol{u}U, \qquad \tilde{t} = \frac{1}{T}t, \qquad \tilde{\nabla} = \frac{1}{L}\nabla, \quad \tilde{p} = U^2p, \quad \tilde{\nu} = \frac{\nu}{UL}, \quad \boldsymbol{f} = UT^{-1}\tilde{\boldsymbol{f}}. \tag{1.14}$$

By substitute equation (1.14) into equation (1.12), we obtain:

$$\frac{1}{T}\frac{\partial}{\partial_t}(U\boldsymbol{u}) + (U\boldsymbol{u}).\frac{1}{L}\nabla(U\boldsymbol{u}) + \frac{1}{L}\nabla U^2p = \frac{\nu}{UL}\frac{1}{L^2}\nabla^2(U\boldsymbol{u}) + UT^{-1}\boldsymbol{f} \tag{1.15}$$

Multiplying by L/U, which gives non-dimensional equation

$$\partial_t\boldsymbol{u} + \boldsymbol{u} \cdot \nabla\boldsymbol{u} + \nabla p = \frac{1}{Re}\nabla^2\boldsymbol{u} + \boldsymbol{f}, \tag{1.16}$$

with this, we obtain one non-dimensional parameter, the Reynolds number Re and the inverse Reynolds number ν

$$Re = UL/\nu, \quad \nu = 1/Re, \tag{1.17}$$

The non-dimensional induction equation will be in MHD section 1.5.1 for consistency.

1.2.3 Waves & instability

Fluid dynamical systems are subject to waves, oscillatory disturbances that propagate through a medium such as surface gravity waves in the ocean, and electromagnetic, for example, radio waves. There are many examples with fluid dynamics applications (Vallis, 2017). Waves are produced by the action of a restoring force that tends to return the system to its undisturbed condition. In this thesis, we will focus on waves that are present in large-scale flows in the atmosphere, e.g. the geophysical waves (Rossby waves), which are known as planetary waves, naturally occur in rotating fluids. They are caused by the action of the Coriolis force and pressure gradient. We observed Rossby waves initially by reproducing the results of Manfroi and Young (2002). The results of this research will be explained in section 2.5. We also have magnetic waves (e.g. Alfvén waves) detailed in section (1.5.3).

Waves in instability show a real growth rate and move with a complex growth rate. We consider wave travelling in the y-direction and a variable $\psi(y,t)$ of the form

$$\psi(y,t) = Ae^{iky+pt} \tag{1.18}$$

$$Ae^{iky+(p_r+ip_i)t} = Ae^{ik(y-\omega t)+p_r t} \tag{1.19}$$

$$e^{i\Phi} = cos(\Phi) + i\sin(\Phi) \tag{1.20}$$

$$\psi(y,t) = e^{p_r t}(A\cos(ky-\omega t) + iA\sin(ky-\omega t)). \tag{1.21}$$

This represents a periodic travelling wave propagating in the positive y-direction $k\omega > 0$; where A is an amplitude, k is the wavenumber, ω is the angular frequency, t

is the time, $c = \omega/k$ wave speed. The wave grow if $p_r > 0$, and decays if $p_r < 0$.

Many physical systems that exhibit wave motion can be modelled using linear equations including the wave equation. These also have periodic solutions of the form (1.21) with the frequency

$$\omega = \Omega(k) \tag{1.22}$$

where $\Omega(k)$ is some function called the dispersion relation. This function takes different forms regarding the different waves, for sound waves light waves Rossby waves and Alfvén waves, see section (1.5.3).

1.2.4 Rossby waves

Rossby waves are planetary waves that occur naturally in rotating fluids and occur in the Earth's ocean and atmosphere. In particular, these waves are associated with pressure systems and the jet stream (around polar vortices).

We know that the β-effect is important to get Rossby waves. we sketch a Local Cartesian model to study the jet instability at a general latitude as shown figure 1.5. Ω rotation rate of the earth, f is the vertical part of the Ω rotation vector. So, we have β-plane approximation which is the local variation of the vertical component of Ω. Also, we have the rotated axes or the general orientation of (x, y) with respect to the variation of Ω bringing in the angle α which explains the different instability of basic flow.

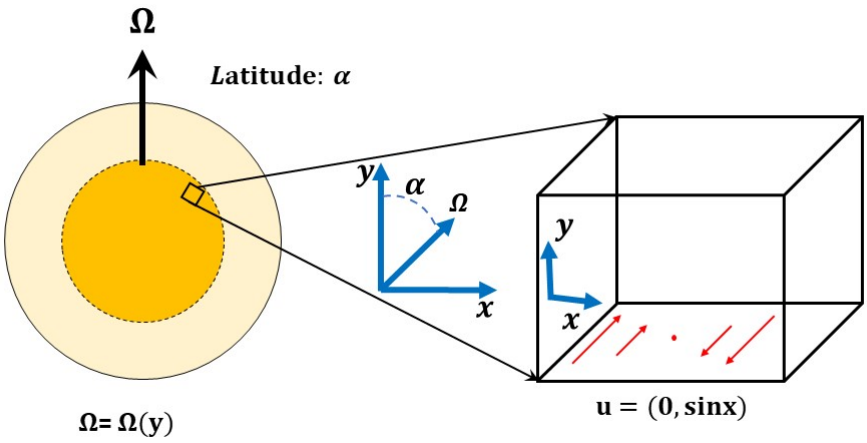

Figure 1.5: Schematic illustrates the classical approximation of β-plan where we keep the linear variation with latitude, the white orange region may represent the convection zone and the yellow region an overlying solar tachocline zone so that the Cartesian domain represents a small patch in the solar tachocline. The rotation vector is inclined by an angle α from y, or by $90° - \alpha$ from the direction x. The red arrows are the fluid flow.

Consider a two-dimensional incompressible flow, where $\boldsymbol{u} = (0, \sin x)$. The dynamics are illustrated in the Cartesian β-plane for which $f = f_0 + \beta y$, where f_0 is constant and doesn't appear in our subsequent derivation. By introducing the Coriolis term in equation (1.16), the momentum equation is written as:

$$\partial_t \boldsymbol{u} + \boldsymbol{u} \cdot \nabla \boldsymbol{u} + 2\boldsymbol{\Omega} \times \boldsymbol{u} + \nabla p = \nu \nabla^2 \boldsymbol{u} + \boldsymbol{f}, \tag{1.23}$$

$$\nabla \cdot \boldsymbol{u} = 0, \quad \nabla \times \boldsymbol{u} = \boldsymbol{\omega}$$

The rotation vector $\boldsymbol{\Omega}$ with the β-effect takes the form

$$2\boldsymbol{\Omega} = (0, 0, f + \beta y \cos\alpha + \beta x \sin\alpha) \tag{1.24}$$

If we set $\alpha = 0$ in equation (1.24), we obtain :

$$2\boldsymbol{\Omega} = (0, 0, f + \beta y) \tag{1.25}$$

The Coriolis term with the β-effect takes the form

$$2\boldsymbol{\Omega} \times \boldsymbol{u} = (-(f + \beta y)v, (f + \beta y)u, 0), \tag{1.26}$$

where $\boldsymbol{u}$ is the velocity observed from the rotating frame. By taking curl of equation (1.26), we obtain:

$$\nabla \times (2\boldsymbol{\Omega} \times \boldsymbol{u}) = (0, 0, (f + \beta y)u_x + (f + \beta y)v_y), \tag{1.27}$$

$$\nabla \times (2\boldsymbol{\Omega} \times \boldsymbol{u}) = (0, 0, \underbrace{\beta v}_{-\beta\psi_y} + (f + \beta y)\underbrace{(u_x + v_y)}_{\nabla\cdot\boldsymbol{u}=0}) \tag{1.28}$$

Equation (1.27), with $\alpha \neq 0$, is

$$\nabla \times (2\boldsymbol{\Omega} \times \boldsymbol{u}) = (0, 0, \beta u \ \sin \ \alpha + \beta v \ \cos \alpha). \tag{1.29}$$

By taking the curl of equation (1.23) we find

$$\partial_t \omega + \boldsymbol{u}.\nabla\omega + \beta \sin \alpha u + \beta \cos \alpha v = \nu \nabla^2 \omega \tag{1.30}$$

Assume $\alpha = 0$ gives

$$\partial_t \omega + \mathcal{J}(\omega, \psi) + \beta v = \nu \nabla^2 \omega \tag{1.31}$$

We consider waves propagating along x and y. We take

$$\omega = Ge^{ikx+i\ell y-iwt}, \qquad \psi = Fe^{ikx+i\ell y-iwt} \tag{1.32}$$

where ψ, ω are the vorticity field and stream function and G, F are the amplitude of the oscillation, and the phase is $kx + \ell y - wt$, where k and ℓ are the x and y-wavenumbers and ω is the frequency of the oscillation.

By substituting equation (1.32) into equations (1.31), where the Jacobin term is vanishing, we obtain

$$-i\omega G + \beta(-ik)F = -\nu(k^2 + \ell^2)G. \tag{1.33}$$

By using the expression $G = (k^2 + \ell^2)F$

$$-i\omega G + \frac{-ik\beta G}{k^2 + \ell^2} = -\nu(k^2 + \ell^2)G \tag{1.34}$$

we obtain the first term a wave frequency and second a wave damping term:

$$\omega = \frac{-k\beta}{k^2 + \ell^2} - i\nu(k^2 + \ell^2) \tag{1.35}$$

Equation (1.35) is useful in interpreting hydrodynamic instability involving Rossby waves. In inviscid flow where the viscosity term $\nu = 0$, the Rossby waves propagate westward forever and the equation (1.35) takes the form $\omega = -k\beta/(k^2 + \ell^2)$.

1.3 Linear hydrodynamic stability of Kolmogorov flow

The study of hydrodynamic stability in fluid dynamics is concerned with the onset of instability in fluid flows by determining whether a flow is stable or unstable, and how these instabilities may result in turbulence. Many theoretical and experimental foundations for hydrodynamic stability were laid during the nineteenth century, most notably by Helmholtz, Kelvin, Rayleigh and Reynolds. The foundations of these theories have provided many useful tools for studying hydrodynamic stability, including the Rayleigh equation, and Orr-Sommerfeld equation. (Drazin, 2002).

The fluid flow initially is affected by disturbances. These disturbances are governed by the initial properties of the system, including velocity, pressure, and density. If the flow is stable, any disturbance will not significantly change the initial state of the system and eventually disappear. In an unstable flow, any variation will increase disturbance amplitude, where the system gradually moves away from its initial state forever. Any growing mode of disturbance will lead to the flow being unstable, (Chandrasekhar, 2013).

Instability is often determined by the Reynolds number, a parameter that can vary considerably in different regimes depending on the dominant balances in the Navier-Stokes equations. This dimensionless parameter gives the ratio of inertial terms and viscous terms. Physically, this number represents a ratio between fluid forces (inertial terms) and forces generated by relative motion between layers of fluid (viscous terms). This can be expressed as follows:

$$Re = \frac{inertial}{viscous} = \frac{UL}{\nu} \tag{1.36}$$

where U is the scale of the velocity of the fluid flow, L is the length scale, and ν is the kinematic viscosity. A high Reynolds number indicates turbulence, while a low Reynolds number indicates laminar flow. The linear stability calculation, however, indicates that the flow becomes unstable at a particular value of the critical Reynolds number R_c. The Reynolds number has been named after Osborne Reynolds who conducted an experiment in 1883, and demonstrated that the transformation of laminar flow into "sinuous motion" occurred at a critical Re, which is defined by the mean laminar velocity and the flow rate of the tube at different viscosities and velocities (Joseph, 1976). Kolmogorov flow is driven by a body force, there are some external forces acting on the fluid parcel in the Navier Stokes or momentum equations, such as the Lorentz force, and it is convenient for a rotating system to include the centrifugal and Coriolis forces.

1.3.1 Kolmogorov flow

Kolmogorov flow is a shear flow $\boldsymbol{u} = (0, \sin x)$ in the (x, y) plane, with a unidirectional, sinusoidal velocity profile and has been used in many applications of fluid dynamics to geophysical and astrophysical systems. First posed by Kolmogorov, an elegant solution to the problem of stability of a Kolmogorov flow was given shortly thereafter by Meshalkin and Sinai (1961). These authors used the continued fraction expansions to establish instability properties of the growth rate $p(k)$, where k is a wavenumber in the y direction and determined the critical Reynolds number $R_c = \sqrt{2}$. If Re is slightly larger than $\sqrt{2}$, then large-scale unstable modes occur in y-direction;

with a wavenumber $k \ll 1$. Using this instability property, amplitude equations governing the flow on large space and time scales can be developed. Examples of these equations are presented in Sivashinsky (1985) and Nepomniashchii (1976). It has been shown that for unmagnetized Kolmogorov flows, 2D perturbations are the most unstable (Drazin and Reid, 2004). Instability is affected by introducing some physical parameters to the Kolmogorov flow, including viscosity ν and wavenumber such as vertical wavenumber k, and the Floquet wavenumber ℓ. Kolmogorov flow is subject to a planetary vorticity gradient and body force can be affected by the magnitude of the β- effect, and the angle of the vorticity gradient α, Manfroi and Young (2002).

The stability of a Kolmogorov flow is an interesting problem from the viewpoint of the general theory of hydrodynamic instability. Numerical simulations by She (1987) showed evolution from the most unstable scale to larger scales via an inverse cascade of vortex pairings, for a large scale allowed only in the y-direction. Sivashinsky (1985) showed evolution to a large-scale flow with chaotic temporal fluctuations for large scales in both x-and y-directions.

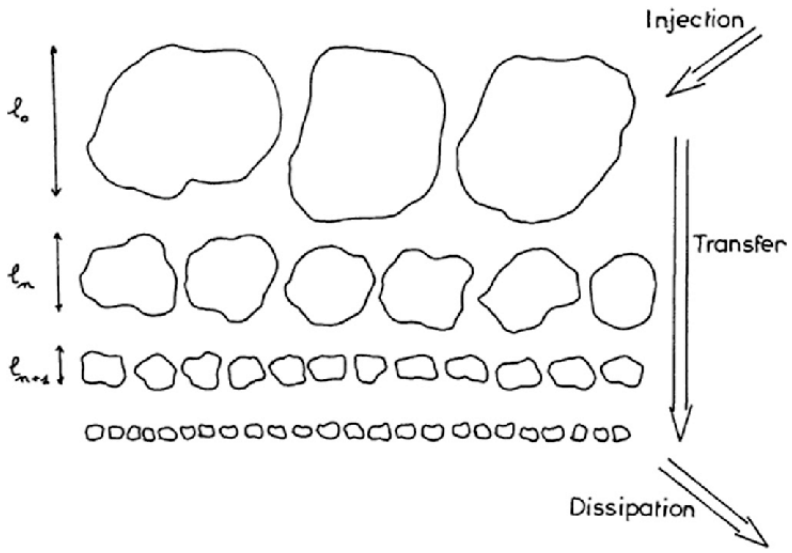

Figure 1.6: Schematic of the energy cascade as derived from the Kolmogorov theory of 1941, illustrates three steps in the energy spectrum of turbulence as it dissipates, taken from (Frisch, Sulem and Nelkin, 1978).

The sketch in figure 1.6 shows a typical energy spectrum of turbulent eddies of wavenumber k. In this study, energy cascades are investigated in high-resolution

3D flows with turbulent configurations under three different scenarios, injection, transfer and dissipation. Kinetic energy is injected into large eddies from the flow and transferred to smaller eddies, which are formed by external forces. However, since the eddies decrease in size geometrically over time, a similar break-up process occurs with these smaller eddies. As a result of these processes, eddy sizes are reduced to the smallest possible size and eddy motions are stabilized, where the non-linear break-up for the large eddies leads to the formation of small eddies. Intermediate eddies are distinct from both the largest and smallest eddies, and they show the evolution of the eddies over time. This process shows the direct energy cascade on a small scale. The transfer of energy between different scales requires that the system's dynamics are nonlinear. In this thesis, we are looking at generation large-scale flow and field and we found the inverse energy cascade (see chapters 6, 8).

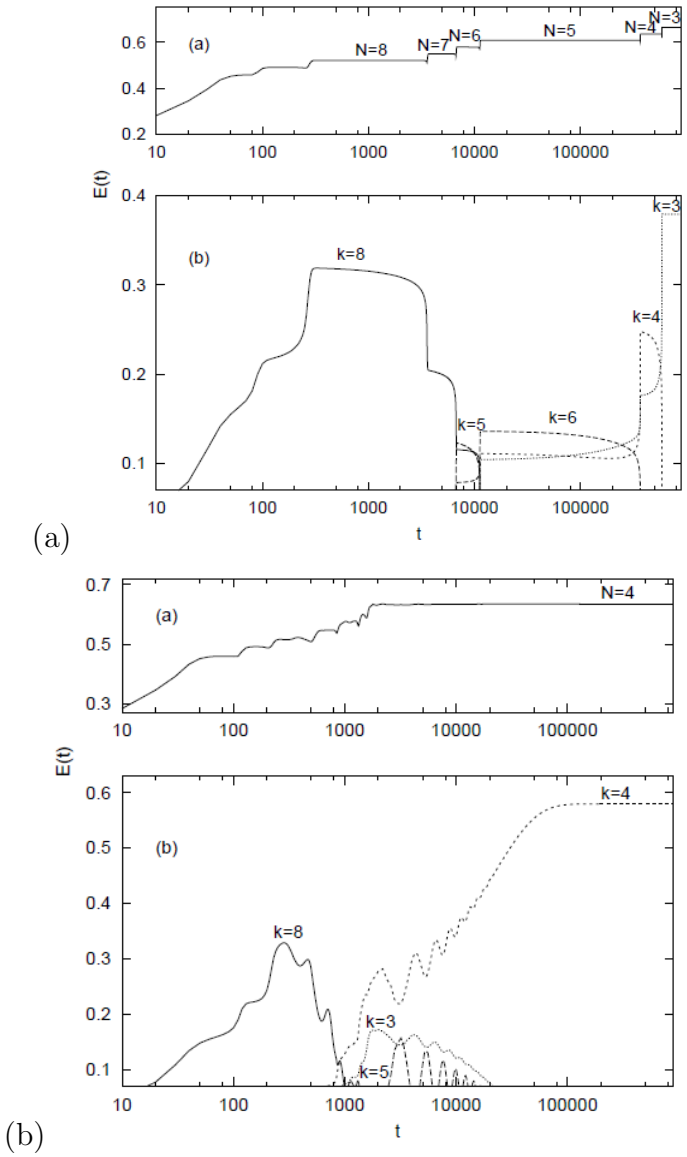

Figure 1.7: Simulation for inverse cascade for kink and anti-kink of the Cahn-Hilliard equation at $N = 8$ to $N = 3$. **Top**: show the evolution of total energy. **Bottom**: shows the evolution of various Fourier modes k (as labelled), panel (a) $\beta = 0$, panel (b) $\beta = 10^{-3}$. The propagation of Rossby waves accelerates the cascade and eventually halts when $N = 4$ (four pairs of kink-antikinks). This figure is taken from Legras, Villone and Frisch (1999).

It has important applications in geophysical systems.Frisch, Legras and Villone (1996) included β effect, giving the gradient of a background planetary vorticity distribution; The gradient is oriented along the x direction and does interact with Kolmogorov flow basic state $\boldsymbol{u_0}$, only on $k \neq 0$ linear mode. These authors used Fourier modes to reduce the question of stability to an algebraic eigenvalue problem and to find the real part of the growth rate corresponding to the most unstable mode, which they called the β-Cahn-Hilliard equation. Simulations show that the inverse cascade of structures to large scales in y is arrested by the β effect. Figure 1.7 shows the

inverse cascade simulation arrested by the β-effect. Panel (a) shows a simulation for $\beta = 0$, where the energy cascade reduces to the PDE of Sivashinsky (1985) and energy moves to wavenumbers k that are smaller and smaller via short kink-anti-kink annihilation episodes. However the inverse cascade of structures to large scales in y is arrested by small values of the β-effect as shown in panel (b).

Kolmogorov's stability problem has been elaborated in several studies by incorporating further physical phenomena. Regarding the geophysical motivation for these stability problems, any orientation of the background vorticity gradient β can be parameterised by the angle α. Here β is the coefficient of the background of the vorticity gradient corresponding to the strength of rotation. In the study of Manfroi and Young (2002), arbitrary angles α are allowed between the Kolmogorov flow and gradient of a background planetary vorticity distribution in the study of linear and non-linear stability evolution, using amplitude equations generalizing previous systems of equations by Sivashinsky (1985) and Frisch, Legras and Villone (1996). Based on their results, it can be concluded that when unstable modes are allowed to take arbitrarily large scales in x and y, the critical Reynolds number is sensitively dependent upon the angle α. With a geophysical motivation Balmforth and Young (2002), considered the sinusoidal Kolmogorov flow in the (x, z) plane with gravity in the z-direction and the flow directed in x, sinusoidal in z. These authors determined the behaviour of linear instabilities, depending on Reynolds, Richardson and Prandtl numbers, and derived an amplitude equation generalising that of (Sivashinsky, 1985). Kolmogorov flow is fundamentally found to be unstable due to negative eddy viscosity in many studies. Eddy viscosity can be described as a flow property in which the growth and decay of the flow are turbulent and can also be described as eddy diffusivity. A classic study (Dubrulle and Frisch, 1991) examined the Kolmogorov instability on large scales with the fastest growing modes, with the growth rate $p = -\nu_E k^2 + ...$ where the eddy viscosity ν_E changes sign from positive below the threshold $Re_c = \sqrt{2}$ to negative above.

1.3.2 Zonostrophic instability

Instabilities in Kolmogorov flows are relevant to the formation of zonal flows in a forced fluid system called zonostrophic instability (Galperin et al., 2006). This process of zonal jet formation has been observed in many different contexts in the simplest possible setting of two-dimensional flow. Parker and Constantinou (2019) interpreted the presence or otherwise of jets in terms of the competition between a positive magnetic eddy viscosity term and a negative, purely hydrodynamic eddy viscosity. Zonal jets also can be observed in a broad range of geophysical flows (Farrell and Ioannou, 2008) with β-effect allowing the propagation of large-scale Rossby waves. Another astrophysical phenomenon in which the jets could play a key role in the generation of the magnetic field by the solar dynamo in the solar tachocline (Tobias, Diamond and Hughes, 2007).

In laboratory plasma experiments, zonal flows are also generated by the nonlinear transfer of energy between small and large scales (Diamond et al., 2007). Many jet regimes can be described concisely by a small number of dimensionless variables, e.g., viscosity, magnetic diffusivity and magnetic field strength. Durston and Gilbert (2016) focused on the couplings between large-scale zonal flow and zonal field in the presence of waves, calculating an effective viscosity and effective magnetic diffusivity, plus an effective cross transport term in which current gradients can drive the zonal vorticity; this and other transport effects are discussed in Chechkin (1999),Kim (2007) and Leprovost and Kim (2009).

In a study of zonal jet properties Galperin et al. (2006), determined the zonostrophic parameter for which $R_\beta > 2$, which is the ratio of scales between the Rhines scale $k_R = \beta/U$ and length-scale of Rossby wave propagation k_β, the scale at which the character of the flow changes from being roughly small scale to being at larger scales, where U represents a typical velocity inside the jet and k_β. Since the work of Rhines (1975) and Williams (1978), the Rhines scale has played an important role in the determination of emergent jets in two-dimensional turbulent flows. Rhines

(1975) studied the interaction between planetary waves and turbulence and concluded that the inverse energy cascade of idealized two-dimensional turbulence is halted by planetary wave motion at large scales, which results in energy transfer into zonal modes and the formation of jets. We briefly reviewed some of what is known about zonal flow in a geophysical context; for more information see the book of Vallis (2017).

1.4 Magnetohydrodynamics

Fluid motion interacts with a background magnetic field through magnetohydrodynamics (MHD). In such systems, (MHD) equations are required to account for both the flow and magnetic field evolution. Alfvén waves can also exist within an MHD system, these being hydromagnetic waves that travel along magnetic field lines and can be generated in any electrically conducting fluid affected by a magnetic field. The Lorentz force is the fundamental force that acts as a restoring force on the fluid flow as it propagates along the magnetic field lines. In this thesis, simplified models of astrophysical systems can be studied by introducing a periodic magnetic field and studying coupled MHD systems.

We first give one observation within the literature related to our work. Tobias, Diamond and Hughes (2007) incorporated a magnetic field aligned with the x-direction of a planar fluid system with a β-effect present, a vorticity gradient in y. The system was driven by a random, time-dependent body force with a given characteristic spatial scale. These authors observed the formation of jets in the x-direction for zero magnetic fields, but then the suppression of jets, even at quite weak field strengths B_0.

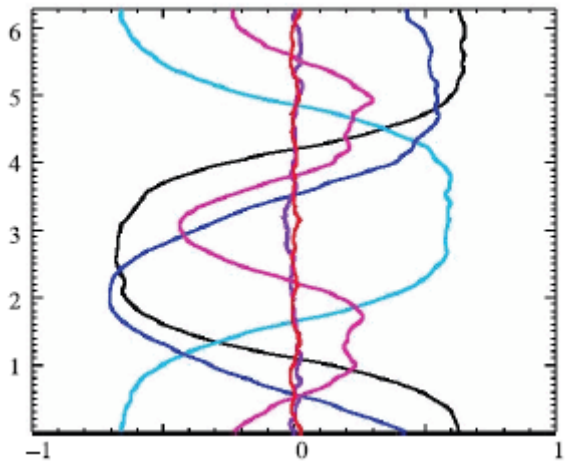

Figure 1.8: Suppression of mean flow U_0 at $\beta = 5$, with $B_0 = 0$ (black), $B_0 = 0.0001$ (dark blue), $B_0 = 0.001$ (light blue) ,$B_0 = 0.005$ (pink), $B_0 = 0.01$ (red), and $B_0 = 0.1$ (purple). Here $\eta = 0.0001$. The figure is taken from Tobias, Diamond and Hughes (2007) .

Initially, their system starts from rest and then reaches a statistically steady state. They found that nonlinear hydrodynamic interactions between Rossby waves generate strong mean zonal flows. However, the presence of a very weak mean magnetic field suppresses the formation of mean flows. In this paper, the system is non-dimensional using the forcing strength G with wavenumber k from 12 to 20. So the strength of the magnetic field & the β effect is measured in these units. They argue that this has implications for the transport of angular momentum in the lower tachocline. An example of their results is shown in figure 1.8 which shows the zonal mean flow suppressed by the mean-field for six values of the weak magnetic field. For small values of B_0 (e.g. $B_0 = 0.001$, light blue), the mean flow remains relatively unchanged in its magnitude and length scale to create a jet structure, whereas the stronger field (e.g. $B_0 = 0.01$, red) lead to complete suppression of jet structure and completely suppresses the mean flow.

For fixed non-dimensional β, forcing and viscosity $\nu = 10^{-4}$, this process was explored by means of a series of runs with varying magnetic field strength B_0 and magnetic diffusivity η and evidence for a threshold scaling law of the suppression of jet formation $B^2 \sim \eta$ was observed in Tobias, Diamond and Hughes (2007). The recent paper Fraser, Cresswell and Garaud (2022) considers a background uniform magnetic field that is aligned with Kolmogorov flow, this has no effect on the basic state flow but

the elasticity of field lines affects perturbations depending on y, through the Lorentz force. These authors observe magnetic suppression of the instability, first discussed by Meshalkin and Sinai (1961) as one might intuitively expect, but also two new families of unstable modes which only exist in the presence of the magnetic field. One family exists for magnetic Prandtl number $P < 1$, for arbitrarily strong magnetic fields, provided the Reynolds number is above a threshold depending on P. This is studied numerically and growth rates are obtained through asymptotic approximations for $k \ll 1$; these authors refer to these modes as Alfvén Dubrulle-Frisch modes as the instability can again be linked to a change of sign of the eddy viscosity (Dubrulle and Frisch, 1991). Although these studies of zonostrophic instability share a number of characteristics with studies of Kolmogorov flow instability, there are however key differences in scaling laws in these studies, which use a forcing with a given spatial scale but a random time scale. There is a fixed force, but other parameters such as viscosity, magnetic diffusivity, magnetic field, and the β-effect, can be varied.

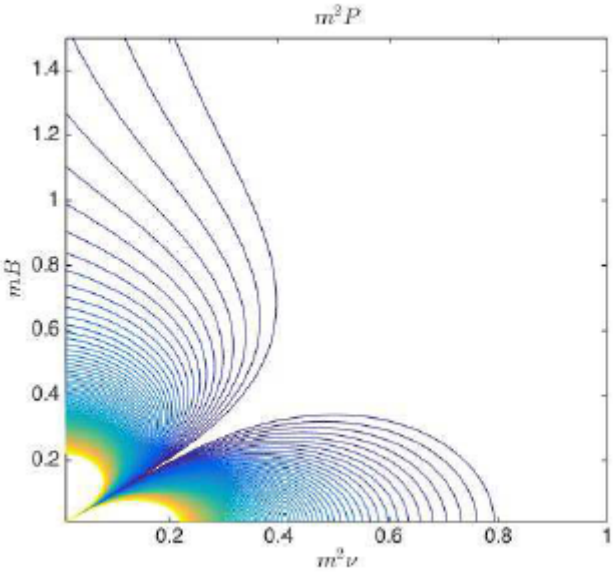

Figure 1.9: Contour plot of instability growth rate m^2p for magnetic field mB_0 against viscocity $m^2\nu$. The figure is taken from Durston and Gilbert (2016).

Instability at large-scale flow with the presence of a zonal field in a flow randomly forced in time with one Fourier mode in space is studied by Durston and Gilbert (2016). They calculated the effect of viscosity and magnetic diffusivity with transport terms in which vorticity gradients can drive the zonal vorticity, they used forcing

which has a given spatial scale but is random in time, and the statistics and strength of the forcing are kept fixed while other parameters such as the viscosity, magnetic diffusivity, magnetic field or β are varied. Here, we give an example from their paper to provide the readers with a sense of the nature of their work. Figure 1.9 shows instability growth rate $m^2 p$ as a function of the $(mB_0, m^2\nu)$-plane, where m is the wavenumber in the x-direction in which the varying values of diffusivity with B_0 lead to the possibility of the field to separate into regions of weaker and stronger B_0 with $\beta = 0$. Typically, they found two branches of instability, the hydrodynamic branch which is suppressed by a weak magnetic field and the second branch which occurs at a strong magnetic field, similar to the result we obtain in this thesis in chapter 4.

1.5 Equations of MHD

MHD describes the interaction of Maxwell's equations governing the electromagnetic field and Navier-Stokes governing the fluid motion. Many applications are attributed to Hannes Alfvén, who was awarded a Nobel Prize in Physics for discovering Alfvén waves, a major contribution to science (Alfvén, 1942). MHD was built on the work of Faraday, Ampere, and Gauss. According to Maxwell, the previous theories of electricity and magnetism can be summarized into four essential laws, which combined, can explain nearly all electromagnetic phenomena. These equations give a simple description of the dynamic coupling between fluid flows and electromagnetic fields. This section begins by introducing the general 3D MHD equations. For details, see e.g. Davidson (2002), Alonso (1999) and Moffatt (1978):

$$\nabla \times \boldsymbol{E} = -\partial_t \boldsymbol{B}, \tag{1.37}$$

$$\nabla \times \boldsymbol{B} = \mu_0(\boldsymbol{J} + \epsilon \partial_t \boldsymbol{E}), \tag{1.38}$$

$$\nabla \cdot \boldsymbol{B} = 0, \tag{1.39}$$

$$\nabla \cdot \boldsymbol{E} = \frac{\rho}{\epsilon_0} \tag{1.40}$$

The fundamental vector fields, $\boldsymbol{E}$ and $\boldsymbol{B}$ represent the electric and magnetic fields, respectively. The current density $\boldsymbol{J}$ is also a vector field. As opposed to their earlier usage in the Navier–Stokes equations, ρ, ϵ and μ now represent charge density, permittivity and magnetic permeability, respectively. Both of these latter parameters are often represented by their free-space values ϵ_0 and μ_0 as a simplification.

Faraday's law (1.37), explains the interaction between a changing magnetic field $\boldsymbol{B}$ and the corresponding electric field $\boldsymbol{E}$. As is shown in (1.38), Ampere's law, modified by Maxwell, describes how magnetic fields can be generated by currents and changes in electric fields, linking magnetic and electric fields.

Based on Ampere's original law (1.38), we approximate $\nabla \times \boldsymbol{B} = \mu \boldsymbol{J}$, $\nabla \cdot \boldsymbol{J} = 0$. Within the approximation that MHD uses, we are able to ignore relativity, quantum mechanics and displacement current $\partial_t \boldsymbol{E}$ in (1.38)(due to considering velocity scales $u \ll c$, where c is the speed of light). Equations (1.37) and (1.38), excluding displacement current, are combined using Ohm's Law, given by

$$\boldsymbol{J} = \sigma(\boldsymbol{E} + \boldsymbol{u} \times \boldsymbol{B}), \tag{1.41}$$

By using the curl of Ohm's law and Faraday's law (1.37), we eliminate the electric field to obtain the induction equation :

$$\partial_t \boldsymbol{B} = \nabla \times (\boldsymbol{u} \times \boldsymbol{B}) - \nabla \times (\eta \nabla \times \boldsymbol{B}). \tag{1.42}$$

The parameter σ denotes the electric conductivity of the medium, and $\eta = (\mu\sigma)^{-1}$ is the magnetic diffusivity. In particular, this equation describes the phenomenon of the magnetic dynamo

$$\partial_t \boldsymbol{B} = -\nabla \times [\frac{\boldsymbol{J}}{\sigma} - (\boldsymbol{u} \times \boldsymbol{B})] \tag{1.43}$$

assuming σ is constant

$$= \frac{-1}{\sigma}\nabla \times [\frac{1}{\mu_0}\nabla \times \boldsymbol{B}] + \nabla \times (\boldsymbol{u} \times \boldsymbol{B}), \tag{1.44}$$

$$= \frac{-1}{\mu_0 \sigma}[\nabla(\nabla \cdot \boldsymbol{B}) - \nabla^2 \boldsymbol{B}] + \nabla \times (\boldsymbol{u} \times \boldsymbol{B}) \tag{1.45}$$

$$\partial_t \boldsymbol{B} = \nabla \times (\boldsymbol{u} \times \boldsymbol{B}) + \underbrace{\frac{1}{\mu_0 \sigma}}_{\eta} \nabla^2 \boldsymbol{B}, \tag{1.46}$$

As in the Navier-Stokes equation, which is similar to the induction equation, the magnetic Reynolds number $R_m = UL/\eta$ represents the ratio of advection, $\nabla \times (\boldsymbol{u} \times \boldsymbol{B})$, to the diffusion, $\eta \nabla^2 \boldsymbol{B}$. The Lorentz force $\boldsymbol{J} \times \boldsymbol{B}$ appears in the Navier-Stokes equation in section (1.2.1), acting back on the flow. The system of equations is effectively nonlinear in $\boldsymbol{B}$. Since flow and magnetic field are divergence-free, it is often useful to reduce the advective term to simplify the equation.

$$\partial_t \boldsymbol{B} + \boldsymbol{u} \cdot \nabla \boldsymbol{B} = \boldsymbol{B} \cdot \nabla \boldsymbol{u} + \eta \nabla^2 \boldsymbol{B}, \tag{1.47}$$

1.5.1 Non-dimensionalized Equations

In dimensional units, the Kolmogorov flow basic state, namely the unidirectional flow in the (x, y)-plane specified by

$$\boldsymbol{u_0} = U_0(0, \sin(x/L_0)) \tag{1.48}$$

We use the length L_0 and velocity U_0 as the basis of our non-dimensionalisation. The non-dimensional Kolmogorov flow is then

$$\boldsymbol{u_0} = (0, \sin x) \tag{1.49}$$

Then we can form a unit of time $T_0 = \frac{L_0}{U_0}$. Let B_0 be the mean magnetic field strength; by identifying dimensions, we measure them by non-dimensional quantities with tilde $\tilde{}$:

$$\boldsymbol{x} = L_0\tilde{x}, \quad T = T_0\tilde{t}, \quad \boldsymbol{u} = U_0\tilde{\boldsymbol{u}}, \quad \boldsymbol{B} = B_0\tilde{\boldsymbol{B}},$$

$$dx = L_0 d\tilde{x}, \quad dt = T_0 d\tilde{t}, \quad \partial_t = \frac{1}{T_0}\tilde{\partial}_t, \quad \nabla = \frac{1}{L_0}\tilde{\nabla}, \quad T_0 = \frac{L_0}{U_0} \tag{1.50}$$

By substituting equation (1.50) into the induction equation we get

$$\partial_t \boldsymbol{B} = \nabla \times (\boldsymbol{u} \times \boldsymbol{B}) + \eta \nabla^2 \boldsymbol{B}, \tag{1.51}$$

$$\frac{1}{T_0}\tilde{\partial}_t(B_0\tilde{\boldsymbol{B}}) = \frac{1}{L_0}\tilde{\nabla}(U_0\tilde{\boldsymbol{u}} \times \tilde{\boldsymbol{B}}B_0) + \frac{\eta}{L_0^2}(\tilde{\nabla})^2(B_0\tilde{\boldsymbol{B}}),$$

$$\frac{U_0}{L_0}\tilde{\partial}_t\tilde{\boldsymbol{B}} = \frac{U_0}{L_0}\tilde{\nabla} \times (\tilde{\boldsymbol{u}} \times \tilde{\boldsymbol{B}}) + \frac{\eta}{L_0^2}(\tilde{\nabla})^2\tilde{\boldsymbol{B}},$$

multiply by $\frac{L_0}{U_0}$

$$\tilde{\partial}_t\tilde{\boldsymbol{B}} = \tilde{\nabla} \times (\tilde{\boldsymbol{u}} \times \tilde{\boldsymbol{B}}) + \frac{L_0\eta}{U_0 L_0^2}\tilde{\nabla}^2\tilde{\boldsymbol{B}}.$$

According to equation 1.51 the evaluation of the magnetic field is controlled by two terms: induction: $\nabla \times (\boldsymbol{u} \times \boldsymbol{B})$ and diffusion: $\eta\nabla^2\boldsymbol{B}$

Dimensionally, their ratio is

$$\frac{\text{induction}}{\text{diffusion}} \sim \frac{U_0 B_0/L_0}{\eta B_0/L_0^2} = \frac{L_0 U_0}{\eta} = R_m. \tag{1.52}$$

We obtain the dimensionless induction equation, by dropping the tilde :

$$\partial_t \boldsymbol{B} = \nabla \times (\boldsymbol{u} \times \boldsymbol{B}) + R_m^{-1}\nabla^2\boldsymbol{B}. \tag{1.53}$$

We also write this as

$$\partial_t \boldsymbol{B} = \nabla \times (\boldsymbol{u} \times \boldsymbol{B}) + \eta\nabla^2\boldsymbol{B} \tag{1.54}$$

where now η is identified as an inverse magnetic Reynolds number, with $R_m = \eta^{-1}$. Likewise, we will write $Re = \nu^{-1}$ as a Reynolds number in the Navier-Stokes equations in the next section.

1.5.2 Diffusive Limit

By making the induction equation dimensionless, we can obtain just one factor in front of the diffusion term that determines what physical process dominates. The evolution of the magnetic field is generated by two terms: Advection $\nabla \times (\boldsymbol{u} \times \boldsymbol{B})$, Diffusion $\eta \nabla^2 \boldsymbol{B}$, the magnetic Reynolds number

$$R_m = \frac{UL}{\eta} = \frac{\text{Advection}}{\text{diffusion}}. \tag{1.55}$$

For the case where $R_m \to \infty$ we have the limit of an ideal fluid. In this case, the magnetic field doesn't diffuse away and the magnetic field lines are frozen with the flow. This is known as Alfvén's theorem.

The dimensionless parameter $R_m = UL/\eta$ significantly impacts identifying the field's evolution. In the case of $R_m \ll 1$, diffusion dominates the field's evolution, whereas an advection dominates in the case of $R_m \gg 1$.

1.5.3 Alfvén waves

The Alfvén wave is a transverse wave that propagates along the direction of the magnetic field. Alfvén waves are now known to play a significant role in the transport of energy and momentum in a variety of geophysical and astrophysical hydromagnetic systems. However, it is difficult to observe this phenomenon directly in the solar atmosphere.

Alfvén waves generate restoring forces based on two physical principles: *Lenz's law* and *Newton's law*, (Davidson, 2002). Figure 1.10 shows a schematic describing the Alfvén waves cycle which propagates along magnetic field lines and is modified by fluid velocity. The fluid flow bends the magnetic field lines due to Alfvén's theorem as shown in panel (b) which resists further curvature by *Lenz's law*, a qualitative law that specifies the direction in which current is induced. The Lorentz force pushes the magnetic field lines to restore equilibrium in panel (c). Increasing the curvature

of the magnetic field lines can enhance the restoring force's strength by the *Newton's second law*, a quantitative law that expresses how the fluid responds to the force. The Lorentz force eventually is strong enough to shift the fluid flow direction thereby returning the field lines to their original position in panel (e).

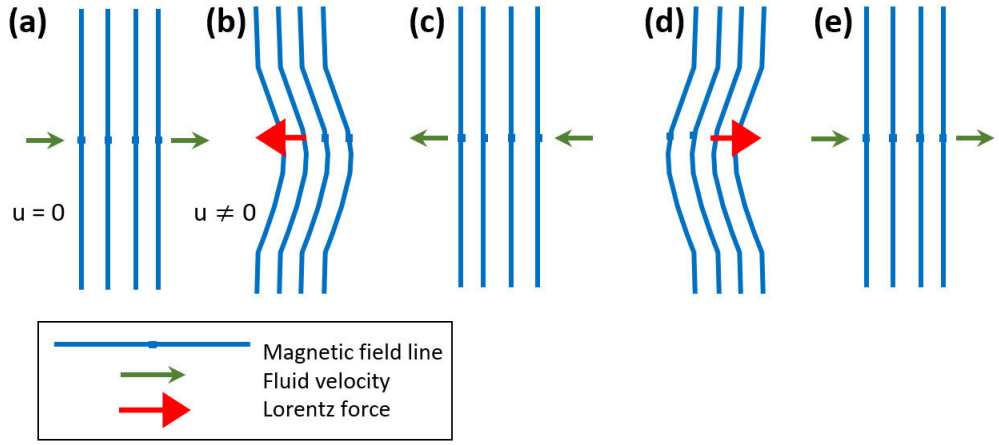

Figure 1.10: Schematic of Alfvén waves restoring by Lorentz force. (a) initial fluid velocity (b) fluid velocity modified the Alfvén waves into the curved lines, (c) the fluid velocity is restored by Lorentz force, where the field lines return to their original configurations, (d) the process of field lines is repeated, (e) the field lines return to the initial configuration.

Consider a viscous, incompressible fluid permeated by a uniform magnetic field $\boldsymbol{B_0} = (0, B_0, 0)$ for Cartesian axes, and $\boldsymbol{B} = \boldsymbol{B_0} + \boldsymbol{b}$, where $\boldsymbol{B_0}$ is a constant vector, and $\boldsymbol{u} = (u(x,t), 0, 0)$, $\boldsymbol{b} = (b(x,t), 0, 0)$. We start with dimensional equations:

$$\rho(\partial_t \boldsymbol{u} + \boldsymbol{u} \cdot \nabla \boldsymbol{u}) = -\nabla p + \frac{1}{\mu_0}(\nabla \times \boldsymbol{B}) \times \boldsymbol{B} + \rho\nu\nabla^2 \boldsymbol{u} \tag{1.56}$$

$$\partial_t \boldsymbol{B} + \boldsymbol{u} \cdot \nabla \boldsymbol{B} = \boldsymbol{B} \cdot \nabla \boldsymbol{u} + \eta\nabla^2 \boldsymbol{B} \tag{1.57}$$

$$\nabla \cdot \boldsymbol{u} = 0, \qquad \nabla \cdot \boldsymbol{B} = 0 \tag{1.58}$$

We can write the momentum equation, as

$$\rho\frac{\partial u}{\partial t} = \frac{B_0}{\mu_0}\frac{\partial b}{\partial x} + \rho\nu\frac{\partial^2 u}{\partial x^2}, \tag{1.59}$$

and the induction equation as

$$\frac{\partial b}{\partial t} = B_0\frac{\partial u}{\partial x} + \eta\frac{\partial^2 b}{\partial x^2}, \tag{1.60}$$

or, more compactly:

$$\rho u_t = \frac{B_0}{\mu_0} b_x + \rho\nu u_{xx}, \qquad b_t = B_0 u_x + \eta b_{xx}, \tag{1.61}$$

For convenience, we can write

$$u_t - \nu u_{xx} - \frac{B_0}{\rho\mu_0} b_x = 0, \qquad -B_0 u_x + b_t - \eta b_{xx} = 0, \tag{1.62}$$

We consider waves propagating along B_0, parallel to the x-axis. We take

$$u = \hat{u} e^{ikx - i\omega t}, \qquad b = \hat{b} e^{ikx - i\omega t}, \tag{1.63}$$

by substituting equation (1.63) into equations (1.62) we obtain

$$\begin{pmatrix} -i\omega + \nu k^2 & \frac{-ikB_0}{\rho\mu_0} \\ -ikB_0 & -i\omega + \eta k^2 \end{pmatrix} \begin{pmatrix} u \\ b \end{pmatrix} = 0 \tag{1.64}$$

We need the determinant of the matrix in (1.64) to vanish for a solution, and so:

$$(-i\omega + \nu k^2)(-i\omega + \eta k^2) + \frac{B_0^2 k^2}{\rho\mu_0} = 0,$$

or

$$-\omega^2 - i\omega k^2 (\nu + \eta) + \nu\eta k^4 + \frac{B_0^2 k^2}{\rho\mu_0} = 0. \tag{1.65}$$

with the quadratic formula

$$ax^2 + bx + c = 0, \qquad x = \frac{-b \pm \sqrt{b^2 - 4ac}}{2a}$$

$$a = -1, \quad b = -ik^2 (\nu + \eta), \quad c = \nu\eta k^4 + \frac{B_0^2 k^2}{\rho\mu_0}$$

$$\omega = \frac{ik^2(\nu + \eta)}{-2} \pm \frac{1}{2}\sqrt{-k^4 (\nu + \eta)^2 + 4\left(\nu\eta k^4 + \frac{B_0^2 k^2}{\rho\mu_0}\right)} \tag{1.66}$$

$$\omega = \frac{ik^2(\nu+\eta)}{-2} \pm \frac{1}{2}\sqrt{k^2\left[-k^2\left(\nu+\eta\right)^2 + 4\left(\nu\eta k^2 + \frac{B_0^2}{\rho\mu_0}\right)\right]}. \tag{1.67}$$

Multiplying by i with $p = -i\omega$ gives:

$$p = \frac{k^2(\nu+\eta)}{-2} \pm ik\sqrt{\frac{-k^2\left(\nu+\eta\right)^2}{4} + \left(\nu\eta k^2 + \frac{B_0^2}{\rho\mu_0}\right)}. \tag{1.68}$$

We can define here a characteristic velocity commonly encountered in analytical studies of MHD waves describing the magnetic state. The Alfvén speed, V_A, arises due to the magnetic field and is defined as:

$$B_0' = V_A = \sqrt{\frac{B_0^2}{\mu_0\rho}} = \frac{B_0}{\sqrt{\mu_0\rho}}. \tag{1.69}$$

$$p = \pm ik\sqrt{B_0'^2 - \frac{1}{4}\left(\nu-\eta\right)^2 k^2} - \frac{1}{2}(\nu+\eta)k^2. \tag{1.70}$$

Different types of solutions are obtained according to whether the discriminant is positive or negative. Equation (1.70) is useful in interpreting magnetic instability involving Alfvén waves; In ideal MHD where the dissipation terms are $\nu = \eta = 0$, the Alfvén waves will repeat forever and the equation (1.70) take the form $p = \pm ikB_0$.

1.6 Physical configuration of Kolmogorov instability

In this thesis, both analytical and numerical results employed previously to study instability are applied to zonostrophic unstable flows. One flow profile and several magnetic field configurations are considered. Much of the previous research on Kolmogorov instabilities focused on the underlying hydrodynamic phase, first observed in the classic work of Meshalkin and Sinai (1961), which is driven by a body force and balanced by viscous dissipation. Manfroi and Young (2002) included a β-effect. We will discuss the magnetic field of the system in subsequent chapters while keeping in mind the results of Manfroi and Young (2002) as a possible direction

for further research. As a general question, we ask: How do MHD effects modify the hydrodynamic instability of Meshalkin and Sinai (1961)? We have provided an answer in seven chapters of this thesis on linear and non-linear systems.

It is important to examine the physical meanings behind Kolmogorov instabilities before we can consider how they may be influenced by magnetic fields. We drew the schematic 1.11, to show the kolmogorov flow in (x, y)- plane, the sinuous velocity profile $\boldsymbol{u_0} = (0, \sin x)$ located along the x-axis. The present study examines a simple periodic model that consists of a two-dimensional viscous fluid with periodic boundary conditions for $0 \leqslant x \leqslant 2\pi, 0 \leqslant y \leqslant 2\pi/k$. The flow becomes unstable due to x-directed sinusoidal motion above a critical Reynolds number $R_c = \sqrt{2}$. For convenience, we will call y the vertical direction and x the horizontal direction. Essentially the perturbation flow varies in the y-direction as e^{iky} indicated by small orange arrows represents the flow instability. The basic Kolmogorov flow is driven by an external force $\boldsymbol{f} = \nu(0, \sin x)$ and continues periodically along the x-axis indicated by the green arrows, the blue vortices taking the same structure in each period.

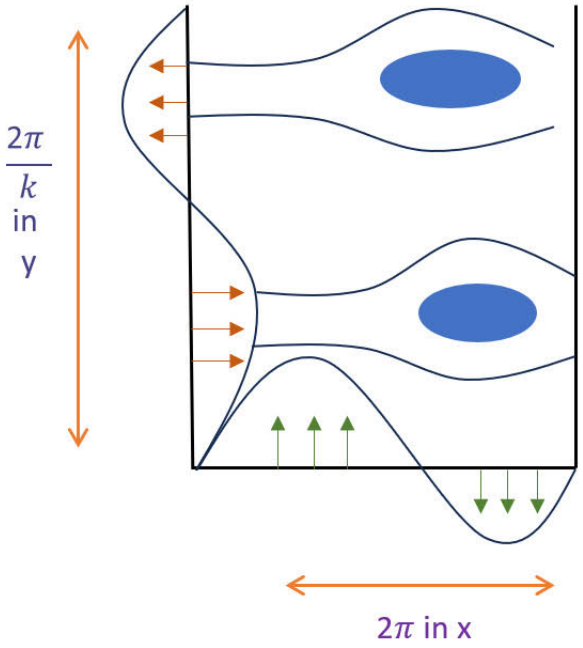

Figure 1.11: Physical set up of the linear problem, with periodic boundary conditions $2\pi/k$ in y-direction, 2π in x-direction, with zero Floquet wavenumber $\ell = 0$. the blue circle is the vortices, the small orange arrows show the instability behaviour, green arrows show Kolmogorov flow.

Figure 1.12 shows instability system periodicity in x and y with boundary conditions in x and y, we take $0 \leqslant y \leqslant 2\pi/k$ and for $\ell > 0$ we take $0 < x < 2\pi/\ell$. The system now includes the small values of Floquet wavenumber ℓ (e.g. $\ell = 1/2, 1/3, ...$), the flow is extended and repeated the same instability structure along the x-axis, for $\ell = 1/2$ the period is 4π and for $\ell = 1/3$ the period is 6π. More generally including $\ell \neq 0$ allows a greater scale of instability in the system. In this thesis, we look for instability at a large scale, which is $k \ll 1$ and $\ell \ll 1$, the Floquet wavenumber in the range $-0.5 < \ell < 0.5$, though in the thesis we also find instabilities that are not particularly large scale, sometimes.

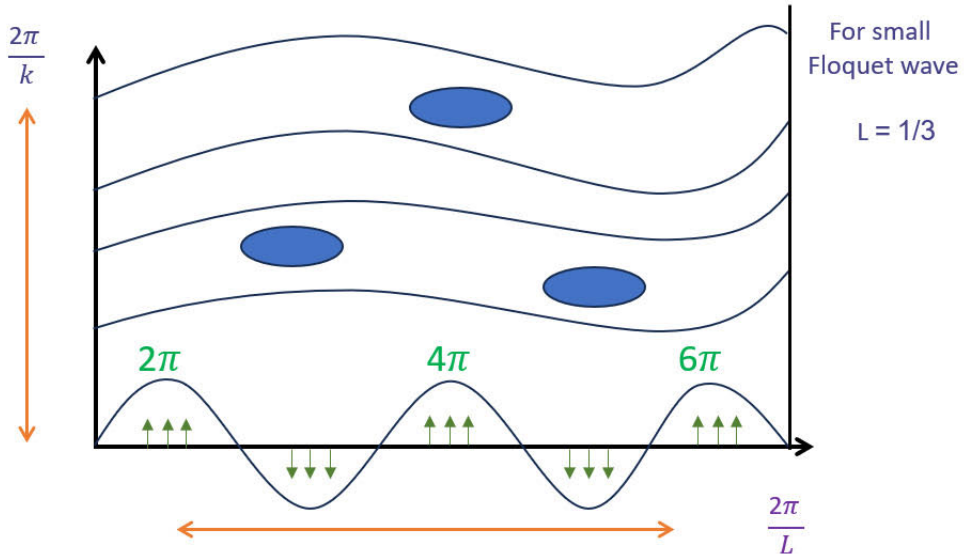

Figure 1.12: Physical set up of the linear problem, with periodic boundary conditions $2\pi/k$ in y-direction, $2\pi/\ell$ in x-direction, with small Floquet wavenumber $\ell = 1/3$, the blue circle is the vortices, the small green arrows show the Kolmogorov flow.

A schematic representation of a non-linear problem is shown in Figure 1.13, where linear growth does not continue indefinitely but evolves into a non-linear process over time. By taking the logarithm of the perturbation Kinetic energy (PKE), we found that our simulation approach started with an initial transient shown in the dark blue curve, then passed through a phase of linear instability that agrees with the linear scale (dashed light blue), and then eventually reached a point of non-linear saturation over time.

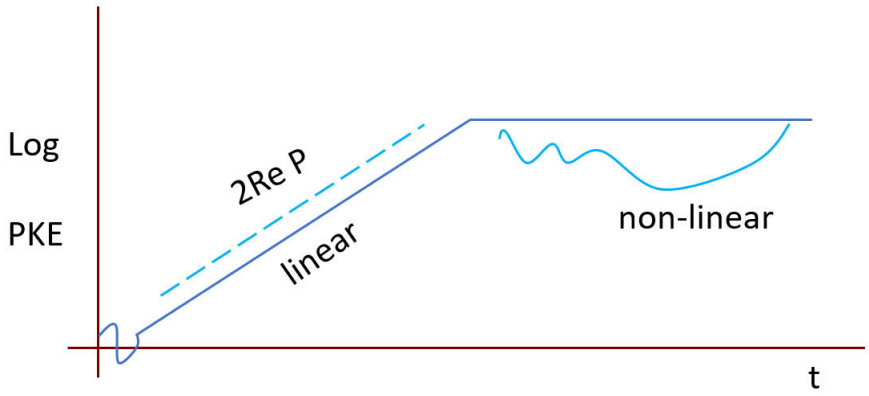

Figure 1.13: Schematic of non-linear evolution, where PKE is the perturbation kinetic energy, $\log PKE \propto 2\,\mathrm{Re}\,pt + C$, t is the simulation time, the dashed blue line is the periodic growth rate from linear theory. In our simulation, we take the logarithm of perturbation energy to show the agreement of the linear growth rate of instability.

Numerical results for this research are performed with the Matlab framework in

the linear regime and the Dedalus framework in the non-linear regime, with a 2D numerical code designed to investigate the dynamics of instabilities across a range of spatial and temporal scales to evaluate their behaviour. While eigenmodes do not interact in linear problems, they can transfer magnetic energy and kinetic energy between each other in non-linear problems. We present some simulations of the non-linear evolution of this system in the last three chapters (6, 7,8) by using direct numerical simulation demonstrating linear growth rate consistent with the prediction from linear stability analysis and finding the saturation of instability in some cases.

1.7 Thesis summary

In this thesis, we consider the steady Kolmogorov flow $\boldsymbol{u_0} = (0, \sin x)$ and consider the effect on its stability from the magnetic field in the x-direction and y-direction. In chapter 2, we set up the equations to solve for linear perturbations and discuss the hydrodynamic problem relevant to Meshalkin and Sinai (1961) and with the β-effect approximation as in Manfroi and Young (2002). We considered these as a test in preparation for the novel results in other chapters. In chapter 3 we solve the linear equations for the vertical field and present numerical and analytical results, showing growth rates, thresholds and unstable mode structure. This chapter has common elements with the recent paper Fraser, Cresswell and Garaud (2022) in the case of the strong vertical field branch even though we give an alternative, matrix-based derivation of the asymptotic growth rate they obtained. Chapter4 sets up the equations for the horizontal magnetic field with $\ell = 0$, with numerical results supported by analytical approximations with $\ell = 0$ in the limit $k \to 0$. We also found the threshold of instability for $\ell \neq 0$ given in chapter 5. To keep this chapter ordered, we have developed the analytical theory in appendices given in (A,B,C). By reducing the system, and expanding the matrix and growth rate, we find the eigenvalue and eigenvector approximately and subsequently determine the instability threshold.

In chapter 5 we include the equations for vertical field with non-zero Floquet wavenumber ℓ. We also present some analytical and numerical results with a general magnetic field at various values of angle γ, the angle between the vertical field and y-axis and zero Floquet wavenumber $\ell = 0$. We use the theoretical approximation in the limit of $k \to 0$ and find the theory works at small γ. Each chapter is supported by analytical theory approximation in the limit $k \to 0$. The method employed is perturbation theory for eigenvalues and eigenvectors of a matrix; it is equivalent to other methods used by other authors e.g. Manfroi and Young (2002) and Fraser, Cresswell and Garaud (2022). However, we find it is a systematic way of handling the problem of increasing complexity and giving insight into the coupling between the flow and field modes that can drive instability.

We observe that the growth rate in the linear problems cannot stop forever. We track the nonlinear evolution of linear instabilities. Starting from the hydrodynamic chapter 6 we solve the equations numerically using the Dedalus framework, where we choose an individual point in parameter space from the linear results and simulate the field at these parameter values. We follow this strategy for vertical magnetic field in chapter 7 and horizontal magnetic field in chapter 8. Chapter 9 offers conclusions and ideas for future work.

2. Work of Meshalkin and Sinai (1961) and Manfroi and Young (2002)

This chapter begins by establishing the basis of our work. We reproduce here the results of Meshalkin and Sinai (1961) and Manfroi and Young (2002), but with a different derivation for the system, then obtain the instability growth rate.

2.1 Non-dimensional Governing equations

Throughout the research in this thesis, we consider an incompressible flow in a Cartesian domain with coordinates (x, y, t). For Kolmogorov stability flow, the basic state is fixed while the forcing is modified to maintain this: the control parameter is a Reynolds number (Godreche and Manneville, 1998). By taking the curl of the non-dimensional equation (1.16) we find:

$$\partial_t \boldsymbol{\omega} = \nabla \times (\boldsymbol{u} \times \boldsymbol{\omega}) + \nu \nabla^2 \boldsymbol{\omega} + \nabla \times \boldsymbol{f}, \tag{2.1}$$

or in another form

$$\partial_t \boldsymbol{\omega} + \boldsymbol{u} \cdot \nabla \boldsymbol{\omega} = \boldsymbol{\omega} \cdot \nabla \boldsymbol{u} + \nu \nabla^2 \boldsymbol{\omega} + \boldsymbol{g}, \tag{2.2}$$

The relations between velocity $\boldsymbol{u}$ and stream function are defined as:

$$\boldsymbol{u} = (\partial_y \Psi, -\partial_x \Psi, 0) \qquad \boldsymbol{\omega} = (0, 0, \omega), \qquad \omega = -\nabla^2 \Psi, \qquad \boldsymbol{g} = \nabla \times \boldsymbol{f} = (0, 0, g) \tag{2.3}$$

which yields:

$$\partial_t \omega + \underbrace{\partial_x \omega . \partial_y \Psi - \partial_y \omega . \partial_x \Psi}_{\mathcal{J}(\omega, \Psi)} = \underbrace{\hat{\boldsymbol{z}} \cdot (\boldsymbol{\omega} \cdot \nabla \boldsymbol{u})}_{=0} + \nu \nabla^2 \omega + g. \tag{2.4}$$

The full version of the vorticity stream function system takes the form

$$\partial_t \omega + \underbrace{\partial_x \omega . \partial_y \Psi - \partial_y \omega . \partial_x \Psi}_{\mathcal{J}(\omega, \Psi)} = \nu \nabla^2 \omega + g, \tag{2.5}$$

where $\mathcal{J}$ stands for the Jacobian of two functions in the plane ω, ψ. We state the basic state

$$\boldsymbol{u_0} = (0, \sin x, 0), \quad \Psi_0 = \cos x, \quad \omega_0 = \cos x, \quad \boldsymbol{\omega} = \nabla \times \boldsymbol{u}, \quad g = \nu \cos x. \tag{2.6}$$

This flow is maintained by the force $\boldsymbol{g} = (0, 0, g)$. The equation governing an infinitesimal disturbance $\psi(x, y, t)$ (superimposed upon the basic flow ψ_0) follows by linearising the equations, setting

$$\boldsymbol{u} = \boldsymbol{u}_0 + \boldsymbol{u}_1, \qquad \Psi = \Psi_0 + \Psi_1, \qquad \omega = \omega_0 + \omega_1, \tag{2.7}$$

Where $(\boldsymbol{u}_1, \Psi_1, \omega_1)$ are small perturbations. We substitute equation (2.7) into (2.5), we obtain

$$\partial_t \omega_1 - \sin x \ \Psi_{1y} + \sin x \ \omega_{1y} = \nu \nabla^2 \omega_1. \tag{2.8}$$

Then we drop the subscript "1" shortly and take the Fourier transform. The point behind this analysis is to get the exact equations for (Ψ, ω) from linearising.

We assume the perturbation $\psi = \Psi_1$ is periodic in y ($\psi \propto e^{iky}$) with period $2\pi/k$ and varies in time ($\psi \propto e^{pt}$), we are imposing $F(x)$ as a periodic function with period 2π

and we will modify this later when we introduce the Floquet wavenumber

$$\psi = \Psi_1 = F(x)e^{iky+pt} + c.c. = e^{iky+pt} \sum_{n=-\infty}^{\infty} F_n e^{inx} + c.c. \quad , \tag{2.9}$$

$$\omega = \omega_1 = G(x)e^{iky+pt} + c.c. = e^{iky+pt} \sum_{n=-\infty}^{\infty} G_n e^{inx} + c.c. \quad . \tag{2.10}$$

Then for any initial disturbance, the solution of equation (2.8) is a linear superposition over different wavenumbers k. First we substitute ψ, ω in terms of F, G in equation (2.8) to give:

$$pG - ik \sin x \; F + ik \sin x \; G = -\nu(G_{xx} + k^2 G), \tag{2.11}$$

Next, we use

$$F \sin x = \frac{1}{2i} \sum_{n=-\infty}^{\infty} [F_n e^{i(n+1)x} - F_n e^{i(n-1)x}], \tag{2.12}$$

which is

$$F \sin x = \frac{1}{2i} \sum_{n=-\infty}^{\infty} [F_{n-1} e^{inx} - F_{n+1} e^{inx}], \tag{2.13}$$

By substituting equations (2.9, 2.10) and (2.13) into equation (2.8), we obtain :

$$pG_n - \frac{k}{2}(F_{n-1} - F_{n+1}) + \frac{k}{2}(G_{n-1} - G_{n+1}) = -\nu(k^2 + n^2)G_n \tag{2.14}$$

we replace the LHS term F in equation (2.11) in terms of G_n using the expression

$$G_n = (k^2 + n^2)F_n$$

which gives:

$$pG_n = \frac{k}{2}\left[\frac{1}{(n-1)^2 + k^2} - 1\right] G_{n-1} - \frac{k}{2}\left[\frac{1}{(n+1)^2 + k^2} - 1\right] G_{n+1} = -\nu(k^2 + n^2)G_n, \tag{2.15}$$

This system is an eigenvalue problem, for the growth rate $p(k, \nu)$, which may be solved numerically in the Matlab framework by taking the whole system (2.15) in terms of G_n and filling the matrix entries as described in the next section (2.4).

2.2 Linear stability analysis

The linear stability analysis is the standard approach to analyzing flow instability. It is also effective for problems involving high Reynolds numbers and complex geometry, for which stability analysis is very expensive.

The linear stability of simple shear flow configurations has been extensively examined. Drazin (2002) provides an overall understanding of the nature of more complex flow profiles early in their development before unstable perturbations grow too large. We consider a planar Kolmogorov flow, and investigate the behaviour of arbitrary 2-D perturbations. These perturbations are governed by the linearized Navier–Stokes equation (NS), which is derived in section (3.2.1). The equation for the vector potential has two dimensions in space and one in time. This means that a Fourier decomposition is appropriate, we consider solutions of the form (3.37) and then maximise over eigenvalues p. These values of p are the eigenvalues of the system and the corresponding fields are their eigenfunctions. Together, they are called the eigenmodes.

We investigate the linear stability of Kolmogorov flow for possible wavenumber k in y-direction in equations (3.28 - 3.30). The eigenvalue p for the unknown growth rate $p = p_r + ip_i$ can be complex; if the real part of the eigenvalue p_r is positive for any value of the wavenumber, the system is unstable to disturbances of this wavenumber. In the absence of such an unstable state, the system is stable. In other words, we say:

$$p_r < 0 : \text{for all } k \rightarrow \text{stable},$$

$$p_r > 0 : \text{for some } k \rightarrow \text{unstable},$$

$$p_r = 0 : \text{for some } k \rightarrow \text{neutrally stable}.$$

For $p_r = 0$, there can be two types of marginal states, depending on whether the imaginary part of eigenvalue p_i is zero or non-zero. If $p_i = 0$, then the instability is

characterized by a stationary pattern of motion. However, if $p_i \neq 0$ in the frequency domain we have complex conjugate modes $p = p_r + ip_i$ and $p = p_r - ip_i$ corresponding to propagating disturbances

2.3 Eigenvalue problem

The fundamental solution for our problem is derived by using the Fourier transform in space and time with two exponential factors, one containing the wavenumber in e^{iky} for spatial dependence and the other containing the frequency and growth rate in e^{pt} for time dependence. One obtains an infinite-dimensional algebraic eigenvalue problem, with Kolmogorov flow (invariant in the y direction) and eigenvalues depending on the k-wavenumber.

2.4 Numerical methods for the hydrodynamic case

We have written the fields as Fourier series in equations F_n (2.9), G_n (2.10). For a numerical solution to the eigenvalues problem, we restrict $-N \leq n \leq N$ for some integer N (typical value $16, 32$), and we sometimes vary N to check our results. We solve a discrete matrix problem written in the tridiagonal form.

To show how the matrix is organised: first, we have a Kolmogorov flow confined to the region $0 \leq x < 2\pi$, $0 \leq y < 2\pi/k$. We have exponential dependence on y and the appearance of the wavenumber k in y-direction. Using equation (2.15) and expanding, the following algebraic eigenvalue problem for the known coefficients is

obtained (2.18).

$$p\begin{pmatrix} G_{-N} \\ G_{-N+1} \\ \vdots \\ G_{N-1} \\ G_N \end{pmatrix} = M \begin{pmatrix} G_{-N} \\ G_{-N+1} \\ \vdots \\ G_{N-1} \\ G_N \end{pmatrix} \qquad p\begin{pmatrix} \vdots \\ G_n \\ \vdots \end{pmatrix} = \left(\begin{array}{ccc|ccc|ccc} \ddots & \ddots & & \ddots & \ddots & & \ddots & & \\ \hline \ddots & a_n & & b_n & c_n & & \ddots & & \\ \hline \ddots & \ddots & & \ddots & \ddots & & \ddots & & \end{array}\right) \begin{pmatrix} \vdots \\ G_n \\ \vdots \end{pmatrix}, \tag{2.16}$$

Comparing linear equation (2.15) with equation (2.17) and then writing the coefficients

$$pG_n = a_n G_{n-1} + b_n G_n + c_n G_{n+1}. \tag{2.17}$$

We set the matrix elements for the matrix rows; we have

$$a_n = \frac{-k}{2} + \frac{k}{2}\left(\frac{1}{(n-1)^2+k^2}\right), \quad b_n = -\nu(n^2+k^2), \quad c_n = \frac{k}{2} - \frac{k}{2}\left(\frac{1}{(n+1)^2+k^2}\right), \tag{2.18}$$

As stated above each row i of the matrix corresponds to the wavenumber $n = i-1-N$, hence $i = 1$ gives $n = -N$ we will further let $i = 2N+1$ corresponding to the wavenumber $n = N$ with

$$M_{ij} = \begin{cases} a_n & j = i-1, \\ b_n & j = i, \\ c_n & j = i+1. \end{cases} \qquad \text{for} \quad n = -N+i-1. \tag{2.19}$$

At a specified truncation N, the $(2N+1)\times(2N+1)$ matrix is set up in Matlab; we fill the matrix entries as described here. Then, call *eig* to determine the eigenvalues p with maximum real part $p(\nu, k)$ is calculated. For a given parameter set (k, ν), the maximum real growth rate is defined as

$$\operatorname{Re} p_{\max}(\nu) = \max_k \operatorname{Re} p(k, \nu), \tag{2.20}$$

The maximisation is then taken over a finite range of k-values, typically 100 values

in the range $0 < k < 1$, and any complex eigenvalues appear in complex conjugate pairs. We let $k_{\max}(\nu)$ be the corresponding maximising wavenumber. It is then often instructive to plot $\mathrm{Re}\, p_{\max}$ and $k_{\max}$.

2.4.1 Critical Reynolds number

Based on stability theory it is appropriate to introduce the critical Reynolds number as follows:

$$R < R_c \text{ the flow is stable.}$$

$$R > R_c \text{ the flow is unstable.}$$

The critical Reynolds number is difficult to derive analytically but may be determined by numerical methods. One assumption is that R_c corresponds to the lowest Reynolds number for which instability can be sustained. This assumption, however, does not hold for all flows. In this case, it is necessary to introduce a separate critical Reynolds number R_c below which the flow will become laminar. Examples of critical Reynolds numbers compiled from literature are shown in Joseph (1976) and Drazin (2002).

The hydrodynamic system is governed by the parameter space (k, ν) and the forcing g. We compare our results with the Meshalkin and Sinai (1961) results, as shown in figure 2.1(a). In order to establish the growth rate properties $p(k)$, the same analysis was conducted in panel 2.1(b) with different scaling of the inverse of Reynolds number ν and find unstable mode and stable mode. We will usually refer to the inverse Reynolds number ν as viscosity for simplicity.

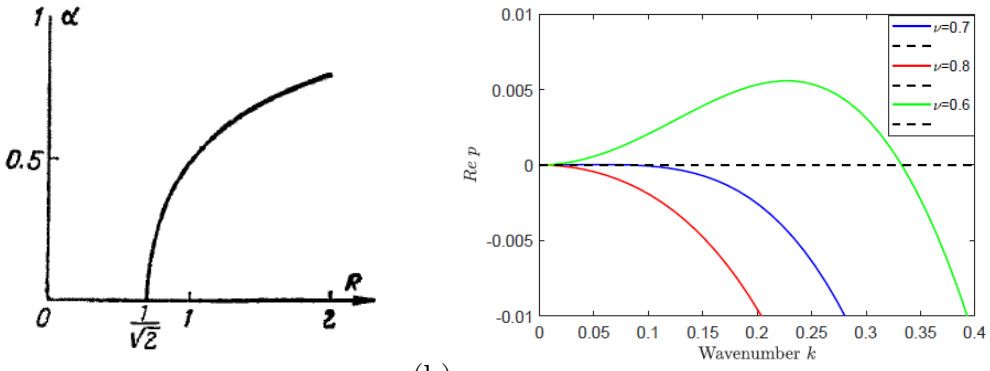

(a) (b)

Figure 2.1: Instability growth rate of the $\mathrm{Re}\, p_{\max}$ against k. Panel (a) shows the growth rate for the Reynolds number R_{M+S} taken from Meshalkin and Sinai (1961), panel (b) shows the growth rate $p(k,\nu)$ for the three values of the inverse Reynolds number $\nu = 1/\sqrt{2} \approx 0.7$ (blue),$\nu = 0.6$ (green), $\nu = 0.8$ (red).

Figure 2.1 shows the maximum growth rate $\mathrm{Re}\, p$ against the wavenumber k. Panel (a) shows that the unstable and stable modes determined by critical Reynolds number of $R_{cM+S} = \frac{1}{\sqrt{2}}$, where the subscript (M+S) refer to Meshalkin and Sinai (1961), the instability occurred above the threshold $R_{cM+S} = \frac{1}{\sqrt{2}}$ and stable below. Panel (b) shows the threshold of instability at $\nu_c \approx 0.7$ (solid blue) determined by $p = 0$ (dashed black) beginning with $k = 0$, the stable mode observed at $\nu = 0.8 > \nu_c$ (solid red). While the most unstable mode occurs at $\nu = 0.6 < \nu_c$ (solid green) occurring between $0 \leqslant k \leqslant 0.35$. This describes precisely the instability region, before going on to incorporate a magnetic field where no results are known. We obtain the instability threshold $1/\sqrt{2}$ analytically (details in chapter 4).

To explain the non-dimensional inverse Reynolds number in figure 2.1(b), we compare the Meshalkin and Sinai (1961) equations with our equations (2.8) and see that ours differ from theirs. They used two dimensionless parameters γ and ν and they considered $\frac{\gamma}{\nu} = 2$ without loss of generality & so ultimately only use one dimensionless parameter, which is ν. Also, they write the vorticity as $\omega = \nabla^2\psi$ whereas we have $\omega = -\nabla^2\psi$ because they have taken $\boldsymbol{u} = (-\psi_x, \psi_y)$ and they appear to have switched the axes x, y compared with mine. Meshalkin and Sinai (1961) expressed the vorticity

equation in the form

$$\partial_t \nabla^2 \Psi + \frac{\gamma}{\nu} \sin y \, \partial_x (\Psi + \nabla^2 \Psi) = \nu \nabla^4 \Psi \quad , \tag{2.21}$$

By dividing the equation (2.21) by $\frac{\nu}{\gamma}$ we obtain :

$$\frac{\nu}{\gamma} \, \partial_t \nabla^2 \Psi + \sin y \, \partial_x (\Psi + \nabla^2 \Psi) = \frac{\nu^2}{\gamma} \, \nabla^4 \Psi, \tag{2.22}$$

They take the scaling $\frac{2\nu}{\gamma} = 1$, where $\gamma = 2\nu$. Hence, the equation becomes.

$$\frac{1}{2} \, \partial_t \nabla^2 \Psi + \sin y \, \partial_x (\Psi + \nabla^2 \Psi) = \frac{\nu_{M+S}}{2} \, \nabla^4 \Psi. \tag{2.23}$$

The inverse of the Reynolds number for Meshalkin and Sinai (1961) is twice the inverse Reynolds number of our work which takes the form

$$R_{cA+G} = \sqrt{2}, \qquad R_{cM+S} = \frac{1}{\nu_{cM+S}} = \frac{1}{\sqrt{2}}. \tag{2.24}$$

$$\nu_{cA+G} = \frac{\nu_{cM+S}}{2} = \frac{1}{\sqrt{2}}, \qquad \nu_{cM+S} = \frac{2}{\sqrt{2}} = \sqrt{2}, \tag{2.25}$$

The subscripts (A+G) refer to Algatheem and Gilbert, respectively, and the subscripts (M+S) refer to Meshalkin and Sinai (1961). with these notes, there is an agreement between their results & ours in figure 2.1.

2.4.2 Purely hydrodynamic solutions

A typical example of hydrodynamic instability of Kolmogorov flows with a perturbation that grows linearly, is shown in figure (2.2).

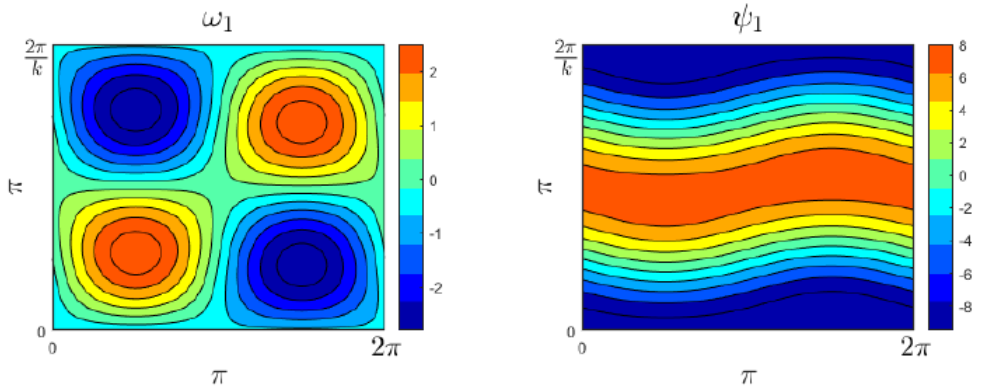

(a)

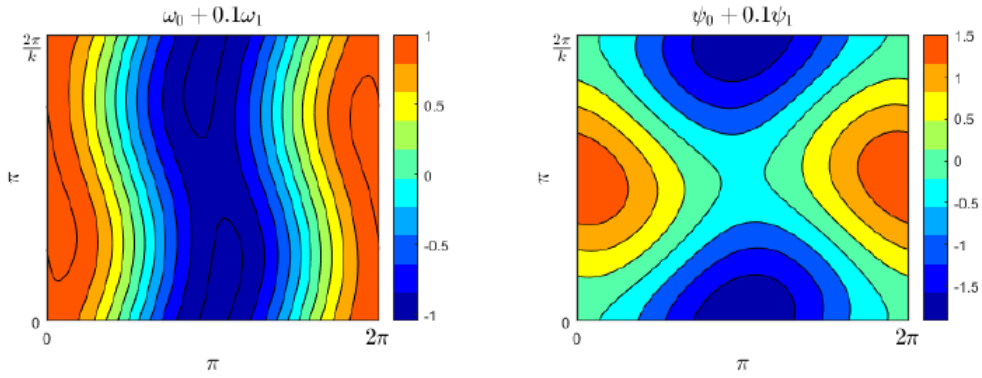

(b)

Figure 2.2: Contour plot of typical unstable mode with $\nu = 0.6, k = 0.25$. Panel (a) shows the perturbation vorticity field ω_1 and stream function ψ_1 of flow, panel (b) shows the basic state of vorticity and stream function with small perturbation $\psi_0 + 0.1\psi_1$, $\omega_0 + 0.1\omega_1$.

We calculate the stream function F_n and vorticity field G_n from the Fourier series equation (2.9, 2.10) and reconstitute the field. According to the expansion of stream function ψ

$$\Psi = \Psi_0 + \Psi_1 + ...$$

$$\Psi = \Psi_0 + ae^{pt} \sum_{n=-\infty}^{\infty} e^{inx+iky} F_n + c.c. \tag{2.26}$$

The typical unstable mode is shown in figure 2.2 for parameter values corresponding to the peak of the highest curve (solid green). We observed that the perturbation vorticity field has formed coherent vortices and the streamlines of flow Ψ_1 exhibit zonostrophic jet with a constant colour that gives streamlines, with (u, v) tangential to the curve. The blue region represents the minimum in $\Psi(x, y)$ gives a clockwise flow. The red region represents the maximum in $\Psi(x, y)$ roughly at $y = \pi$ giving anticlockwise flow.

Panel (b) shows the basic state of the stream function ψ_0 & vorticity field ω_0 with small perturbation. Hence, to get a sense of a flow evolving we multiply the perturbation with a small amount $a = 0.1$. We can see clearly that the system evolves to form a sausage mode in ψ_1 and a sinuous mode in ω_1 with small vortices. Our motivation is to investigate whether this behaviour persists when magnetic fields are present on top of pure hydrodynamics (see chapters 3-4).

2.5 Unstable flow with β effect

Linear stability with geophysical Kolmogorov flow has been studied by (Lorenz, 1972; Gill, 1974) who considered the stability with $\alpha = 0$ in an inviscid case where α is the angle between the flow direction and the background vorticity gradient. Frisch, Legras and Villone (1996) considered instability with $\alpha = \pi/2$. We will limit our study here to Manfroi and Young (2002), who considered the stability of Kolmogorov flow with β-effect in the viscous case and the intermediate value of $0 < \alpha < \pi/2$ and found instability at critical Reynolds number $R_c = \sqrt{2}$. They conclude that the parameter β plays an important role in reducing the critical Reynolds number from $\sqrt{2} \to 0$. From this point, we make a comparison between our results and their results, with different scaling of β values.

We start from vorticity equation (1.30), and we obtain:

$$\partial_t \omega + \boldsymbol{u} \cdot \nabla \omega + \beta \sin\alpha \; u + \beta \cos\alpha \; v = \nu \nabla^2 \omega + g, \tag{2.27}$$

by substituting equation (2.3) into equation (2.27) we obtain:

$$\partial_t \omega + \mathcal{J}(\omega, \Psi) + \beta \sin\alpha \Psi_y - \beta \cos\alpha \Psi_x = \nu \nabla^2 \omega + g, \tag{2.28}$$

where $\mathcal{J}$ is the Jacobian of ω and ψ and we set the basic state.

$$\boldsymbol{u_0} = (0, \sin x), \qquad \Psi_0 = \cos x, \qquad \omega_0 = \cos x, \tag{2.29}$$

By substituting the basic state (2.29) in equation (2.28), we obtain the force g

$$-\beta\cos\alpha\ \underbrace{\psi_{0x}}_{-\sin x}-\underbrace{\nu\nabla^2\omega_0}_{-\nu\cos x}=g,\qquad g=\beta\cos\alpha\sin x+\nu\cos x. \tag{2.30}$$

By linearising the equation (2.28) using equations (2.31), and neglecting quadratic terms we obtain the linear equation with β

$$\boldsymbol{u}=\boldsymbol{u}_0+\boldsymbol{u}_1,\qquad \Psi=\Psi_0+\Psi_1,\qquad \omega=\omega_0+\omega_1, \tag{2.31}$$

$$\partial_t w_1+\Psi_{1y}\,\omega_{0x}-\Psi_{0x}\,\omega_{1y}+\beta\sin\alpha\ \Psi_{1y}-\beta\cos\alpha\ \Psi_{1x}=\nu\nabla^2\omega_1 \tag{2.32}$$

By substituting equation (2.29) into equation (2.32), the linearized equation becomes

$$\partial_t\omega_1-\sin x\ \Psi_{1y}+\sin x\ \omega_{1y}+\beta\sin\alpha\ \Psi_{1y}-\beta\cos\alpha\ \Psi_{1x}=\nu\nabla^2\omega_1. \tag{2.33}$$

We substitute the Fourier expansion of ψ and ω of equations (2.9 - 2.10) into equation (2.33), we obtain:

$$pG-ik\sin x\ F+ik\ \sin x\ G+ik\ \beta\sin\alpha\ F-in\beta\cos\alpha\ F=-\nu(G_{xx}+k^2G) \tag{2.34}$$

$$pG_n-\frac{k}{2}(F_{n-1}-F_{n+1})+\frac{k}{2}(G_{n-1}-G_{n+1})+ik\beta\sin\alpha\ F_n-in\beta\cos\alpha\ F_n=-\nu(k^2+n^2)G_n. \tag{2.35}$$

where k is the wavenumber in the y direction and n is the wavenumber in the x direction for each Fourier component. By using the Fourier series in equation (2.13), the equation (2.35) becomes:

$$pG_n=\frac{k}{2}\left[\frac{1}{(n-1)^2+k^2}-1\right]G_{n-1}-\frac{k}{2}\left[\frac{1}{(n+1)^2+k^2}-1\right]G_{n+1}-ik\beta\ \sin\alpha F_n$$

$$+in\beta\ \cos\alpha F_n=-\nu(k^2+n^2)G_n, \tag{2.36}$$

with

$$G_n=(k^2+n^2)F_n.$$

We obtain the similar growth rate of instability of equation (2.15) with β-pane

approximation obtained by the eigenvalue problem for $p(k,\nu)$ which is solved numerically by Matlab framework by filling the matrix entries as described in section 2.5.1, taking into account the parameter space now involves the parameter β.

2.5.1 Numerical method for β effect

Following the same method in section (2.4), our matrix is in tridiagonal form, we add the β- plane approximation term in the elements $j = i$ then the coefficients equation (2.36) becomes :

$$a_n = \frac{-k}{2} + \frac{k}{2}\left(\frac{1}{(n-1)^2+k^2}\right), \qquad b_n = -\nu(n^2+k^2) - \frac{ik\beta\sin\alpha + in\beta\cos\alpha}{n^2+k^2},$$

$$c_n = \frac{k}{2} - \frac{k}{2}\left(\frac{1}{(n+1)^2+k^2}\right) \tag{2.37}$$

At specified truncation, N the $(2N+1)\times(2N+1)$ matrix is set in Matlab; we fill the matrix entries as described in section (2.4), then call `eig` to calculate the eigenvalues, we also create another script to vary the parameters. For a given parameter set $p(k,\nu,\alpha,\beta)$, the maximum real growth rate is defined as

$$\mathrm{Re}\, p_{\max}(\nu,\alpha,\beta) = \max_k \mathrm{Re}\, p(k,\nu,\alpha,\beta) \tag{2.38}$$

The maximisation is then taken over a finite range of k-values, typically 100 values in the range $0 < k < 1$, and any complex eigenvalues appear in complex conjugate pairs. To generate figure 2.3, we need $p(\nu,\alpha,\beta,k)$ and used a Matlab framework to find the maximum $p(\nu,\alpha,\beta)$ over k. Then we looked at different values of α to make a comparison with Manfroi and Young (2002).

2.5.2 Unstable mode with the parameter space (k,β,α,ν)

We perform a numerical simulation of unstable flow using the Matlab framework with the β-effect present in the system. We will first do an approximate check on two data points from Manfroi and Young (2002). They found the same critical Reynolds

number as in Meshalkin and Sinai (1961): $R_c = \sqrt{2}$ for $\beta = 0$. We observe that the value of Reynolds number R_{M+Y} is similar to ours namely R_{A+G}, while they used a different value of β. To explain the difference mathematically, we write the equation (2.39) from the Manfroi and Young (2002) paper as follows:

$$\nabla^2\Psi_t + R\sin x\,[\nabla^2\Psi + \Psi]_y + J(\Psi, \nabla^2\Psi) + \beta\cos\alpha\;\Psi_x - \beta\sin\alpha\;\Psi_y = \nabla^4\Psi - \mu\nabla^2\Psi, \tag{2.39}$$

where the Reynolds number takes the value $R = \frac{\Psi_0}{\nu}$, with ν indicating the viscosity, Ψ_0 is the strength of the stream function, μ is the non-dimensional bottom drag. They wrote the total stream function of a forced two-dimensional flow plus perturbation $\Psi(x, y, t)$. Then they obtained the above non-dimensional equation for ψ. By dividing equation (2.39) by R, the Jacobian term neglected for linear theory and the time derivative terms are scaled differently $\partial_t\nabla^2\psi$ (for our work) and $\frac{1}{R}\partial_t\nabla^2\psi$ for Manfroi and Young (2002). However at the threshold of zero growth rate (which is what we compare), these terms are zero in any case. We compare easily with our equation for vorticity and stream function (2.33)

$$\frac{1}{R}\nabla^2\Psi_t + \sin x\,[\nabla^2\Psi + \Psi]_y + \frac{J(\Psi, \nabla^2\Psi)}{R} + \frac{\beta}{R}\cos\alpha\;\Psi_x - \frac{\beta}{R}\sin\alpha\;\Psi_y = \frac{(\nabla^4\Psi - \mu\nabla^2\Psi)}{R}. \tag{2.40}$$

We have the same coupling terms $\sin x[\nabla^2\psi + \Psi]_y$. We can then identify that R_{M+Y} is R_{A+G} and $\frac{\beta}{R}$ is β_{A+G}, we mentioned before the subscripts A+G refer to (Algatheem +Gilbert), and subscripts M+Y refer to (Manfroi+Young), we set μ to zero for our work. The significant change appears in β as shown in the relationship between our parameters and their parameters in equation (2.41):

$$R_{A+G} = R_{M+Y}, \quad \nu_{M+Y} = \frac{1}{R_{M+Y}}, \quad \nu_{A+G} = \frac{1}{R_{A+G}}, \quad \beta_{A+G} = \frac{\beta_{M+Y}}{R_{M+Y}} \quad . \tag{2.41}$$

R_{M+Y}	β_{M+Y}	R_{A+G}	β_{A+G}
3	1	3	$1/3$
2	0.5	2	0.25
4	2	4	0.5
$\sqrt{2}$	0.5	$\sqrt{2}$	$1/\sqrt{2}$

Table 2.1: Comparison between our work and Manfroi and Young (2002) at the parameters values R, β, α, with two choice of the angle α as set in Manfroi and Young (2002) and arbitrary values of β and R.

The table 2.1 provides several examples illustrating the comparison between the β values in Manfroi and Young (2002) and our work. This also illustrates the relationship that we concluded in equation (2.41), allowing us to identify the similarities in Reynolds numbers and the differences in β-effect as outlined in that table.

A brief explanation of figure 2.3, panel (a) shows a plot at the parameter values $\beta_{M+Y} = 1, R_{M+Y} = 3$ from Manfroi and Young (2002). By substituting these values into the equation (2.41), we obtain $\beta_{A+G} = \frac{1}{3}$, as shown in the table 2.1. The growth rate increases slightly when $\alpha = \pi/2$. In order to investigate the system, we plot the growth rate against the wavenumber k as shown in panel (c) We run our script at $\beta_{A+G} = \frac{1}{3}$ and vary the Reynolds number R_{A+G}, the Reynolds number is the same in both panels where $R \to R_c$ at the parameters $p_{max}(k, \alpha, \beta)$, the colour curves reading up the curves of Reynolds number $R_{A+G} = 3,\ 4.5,\ 6,\ 7.5,\ 9,\ 10.5$. When we read up or down the curves, we can see that $R_{A+G} = 3$ is roughly the critical value (dark blue) that agrees with Manfroi and Young (2002) in panel (a).

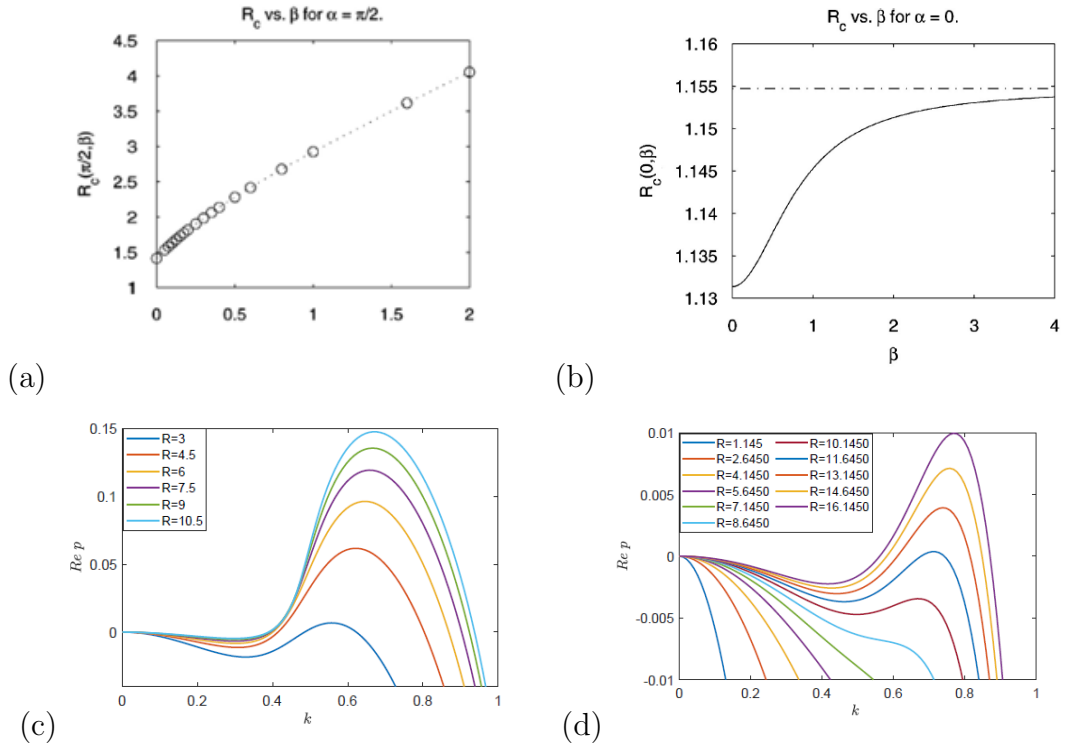

Figure 2.3: Instability of growth rate, panels (a,b) show the critical Reynolds number R_c against β taken from Manfroi and Young (2002), panels (c,d) show the maximum growth rate $p_{\max}$ against wavenumber k for various values of R_{A+G}, panel (c) plot at $\alpha = \pi/2$, $\beta_{A+G} = 1/3$ reading up the curves $R_{A+G} = 3,\ 4.5,\ 6,\ 7.5,\ 9,\ 10.5$, panel (d) plot at $\alpha = 0$, $\beta_{A+G} = 0.8734$, reading up the curves $R_{A+G} = 1.145,\ 2.6450,\ 4.1450,\ 5.6450,\ 7.1450,\ 8.6450,\ 10.1450,\ 11.6450,\ 13.1450,\ 14.6450,\ 16.1450$.

Panel (b) shows a plot at the parameter values $\alpha = 0$, and takes $\beta_{M+y} = 1, R_{c(M+Y)} = 1.145$. Using the equation (2.41) we found $\beta_{A+G} = 0.87$ as plotted in panel (d). At these parameter values, we observed a stable mode (blue curve) for $R_{A+G} = 1.145$, we also gained stable mode as we increased R as set out in panel (b). All parameters in panel (b) were checked and no agreement was found. We can see clearly that the instability occurs as we increase the Reynolds number further $R_{A+G} > R_{M+Y}$, detailed in figure 2.4.

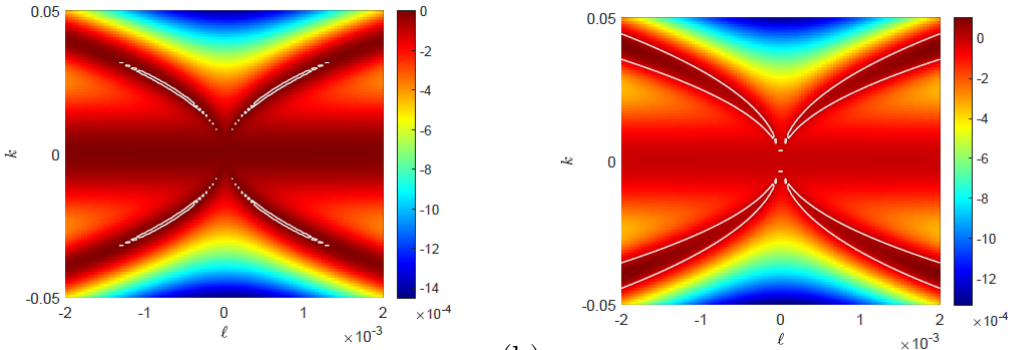

Figure 2.4: Colour plots of instability growth rate as a function of wavenumbers (ℓ, k) at $\alpha = 0$, panel (a) shows the values $R = 1.152, \beta = 1/1.152$, panel (b) shows the values $R = 1.2, \beta = 1/1.2$.

By plotting the stability growth rate as a function of wavenumbers (ℓ, k) shown in figure 2.4, we found unstable mode at $R = 1.152$, which differs from Manfroi and Young (2002) results in figure 2.3(d), where we found stable mode at $R = 1.145$. The disagreement is only in figure 2.3(d) and is because we did not include the Floquet wavenumber ℓ but only k. In this figure 2.4 by increasing R further, we can see that initial instability appears in figure 2.4 panel (a) as outlined by the contour white line with zero growth rate $\mathrm{Re}\, p = 0$. We find that as the Reynolds number is increased, the level of instability increases as shown in panel (b). Both panels reveal unstable modes when $\ell \neq 0$, $k \neq 0$ is non-zero, whereas stable modes are found when $\ell = 0$ in figure 2.3(d). We observed that including $\ell \neq 0$ gives agreement between our numerical results & the Manfroi and Young (2002) results.

2.6 Instability in terms of Rossby waves

We look at the spatial structure of eigenfunctions of vorticity field ω, and stream function ψ. Then, we select an individual point from figure 2.3(c) for parameter values corresponding to the peak of the lowest curve (blue) at $\alpha = \pi/2, \beta = 0.33, \nu = 1/3, k = 0.7$. Figure 2.5 panel (a) shows the coherent structure of vortices that have formed at vorticity field ω_1. The perturbation stream function ψ_1 shown in the right figure exhibits zonostrophic jets and we can refer to this as a sinuous mode with similar instability structure found at $(\alpha, \beta) = (0, 0)$ in section 2.4.2. The basic state

is shown with a small amount of perturbation added in panel (b) the sausage mode has emerged along streamlines of flow ψ_1 and ω_1.

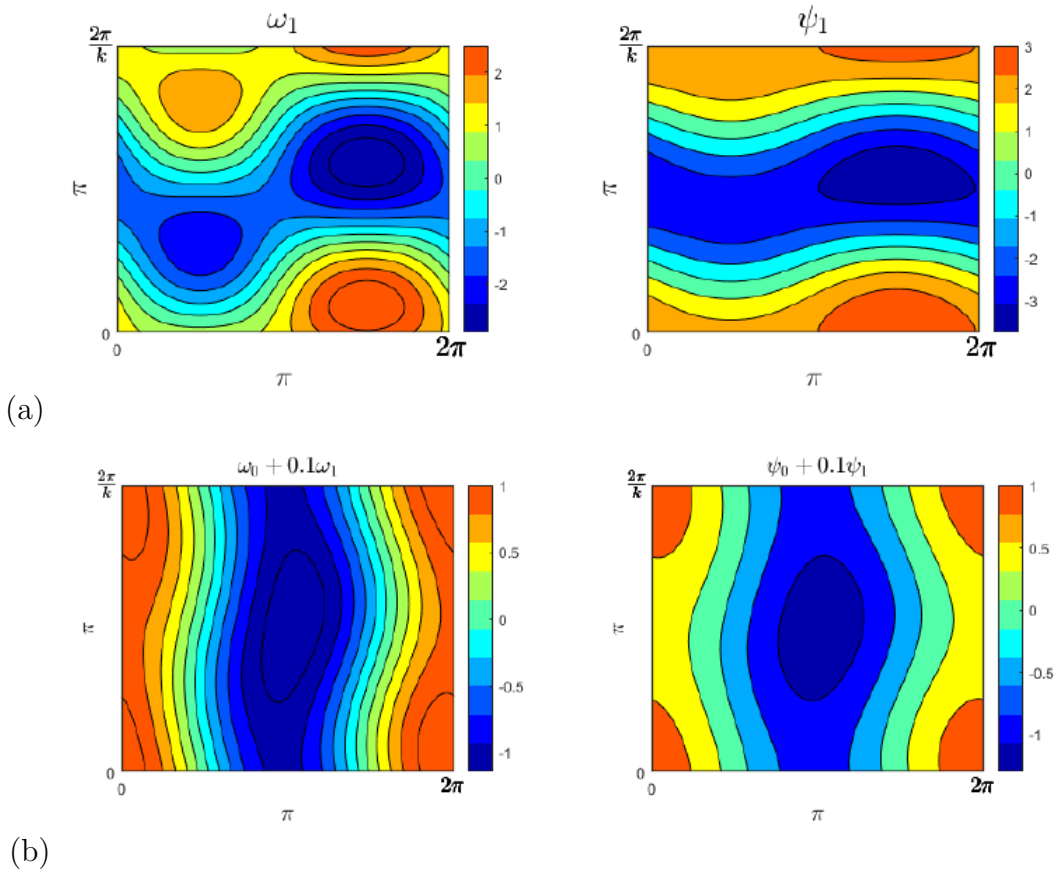

Figure 2.5: Contour plot shows instability in terms of the stream function ψ & vorticity field ω at the parameter values $\alpha = \pi/2, \beta = \frac{1}{3}, k = 0.7, R_{A+G} = 3$, Panel (a) shows perturbation of ψ_1, ω_1, panel (b) shows basic state plus perturbation for both $\omega_0 + 0.1\omega_1$, $\psi_0 + 0.1\psi_1$.

Figure 2.6 shows instability structure corresponding to the peak of the lowest curve (solid blue) in figure 2.3 panel (d) at $\alpha = 0, k = 0.7, \beta = 0.87, R = 1.145$. Panel (a) shows zonostrophic instability in the vorticity field ω_1 with small vortices appearing in the flow lines, and the perturbation stream function ψ_1 exhibits a clear jet formation. Panel (b) shows the basic state with a small amount of perturbation added in both vorticity field ω_1 and stream function ψ_1. The instability structure is similar to figure 2.5(b). The blue region with minimum values represents the sinuous mode in the plot of ω_1 and sausage modes in the plot of ψ_1 that are slightly expanding along the vertical axis in both figures in panel (b).

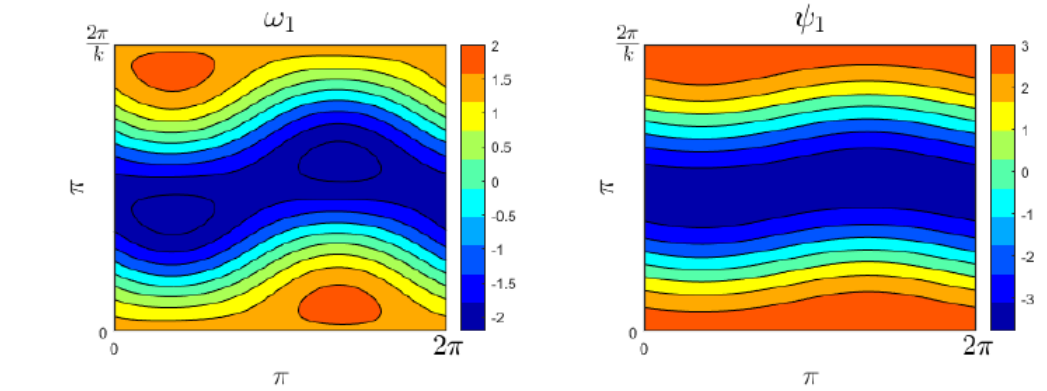

(a)

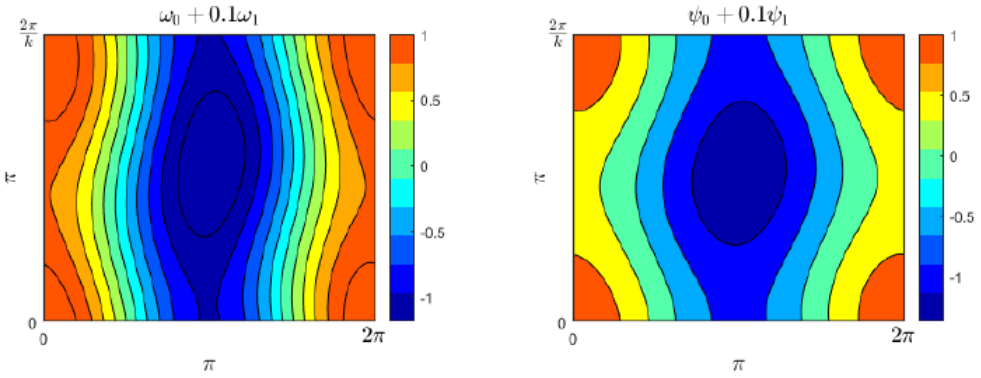

(b)

Figure 2.6: Contour plot shows the instability in terms of the stream function ψ & vorticity field ω at the parameters values $\alpha = 0, \beta = 0.87, k = 0.7, R_{A+G} = 1.145$, Panel (a) shows perturbation of ψ_1, ω_1, panel (b) shows basic state plus perturbations for both $\omega_0 + 0.1\omega_1$, $\psi_0 + 0.1\psi_1$.

2.6.1 Unstable region with the parameter space (k, ℓ)

In this section, we introduce the Floquet wavenumber ℓ in the x-direction through the Fourier series $\psi = e^{pt} \sum_n F_n e^{iky+i(n+l)x}$ with $-0.5 < \ell \leqslant 0.5$, where ℓ allowing more freedom of instability in case of $(\alpha, \beta) = (0, 0)$. Previous figures represent a single Fourier mode k in y-direction. We found α and β affect the instability behaviour in particular with an increase in the Reynolds number. In this study, we will expand the model by introducing the wavenumbers (k, ℓ) and varying α and β following the Manfroi and Young (2002) results, where they contour the linear growth rate over the (k, ℓ)-plane with four choices of the parameters (α, β, ν), in the range $-0.5 < \ell \leqslant 0.5$. Figure 2.7 shows instability determined by the silver region at $\alpha = 0, \pi/2, \pi/6$. So we can compare our results and the Manfroi and Young (2002) results through the previous relationship equation (2.41).

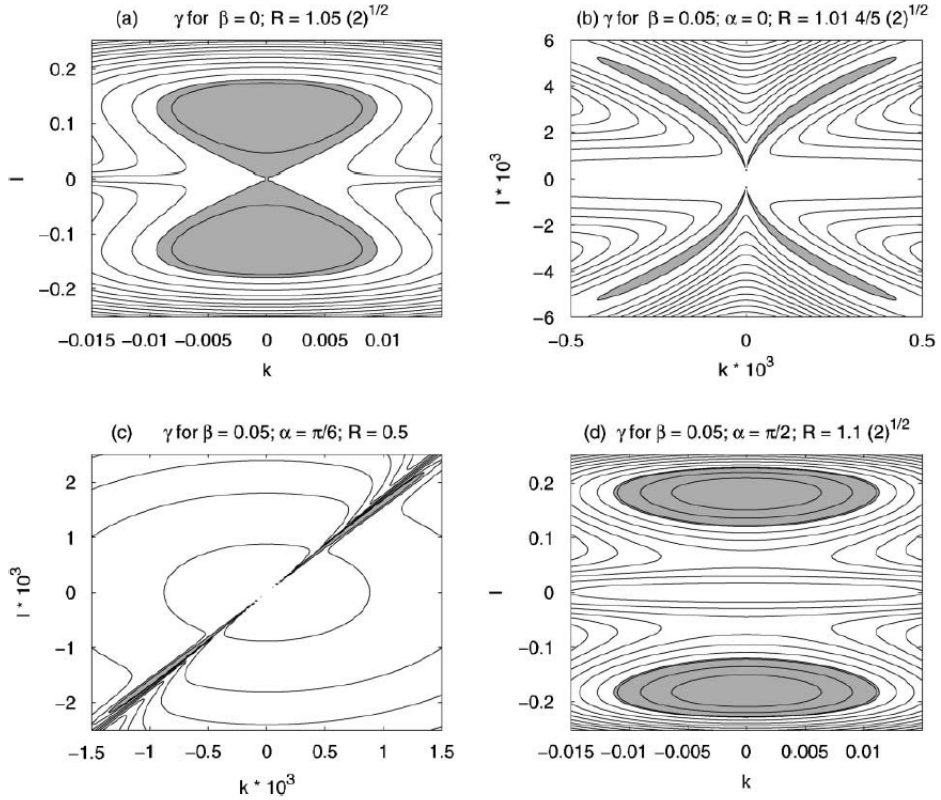

Figure 2.7: Contour plots of growth rate over wavenumbers (k, ℓ) for four sets of parameters. The shaded regions represent instability. (a)$\beta_{M+Y} = 0, R_{M+Y} = 1.05\sqrt{2}$, (b) $\beta_{M+Y} = 0.05, \alpha = 0, R_{M+Y} = 1.01 \times 4\sqrt{2}/5$, (c) $\beta_{M+Y} = 0.05, \alpha = \pi/6, R_{M+Y} = 0.5$, (d) $\beta_{M+Y} = 0.05, \alpha = \pi/2, R_{M+Y} = 1.1\sqrt{2}$. The figures are taken from Manfroi and Young (2002) paper, using their definition of k, ℓ.

We generate figure 2.8 by introducing wavenumbers (k, ℓ) in the x, y-directions from the Fourier expansion:

$$\omega_1 = e^{pt} \sum_{n=-\infty}^{\infty} G_n(x) e^{iky + i(n+l)x}. \tag{2.42}$$

The growth rate in equation (2.36) with Floquet wavenumber ℓ take the form:

$$pG_n = \frac{k}{2}\left[\frac{1}{((n+\ell)-1)^2 + k^2} - 1\right] G_{n-1} - \frac{k}{2}\left[\frac{1}{((n+\ell)+1)^2 + k^2} - 1\right] G_{n+1} -$$

$$ik\beta \ \sin\alpha \ F_n + i(n+\ell)\beta \ \cos\alpha \ F_n = -\nu(k^2 + (n+\ell)^2) G_n, \tag{2.43}$$

We make a comparison between the figure 2.7 and figure 2.8. We can see clearly that the same Reynolds number $R_{M+Y} = R_{A+G}$, while β is different as expressed in the equation (2.41), we exchange the wavenumbers labels k, ℓ in figure 2.8.

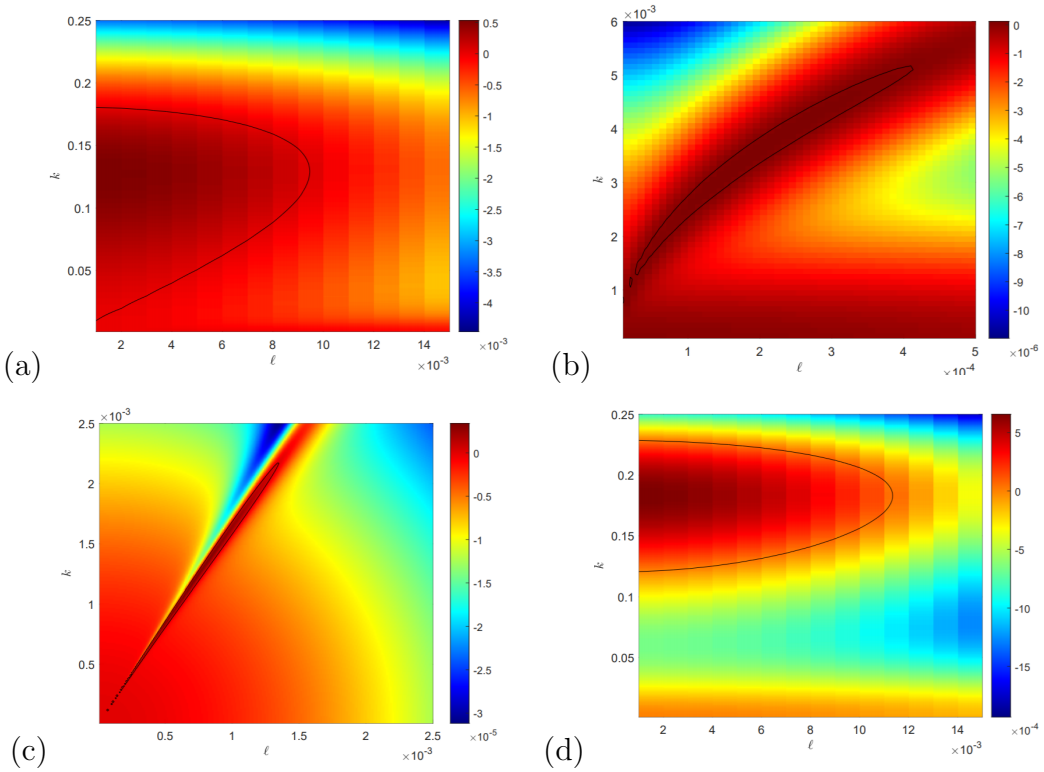

Figure 2.8: Colour coded of linear growth rate instability as a function of (ℓ, k) plane for four sets of parameters space, panel (a) $\beta_{A+G} = 0, \alpha = 0, R_{A+G} = 1.05\sqrt{2}$, panel (b) $\beta_{A+G} = 0.05/R_{M+Y}, \alpha = 0, R_{A+G} = 1.01 \times 4\sqrt{2}/5$, panel (c) $\beta_{A+G} = 0.05/R_{M+Y}, \alpha = \pi/6, R_{A+G} = 0.5$, panel (d) $\beta_{A+G} = 0.05/R_{M+Y}, \alpha = \pi/2, R_{A+G} = 1.1\sqrt{2}$. The real part of the growth rate $\mathrm{Re}\, p > 0$ is outlined by the black contour line in each panel.

Figure 2.8 shows the regions of instability reproduced from the results in figure 2.7 with four choices of parameter values α, $\beta_{A+G} = \frac{\beta_{M+Y}}{R_{M+y}}$, R_{A+G}. Therefore, instability structure in the (ℓ, k)-plane sensitively depends on α and β_{A+G}. We observed that $\alpha = 0$ allows more instability as shown in panel (a), where the parameter values (α, β_{A+G}) are zero and the value of R_{A+G} is slightly above $\sqrt{2}$ the most unstable wavenumber at $k \neq 0$ determined by the contour black line of instability threshold $\mathrm{Re}\, p = 0$. Panel (b) shows plot at the parameter $(\alpha, \beta_{A+G}) = (0, 0.05)$, and R_{A+G} is slightly above $4\sqrt{2}/5$, we observed that non-zero $\beta \neq 0$ has a stabilizing effect.

The significant change occurs at $(\alpha, \beta_{A+G}) = (\pi/6, 0.05)$ and $R_{A+G} = 0.5$ in panel (c) where the black line becomes narrow indicating as we increase α the region of instability vanishes. The unstable region is determined by the threshold (dark line) $\mathrm{Re}\, p = 0$ and the most unstable wavenumber has both x, y dependence with both k, ℓ small. Finally, panel (d) shows a plot for (α, β_{A+G})=$(\pi/2, 0.05)$ the instability

structure is similar to panel(a), with the most unstable wavenumber appearing at $k \neq 0$. We generate figure 2.8, by calculating $p(\nu, \alpha, \beta, \ell, k)$. We used the contour plot of linear growth rate as a function of wavenumbers (ℓ, k) for sets of parameters (α, β, R_{A+G}) we have obtained four figures represent the instability for different parameter values which agrees with Manfroi and Young (2002) figure 2.7.

2.7 Conclusion

Our key findings are summarized in the following list:

- We have found and given the matrix equation for linear growth rate in terms of the vorticity field ω and stream function ψ for instabilities of Kolmogorov flow (see equation 2.15). This can be used to find instability for any parameters or approximation governing our system (the vorticity stream function system).

- We use the eigenvalue problem to solve the algebraic equations numerically for vorticity ω and stream function ψ with Fourier transformation in time and space which describe the system and so determine the dispersion relation for instability.

- We determined the instability criteria depending on the control parameter Reynolds number $\nu_c = 1/R_c$ and found numerical results that agree with Meshalkin and Sinai (1961). We checked the value $\nu_c = 1/\sqrt{2}$ as the instability threshold of our results before incorporating the magnetic field in the system.

- We expand our governing equations to include the β-plane approximation and found numerical results that agree with Manfroi and Young (2002), indicating that β has an influence on the flow and also the angle α, which reduces the region of instability. Considering the large-scale wavenumbers k, ℓ, these results will be developed in the next chapters to include the magnetic field and $\beta = 0$.

The following chapters 3,4,5 will discuss the MHD extension to this linear analysis, and we will look at a numerical simulation of the full nonlinear governing equations in chapters 6, 7, 8.

3. MHD stability: Vertical magnetic field

3.1 Introduction

In this chapter, we return to the classic set-up of steady, planar, Kolmogorov flow $u_0 = (0, \sin x)$ and consider the effect of magnetic fields in the y-direction, parallel to Kolmogorov flow which we describe as a *vertical field*. We will introduce a Lorentz force term to the Navier-Stokes equations, allowing the magnetic field to influence the flow.

A magnetic field can be introduced and studied as a coupled MHD system with astrophysical applications. Our motivation is to introduce a magnetic field and to examine how this affects the Meshalkin and Sinai (1961) curve obtained in the hydrodynamic in chapter 2. We set up the equations solved for linear perturbation theory for eigenvalues and eigenvectors and present numerical results. The matrices become twice as large as we have two fields, and we look for real or complex eigenvalues, perhaps there are Alfvén waves in the coupled system. We will show growth rates, thresholds and stable & unstable mode structure, and we present new analytical & numerical results with magnetic Prandtl number $P < 1$ for the '*vertical strong field branch*' as discussed by Fraser, Cresswell and Garaud (2022), published while the present chapter was being finalized and our paper was in preparation, (Algatheem, Gilbert and Hillier, 2023). We will usually refer to the magnetic Prandtl number P as the Prandtl number for simplicity.

3.2 Governing equations

The magnetic field can easily be rewritten in two-dimensional systems by using the vector potential $\boldsymbol{A}$

$$\partial_t \boldsymbol{B} + \boldsymbol{u} \cdot \nabla \boldsymbol{B} = \boldsymbol{B} \cdot \nabla \boldsymbol{u} + \eta \nabla^2 \boldsymbol{B}, \tag{3.1}$$

$$\nabla \cdot \boldsymbol{B} = 0, \qquad \boldsymbol{B} = \nabla \times \boldsymbol{A}. \tag{3.2}$$

In 2-dimensions, we can write

$$\boldsymbol{B} = (B_1(x,y,t), B_2(x,y,t), 0), \qquad \boldsymbol{A} = (0,0,A(x,y,t)), \qquad \nabla \times \boldsymbol{A} = (A_y, -A_x, 0), \tag{3.3}$$

$$B_1 = A_y, \qquad B_2 = -A_x. \tag{3.4}$$

The vector potential equation is given by:

$$\partial_t A + \boldsymbol{u} \cdot \nabla A = \eta \nabla^2 A,$$

$$\partial_t A + u_1 \partial_x A + u_2 \partial_y A = \eta \nabla^2 A. \tag{3.5}$$

We will check this by differentiating with respect to y and substituting equation (3.4) into equation (3.5) to give:

$$B_1 = A_y: \qquad \partial_t B_1 + u_1 \partial_x B_1 + (\partial_y u_1) \underbrace{(\partial_x A)}_{-B_2} + u_2 \partial_y B_1 + (\partial_y u_2) \underbrace{(\partial_y A)}_{B_1} = \eta \nabla^2 B_1, \tag{3.6}$$

$$\partial_t B_1 + \boldsymbol{u} \cdot \nabla B_1 - B_2 \partial_y u_1 + \underbrace{B_1 \partial_y u_2}_{-B_1 \partial_x u_1} = \eta \nabla^2 B_1. \tag{3.7}$$

by removing the term $\partial_y u_2 = -\partial_x u_1$ as $\quad \nabla \cdot \boldsymbol{u} = 0$

$$\partial_t B_1 + \boldsymbol{u} \cdot \nabla B_1 = \underbrace{B_1 \partial_x u_1 + B_2 \partial_y u_1}_{\boldsymbol{B} \cdot \nabla \boldsymbol{u_1}} + \eta \nabla^2 B_1. \tag{3.8}$$

Likewise we can compute $B_2 = -A_x$ by differentiating with respect to x and substituting into equation (3.5) we obtain:

$$B_2 = -A_x : \qquad \partial_t B_2 - (\partial_x u_1)(\partial_x A) + u_1 \partial_x \underbrace{(-\partial_x A)}_{B_2} - (\partial_x u_2)(\partial_y A) + u_2 \partial_y \underbrace{(-\partial_x A)}_{B_2} = \eta \nabla^2 B_2 \tag{3.9}$$

From equation (3.9) we obtain:

$$\partial_t B_2 + \boldsymbol{u} \cdot \nabla B_2 - (\partial_x u_1) \underbrace{(\partial_x A)}_{-B_2} - (\partial_x u_2) \underbrace{(\partial_y A)}_{B_1} = \eta \nabla^2 B_2 \tag{3.10}$$

$$\partial_t B_2 + \boldsymbol{u} \cdot \nabla B_2 + B_2 \partial_x u_1 - B_1 \partial_x u_2 = \eta \nabla^2 B_2 \tag{3.11}$$

Now $\partial_x u_1 = -\partial_y u_2$

$$\partial_t B_2 + \boldsymbol{u} \cdot \nabla B_2 - B_2 \partial_y u_2 - B_1 \partial_x u_2 = \eta \nabla^2 B_2 \tag{3.12}$$

Comparing with equation (3.8) we obtain :

$$\partial_t B_2 + \boldsymbol{u} \cdot \nabla B_2 = \underbrace{B_2 \partial_y u_2 + B_1 \partial_x u_2}_{\boldsymbol{B} \cdot \nabla \boldsymbol{u_2}} + \eta \nabla^2 B_2 \tag{3.13}$$

Many electromagnetism equations can be formulated in terms of the fields $\boldsymbol{E}$ and $\boldsymbol{B}$, or alternatively in terms of a potential $\boldsymbol{A}$ & electric potential ϕ. Most equations in more advanced theories, such as quantum mechanics, use potentials $\boldsymbol{A}$ and ϕ rather than fields $\boldsymbol{B}$ and $\boldsymbol{E}$. We find that it is more convenient for our analysis to use the vector potential $\boldsymbol{A}$ in two dimensions instead of $\boldsymbol{B}$.

3.2.1 Vorticity & vector potential equations

Our starting point is the system of equations for incompressible fluid flow in the (x, y)-plane, with constant fluid properties, written in the form of the Navier-Stokes Equations (1.7-1.11); the vorticity is then entirely in the z-direction, (i.e. $\boldsymbol{\omega} = \nabla \times \boldsymbol{u} = (0, 0, \omega(x, y, t))$, and obtained by taking the curl of equation (1.7), giving

the vorticity equation:

$$\partial_t \boldsymbol{\omega} = \nabla \times (\boldsymbol{u} \times \boldsymbol{\omega}) + \nu \nabla^2 \boldsymbol{\omega} + \nabla \times \boldsymbol{f}, \tag{3.14}$$

Expanding the advection term in (3.14) gives

$$\nabla \times (\boldsymbol{u} \times \boldsymbol{\omega}) = \boldsymbol{\omega} \cdot \nabla \boldsymbol{u} - \boldsymbol{u} \cdot \nabla \boldsymbol{\omega} + \underbrace{\boldsymbol{u} \nabla \cdot \boldsymbol{\omega} - \boldsymbol{\omega} \nabla \cdot \boldsymbol{u}}_{=0}. \tag{3.15}$$

as

$$\nabla \cdot \boldsymbol{u} = 0, \qquad \nabla \cdot \boldsymbol{\omega} = 0. \tag{3.16}$$

The Navier–Stokes equations can be simplified by introducing the stream function ψ and vorticity ω as dependent variables, considering flows $\boldsymbol{u}$ located in the (x, y)-plane; we use a stream function ψ & vorticity ω defined by

$$\boldsymbol{u} = \left(\frac{\partial \psi}{\partial y}, -\frac{\partial \psi}{\partial x}, 0 \right), \qquad \omega = -\nabla^2 \psi. \tag{3.17}$$

By substituting (3.17) into (3.14), we obtain the vorticity stream function equation as set out in equation (2.5)

$$\partial_t \omega + \mathcal{J}(\omega, \psi) = \nu \nabla^2 \omega + g, \tag{3.18}$$

The Jacobian of ω and ψ is given by

$$\mathcal{J}(\omega, \psi) = (\partial_x \omega)(\partial_y \psi) - (\partial_y \omega)(\partial_x \psi), \tag{3.19}$$

With the vertical magnetic field present in the system, equation (3.18) needs to include the Lorentz force, we first set the basic state:

$$\boldsymbol{B} = (A_y, -A_x, 0), \quad \boldsymbol{B}_0 = (0, B_0, 0), \quad A_0 = -B_0 x, \tag{3.20}$$

by use of the linearization of vector potential A

$$A = A_0 + A_1, \quad \boldsymbol{B} = (\partial_y A_1, B_0 - \partial_x A_1, 0), \tag{3.21}$$

The magnetic current:

$$\boldsymbol{J} = \nabla \times \boldsymbol{B} = (0, 0, -\nabla^2 A_1), \tag{3.22}$$

So we have a nice symmetry between flow & field perturbation:

$$\Psi_1, \omega_1 = -\nabla^2 \Psi_1, \qquad A_1, J_1 = -\nabla^2 A_1, \tag{3.23}$$

The Lorentz force

$$\boldsymbol{J} \times \boldsymbol{B} = (B_0 \nabla^2 A_1 - (\partial_x A_1)\nabla^2 A_1, -(\partial_y A_1)\nabla^2 A_1, 0). \tag{3.24}$$

By taking the curl of Lorentz force:

$$\nabla \times (\boldsymbol{J} \times \boldsymbol{B}) = (0, 0, -(\partial_y A_1)\nabla^2 \partial_x A_1 - B_0 \partial_y \nabla^2 A_1 + (\partial_x A_1)\nabla^2 \partial_y A_1). \tag{3.25}$$

However, under linearisation, we discussed the products of A_1:

$$\boldsymbol{J} \times \boldsymbol{B} \simeq (B_0 \nabla^2 A_1, 0, 0) = \boldsymbol{J} \times \boldsymbol{B_0}. \tag{3.26}$$

$$\nabla \times (\boldsymbol{J} \times \boldsymbol{B}) \simeq (0, 0, -B_0 \partial_y \nabla^2 A_1) = \nabla \times (\boldsymbol{J} \times \boldsymbol{B_0}). \tag{3.27}$$

Then we obtain the vorticity stream function formulation with the Lorentz force (linearised)

$$\partial_t \omega + \mathcal{J}(\omega, \psi) = (\nabla \times (\boldsymbol{J} \times \boldsymbol{B}))_{\boldsymbol{z}} + \nu \nabla^2 \omega + g \tag{3.28}$$

$$\partial_t \omega_1 + \sin x \; \omega_{1y} - \sin x \; \psi_{1y} = -B_0 \partial_y \nabla^2 A_1 + \nu \nabla^2 \omega_1, \tag{3.29}$$

Recall that $\psi(x, y, t)$ is the stream function, and ν is the inverse Reynolds number, $\boldsymbol{B}(x, y, t)$ is the magnetic field, $\boldsymbol{J}$ is the magnetic current. Equation (3.30) is found by 'un-curling' the magnetic induction equation (see section 3.2), η is the inverse magnetic Reynolds number, $A(x, y, t)$ is the vector potential.

We also have the induction equation (3.5)

$$\partial_t A + \boldsymbol{u} \cdot \nabla A = \eta \nabla^2 A, \tag{3.30}$$

To satisfy the vorticity and induction equations (3.28-3.30), consider the steady solution of the equations as the following basic state :

$$\boldsymbol{u_0} = (0, \sin x, 0), \quad A_0 = -B_0 x \quad g = \nu \cos x, \tag{3.31}$$

We linearize this basic state, replacing

$$\boldsymbol{u} = \boldsymbol{u}_0 + \boldsymbol{u}_1, \quad \boldsymbol{B} = \boldsymbol{B}_0 + \boldsymbol{B}_1, \quad J = J_0 + J_1, \quad A = A_0 + A_1, \quad \psi = \psi_0 + \psi_1, \quad \omega = \omega_0 + \omega_1, \tag{3.32}$$

The subscript 1 denotes a small perturbation to the equilibrium, shown by subscript 0, $J_0 = 0$. The perturbations are assumed to be small and thus any products of these perturbations are negligible. Then the linearized set of equations (3.28 - 3.30) for uniform equilibrium with a vertical magnetic field can be written as:

$$\partial_t \omega_1 - \sin x \; \psi_{1y} + \sin x \; \omega_{1y} = \underbrace{-B_0 \partial_y \nabla^2 A_1}_{B_0 \partial_y J_1} + \nu \nabla^2 \omega_1, \tag{3.33}$$

Substituting the magnetic equilibrium (3.31) into equation (3.34), then linearizing, we obtain

$$\partial_t A + \boldsymbol{u} \cdot \nabla A = \eta \nabla^2 A, \tag{3.34}$$

$$\partial_t A_1 + \boldsymbol{u_1} \cdot \nabla A_0 + \boldsymbol{u_0} \cdot \nabla A_1 = \eta \nabla^2 A_1, \tag{3.35}$$

Here $\boldsymbol{u_1} = (u_1, v_1, 0)$, from $u_1 = \partial_y \psi_1, v_1 = -\partial_x \psi_1$, we obtain:

$$\partial_t A_1 + \partial_y \psi_1 (-B_0) + ikA_1 \sin x = \eta \nabla^2 A_1, \tag{3.36}$$

Assuming wave-like solutions, we expand the fields in Fourier modes as:

$$\Psi_1 = F(x)e^{iky+pt} + c.c. = e^{iky+pt} \sum_{n=-\infty}^{\infty} F_n e^{inx} + c.c. \tag{3.37}$$

$$\omega_1 = G(x)e^{iky+pt} + c.c. = e^{iky+pt} \sum_{n=-\infty}^{\infty} G_n e^{inx} + c.c. \tag{3.38}$$

$$A_1 = H(x)e^{iky+pt} + c.c. = e^{iky+pt} \sum_{n=-\infty}^{\infty} H_n e^{inx} + c.c. \tag{3.39}$$

$$J_1 = J(x)e^{iky+pt} + c.c. = e^{iky+pt} \sum_{n=-\infty}^{\infty} J_n e^{inx} + c.c. \tag{3.40}$$

where *c.c.* refers to the complex conjugate of the preceding terms. We compare Fourier terms e^{inx}, and the corresponding complex conjugate parts. Substituting equations (3.37-3.40) into the linear equations (3.33) we obtain:

$$pG - ik\sin x\ F + ik\sin x\ G = -B_0 ik\left[-k^2 + \frac{\partial^2}{\partial x^2}\right] H - \nu\left(k^2 + \frac{\partial^2}{\partial x^2}\right) G. \tag{3.41}$$

By extracting the Fourier wave terms in e^{inx} we fined:

$$\sin x\ F = \frac{1}{2i}\sum_{n=-\infty}^{\infty}[F_n e^{i(n+1)x} - F_n e^{i(n-1)x}] \quad = \frac{1}{2i}\sum_{n=-\infty}^{\infty}[F_{n-1}e^{inx} - F_{n+1}e^{inx}] \tag{3.42}$$

$$\sin xH = \frac{1}{2i} \sum_{n=-\infty}^{\infty}[H_n e^{i(n+1)k} - H_n e^{i(n-1)x}] = \frac{1}{2i} \sum_{n=-\infty}^{\infty}[H_{n-1}e^{inx} - H_{n+1}e^{inx}], \tag{3.43}$$

Substitute Fourier modes in x (3.42) into equation (3.41), we obtain:

$$pG_n - \frac{k}{2}(F_{n-1} - F_{n+1}) + \frac{k}{2}(G_{n-1} - G_{n+1}) = -\nu(k^2+n^2)G_n - ikB_0(-k^2-n^2)H_n, \tag{3.44}$$

$$\begin{aligned} pG_n - \frac{k}{2}\left(\frac{G_{n-1}}{(n-1)^2+k^2} - \frac{G_{n+1}}{(n+1)^2+k^2}\right) + \frac{k}{2}(G_{n-1} - G_{n+1}) \\ = -\nu(k^2+n^2)G_n + ikB_0(k^2+n^2)H_n, \end{aligned} \tag{3.45}$$

or:

$$\begin{aligned} pG_n =& \frac{k}{2}\left[\frac{1}{(n-1)^2+k^2}-1\right]G_{n-1} - \frac{k}{2}\left[\frac{1}{(n+1)^2+k^2}-1\right]G_{n+1} \\ & -\nu(n^2+k^2)G_n + ikB_0(k^2+n^2)H_n. \end{aligned} \tag{3.46}$$

Substitute the Fourier series (3.39) and extract sine wave terms in e^{inx} (3.43), into equation (3.36) we obtain:

$$pH_n + (-ikB_0)F_n + \frac{k}{2}(H_{n-1} - H_{n+1}) = -\eta(k^2+n^2)H_n, \tag{3.47}$$

We have the flow & field relations

$$F_n = \frac{1}{k^2+n^2}G_n, \qquad J_n = (k^2+n^2)A_n, \tag{3.48}$$

The eigenvalue problem comprises a pair of equations (3.46) and (3.49) :

$$pH_n = \left[-\frac{k}{2}\right]H_{n-1} + \left[\frac{k}{2}\right]H_{n+1} - \eta(k^2+n^2)H_n + \left[\frac{ikB_0}{k^2+n^2}\right]G_n. \tag{3.49}$$

Further progress on the flow cannot be made without looking for solutions to the system of equations given by (3.46 - 3.49). Next section, we aim to find a numerical solution using the Matlab framework for a linear system of coupling equations for flow G_n & field H_n.

3.2.2 Numerical methods

In our eigenvalue problem, we have written the fields as Fourier series. For a numerical solution, we restrict $-N \leq n \leq N$ for some integer N (typical value $16, 32$), and we sometimes vary N to check our results. We solve a discrete matrix problem written in a pentadiagonal form.

To show how the matrix is organised: first, we have a Kolmogorov flow confined with periodic boundary condition to the region $0 \leq x < 2\pi$, $0 \leq y < 2\pi/k$. Our exponential dependence on y is given by the appearance of the wavenumber k in

y-direction. Upon inserting (3.37) into (3.33-3.36) and expanding, the following algebraic eigenvalue problem for the unknown coefficients is obtained (3.51).

$$p\begin{pmatrix} G_{-N} \\ H_{-N} \\ G_{-N+1} \\ H_{-N+1} \\ \vdots \\ G_{N-1} \\ G_N \\ H_N \end{pmatrix} = M \begin{pmatrix} G_{-N} \\ H_{-N} \\ G_{-N+1} \\ H_{-N+1} \\ \vdots \\ G_{N-1} \\ G_N \\ H_N \end{pmatrix} \qquad p\begin{pmatrix} \vdots \\ G_n \\ H_n \\ \vdots \end{pmatrix} = \left(\begin{array}{ccc|cc|cc} \ddots & \ddots & \ddots & \ddots & \ddots & \ddots & \ddots \\ \hline \ddots & a_n & 0 & b_n & d_n & c_n & \ddots \\ \ddots & e_n & h_n & f_n & 0 & g_n & \ddots \\ \hline \ddots & \ddots & \ddots & \ddots & \ddots & \ddots & \ddots \end{array}\right) \begin{pmatrix} \vdots \\ G_n \\ H_n \\ \vdots \end{pmatrix} \tag{3.50}$$

Comparing linear equations for G_n & H_n (3.46 - 3.49) with the matrix system (3.50) and then writing the coefficients:

$$pG_n = a_nG_{n-1} + b_nG_n + c_nG_{n+1} + d_nH_n, \qquad pH_n = e_nH_{n-1} + f_nH_n + g_nH_{n+1} + h_nG_n \tag{3.51}$$

we set the matrix elements n for the matrix rows; we have

$$a_n = \frac{-k}{2} + \frac{k}{2}\left(\frac{1}{(n-1)^2+k^2}\right), \quad b_n = -\nu(n^2+k^2), \quad c_n = \frac{k}{2} - \frac{k}{2}\left(\frac{1}{(n+1)^2+k^2}\right),$$

$$d_n = ikB_0(k^2+n^2), \quad e_n = \frac{-k}{2}, \quad f_n = -\eta(k^2+n^2), \quad g_n = \frac{k}{2}, \quad h_n = \frac{iB_0k}{k^2+n^2} \tag{3.52}$$

As stated above, for each k in $0 < k < 1$ we let $i = 1$ odd, $n = -N$ refer to the mode G_n, which corresponds to wavenumber $n = -N + \frac{1}{2}(i-1)$. Hence, $i = 3$ gives $n = -N + 1$, etc. We will further let $i = 2$ refer to the corresponding mode H_n,

where i even to all other modes, corresponding to wavenumber $n = -N + \frac{1}{2}(i-2)$

$$M_{ij} = \begin{cases} a_n & j = i-2, \\ b_n & j = i, \\ d_n & j = i+1 \\ c_n & j = i+2. \end{cases} \qquad \text{for } i \text{ odd}, \quad n = -N + \tfrac{1}{2}(i-1). \tag{3.53}$$

and then a similar equation for even rows.

$$M_{ij} = \begin{cases} e_n & j = i-2, \\ f_n & j = i, \\ h_n & j = i-1 \\ g_n & j = i+2. \end{cases} \qquad \text{for } i \text{ even}, \quad n = -N + \tfrac{1}{2}(i-2). \tag{3.54}$$

At a specified truncation N, the $(4N+2)\times(4N+2)$ matrix is set up in Matlab; we fill the matrix entries as described here. Then, we call *eig* to determine the eigenvalues, and we create another script to vary the parameters. For a given parameter set (ν, B_0, η), the maximum real growth rate is defined as

$$\operatorname{Re} p_{\max}(\nu, B_0, \eta) = \max_k \operatorname{Re} p(k, \nu, \eta, B_0), \tag{3.55}$$

The maximisation is then taken over a finite range of k-values, typically 100 values in the range $0 < k < 1$, and any complex eigenvalues appear in complex conjugate pairs. We let $k_{\max}(\nu, B_0, \eta)$ be the corresponding maximising wavenumber. We attach the appropriate (zero or positive) imaginary part to give $p_{\max}(\nu, B_0, \eta)$ as the (maximum) complex instability growth rate. It is then often instructive to plot $\operatorname{Re} p_{\max}, \operatorname{Im} p_{\max}$ and $k_{\max}$.

3.3 Numerical and analytical results: vertical field

By running the numerical code in the Matlab framework as described above, we can obtain eigenvalues and explore the dependence on parameters. Initially, we will

investigate the effect of increasing the vertical magnetic field strength B_0 on the classic hydrodynamic instability of Kolmogorov flow. The magnetic field aligned with Kolmogorov flow gives straightforward vertical field lines, and any jets here in the x-direction distort field lines, as seen in figure 3.1.

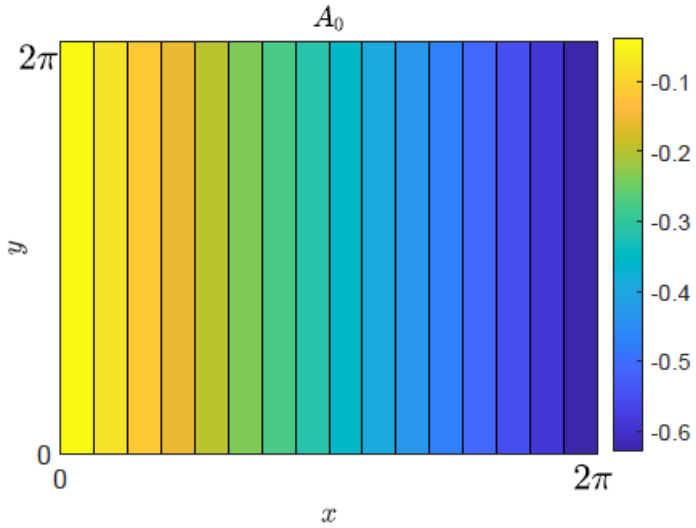

Figure 3.1: The magnetic field basic state for vertical field with $B_0 = 0.7$, the field lines are depicted as contours of the corresponding vector potential A_0, with $\boldsymbol{B_0} = (\partial_y A_0, -\partial_x A_0)$

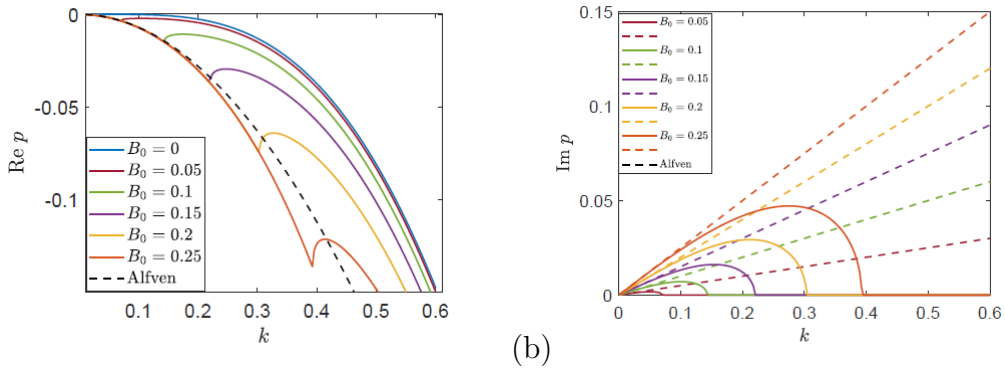

(a) (b)

Figure 3.2: Instability growth rate p for vertical magnetic field as a function of wave number k for $\nu = \eta = 0.7$ ($P = 1$), and $B_0 = 0$ (blue), $B_0 = 0.05$ (dark red), $B_0 = 0.10$ (green), $B_0 = 0.15$ (purple), $B_0 = 0.20$ (yellow) and $B_0 = 0.25$ (orange). Panels (a) and (b) show $\mathrm{Re}\, p$ and $\mathrm{Im}\, p$ respectively, and dashed curves show the Alfvén wave branch in (1.70)

Figure 3.2 shows the real part of the growth rate p for $\nu = \eta = 0.7$, and so $P = 1$, plotted against vertical wavenumber k for given values of the magnetic field strength B_0. The top curve is related to a purely hydrodynamic case (blue curve $B_0 = 0$). Initially, as we increase B_0, we gain two branches that emerge as we vary k. For example, for $B_0 = 0.10$ (green), we see a branch for $k = 0.2$ with the imagin-

ary part of p is zero, which we can identify with the original $B_0 = 0$ mode, but with a reduced growth rate, so the vertical magnetic field suppresses the original hydrodynamic instability. At the same time, we have a new stable mode with a non-zero imaginary part. This corresponds to propagating waves that are damped, which are stable oscillatory disturbances with low k; for this branch, we have a negative growth rate $\mathrm{Re}\, p$ (so the modes are decaying), which is approximately independent of the field strength, as may be seen since the curves overlap for increased B_0.

Figure 3.2(b) shows a stable mode characterized by $p_i \neq 0$ with an increasing range of k as B_0 increases, where instability is suppressed by the magnetic field and corresponds to an Alfvén wave curve at small k. We have p_i is zero for the pure hydrodynamic branch (blue) and also zero for the dashed black branch, for zero background flow $\boldsymbol{u_0} = 0$. The real part of this wave is damped by viscosity and magnetic diffusivity shown by the dashed black line in figure 3.2. See equation (1.70), which describes the wave damping mathematically. The real part in panel (a) for this $\boldsymbol{u_0}$ mode corresponds to all field strengths and is dotted black. In panel (b) the straight dotted lines for $B_0 > 0$, are coloured appropriately and tangential at the origin to the curve of $p_i(k)$ for each field strength.

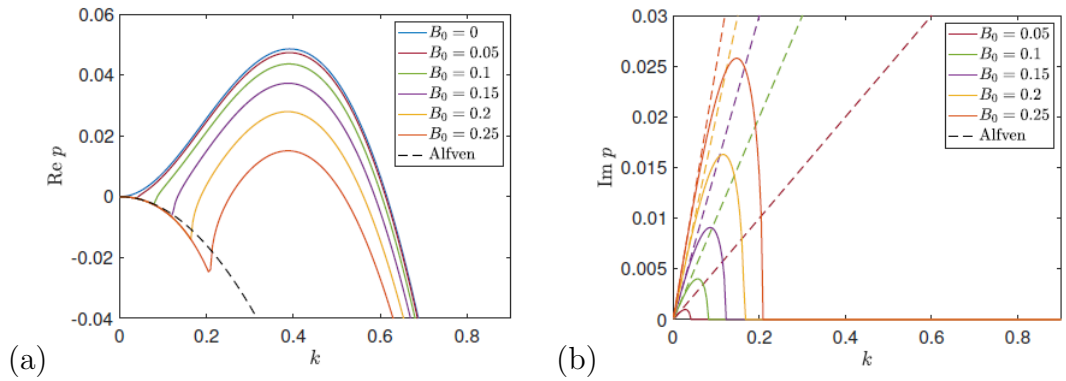

Figure 3.3: Instability growth rate p for vertical magnetic field as a function of wave number k for $\nu = \eta = 0.4$ ($P = 1$), and $B_0 = 0$ (blue), $B_0 = 0.05$ (red), $B_0 = 0.10$ (green), $B_0 = 0.15$ (purple), $B_0 = 0.20$ (yellow) and $B_0 = 0.25$ (dark orange). Panels (a) and (b) show $\mathrm{Re}\, p$ and $\mathrm{Im}\, p$ respectively, and dashed curves show the Alfvén wave branch in (1.70).

Figure 3.3 shows the real part of the growth rate p for $\nu = \eta = 0.4$ and so $P = 1$, plotted against k for given values of the magnetic field strength B_0. Here B_0 is increased from zero in steps of 0.05 as we read down the family of curves. The top

curve relates to the purely hydrodynamic case (blue curve $B_0 = 0$). As we increase B_0, we note the growth is reduced; in other words, the magnetic field acts to suppress the instability, as found by Fraser, Cresswell and Garaud (2022). Panel (b) shows the imaginary part of the growth rate p. This is zero for the purely hydrodynamic case and remains zero for this branch as it is suppressed by the field. We reduce the viscosity here in order to clarify the magnetic field influence on the growth rate p. The Alfvén waves are modified by the Kolmogorov flow, the agreement is clear for small k damped modes.

3.4 Weak vertical field branch

We have seen how the magnetic field suppresses hydrodynamic instability by plotting $p(k, \nu, B_0, \eta)$, and we now present results where we maximize over k for each set of parameters. Initially, we set $\nu = \eta$ and consider $B_0 \neq 0$. Figure 3.4 shows the numerical result for $\mathrm{Re}\, p_{\max}(\nu, B_0)$ for $P = 1$ as colour plot across the (ν, B_0)-plane. The white line shows the threshold of instability and has a small positive value $\mathrm{Re}\, p = 0$ for the actual value but this makes no difference in the figures to graphical accuracy. The horizontal axis $B_0 = 0$ is the hydrodynamic case, where the white curve crosses at $\nu = 1/\sqrt{2}$. Instability occurs in the region below the white line from blue to yellow and red region we can see that it is suppressed as B_0 increases, above the white line the dark blue for stability, up to the point where $B_0 \approx 0.7$ and the instability is entirely eliminated. We also show that this instability appears in the plot of $k_{\max}$ and disappears in $\mathrm{Im}\, p_{\max}$ with dark blue below the white line of instability threshold, corresponding to $\mathrm{Im}\, p_{\max} = 0$ within the region of instability.

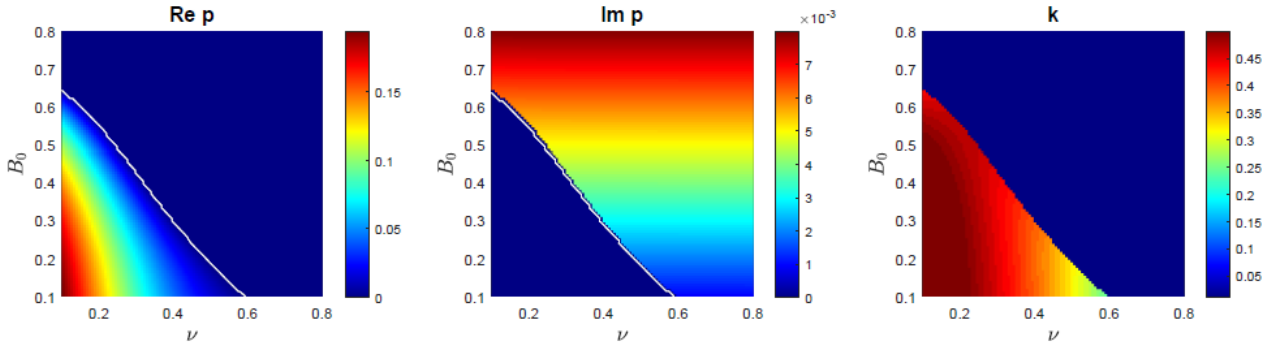

Figure 3.4: Instability growth rate $\mathrm{Re}\, p_{\max}$ plotted in the (ν, B_0) plane for $P = 1$. shows $\mathrm{Re}\, p_{\max}$, frequency $\mathrm{Im}\, p_{\max}$ and wavenumber $k_{\max}$ of their respective eigenfunction, instability threshold $\mathrm{Re}\, p_{\max} = 0$ given by a contour white line .

We developed perturbation theory as set out in Frisch, Legras and Villone (1996), Manfroi and Young (2002) to calculate approximate growth rates valid for $k \to 0$ and show clearly how the effect of the weak magnetic field is to suppress the hydrodynamic $B_0 = 0$ instability, the details shown in appendix C of Algatheem, Gilbert and Hillier (2023).

3.5 Instability in terms of Alfvén waves

We are looking at the structure of the instability for four perturbation eigenfunctions of flows & fields $\psi_1, \omega_1, j_1, a_1$ which is the same as J_1, A_1 in equation (3.23). Figure 3.5 shows an example of an unstable mode for parameter values corresponding to the peak of the lowest curve (dark orange) in figure 3.3 at $B_0 = 0.25, \nu = \eta = 0.4, k = 0.4$, which represents the strongest field used. Panel (a) shows coherent structures of vortices that have formed in the vorticity field ω_1 and electric current j_1 in panel (b) in the plots with $0 \leqslant x \leqslant 2\pi$, $0 \leqslant y \leqslant \frac{2\pi}{k}$. The perturbation stream function ψ_1 in panel (a) and the magnetic potential a_1 in panel (b) both exhibit clear zonostrophic jets; Fraser, Cresswell and Garaud (2022) refer to these as sinuous Kelvin-Helmholtz modes. Since the instabilities we observe here result from the hydrodynamic problem as B_0 increases, we refer to this as the weak vertical field branch, in contrast with the strong vertical field branch we will see in Figure 3.8. In panel (c), the basic equilibrium state is shown with a small amount of perturbation added. Hence, the kink modes have emerged along magnetic lines a_1, and the sausage modes along

streamlines of flow ψ_1.

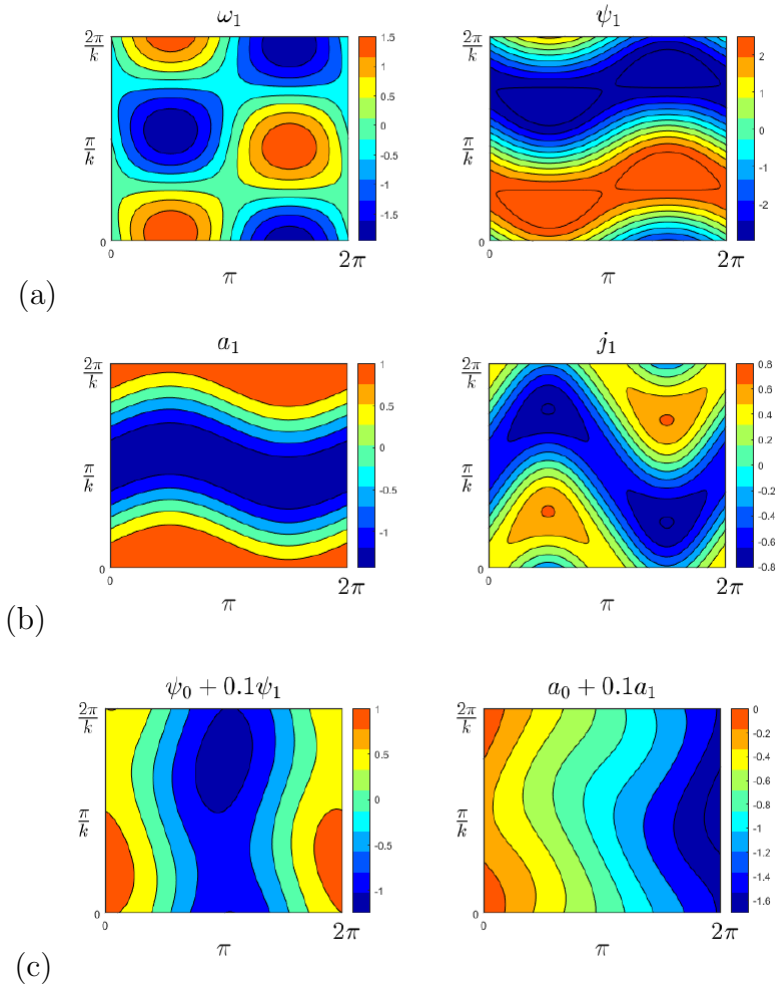

Figure 3.5: Shaded contour plot of the unstable mode of instability displayed the case $B_0 = 0.25,\ k = 0.4,\ \nu = \eta = 0.4$. Panel (a) vorticity ω_1 and stream function ψ_1, panel (b) the magnetic field a_1 and the magnetic current j_1. (c) Superposition of basic flow $\psi_0 + 0.1\psi_1$ and field $a_0 + 0.1a_1$. The real part of the stream function and the associated vorticity $\omega_1 = -\nabla^2\psi_1$ is plotted.

Having implemented the unstable mode and shown the instability structure in figure 3.5, we now select parameter values corresponding to the peak of the (green curve) in figure 3.2 at $(B_0 = 0.10, \nu = \eta = 0.7, k = 0.4)$, which represents a weak field used, we also refer to this as weak vertical field branch. Figure 3.6(a) shows the same coherent structures of vortices in the vorticity field ω_1 in panel (a) and magnetic current j_1 in panel (b). The perturbation stream function $\psi_1$in panel (a) and the magnetic potential a_1 in panel (b) both exhibit a clear jet formation, we observe that increased viscosity $\nu = 0.7$ leads to vanishing of the two vortices in the centre of ψ_1 in figure 3.5(a) and forms a jet structure as shown in figure 3.6 (a). We also observed the flow bends the field lines in the plot of $a_0 + 0.1a_1$ in panel (c).

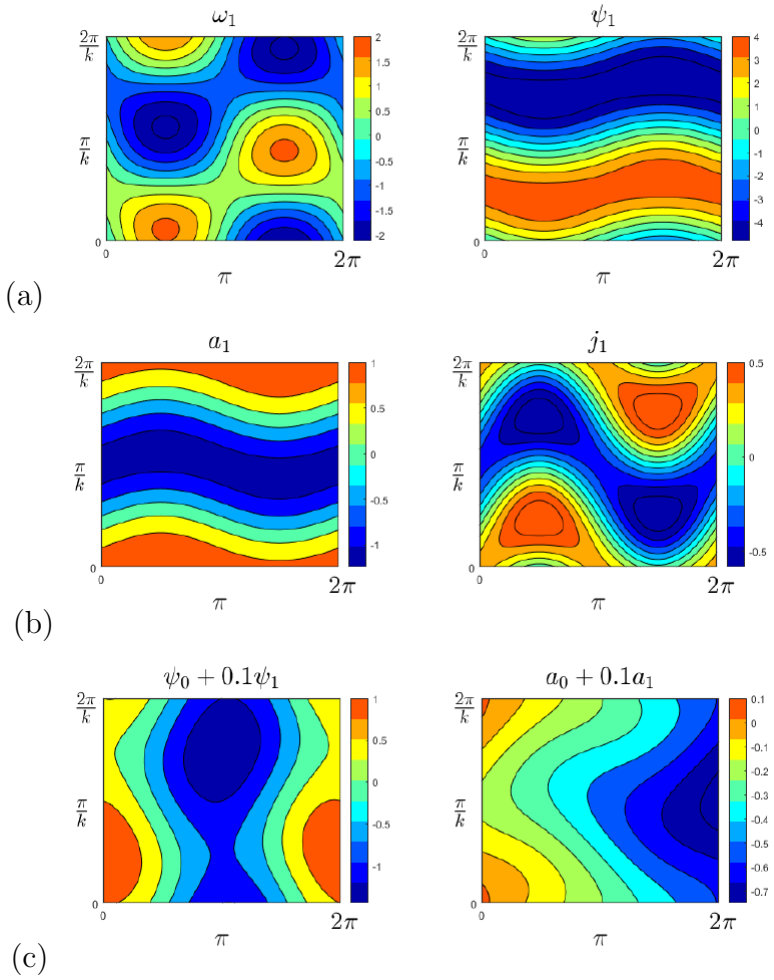

Figure 3.6: Shaded contour plot of the decaying mode of instability displayed the case $B_0 = 0.10,\ k = 0.4,\ \nu = \eta = 0.7$. Panel (a) Vorticity ω_1 and Stream function ψ_1, panel (b) the magnetic field a_1 and the magnetic current j_1, panel (c) Superposition of basic flow $\psi_0 + 0.1\psi_1$ and field $a_0 + 0.1a_1$. The real part of the stream function and of the associated vorticity $\omega_1 = -\nabla^2\psi_1$ is plotted.

3.5.1 Linear instability with $P < 1$

Although the magnetic field suppresses the instability for magnetic Prandtl numbers of unity $P = 1$, investigation for $P = 0.5$ indicates the presence of a *strong vertical field branch*, as found by Fraser, Cresswell and Garaud (2022). Figure 3.7 shows a new instability at a large scale as $B_0 \to \infty$. This instability occurs for strong fields with a small growth rate and the figure shows the real and imaginary parts of the growth rate $p_{\max}(\nu, B_0, P)$ for $\eta = 2\nu$, that is $P = 0.5$, the instability threshold $\mathrm{Re}\, p_{\max} = 0$ determined by a white curve. By looking at $\mathrm{Re}(p)$ we see that the curving white lines, showing the weak field branch in figure 3.4(a) shift to become a near-vertical line, creating a new branch with non-zero frequency $\mathrm{Im}\, p_{\max}$ and

non-zero $k_{\max}$ (large scale instability) as shown in figure 3.7.

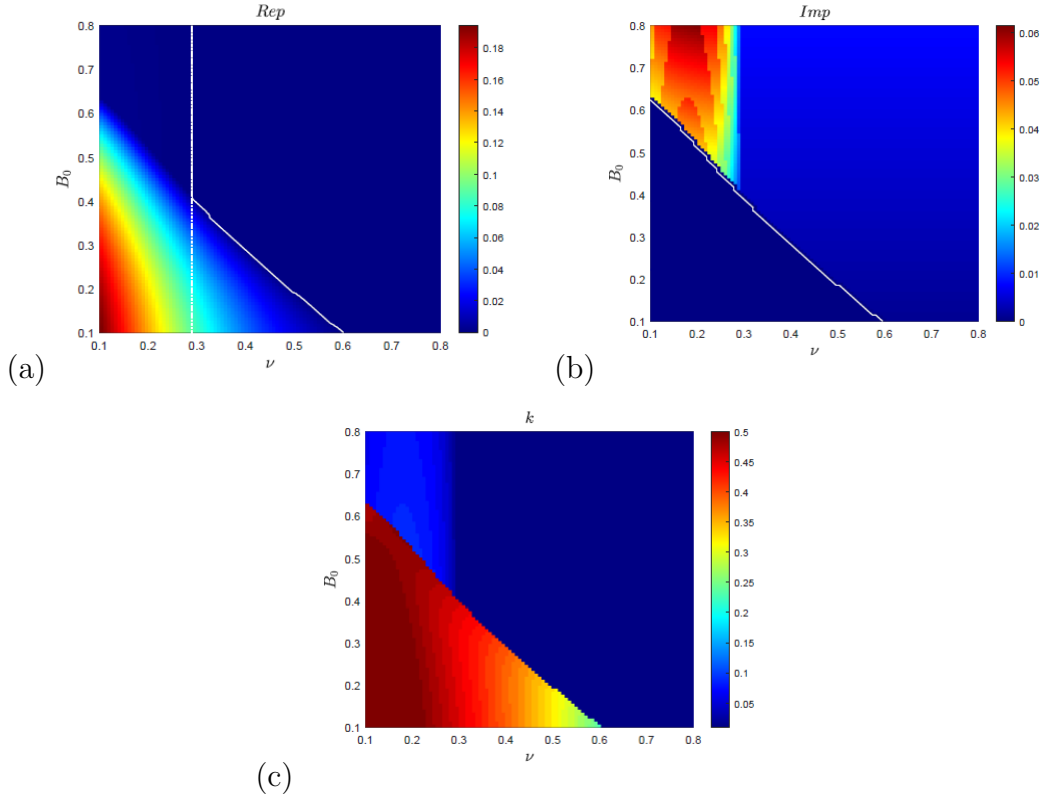

Figure 3.7: Instability growth rate for vertical field plotted in the (ν, B_0)-plane, with $\eta = 2\nu, P = 0.5$, shows $\mathrm{Re}\, p_{\max}$, frequency $\mathrm{Im}\, p_{\max}$ and wavenumber $k_{\max}$ of their respective eigenfunction, the contour line $\mathrm{Re}\, p = 0$ overlayed in white shows zero growth rate.The dotted white line in panel (a) shows the theoretical threshold from (3.109). In panel(a) the white line shows $\mathrm{Re}\, p = 0$ and the white line in panel (b) shows $\mathrm{Im}\, p = 0$.

Magnetic fields suppress instability due to the elastic nature of their field lines. However, elasticity can increase instability, this occurs here in strong vertical fields at $P = 0.5$. Magnetic fields, in this case, are more subtle than suppressing instability, this is one of the reasons why these systems should be studied.

In the previous section 3.5, we used $\nu = \eta$ and found unstable & stable modes; these two parameters can be varied independently. Figure 3.8 simply shows instability behaviour at small Prandtl number $P = 0.5$ and double magnetic diffusivity $\eta = 2\nu$ for parameter values $\nu = 0.28, k = 0.1$ and $B_0 = 0.7$, which corresponds to a new instability in figure 3.7. Initially, we can see clearly a jet instability structures are still present in the magnetic potential a_1 in panel (b) and stream function ψ_1 in panel (a); however, the perturbation vorticity ω_1 in panel (a) and the magnetic current j_1

in panel (b) exhibit more systematic vortices. Instability filaments in the sausage and kink modes in panel (c) become more narrow, leading to the approximately uniform vertical flow in streamlines of flow ψ_1 and magnetic lines a_1 due to the strong magnetic field and as shown in panel (c).

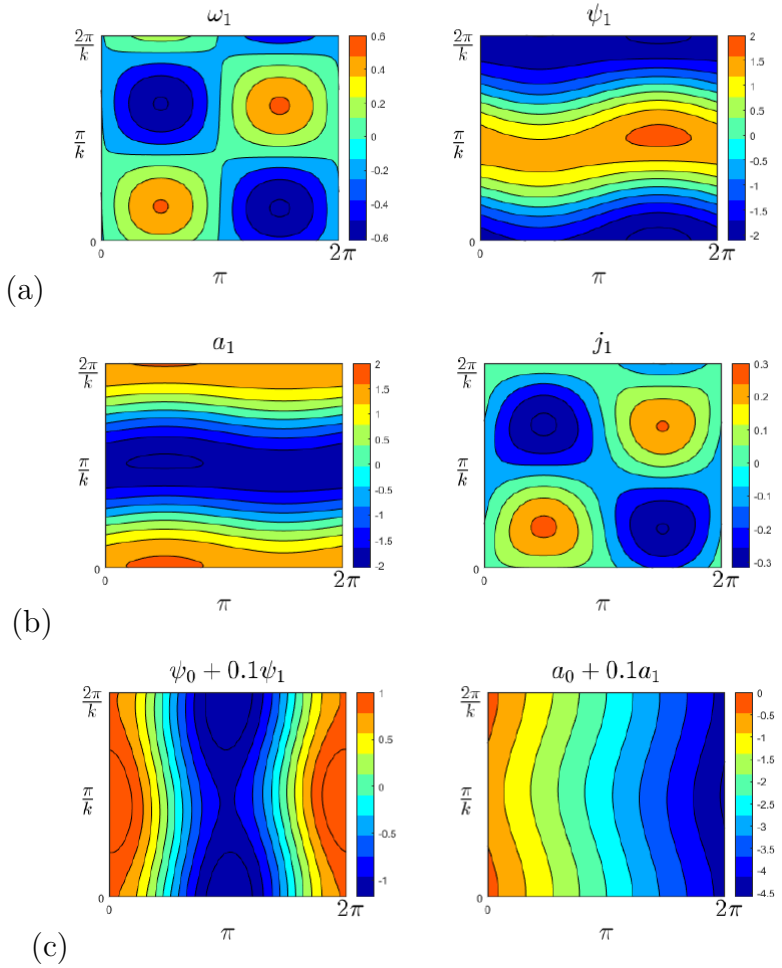

Figure 3.8: Shaded contour plot of the oscillatory mode of instability displayed the case $B_0 = 0.7,\ k = 0.1,\ \nu = 0.28, \eta = 2\nu$. Panel (a) vorticity ω_1 and stream function ψ_1, panel (b) the magnetic field a_1 and the magnetic current j_1, panel (c) Superposition of basic flow $\psi_0 + 0.1\psi_1$ and field $a_0 + 0.1a_1$. The real part of the stream function and of the associated vorticity $\omega_1 = -\nabla^2\psi_1$ is plotted.

Instability at large Prandtl number $P = 2$ has no effect on the system in the case of the vertical magnetic field due to the low magnetic diffusion, the system no longer exhibits instability for strong fields as shown in figure 3.9. We plot instability growth rate with the same structure of figure 3.4 for $\mathrm{Re}\, p_{\max}, \mathrm{Im}\, p_{\max}, k_{\max}$ but for Prandtl number $P = 2$ that is $\eta = 0.5\nu$, where the magnetic field is suppressing the growth rate, giving the same suppression at $P = 1$ in figure 3.4.

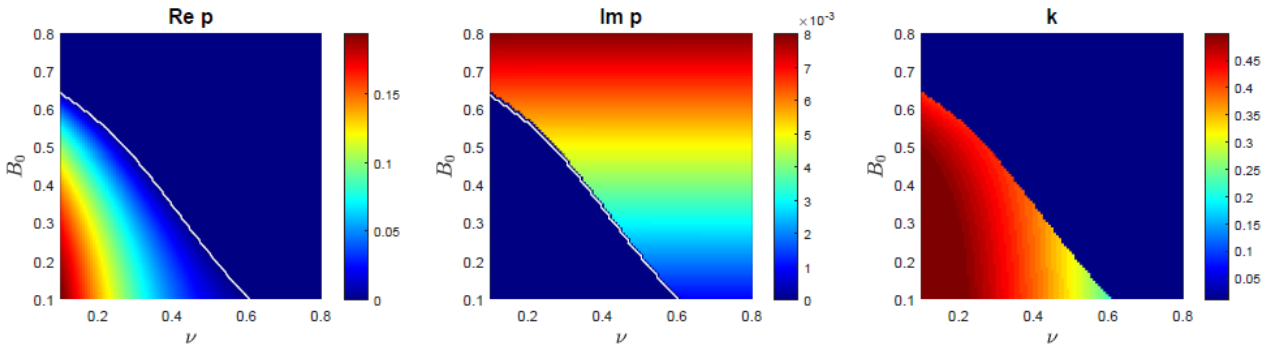

Figure 3.9: Contour plots of instability growth rate for vertical field plotted in the (ν, B_0)-plane, with $\eta = 0.5\nu, P = 2$. Plotted for $\mathrm{Re}\, p_{\max}$, frequency $\mathrm{Im}\, p_{\max}$ and wavenumber $k_{\max}$ of their respective eigenfunction, the contour line $\mathrm{Re}\, p = 0$ overlayed in white shows zero growth rate.

We conclude that as B_0 is increased, two families of instability are observed: first, a reduction in the peak and the magnetic field suppresses the hydrodynamic instability, shown in figure 3.4, and a distinct branch of decaying modes which appears at strong field strength and small Prandtl number; this branch has a small growth rate (see figure 3.7). Observations have shown that the new branch is a destabilised Alfvén wave as stated in Fraser, Cresswell and Garaud (2022). Therefore, we develop perturbation theory based on some basic assumptions to demonstrate clearly how strong fields enhance this instability. We will explain these numerical results in more detail in the following section.

3.6 Perturbation theory with $k \ll 1$

Perturbation theory is a set of approximation methods directly related to mathematical methods in fluid dynamics and magnetohydrodynamics to describe a complex system using a simpler one (Bender and Orszag, 1999). Perturbation theory has been applied in a wide range of fields including geophysical and astrophysical systems for finding an approximate solution to a linear problem by starting from an nearby exact solution; the solution is expressed as a power series with a small parameter ϵ. The first term represents the known solution to the solvable problem. Successive terms in the series at higher powers of ϵ usually become smaller. A 'perturbation solution' is obtained by truncating the series, usually keeping only the first two terms, the

linear problem solution and the 'first order' perturbation correction. Our motivation is to determine how the magnetic field affects such instabilities using classical linear stability theory, as described in Frisch, Legras and Villone (1996) and Manfroi and Young (2002), though written in a different way. In this chapter we will look at *strong magnetic field* and small Prandtl number $P < 1$.

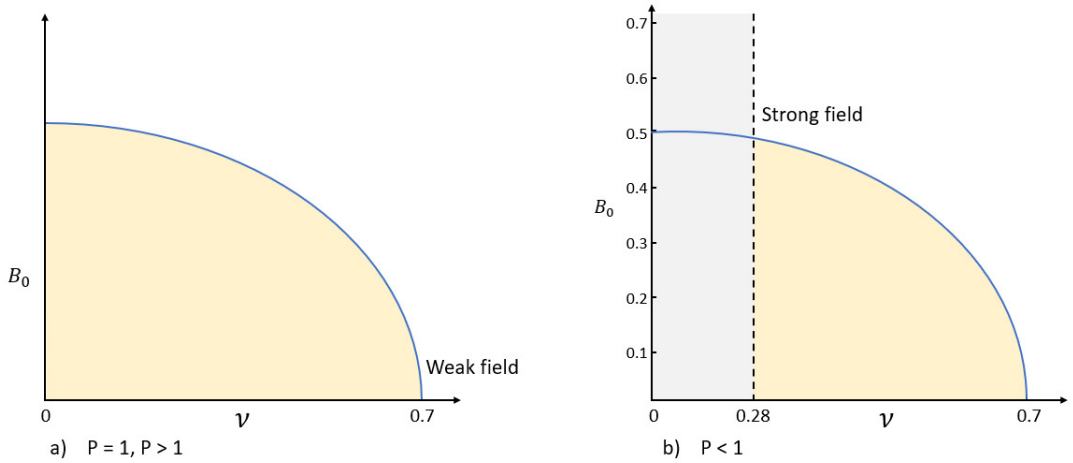

Figure 3.10: Schematic of the instability growth rate modified by the vertical magnetic field. Two possible behaviours occur, (a) instability with the weak field at $P = 1, P > 1$ (b) instability at the strong magnetic field and $P = 0.5$. dashed lines show the instability threshold around $\nu = 0.28$. The region dashed with yellow shows a fast growth rate, and the grey-shaded region extends along the vertical axis showing instability with a small growth rate. This schematic describes the figures 3.4 - 3.7 & 3.9 for ($P > 1$).

We provide the reader with the schematic figure 3.10 as a means of explaining the figures 3.4-3.7 with a clear interpretation, as well as illustrating the region in which this theory can be applied. Panel (a) shows a weak field suppresses hydrodynamic instability for $P = 1$ & $P > 1$ and panel (b) shows the weak field branch up to $B_0 \approx 0.5$ determined by the yellow region and a strong field branch visible for $B_0 \geqslant 0.5$ for the region of diffusion dominance (grey region) at $P = 0.5$. The instability threshold is marked by a dashed line $\nu < \nu_c = 0.28$. The linear theory will develop the mathematical reasons for this instability phenomenon and verify our numerical results. Next section, we will look for the linear theory analysis of these numerical results in more detail.

3.7 Perturbation theory outline

First, we outline the common method for all the perturbation analysis in this thesis. In each case, we write the governing eigenvalue problem in a matrix form, where the matrix $M(k, \nu, P, B_0)$ depends on wavenumber k, viscosity ν, Prandtl number P, magnetic field B_0. The eigenvector is $\boldsymbol{v}$, eigenvalue is p with

$$M\boldsymbol{v} = p\boldsymbol{v}. \tag{3.56}$$

We may rescale some quantities in the matrix M, and we then take a series expansion of M in powers of the small parameter k as

$$M = M_0 + kM_1 + k^2 M_2 + \cdots, \tag{3.57}$$

and likewise $\boldsymbol{v}$ and p. For the limit $k \to 0$ we solve

$$(M_0 + kM_1 + \cdots)(\boldsymbol{v}_0 + k\boldsymbol{v}_1 + \cdots) = (p_0 + kp_1 + \cdots)(\boldsymbol{v}_0 + k\boldsymbol{v}_1 + \cdots), \tag{3.58}$$

order by order in k. Here we set out the equations for different orders of k given by :

$$O(1), p_0\boldsymbol{v}_0 = M_0\boldsymbol{v}_0, \tag{3.59}$$

$$O(k), p_1\boldsymbol{v}_0 = (M_0 - p_0 I)\boldsymbol{v}_1 + M_1\boldsymbol{v}_0, \tag{3.60}$$

$$O(k^2), p_2\boldsymbol{v}_0 = (M_0 - p_0 I)\boldsymbol{v}_2 + M_2\boldsymbol{v}_0 + M_1\boldsymbol{v}_1 - p_1\boldsymbol{v}_1, \tag{3.61}$$

$$O(k^3), p_3\boldsymbol{v}_0 = (M_0 - p_0 I)\boldsymbol{v}_3 + M_3\boldsymbol{v}_0 + M_2\boldsymbol{v}_1 + M_1\boldsymbol{v}_2 - p_2\boldsymbol{v}_1 - p_1\boldsymbol{v}_2, \tag{3.62}$$

$$O(k^4), p_4\boldsymbol{v}_0 = (M_0 - p_0 I)\boldsymbol{v}_4 + M_4\boldsymbol{v}_0 + M_3\boldsymbol{v}_1 + M_2\boldsymbol{v}_2 + M_1\boldsymbol{v}_3 - p_3\boldsymbol{v}_1 - p_2\boldsymbol{v}_2 - p_1\boldsymbol{v}_3. \tag{3.63}$$

First, we choose an eigenvalue p_0 and corresponding eigenvector $\boldsymbol{v}_0$ of M_0; at the level of M_0 the mode is undamped, and so the real part of p_0 is zero. Assuming this is a simple (non-repeated eigenvalue), there is also a single left eigenvector $\boldsymbol{w}_0$ with $\boldsymbol{w}_0(M_0 - p_0) = 0$. For order one in equation (3.59) thus dealt with, we note that we

gain successive eigenvalues from applying $\boldsymbol{w}_0$ to the left of the remaining equations.

$$p_1\,\boldsymbol{w}_0\boldsymbol{v}_0 = \boldsymbol{w}_0 M_1 \boldsymbol{v}_0, \tag{3.64}$$

$$p_2\,\boldsymbol{w}_0\boldsymbol{v}_0 = \boldsymbol{w}_0(M_2\boldsymbol{v}_0 + M_1\boldsymbol{v}_1 - p_1\boldsymbol{v}_1), \tag{3.65}$$

$$p_3\,\boldsymbol{w}_0\boldsymbol{v}_0 = \boldsymbol{w}_0(M_3\boldsymbol{v}_0 + M_2\boldsymbol{v}_1 + M_1\boldsymbol{v}_2 - p_2\boldsymbol{v}_1 - p_1\boldsymbol{v}_2), \tag{3.66}$$

$$p_4\,\boldsymbol{w}_0\boldsymbol{v}_0 = \boldsymbol{w}_0(M_4\boldsymbol{v}_0 + M_3\boldsymbol{v}_1 + M_2\boldsymbol{v}_2 + M_1\boldsymbol{v}_3 - p_3\boldsymbol{v}_1 - p_2\boldsymbol{v}_2 - p_1\boldsymbol{v}_3). \tag{3.67}$$

In this way once having chosen the eigenvalue p_0 to perturb from (3.59) together with $\boldsymbol{v}_0$ and $\boldsymbol{w}_0$, we find p_1 from (3.64). We then need $\boldsymbol{v}_1$ from second order $O(k^1)$ in (3.60), and while $M_0 - p_0$ is not invertible, having fixed the value of p_1, there is a solution for $\boldsymbol{v}_1$. It is not unique, but we will see that this does not matter. We can then calculate p_2 from (3.65) and so forth.

3.7.1 Strong vertical field branch

The analyses presented in this section are designed to capture the properties of the strong field branch seen for $P < 1, \eta > \nu$ in figure 3.7. Mathematically we need to consider the limit when $B_0 \to \infty$ as $k \to 0$, and we find that relating these via $B_0 = O(k^{-1})$ is most informative. We reduce the system by writing out the vertical field equations (3.68-3.69) truncated to G_0, H_0, $G_{\pm1}$ and $H_{\pm1}$, and drop any terms involving $G_{\pm2}$ and $H_{\pm2}$

$$pG_n = \frac{k}{2}\left[\frac{1}{(n-1)^2+k^2} - 1\right] G_{n-1} - \frac{k}{2}\left[\frac{1}{(n+1)^2+k^2} - 1\right] G_{n+1}$$

$$- \nu(n^2+k^2)G_n + ikB_0(n^2+k^2)H_n. \tag{3.68}$$

$$pH_n = \left[-\frac{k}{2}\right] H_{n-1} + \left[\frac{k}{2}\right] H_{n+1} - \eta(k^2+n^2)H_n + \left[\frac{ikB_0}{k^2+n^2}\right] G_n \tag{3.69}$$

$n = 0$

$$pG_0 = \frac{k}{2}\left[\frac{1}{1+k^2} - 1\right] G_{-1} - \frac{k}{2}\left[\frac{1}{1+k^2} - 1\right] G_1 - \nu k^2 G_0 + ik^3 B_0 H_0, \tag{3.70}$$

$$pH_0 = \frac{-k}{2} H_{-1} + \frac{k}{2} H_1 - \eta k^2 H_0 + ik^{-1} B_0 G_0, \tag{3.71}$$

$n = \pm 1$

$$pG_{\pm 1} = \pm\frac{k}{2}\left[\frac{1}{k^2} - 1\right] G_0 - \nu(1+k^2)G_{\pm 1} + ikB_0(1+k^2)H_{\pm 1}, \tag{3.72}$$

$$pH_{\pm 1} = \pm\frac{k}{2}H_0 - \eta(1+k^2)H_{\pm 1} + \frac{ikB_0}{1+k^2}G_{\pm 1}, \tag{3.73}$$

We rewrite the equations (3.72 - 3.73)in terms of $G_\pm$ and $H_\pm$ defined in (A.29)

$$G_\pm = \frac{1}{2}(G_1 \pm G_{-1}), \qquad H_\pm = \frac{1}{2}(H_1 \pm H_{-1}) \tag{3.74}$$

$$pG_+ = -\nu(1+k^2)G_+ + ikB_0(1+k^2)H_+, \tag{3.75}$$

$$pH_+ = -\eta(1+k^2)H_+ + \frac{ikB_0}{1+k^2}G_+, \tag{3.76}$$

The fields G_+ and H_+ are decoupled from G_0, H_0 & so may be dropped. We then have for G_0, H_0, G_-, H_-.

$$pG_0 = \frac{k^3}{1+k^2}G_- - \nu k^2 G_0 + ikB_0 k^2 H_0 \tag{3.77}$$

$$pH_0 = kH_- - \eta k^2 H_0 + \frac{ikB_0}{k^2}G_0 \tag{3.78}$$

$$pG_- = \frac{1-k^2}{2k}G_0 - \nu(1+k^2)G_- + ikB_0(1+k^2)H_- \tag{3.79}$$

$$pH_- = \frac{-k}{2}H_0 - \eta(1+k^2)H_- + \frac{ikB_0}{1+k^2}G_- \tag{3.80}$$

Now rescale $G_0 = k^2 G_0'$ by divided equation (3.77) by k^2 we obtain equation (3.81) and other rescalings $H_0 = H_0', \quad G_- = G_-', \quad H_- = H_-', \quad p = p', \quad \nu = \nu', \quad \eta = \eta', \quad ikB_0 = iB_0',$

$$p'G_0' = \frac{k}{1+k^2}G_-' - \nu' k^2 G_0' + iB_0' H_0' \tag{3.81}$$

$$p'H_0' = kH_-' - \eta' k^2 H_0' + iB_0' G_0' \tag{3.82}$$

$$p'G_-' = \frac{1}{2}k(1-k^2)G_0' - \nu'(1+k^2)G_-' + iB_0'(1+k^2)H_-' \tag{3.83}$$

$$p'H'_- = \frac{-k}{2}H'_0 - \eta'(1+k^2)H'_- + \frac{iB'_0}{1+k^2}G'_- \tag{3.84}$$

Then we obtain the matrix, by dropping the primes: (without any further approximation) in the form $M\boldsymbol{v} = p\boldsymbol{v}$ with

$$M = \left(\begin{array}{cc|cc} -\nu k^2 & ikB_0 & k(1+k^2)^{-1} & 0 \\ ikB_0 & -\eta k^2 & 0 & k \\ \hline \frac{1}{2}k(1-k^2) & 0 & -\nu(1+k^2) & ikB_0(1+k^2) \\ 0 & -\frac{1}{2}k & ikB_0(1+k^2)^{-1} & -\eta(1+k^2) \end{array}\right), \quad \boldsymbol{v} = \begin{pmatrix} G_0 \\ H_0 \\ G_- \\ H_- \end{pmatrix}, \tag{3.85}$$

Before expanding M in powers of k, for strong vertical field we rescale $iB_0 = ik^{-1}B'_0$ with B'_0 fixed in the limit $k \to 0$. This rescaling for strong fields is a careful choice, to pick up the strong field instability, we also apply (3.86) into (3.85)

$$\frac{k}{1+k^2} = k(1+k^2)^{-1} = k - k^3 + k^5 - \cdots \tag{3.86}$$

gives

$$M = \left(\begin{array}{cc|cc} -\nu k^2 & iB'_0 & k - k^3 + k^5 - \cdots & 0 \\ iB'_0 & -\eta k^2 & 0 & k \\ \hline \frac{1}{2}k - \frac{1}{2}k^3 & 0 & -\nu - \nu k^2 & iB'_0 + ik^2 B'_0 \\ 0 & -\frac{1}{2}k & iB'_0 - ik^2 B'_0 & -\eta - \eta k^2 \end{array}\right), \quad \boldsymbol{v} = \begin{pmatrix} G_0 \\ H_0 \\ G_- \\ H_- \end{pmatrix}, \tag{3.87}$$

Then expanding M by 3.57 and drop any term of of k^3 or k^5 in 3.87, we obtain the matrices

$$M_0 = \left(\begin{array}{cc|cc} 0 & iB'_0 & 0 & 0 \\ iB'_0 & 0 & 0 & 0 \\ \hline 0 & 0 & -\nu & iB'_0 \\ 0 & 0 & iB'_0 & -\eta \end{array}\right), \quad M_1 = \left(\begin{array}{cc|cc} 0 & 0 & 1 & 0 \\ 0 & 0 & 0 & 1 \\ \hline \frac{1}{2} & 0 & 0 & 0 \\ 0 & -\frac{1}{2} & 0 & 0 \end{array}\right),$$

$$\mathrm{M}_2 = \left(\begin{array}{cc|cc} -\nu & 0 & 0 & 0 \\ 0 & -\eta & 0 & 0 \\ \hline 0 & 0 & -\nu & iB_0' \\ 0 & 0 & -iB_0' & -\eta \end{array}\right) . \quad (3.88)$$

Then $M_0 \boldsymbol{v_0} = p_0 \boldsymbol{v_0}$ is the exactly solvable initial problem, and M_1, M_2, ... represent the first-order, second-order and higher-order corrections. An approximate perturbation solution is obtained by truncating the series, often by keeping only the first two terms, expressing the final solution as a sum of the initial (exact) solution and the first-order & second-order perturbation correction.

Figure 3.11 shows that in M_0 there are undamped Alfvén waves where there is flow G_0 and field H_0, damped Alfvén waves in terms of G_-, H_-. So, there is no coupling between these waves.

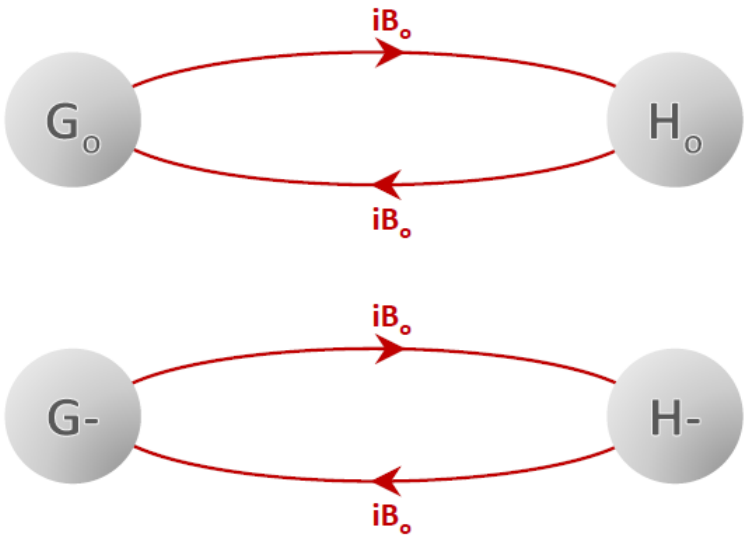

Figure 3.11: Schematic of the matrix M_0

Figure 3.12 shows that in M_1 (a) there are coupling terms between the terms for undamped waves G_0, H_0 and damped Alfvén waves G_-, H_-. As for the terms of G_+, H_+ in (b), there is no coupling. The Kolmogorov flow allows the possibility of instability, though the G_0, H_0 couplings to G_-, H_-.

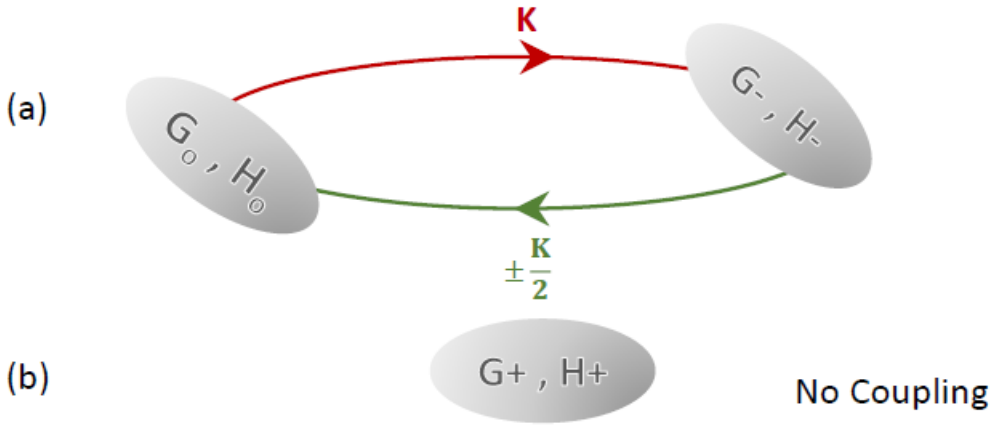

Figure 3.12: Schematic of the matrix M_1

Figure 3.13 shows that in the matrix M_2, there are damped Alfvén waves in (a) for the flow G_0, the field H_0 and damped Alfven waves for G_-, H_- in (b). There are more damped Alfvén waves in this matrix and no couplings between these waves. We now have M_2 which can bring in that extra $-\frac{\nu+\eta}{2}k^2$ damping term.

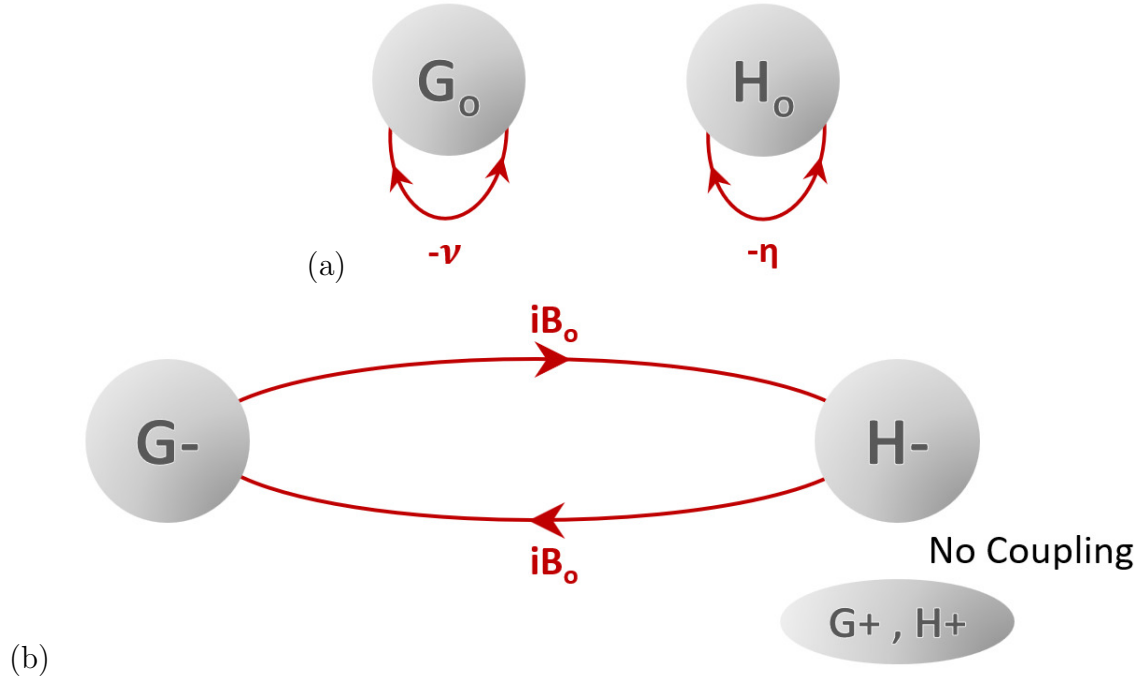

Figure 3.13: Schematic of the matrix M_2

For an approximate growth rate p we use the expansion equation (3.58) and solve by order. At leading to first order $O(k^0) = O(1)$ as $k^0 = 1$ in equation (3.59), we focus on the eigenvalues given by $p_0 = \pm iB_0'$, corresponding to large-scale undamped

Alfvén waves. We will focus on the first correction of growth rate p and take

$$p_0 = iB_0', \quad \boldsymbol{v}_0 = (1,1,0,0)^T, \quad \boldsymbol{w}_0 = (1,1,0,0). \tag{3.89}$$

Here, $\boldsymbol{w}_0$ is the left eigenvector, with $\boldsymbol{w}_0(M_0 - p_0 I) = 0$ and here $\boldsymbol{w}_0\boldsymbol{v}_0 = 2$.

The first order, from (3.64), shows the first correction to p_0 gives

$$M_1\boldsymbol{v}_0 = (0,0,\frac{1}{2},-\frac{1}{2})^T, \quad p_1 = \frac{\boldsymbol{w}_0 M_1 \boldsymbol{v}_0}{\boldsymbol{w}_0\boldsymbol{v}_0} = 0. \tag{3.90}$$

We now need to solve first order $O(k^1)$ in equation (3.60) for $\boldsymbol{v}_1$. To find a solution, we clearly need only invert the 2×2 lower right block of $M_0 - p_0 I$ to calculate

$$\begin{pmatrix} -\nu - iB_0' & iB_0' \\ iB_0' & -\eta - iB_0' \end{pmatrix}^{-1} = \frac{1}{(-\nu - iB_0')(-\eta - iB_0') + B_0'^2} \begin{pmatrix} -\eta - iB_0' & -iB_0' \\ -iB_0' & -\nu - iB_0' \end{pmatrix} \tag{3.91}$$

we found $p_1 = 0$, then equation (3.60) becomes:

$$(M_0 - p_0 I)\boldsymbol{v}_1 = -M_1\boldsymbol{v}_0, \qquad \boldsymbol{v}_1 = -M_1\boldsymbol{v}_0(M_0 - p_0 I)^{-1} \tag{3.92}$$

$$\boldsymbol{v}_1 = \Delta \begin{pmatrix} -\eta - iB_0' & -iB_0' \\ -iB_0' & -\nu - iB_0' \end{pmatrix} \begin{pmatrix} -\frac{1}{2} \\ \frac{1}{2} \end{pmatrix} = \Delta \begin{pmatrix} \frac{1}{2}\eta \\ -\frac{1}{2}\nu \end{pmatrix} \tag{3.93}$$

with the inverse determinant Δ defined as

$$\Delta^{-1} = \eta\nu + iB_0'(\eta + \nu). \tag{3.94}$$

Thus a solution for $\boldsymbol{v}_1$ is

$$\boldsymbol{v}_1 = \tfrac{1}{2}\Delta(0,0,\eta,-\nu)^T. \tag{3.95}$$

With this, it is straightforward to calculate p_2 from (3.65). So the second order

correction to p_0 is given by

$$p_2 = \frac{\boldsymbol{w}_0 M_1 \boldsymbol{v}_1}{\boldsymbol{w}_0 \boldsymbol{v}_0} + \frac{\boldsymbol{w}_0 M_2 \boldsymbol{v}_0}{\boldsymbol{w}_0 \boldsymbol{v}_0} \tag{3.96}$$

$$p_2 = \frac{1}{2}\begin{pmatrix} 1 & 1 & 0 & 0 \end{pmatrix} \left(\begin{array}{cc|cc} 0 & 0 & 1 & 0 \\ 0 & 0 & 0 & 1 \\ \hline \frac{1}{2} & 0 & 0 & 0 \\ 0 & -\frac{1}{2} & 0 & 0 \end{array}\right) \begin{pmatrix} 0 \\ 0 \\ \frac{1}{2}\Delta\eta \\ -\frac{1}{2}\Delta\nu \end{pmatrix} + \frac{1}{2}(-\eta - \nu) \tag{3.97}$$

$$p_2 = \tfrac{1}{4}\Delta(\eta - \nu) - \frac{1}{2}(\nu + \eta). \tag{3.98}$$

The growth rate $p = p_0 + kp_1 + k^2 p_2 + ...$ gives:

$$p = iB_0' + \frac{1}{4}\Delta(\eta - \nu)k^2 - \frac{1}{2}(\nu + \eta)k^2 + ...$$

$$p = iB_0' + \frac{\frac{1}{4}(\eta - \nu)}{\eta\nu + iB_0'(\eta + \nu)}k^2 - \frac{1}{2}(\nu + \eta)k^2 + ... \tag{3.99}$$

This can be rewritten by multiplying by the complex conjugate of the denominator.

$$p = iB_0' + \frac{1}{4}\frac{(\eta - \nu)(\eta\nu - iB_0'(\eta + \nu))k^2}{\eta^2\nu^2 + B_0'^2(\eta + \nu)^2} - \frac{1}{2}(\nu + \eta)k^2 + ...$$

$$\mathrm{Re}\, p = \frac{1}{4}\frac{\nu\eta(\eta - \nu)}{\nu^2\eta^2 + B_0'^2(\nu + \eta)^2}k^2 - \frac{1}{2}(\nu + \eta)k^2 + \cdots . \tag{3.100}$$

If we put this over a common denominator and reinstate B_0 with $B_0' = kB_0$, we obtain

$$\mathrm{Re}\, p = \frac{1}{4}\frac{\nu\eta(\eta - \nu)k^2 - 2(\nu + \eta)k^2(\nu^2\eta^2 + k^2B_0^2(\nu + \eta)^2)}{\nu^2\eta^2 + k^2B_0^2(\nu + \eta)^2} + \cdots . \tag{3.101}$$

$$\mathrm{Re}\, p = \frac{1}{4}\frac{[\nu\eta(\eta - \nu) - 2(\nu + \eta)\nu^2\eta^2]k^2 - 2(\nu + \eta)^3B_0^2k^4}{\nu^2\eta^2 + k^2B_0^2(\nu + \eta)^2} + \cdots . \tag{3.102}$$

From equation 3.102 we have $2(\nu+\eta)^3 B_0^2 k^4$ term in the nominator which is always negative and can not give instability. So we have $Rep > 0$ it is essential that $[\nu\eta(\eta-\nu) - 2(\nu+\eta)\nu^2\eta^2]k^2 > 0$, setting this equal zero, gives instability threshold

$$\nu\eta(\eta-\nu) - 2(\nu+\eta)\nu^2\eta^2 = 0 \tag{3.103}$$

$$\eta - \nu = 2(\nu+\eta)\nu\eta \tag{3.104}$$

By substituting η by $\frac{\nu}{P}$ we obtain:

$$\frac{\nu}{P} - \nu = 2(\nu + \frac{\nu}{P})\frac{\nu^2}{P} \tag{3.105}$$

$$(\frac{1}{P} - 1)\nu = 2\nu^3(1+\frac{1}{P})\frac{1}{P} \tag{3.106}$$

$$2\nu^2 = \frac{\frac{1}{p} - 1}{\frac{1}{P}(1+\frac{1}{P})} = \frac{P(1-P)}{1+P} \tag{3.107}$$

which amounts to

$$\nu < \nu_c = \sqrt{\frac{P}{2}\frac{1-P}{1+P}}, \tag{3.108}$$

$$P = 0.5 \Rightarrow \qquad \nu_c = \frac{1}{\sqrt{12}} \simeq 0.28 \tag{3.109}$$

We can change the ordering using larger viscosity and smaller magnetic diffusion; we will obtain a decaying mode that appears at large Prandtl numbers $P > 1$, resulting in qualitatively different results, and a stable mode. Figure 3.7 shows excellent agreement outlined by the threshold of instability of k_*.

From equation (3.101), we set the numerator to zero, as $B_0 \to 0$, we found the threshold of instability of the wavenumber k

$$(\eta-\nu)\eta\nu k^2 = 2(\nu+\eta)k^2(\eta^2\nu^2 + B_0^2(\eta+\nu)^2 k^2) \tag{3.110}$$

$$k^2 = \frac{1}{B_0^2(\eta+\nu)^2}\left(\frac{(\eta-\nu)\eta\nu}{2(\eta+\nu)} - \eta^2\nu^2\right) \tag{3.111}$$

$$k_* = \frac{1}{B_0(\eta+\nu)}\sqrt{\left(\frac{(\eta-\nu)\eta\nu}{2(\nu+\eta)} - \nu^2\eta^2\right)} \tag{3.112}$$

Equation (3.112) represents the instability threshold of real part of p against k in figure 3.14 at any k , if we choose the field strength $B_0 = 2$ and substitute the parameter values $\nu = 0.2, \eta = 0.4$, we found $k_* = 0.07$ corresponding to the dotted blue line in figure 3.14 (a).

Double diffusivity generates oscillatory modes characterized by small values of growth rate, which are called "overstable" modes and have a frequency $\mathrm{Im}\, p \neq 0$. Double diffusion occurs when two components contribute to the density and the classic example is the temperature and salt. The process can also take place in the ocean, where both temperature and salinity either increase or decrease in depth (Hughes and Brummell, 2021). There are two impotent regimes in double diffusion and double-diffusive convection, one is the salt finger regime and the other is a diffusive regime. The diffusive regime consists of destabilizing temperature and stabilising salt gradient. Figure 3.15 shows a 2D colour plot for this important regime in the double-diffusive system at $P < 1$ and strong field. These two damped waves are destabilized by the Kolmogorov flow. According to Jones and Roberts (2000), they determined instability driven by magneto convection and using double diffusion, and they investigated the limit $P \to \infty$, which eliminates Alfvén waves. The study also identified marginal modes for both steady and oscillatory modes at general wavenumbers k and found oscillatory convection at large Prandtl numbers $P \gg 1$, whereas steady modes at $P \ll 1$. Whereas our results show unsteady modes for $P < 1$ and no such modes for $P \geqslant 1$.

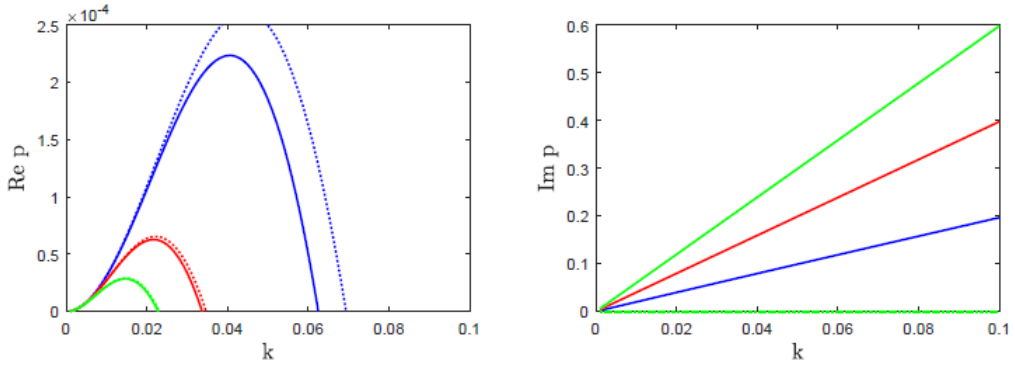

Figure 3.14: Instability growth rate as a function of k for $\nu = 0.2, \eta = 2\nu$, B_0 values are $2, 4, 6$, (a) $\mathrm{Re}\, p$ (b) $\mathrm{Im}\, p$. The solid lines are obtained numerically, while the dotted lines in panel (a) are the analytical expressions given in (3.100).

There is a good agreement between theory and numerical calculations for the *strong vertical field branch* at small k shown in figure 3.14, comparison between the exact numerical solution (solid curves) and the analytical approximation (dotted curves) from equation (3.100). We can see clearly the theory improves as we increase B_0 as we expect. We run the script at $P = 0.5$, $\nu = 0.2$ and for $B_0 = 2, 4, 6$. By using the analytical expression (3.100). We see that the agreement between solid curves and dotted curves is not good in (blue curve) at $B_0 = 2$, and in (red curve) at $B_0 = 4$ is better, we found the agreement is very good in (green curve) at $B_0 = 6$, so the theory works for small k and large B_0. We see that $\mathrm{Re}\, p$ can only be positive when for $\nu < \eta$, or in other words $P < 1$. Likewise, $\mathrm{Re}\, p$ is negative when $\nu > \eta$, or $P > 1$.

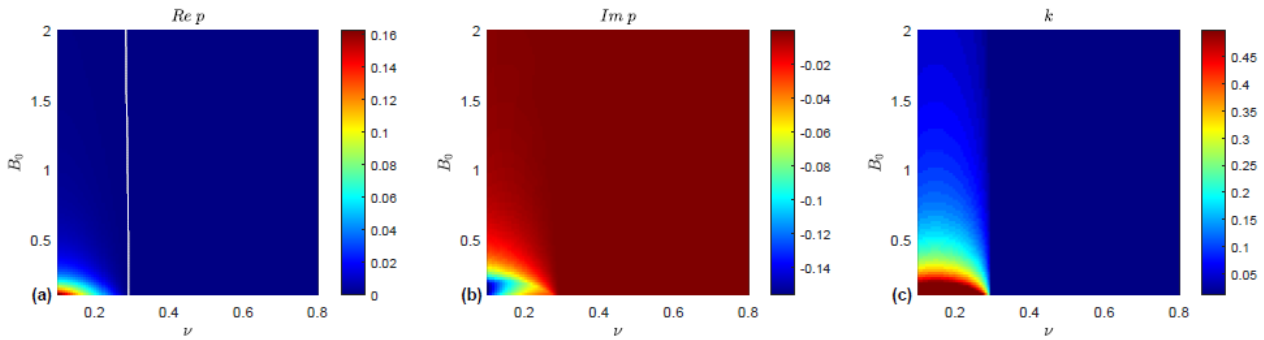

Figure 3.15: Colour plots of instability growth rate as a function of (ν, B_0) predicted by perturbation theory for $P = 0.5$. Plotted for $\mathrm{Re}\, p_{\max}$, frequency $\mathrm{Im}\, p_{\max}$ and Fourier mode $k_{\max}$ of their respective eigenfunction, a blue region is mostly a zero growth rate and the contour line $\mathrm{Re}\, p = 0$ overlayed in white.

Figure 3.15 shows how the growth rate behaves across the range of parameter space with $\eta = 2\nu$. Where $\mathrm{Re}\, p$ gives an indicator of the theoretical instability at $\nu \approx 0.28$

determined with white contour line $\mathrm{Re}\, p = 0$ and extends along the vertical axis and visible in plots of $\mathrm{Re}\, p$ and $\mathrm{Im}\, p$ and in $k_{\max}$ plot, we can see clearly this instability has frequency with small values clearly observable in the imaginary part $\mathrm{Im}\, p$. Figure 3.14, shows the instability at different magnetic field strengths. The blue curve represents the most unstable mode at $B_0 = 2$ appearing in the figure 3.15 (a,b,c), we keep the B_0 scale up to $B_0 = 2$ in this figure, so the curves $B_0 = 4$ (red), $B_0 = 6$ (green) show instability but are not visible in figure 3.15. This theoretical branch occurs as we increase $B_0 \to \infty$.

3.8 Conclusion

We give a summary of the results of this chapter through the following points:

- We have established the various parameters (ν, η, P, B_0) of Kolmogorov flow relating to the vertical magnetic field. The general form of these equations is similar to that given in the hydrodynamic case (compare (2.5) and (3.29 – 3.36) with vertical magnetic field B_0 now appearing in the system.

- We look at the effect of the magnetic field on the instabilities. The direction of the field will be important in how it combines with the basic state & instabilities. We see it can both suppress & enhance the hydrodynamic instabilities.

- A large-scale instability (small wavenumber) in hydrodynamic and MHD problems, leads to exhibiting the zonostrophic instability, potentially encouraging and creating jets in the system; solutions can only be clarified through numerical methods, which we set out in this chapter in section 3.5, figure 3.5.

- Introducing magnetic field in the z-direction $B_0 = (0, 0, B_0)$, in form $\nabla p + \nabla(\frac{B^2}{2\mu_0})$. leads to a magnetic pressure term that can be absorbed into the fluid pressure and does not affect incompressible Kolmogorov flow, while a compressible flow will give rise to magnetic buoyancy. Perhaps this is another mechanism by which the magnetic field disrupts jet-like profiles.

- We found a weak field instability in figure 3.4 and strong field instability that exists only for small Prandtl number $P < 1$ in figure 3.7, which brings different feedback to the strong vertical magnetic field, and allows for a new instability to occur. We used theoretical analysis and found instability growth rate (3.100) and threshold (3.109). We have confirmed the numerical results of Fraser, Cresswell and Garaud (2022) with an alternative derivation of their growth rate formula.

- Increasing the strength of B_0 in case $P = 1$ leads to the suppression of instability and switches off the Meshalkin and Sinai (1961) instability. We also obtained the same instability structure for $P > 1$.

4. MHD stability: Horizontal magnetic field

4.1 Introduction

In this chapter, we consider how a magnetic field in the x-direction affects stability, where the magnetic field in this case is aligned with possible jet formation. Even though any calculations become somewhat complex at this point, these complications are that there are both a uniform horizontal component and a sinusoidal vertical component coming from the external force. Most often the magnetic field suppresses the instability due to the magnetic tension, where the magnetic field lines are frozen into fluid lines, and when fluid lines extend, the magnetic field lines also extend. So, the magnetic tension acts against this stretching and thus suppresses any instability. However, the horizontal field in this study has two pieces as shown in figure 4.1 (a,b), a uniform horizontal component in (a) and a sinusoidal vertical component in (b) where field lines are bent by fluid motion as a consequence of the Alfv́en theorem and satisfy the induction equation. The difference between the values of η in the two panels is intended to demonstrate the differences in field line behaviour between panels (a) and (b).

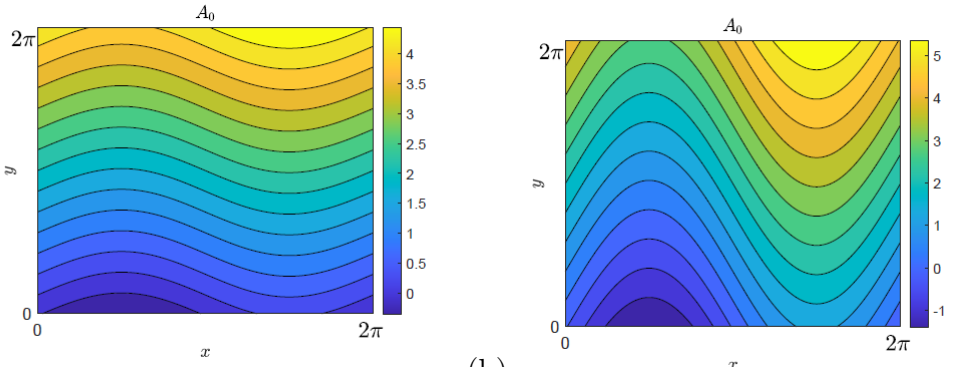

(a) (b)

Figure 4.1: The horizontal magnetic field lines with $B_0 = 0.7$. The field lines are depicted as a contour of the corresponding vector potential A_0 with $\boldsymbol{B}_0 = (\partial_y A_0, -\partial_x A_0)$. Panel (a) $\eta = 2$, panel(b) $\eta = 0.5$.

In an astrophysical system with a high magnetic Reynolds number $\eta = R_m^{-1}$, we can suppose that magnetic field lines are frozen into a fluid motion where the magnetic lines pass through plasma columns as shown in panel (a). For $R_m = 2$, the magnetic field lines are bent if the plasma column is bent as shown in both panels (a,b), as a consequence of Alfv́en's theorem, (Davidson, 2001). In this chapter, we investigate instabilities as a function of (ν, B_0, k, η), and we initially verify our results by setting $B_0 = 0$ to refer to the hydrodynamic case. The vertical magnetic field tends to suppress instability since the field lines are elastic as shown in chapter 3. Moreover, there are several ways in which a horizontal mean magnetic field can lead to instability as the background field now has non-zero current due to the sinusoidal vertical component that comes from the external force, and can also be unstable to ideal MHD perturbations and resistive instabilities.

4.2 Governing equations

Now we look at the horizontal mean magnetic field (x-directed) and switch off the vertical field. This depends only on x, so that once the basic state is written down the calculation will go through in a similar way.

To satisfy the vorticity and induction equations (3.28, 3.30) we state the basic state. The extra term $a_0(x)$ is needed to satisfy the induction equation. In the Navier-Stokes

momentum equations, we require additional force in the equations for the basic state to balance the Lorentz force. To see this, first we try:

$$\boldsymbol{u_0} = (0, \sin x, 0), \qquad \boldsymbol{B_0} = (B_0, 0, 0) = (A_{0y}, -A_{0x}, 0), \qquad A_0 = B_0 y. \tag{4.1}$$

The flow $\boldsymbol{u_0}$ will bend the field lines to give:

$$\partial_t A_0 + \mathcal{J}(A_0, \psi) = \eta \nabla^2 A_0, \tag{4.2}$$

$$\partial_t A_0 + A_{0x}\ \psi_y - \underbrace{A_{0y}\ \psi_x}_{\text{non-zero}} = \eta(A_{0xx} + A_{0yy}), \tag{4.3}$$

All terms in equation (4.3) are zero except the term labelled as non-zero, so this does not satisfy the induction equation. Instead, we impose an extra term in our basic state that balances the Lorentz force and to satisfy the induction equation; we set:

$$\boldsymbol{B_0} = (B_0, b_0(x), 0) = (A_{0y}, -A_{0x}, 0), \tag{4.4}$$

$$A_0 = B_0 y + a_0(x), \qquad b_0 = -\frac{\partial a_0}{\partial x}, \tag{4.5}$$

Try to find the extra term $a_0(x)$, we have:

$$0 + \sin x \frac{\partial A_0}{\partial y} = \eta \frac{\partial^2 A_0}{\partial x^2}, \tag{4.6}$$

hence

$$0 + \sin x\ B_0 = \eta \frac{\partial^2 a_0}{\partial x^2}, \qquad a_0 = -\frac{B_0}{\eta} \sin x. \tag{4.7}$$

So we get the basic state with a steady solution that gives figure 4.1,

$$\boldsymbol{B_0} = (B_0, \frac{B_0}{\eta} \cos x, 0), \qquad A_0 = B_0 y + a_0(x), \qquad a_0(x) = -\frac{B_0}{\eta} \sin x, \qquad J_0 = -\frac{B_0}{\eta} \sin x, \tag{4.8}$$

By setting the linear perturbation, we obtain:

$$\boldsymbol{B} = \boldsymbol{B_0} + \boldsymbol{B_1}, \qquad A = A_0 + A_1, \tag{4.9}$$

$$A = B_0 y - \frac{B_0}{\eta}\sin x + A_1, \qquad \boldsymbol{B} = (B_0 + A_{1y}, \frac{B_0}{\eta}\cos x - A_{1x}, 0), \tag{4.10}$$

The basic state in equation (4.8) satisfies the vector potential equation,

$$\partial_t A_0 + \boldsymbol{u}\cdot\nabla A_0 = \eta\nabla^2 A_0 \tag{4.11}$$

Now we substitute the basic state as given $(A_0, B_0, \boldsymbol{u_0})$ into equation (3.28), we get the curl of the body force g which is needed to maintain the basic state.

$$\partial_t\omega_0 + \frac{\partial(\omega_0,\Psi_0)}{\partial(x,y)} = \frac{\partial(J_0,A_0)}{\partial(x,y)} + \nu\nabla^2\omega_0 + g, \tag{4.12}$$

$$\partial_x\omega_0 \underbrace{\partial_y\psi_0 - \partial_y\omega_0}_{I}\partial_x\psi_0 = \partial_x J_0\partial_y A_0 - \underbrace{\partial_y J_0\partial_x}_{II} A_0 + \nu\nabla^2\omega_0 + g, \tag{4.13}$$

Term $I = 0$, since ω, ψ depends on x only, and $II = 0$, since J_0 depends on x only.

$$0 = \partial_x J_0\partial_y A_0 + \nu\nabla^2\omega + g \tag{4.14}$$

$$0 = -\frac{B_0}{\eta}\cos x B_0 + \nu(-\cos x) + g, \tag{4.15}$$

$$g = \frac{B_0^2}{\eta}\cos x + \nu\cos x, \tag{4.16}$$

By linearising the equations, and substituting the linearised equation (3.32) into equation (4.12), we obtain:

$$\begin{aligned}&\partial_t(\omega_0+\omega_1) + \partial_x(\omega_0+\omega_1)\partial_y(\Psi_0+\Psi_1) - \partial_y(\omega_0+\omega_1)\partial_x(\Psi_0+\Psi_1)\\ &= \partial_x(J_0+J_1)\partial_y(A_0+A_1) - \partial_y(J_0+J_1)\partial_x(A_0+A_1) + \nu\nabla^2(\omega_0+\omega_1) + g\end{aligned} \tag{4.17}$$

to give

$$\partial_t\omega_1 + [\frac{\partial\omega_0}{\partial x}\frac{\partial\Psi_1}{\partial y} - \frac{\partial\Psi_0}{\partial x}\frac{\partial\omega_1}{\partial y}] = [\frac{\partial J_0}{\partial x}\frac{\partial A_1}{\partial y} + \frac{\partial J_1}{\partial x}\frac{\partial A_0}{\partial y} - \frac{\partial A_0}{\partial x}\frac{\partial J_1}{\partial y}] + \nu\nabla^2\omega_1 \quad (4.18)$$

and so

$$\partial_t\omega_1 - \sin x\ \partial_y\Psi_1 + \sin x\ \partial_y\omega_1 = \frac{-B_0}{\eta}\cos x\ \partial_y A_1 + B_0\partial_x J_1 + \frac{B_0}{\eta}\cos x\partial_y J_1 + \nu\nabla^2\omega_1, \quad (4.19)$$

By using the Fourier expansion equations (3.37 - 3.40), seek a normal mode in ψ, ω, A, J proportional to an exponential. We extract sine and cos waves terms in e^{inx} (3.43, 4.20), and we obtain:

$$\cos x\ A = \frac{1}{2}\sum_{n=-\infty}^{\infty}[H_n e^{i(n+1)x} + H_n e^{i(n-1)x}] = \frac{1}{2}\sum_{n=-\infty}^{\infty}[H_{n-1}e^{inx} + H_{n+1}e^{inx}] \quad (4.20)$$

The vorticity equation becomes

$$pG_n = -\frac{k}{2}(F_{n-1}-F_{n+1})+\frac{k}{2}(G_{n-1}-G_{n+1})-\frac{ikB_0}{2\eta}(H_{n-1}+H_{n+1})+inB_0\ J_n+\frac{ikB_0}{2\eta}(J_{n-1}+J_{n+1}). \quad (4.21)$$

$$pG_n = \frac{k}{2}\left[\frac{1}{(n-1)^2+k^2} - 1\right]G_{n-1} - \frac{k}{2}\left[\frac{1}{(n+1)^2+k^2} - 1\right]G_{n+1}$$

$$-\frac{ikB_0}{2\eta}\underbrace{(H_{n-1}+H_{n+1})}_{I}+\frac{ikB_0}{2\eta}\underbrace{(J_{n-1}+J_{n+1})}_{II}+inB_0\ J_n = -\nu(k^2+n^2)G_n. \quad (4.22)$$

By linking the two terms (I, II) in equation (4.22) and replacing J_n by H_n via $J_n = (k^2+n^2)H_n$, we obtain:

$$-\frac{ikB_0}{2\eta}(H_{n-1}+H_{n+1}) + \frac{ikB_0}{2\eta}(J_{n-1}+J_{n+1}) = \quad (4.23)$$

$$\frac{ikB_0}{2\eta}(-1+[(n-1)^2+k^2])H_{n-1} + \frac{ikB_0}{2\eta}(-1+[(n+1)^2+k^2])H_{n+1}, \quad (4.24)$$

Then the growth rate as a solution of the vorticity stream function equation becomes:

$$pG_n = \frac{k}{2}\left[\frac{1}{(n-1)^2+k^2} - 1\right]G_{n-1} - \frac{k}{2}\left[\frac{1}{(n+1)^2+k^2} - 1\right]G_{n+1} - \nu(k^2+n^2)G_n$$

$$+\frac{ikB_0}{2\eta}((n-1)^2+k^2-1)H_{n-1}+\frac{ikB_0}{2\eta}((n+1)^2+k^2-1)H_{n+1}+inB_0(k^2+n^2)\ H_n. \quad (4.25)$$

By setting the linear perturbation equation for velocity and vector potential, we obtain :

$$\partial_t A_1 + \boldsymbol{u}_0 \cdot \nabla A_1 + \boldsymbol{u}_1 \cdot \nabla A_0 = \eta \nabla^2 A_1, \quad (4.26)$$

Where

$$\boldsymbol{u_0} = (0, \sin x), \quad \boldsymbol{u}_1 = (\Psi_{1y}, -\Psi_{1x}), \quad A_0 = B_0 y - \frac{B_0}{\eta}\sin x, \quad (4.27)$$

Substituting equation (4.27) into equation (4.26), we obtain:

$$\partial_t A_1 + \sin x\ \partial_y\ A_1 + \underbrace{u_0 \partial_x A_1}_{=0} - B_0 \Psi_{1x} - \frac{B_0}{\eta}\cos x\ \Psi_{1y} = \eta \nabla^2 A_1, \quad (4.28)$$

We also use the Fourier expansion equations (3.37 - 3.40), to obtain:

$$pH + ik\sin x\ H - B_0 F_x - \frac{ikB_0}{\eta}\cos x\ F = \eta(-k^2 + \frac{\partial^2}{\partial x^2})H, \quad (4.29)$$

Substitute Fourier modes in x (3.42 - 4.20) into equation (4.29), we obtain:

$$pH_n + \frac{k}{2}(H_{n-1} - H_{n+1}) - inB_0\ F_n - \frac{ikB_0}{2\eta}(F_{n-1} + F_{n+1}) = -\eta(k^2+n^2)H_n, \quad (4.30)$$

By replace F_n by G_n via $F_n = 1/(k^2+n^2)G_n$, we obtain:

$$pH_n = -\frac{k}{2}H_{n-1} + \frac{k}{2}H_{n+1} - \eta(k^2+n^2)H_n + \frac{inB_0}{k^2+n^2}G_n + \frac{ikB_0}{2\eta}\frac{1}{(n-1)^2+k^2}G_{n-1}$$

$$+ \frac{ikB_0}{2\eta}\frac{1}{(n+1)^2+k^2}G_{n+1}. \quad (4.31)$$

Further progress on the flow & magnetic field cannot be made without looking for numerical solutions to the system of equations given by (4.25 - 4.31). In this chapter, we aim to find a numerical solution by using the Matlab framework for this linear system of coupling equations for the flow G_n and field H_n.

4.2.1 Numerical methods

In our eigenvalue problem we have written the horizontal magnetic field as a Fourier series by writing eigenmode decomposition we consider our problem as the eigenvalue problem. We use truncation and keep all modes for $-N \leq n \leq N$, for some integer N (typical values $N = 16, 32$). In some cases, we vary N to check the results. We solve the matrix problem written in hexadiagonal form, where N is the number of Fourier mode

$$p\begin{pmatrix} G_{-N} \\ H_{-N} \\ G_{-N+1} \\ H_{-N+1} \\ \vdots \\ G_{N-1} \\ G_N \\ H_N \end{pmatrix} = M \begin{pmatrix} G_{-N} \\ H_{-N} \\ G_{-N+1} \\ H_{-N+1} \\ \vdots \\ G_{N-1} \\ G_N \\ H_N \end{pmatrix} \qquad p\begin{pmatrix} \vdots \\ G_n \\ H_n \\ \vdots \end{pmatrix} = \left(\begin{array}{cccc|cc|ccc} \ddots & \ddots & \ddots & & \ddots & & \ddots & \ddots & \ddots \\ \hline \ddots & a_n & d_n & & b_n & g_n & c_n & f_n & \ddots \\ \ddots & t_n & e_n & & z_n & r_n & \omega_n & s_n & \ddots \\ \hline \ddots & \ddots & \ddots & & \ddots & & \ddots & \ddots & \ddots \end{array}\right) \begin{pmatrix} \vdots \\ G_n \\ H_n \\ \vdots \end{pmatrix} \tag{4.32}$$

Comparing linear equations (4.25 - 4.31) for G_n & H_n with the matrix equation (4.32) and then writing the coefficients, gives

$$pG_n = a_n G_{n-1} + b_n G_n + c_n G_{n+1} + d_n H_{n-1} + g_n H_n + f_n H_{n+1}, \tag{4.33}$$

$$pHn = e_n H_{n-1} + r_n H_n + s_n H_{n+1} + t_n G_{n-1} + z_n G_n + w_n G_{n+1}, \tag{4.34}$$

We set a matrix element n for odd & even rows, and we obtain:

$$a_n = \frac{-k}{2} + \frac{k}{2}\left(\frac{1}{(n-1)^2+k^2}\right), \quad b_n = -\nu(n^2+k^2), \quad c_n = \frac{k}{2} - \frac{k}{2}\left(\frac{1}{(n+1)^2+k^2}\right),$$

$$g_n = inB(k^2+n^2), \quad d_n = \frac{ikB}{2\eta}(-1+(n-1)^2+k^2)), \quad f_n = \frac{ikB}{2\eta}(-1+(n+1)^2+k^2)), \quad e_n = \frac{-k}{2},$$

$$r_n = -\eta(k^2+n^2), \quad s_n = \frac{k}{2}, \quad t_n = \frac{iBk}{2\eta[(n-1)^2+k^2]}, \quad z_n = \frac{inB}{k^2+n^2}, \quad w_n = \frac{ikB}{2\eta[(n+1)^2+k^2]}. \tag{4.35}$$

As stated above, we let $i = 1$ giving $n = -N$, this corresponds to Fourier mode G_n at the wavenumber $n = -N + \frac{1}{2}(i-1)$, hence $i = 3$ gives $n = -N+1$, we will further let $i = 2$ correspond to H_n Fourier mode at the wavenumber $n = -N + \frac{1}{2}(i-2)$. Hence, $i = 2$ gives $n = -N$.

$$M_{ij} = \begin{cases} a_n & j = i-2, \\ d_n & j = i-1, \\ b_n & j = i \\ g_n & j = i+1 \\ c_n & j = i+2 \\ f_n & j = i+3 \end{cases} \qquad \text{for } i \text{ is odd} \quad n = -N + \tfrac{1}{2}(i-1). \tag{4.36}$$

and then a similar equation for even rows.

$$M_{ij} = \begin{cases} t_n & j = i-3, \\ e_n & j = i-2, \\ z_n & j = i-1 \\ r_n & j = i \\ w_n & j = i+1 \\ s_n & j = i+2 \end{cases} \qquad \text{for } i \text{ is even} \quad n = -N + \tfrac{1}{2}(i-2). \tag{4.37}$$

At a specified truncation N, the $(4N+2)\times(4N+2)$ matrix is set up in Matlab; we fill the matrix entries as described here. Then, call *eig* to determine the eigenvalues, and we create another script to vary the parameters, for a given parameter set (ν, B_0, η), The same details have been discussed in the previous chapter 3.

4.3 Numerical results: horizontal magnetic field

The horizontal magnetic field is expressed by the full steady solution $A_0 = B_0 y + \frac{B_0}{\eta} \sin x$ as shown in section 4.2: the extra term has an oscillatory component, which creates a strong branch of instabilities. If $\eta > 1$, there is a strong diffusion and weakly curved magnetic lines as shown in figure 4.1(a). If $\eta < 1$, there is a weak diffusion and strongly curved magnetic lines as shown in figure 4.1(b). We explore a number of instabilities in this section with different viscosities and magnetic field strengths to gain a better understanding of instability behaviour.

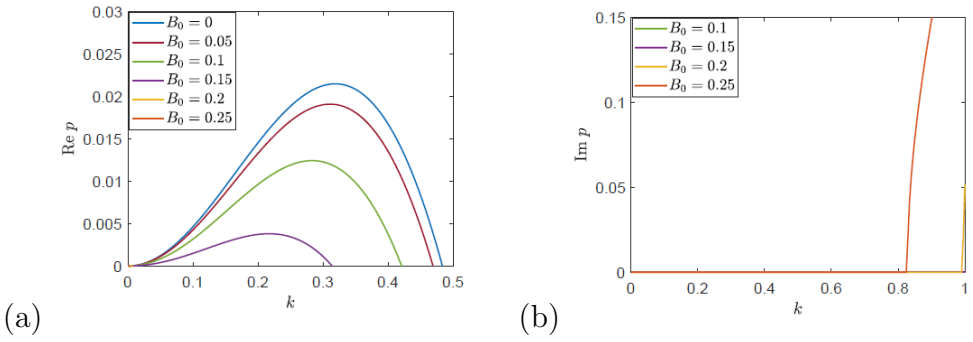

(a) (b)

Figure 4.2: Instability growth rate p as a function of k for $\nu = \eta = 0.5$, with $B_0 = 0$ (blue), $B_0 = 0.05$ (dark red), $B_0 = 0.10$ (green), $B_0 = 0.15$ (purple), $B_0 = 0.20$ (yellow), $B_0 = 0.25$ (orange). Panels (a) and (b) show $\mathrm{Re}\, p$ and $\mathrm{Im}\, p$ respectively.

Figure 4.2 shows instability growth rate p against the wavenumber k for $\nu = \eta = 0.5$ and B_0 increased as detailed in the caption. We start with $B_0 = 0$, and we can see clearly that the hydrodynamic branch of instability is represented by the blue curve $B_0 = 0$. We also see a green curve occur at $B_0 = 0.10$ and give roughly instability for $k < 0.4$, with a zero frequency in the imaginary part $\mathrm{Im}\, p = 0$ in panel (b). Nevertheless, if we increase B_0 further, the real part of the growth rate $\mathrm{Re}\, p$ decreases in panel (a), while in panel (b) we observed the frequencies grow for $B_0 = 0.20$ (yellow curve) and at $B_0 = 0.25$ (orange curve) with $\mathrm{Im}\, p \neq 0$. We can see a reduction in the hydrodynamic instability by a horizontal field. Alfvén waves are not relevant here unlike for vertical magnetic field.

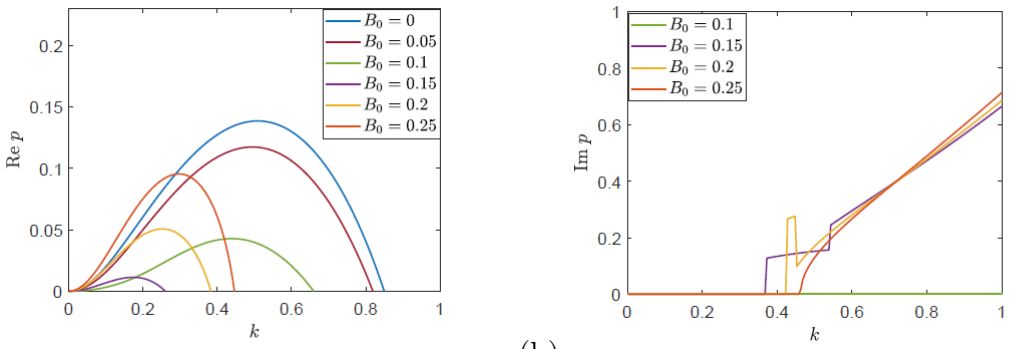

(a) (b)

Figure 4.3: Instability growth rate p as a function of k for $\nu = \eta = 0.2$ with $B_0 = 0$ (blue), $B_0 = 0.05$ (dark red), $B_0 = 0.10$ (green), $B_0 = 0.15$ (purple), $B_0 = 0.20$ (yellow), $B_0 = 0.25$(red). Panels (a) and (b) show $\mathrm{Re}\, p$ and $\mathrm{Im}\, p$ respectively.

Figures 4.3 and 4.4 show instability growth rate p against k for smaller values of viscosity $\nu = 0.2, \nu = 0.1$ respectively, and B_0 increased as detailed in the caption in figure 4.3. We see the magnetic field suppresses the hydrodynamic instability, going from the blue curve $B_0 = 0$ to the lower, dark red curve $B_0 = 0.05$. When we increase B_0 further, we obtain the green curve for $B_0 = 0.10$, which exhibits a double-peaked growth rate and these two peaks increase as B_0 increases, The second peaks are associated with non-zero imaginary part $\mathrm{Im}\, p$ as shown in panel (b), while the first peaks have $\mathrm{Im}\, p = 0$. In fact, we observe that the most unstable mode has zero frequency $\mathrm{Im}\, p = 0$. We also observed that as we reduce the value of viscosity from figure 4.3 to figure 4.4 the system gets more complicated and there is no agreement with Alfv́en waves and instability curves. We conclude that in panels 4.3 (b), 4.4 (b) show the imaginary part of $\mathrm{Im}\, p$ with no agreement of Alfvén waves, unlike the case for vertical field.

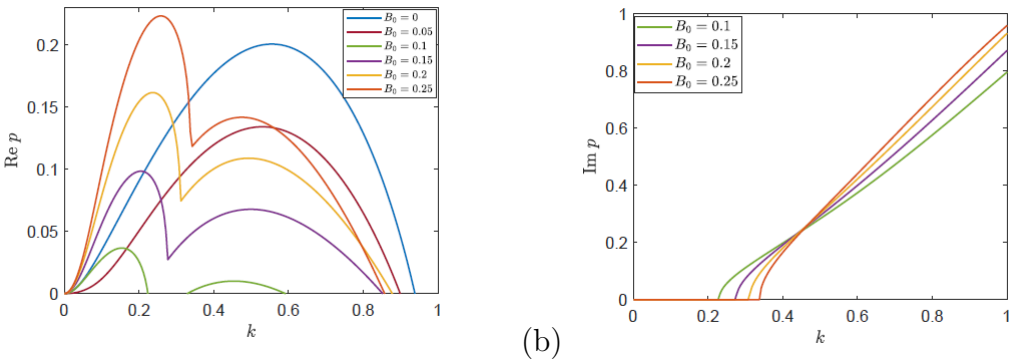

Figure 4.4: Instability growth rate p as a function of k for $\nu = \eta = 0.1$, with $B_0 = 0$ (blue),$B_0 = 0.05$ (dark red),$B_0 = 0.10$ (green),$B_0 = 0.15$ (purple),$B_0 = 0.20$ (yellow),$B_0 = 0.25$ (dark orange). Panels (a) and (b) show $\mathrm{Re}\, p$ and $\mathrm{Im}\, p$ respectively.

4.3.1 Linear instability as a function (ν, B_0)-plane

To give a more global picture of the above results we plot the maximum growth rate as a colour plot in the (ν, B_0)-plane with $\nu = \eta$ and consider $B_0 = 0$ initially referring to Meshalkin and Sinai (1961) for the hydrodynamic instability determined by the threshold value $\nu = \frac{1}{\sqrt{2}}$.

We observed two families of instability shown in figure 4.5, a suppression of purely hydrodynamic instability (as in the case of vertical field in figure 3.2) shown in panel (a), we refer to this as *the flow branch*. As we increase B_0 further another branch of instability emerges in panel (b), we refer to this as *the field branch* and the intermediate case between these two instabilities has zero growth rate outlined by the contour white line $\mathrm{Re}\, p = 0$. A region of instability below the white line appears from blue to yellow and red, while the region of stability is above the white line (dark blue) in both panels (a,b). A similar suppression of the hydrodynamic instability with β-effect and planar flow is observed also in turbulent context Tobias, Diamond and Hughes (2007) demonstrated that even weak magnetic fields B_0 can suppress the instability.

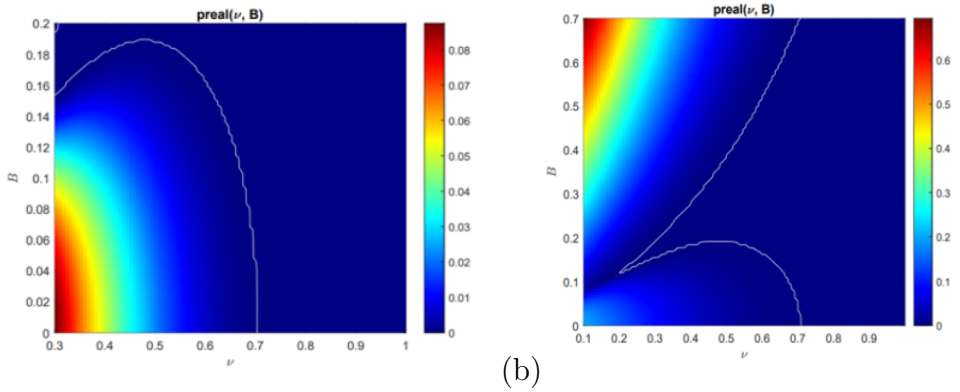

(a) (b)

Figure 4.5: Instability growth rate , the maximum real part $p_{max}(\eta = \nu)$ plotted as a function of B_0, ν. Panel (a) shows instability up to a weak field $B_0 = 0.2$, and panel (b) shows instability up to a strong field $B_0 = 0.7$.

The physical meaning behind these two branches of instability is our Kolmogorov flow is generated by a stationary sinusoidal force that varies in space and is known to lead to instabilities resulting in a zonal flow. By choosing a horizontal magnetic field direction in the system, similar results were found by Durston and Gilbert (2016). They studied the instability of random forced, anisotropic flow and they also found two branches of instability. Many studies use the Prandtl number of unity $P = 1$ without seeing fundamental changes. In the next section, we extend our linear analysis by varying the Prandtl number in order to gain a better understanding of instability behaviour.

4.3.2 Linear instability for varying Prandtl number P

In this section, we are looking for instability by varying the Prandtl number as shown in figure 4.6 with the white contour line $\mathrm{Re}\, p = 0$ determined the threshold of instability. Panels (a,b) show the instability of the growth rate at $P = 0.5$; we can see clearly the similar structure of instability in figure 4.5 at $P = 1$, while there is overlap between the two branches of instability appearing in the plot of k in panel (b).

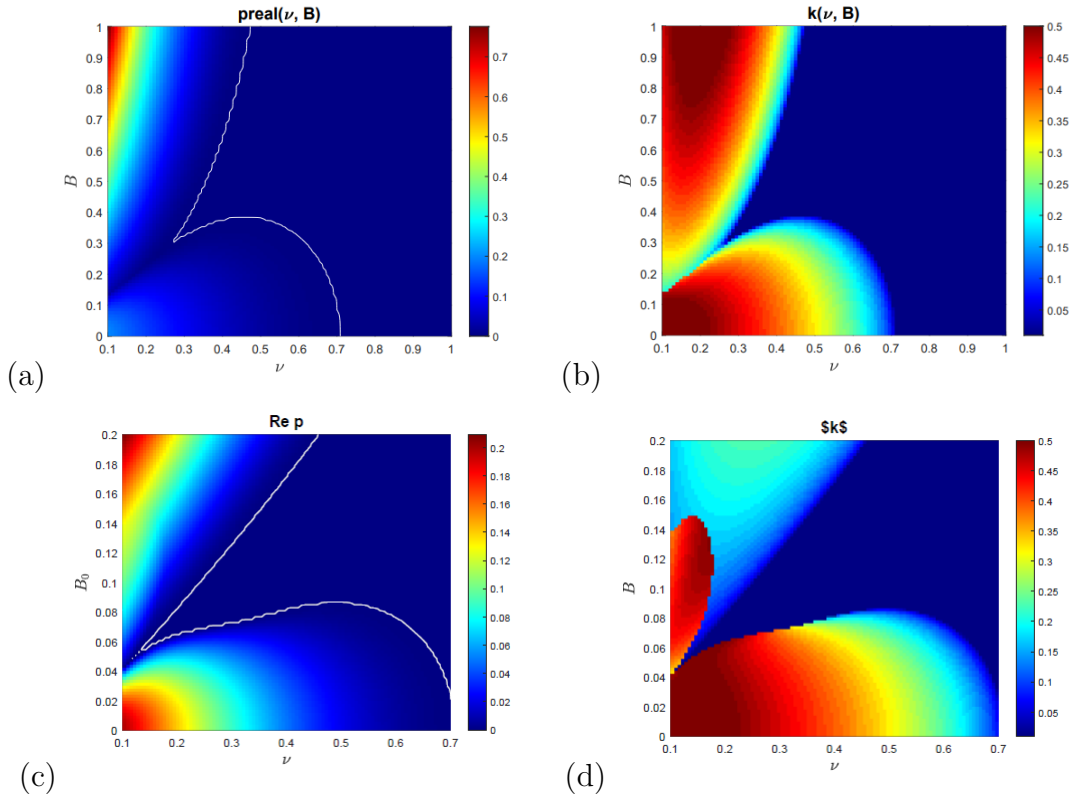

Figure 4.6: Colour plot of the maximum real part $\mathrm{Re}\, p$ as a function of (ν, B_0). Panels (a,b) shows $p_{max}(\eta = 2\nu, P = 0.5)$, panels (c,d) shows $p_{max}(\eta = 0.5\nu, P = 2)$.

Panels (c,d) show instability at large Prandtl number $P = 2$. we observed that there is a suppressed purely hydrodynamic branch *flow branch* by weak field B_0 and as we increase the magnetic field, we obtain *the field branch*; also we observed an island of instability appearing in the plot of k in panel (d) attached to the field branch of instability. This island occurs at the weak magnetic field in the range $0.04 < B_0 < 0.14$ marked by red colour (see next section 4.3.3). The physical meaning behind this instability is at low diffusion η, the magnetic field effectively can be seen to be frozen into the fluid as it moves and magnetic tension also grows leading to instability. Compared with instability caused by the strong vertical magnetic field in figure 3.7 with small Prandtl number $P = 0.5$, the field lines are not frozen into fluid flow and move through the flow due to high diffusion as shown in figure 3.7.

4.3.3 Linear instability at Prandtl number $P \neq 1$

We have investigated instability with modest values such as $P = 0.5$ and $P = 2$ to make a good comparison between the vertical and horizontal magnetic field of the

effect of the Prandtl number for a fixed range of physical parameters (ν, η, B_0, P) and all possible wavenumbers k. However, considering the very small Prandtl number $P = 0.1, 0.2$ as shown in figure 4.7, we can see clearly *the flow branch* is dominant in both panels (a,b), and *the field branch* nearly vanishes due to a high magnetic diffusion $\eta = 10\nu$, also this phenomenon can be seen in panels (c,d) at $\eta = 5\nu$, the physical meaning behind this is the magnetic field are not frozen into the fluid flow, and then the magnetic tension is reduced leading the field branch to vanish.

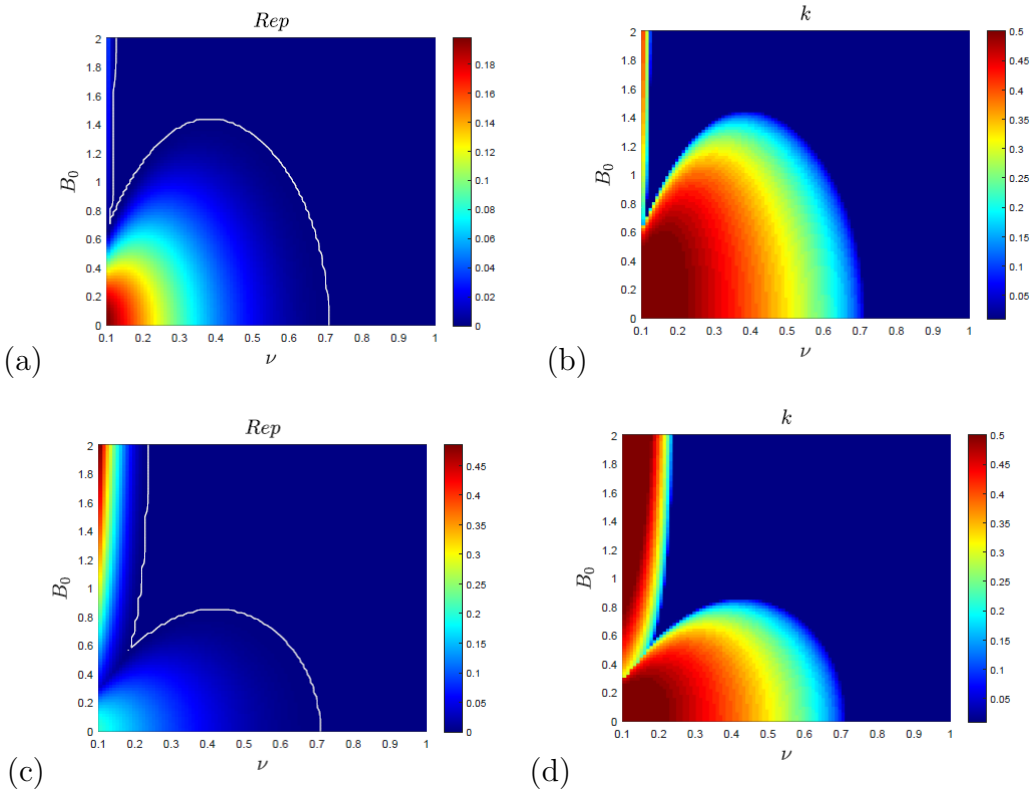

Figure 4.7: Colour plot of the growth rate at $Re(p_{\max})$ and wavenumber k as a function of (B_0, ν) for small Prandtl number $P < 1$: (a,b) $P = 0.1$, (c,d) $P = 0.2$,

We also consider large Prandtl number $P = 5, P = 10$ shown in figure 4.8, We can see clearly that *the flow branch* is suppressed, and *the field branch* is enhanced with an island of instability emerging around the origin involving the field branch. This island of instability emerges clearly in the plot of $\mathrm{Im}\, p$ and the plot of $k_{\max}$ in both panels but is scarcely visible in $\mathrm{Re}\, p$. We also see that this island starts with small instability near the origin in $\mathrm{Im}\, p$ at $P = 2$ as shown in figure 4.6(c,d) and increases as the Prandtl number increases as shown in figure 4.8. The islands occur at a weak field at $B_0 \approx 0.1$ and have small values of the growth rate. However, for all studies

of the horizontal field in this chapter, we observe that instability has $\operatorname{Im} p = 0$ for small Prandtl numbers, see figures 4.7, while we have the non-zero imaginary part $\operatorname{Im} p \neq 0$ only for the island branch at large Prandtl number, see figure 4.8.

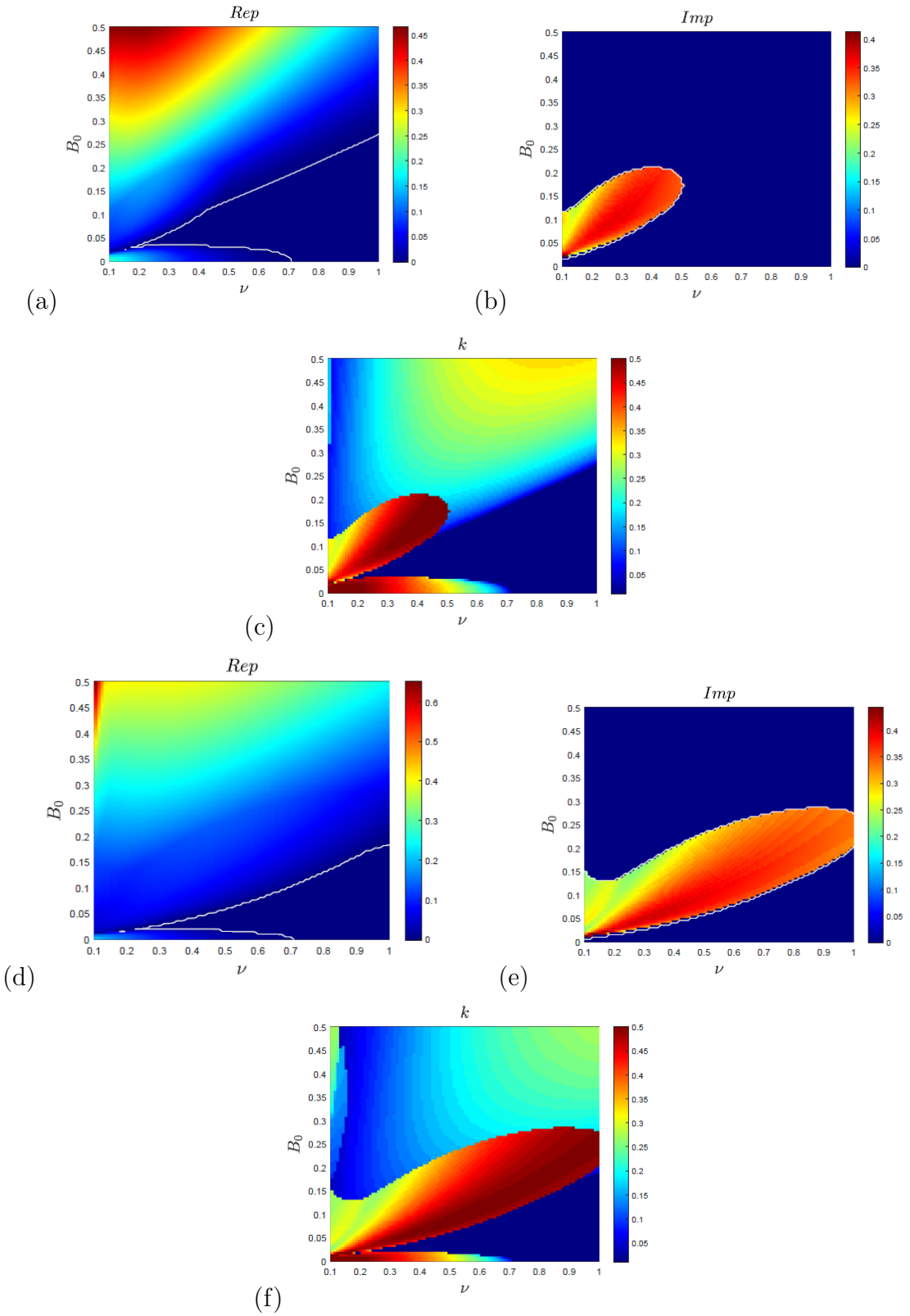

Figure 4.8: Colour plot of the growth rate as a function of (B_0, ν) for larger Prandtl number $P > 1$: panels (a,b,c) show $P = 5$, panels (d,e,f) show $P = 10$. Panels (a,d) show $\mathrm{Re}\, p_{\max}$, panels (b,e) show $\mathrm{Im}\, p_{\max}$, panels (c,f) show $k_{\max}$.

4.4 Instability structure

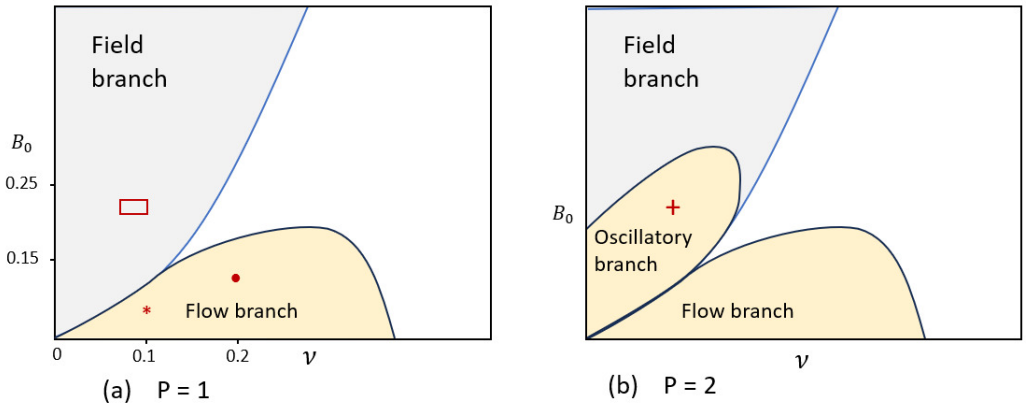

Figure 4.9: Schematic of instability growth rate for $P = 1$ in panel (a) and $P = 2$ for panel (b) with three red markers explaining our choosing of parameters value. The marker ($\square$) refer to figure 4.12 and the marker ($\circ$) refer to figure 4.10 and the marker ($+$) refer to figure 4.13, marker($*$) refer to figure 4.11. This schematic refers to figure 4.5(b).

We drew the schematic in figure 4.9 to show instability for varying Prandtl numbers, and to show the reader why we have chosen the particular values in this section. Panel (a) shows $P = 1$ and panel (b) shows $P = 2$. This schematic is derived from figure 4.6, the red markers indicate the figures in this section as described in the caption. We look at the instability for four perturbation eigenfunctions of flows & fields $\psi_1, \omega_1, j_1, a_1$. We select individual points from the flow branch, the field branch and the oscillatory branch as illustrated in figure 4.9 (a,b).

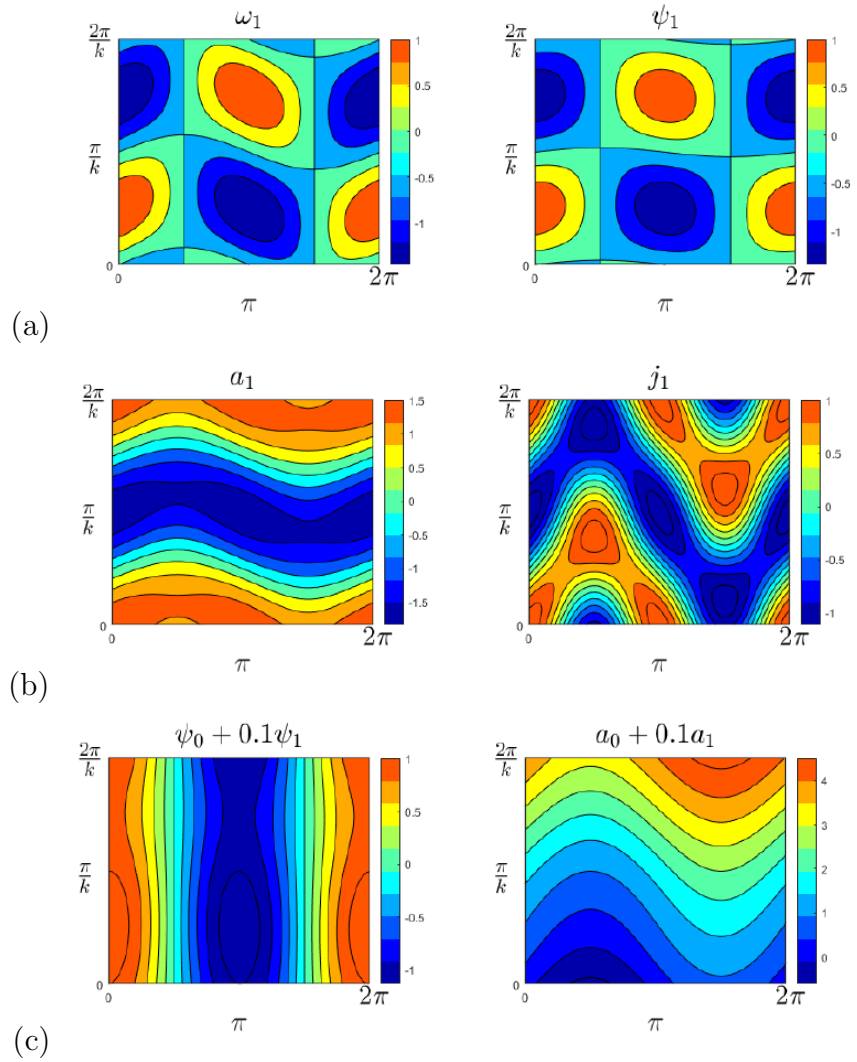

Figure 4.10: Shaded contour plot from *the flow branch* at ($B_0 = 0.15,\ k = 0.25,\ \nu = \eta = 0.2$). Panel (a) shows vorticity ω_1 and stream function of Ψ_1, , panel (b) magnetic field a_1 and magnetic current j_1.(c) superposition $\psi_0 + 0.1\psi_1$, of basic flow & field.

An example of an unstable mode for *the flow branch* in figure 4.3 occurs at $B_0 = 0.15, \nu = \eta = 0.2$ and $k = 0.25$ corresponding to the red ($\circ$) in figure 4.9 and also corresponding to the purple curve indicating the unstable mode. Figure 4.10(a) shows coherent vortices in the vorticity field ω_1 and perturbation stream function ψ_1. The magnetic field a_1 exhibits horizontal field bands driven by fluid flow for $0 \leqslant x \leqslant 2\pi, 0 \leqslant y \leqslant 2\pi/k$, with modifications to the magnetic current j_1 in panel (b). In panel (c) the basic equilibrium state is shown with a small amount of perturbation added. Hence, we observe wavy magnetic lines in the plot of a and the sausage mode along the streamlines of the flow ψ.

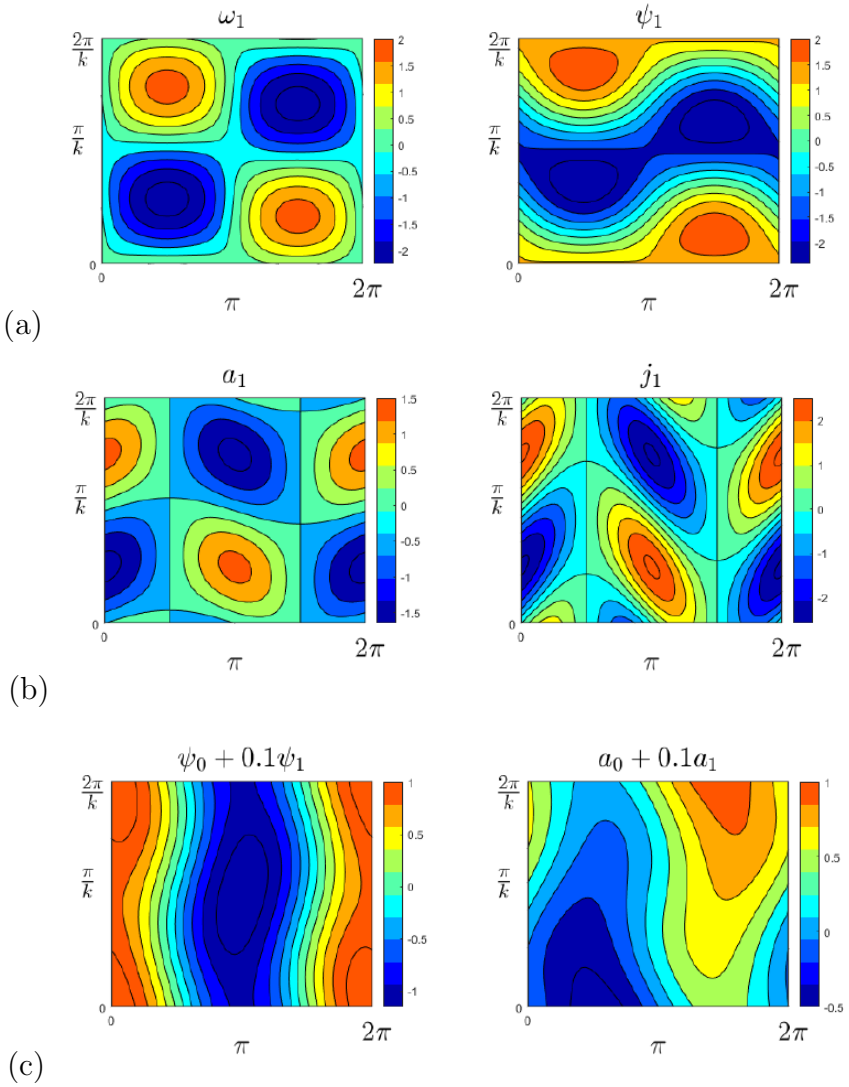

Figure 4.11: Shaded contour from *the flow branch* at ($B_0 = 0.05,\ k = 0.5,\ \nu = \eta = 0.1$, (a) vorticity ω_1 and stream function ψ_1, (b) magnetic field a_1 and magnetic current j_1, panel (c) superposition $\psi_0 + 0.1\psi_1$, of basic flow & field $a_0 + 0.1a_1$.

An example of unstable mode is shown in figure 4.11 for parameter values chosen corresponding to the peak of the dark red curve in figure 4.4 also corresponding to the marker $(*)$ in figure 4.9, which represents the weak field used. Panel (a) shows coherent structures of vortices formed at vorticity field ω_1 and magnetic field a_1 in Panel (b) for $0 \leqslant x \leqslant 2\pi, 0 \leqslant y \leqslant 2\pi/k$. The perturbation stream function ψ and magnetic current j both exhibit zonostrophic instability giving horizontal jets. We refer to this as the weak horizontal field branch which is the same as the flow branch, in contrast with the strong horizontal field branch, we encounter in figure 4.12. In panel (c) the basic equilibrium state is shown with a small amount of perturbation added. Here the sausage mode has emerged along the streamlines of flow ψ_1 and

strong wavy magnetic lines along the magnetic field a_1.

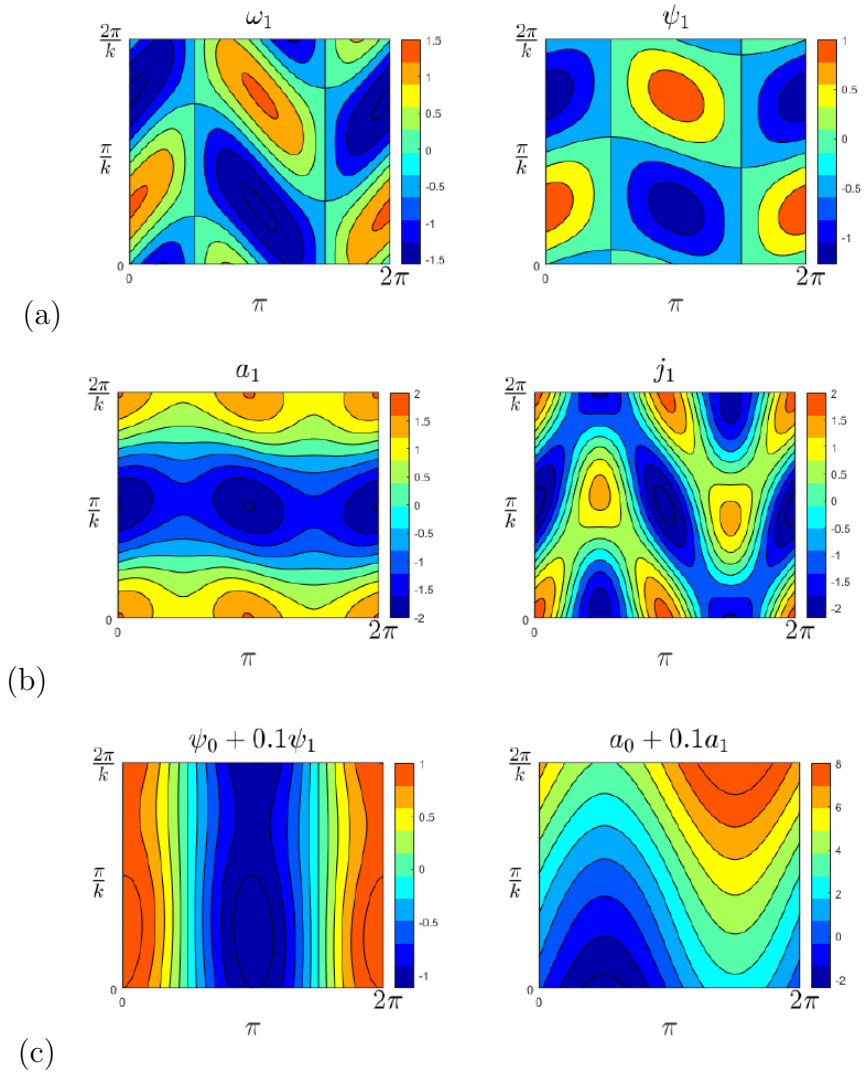

Figure 4.12: Shaded contour plot from *the field branch* at ($B_0 = 0.25,\ k = 0.25,\ \nu = \eta = 0.1$), panel (a) vorticity ω_1 and stream function Ψ_1, (b) magnetic field a_1 and magnetic current j_1. panel (c) superposition $\psi_0 + 0.1\psi_1$, of basic flow & field $a_0 + 0.1a_1$

Figure 4.12 shows the most unstable mode at $B_0 = 0.25,\ k = 0.25,\ \nu = \eta = 0.1$ corresponding to the dark orange curve in figure 4.4 and also corresponding to the red □ in the field branch in figure 4.9. The perturbation stream function ψ_1 and vorticity field ω_1 form closed eddies in panel (a). However, panel (b) shows a banded structure in the magnetic field a_1 and a banded island in the plot of magnetic current j_1 (showing the dominant role of field branch), and indicates a tendency for the background mean-field to segregate into bands of stronger and weaker horizontal field, allowing the field mode to be identified also as a tearing mode. In panel (c) the basic equilibrium state is shown with a small amount of perturbation added. Hence,

the strong wavy lines have emerged along the magnetic lines a_1 and the sausage mode along the streamlines of the flow ψ_1.

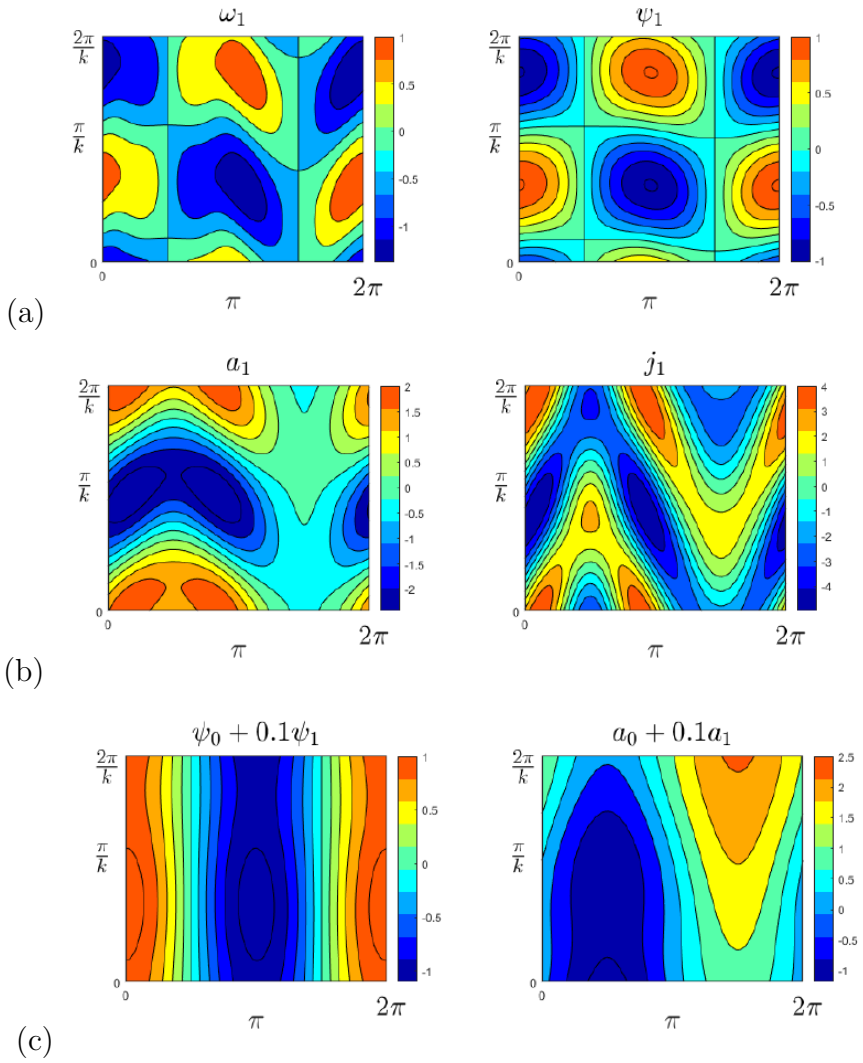

Figure 4.13: Shaded contour plot of island branch at ($B_0 = 0.1, k = 0.5, \nu = 0.15, \eta = 0.5\nu$),(a) vorticity ω_1 stream function Ψ_1,(b) and the magnetic field a_1 and magnetic current j_1.(c) superposition $\psi_0 + 0.1\psi_1$, of basic flow & field $a_0 + 0.1a_1$

Another example of an unstable mode is shown in figure 4.13 for parameter values chosen corresponding to the island of oscillatory behaviour marked by (+) in figure 4.9(b), which occurs at the weak field used. Panel (a) shows coherent structures of vortices formed at stream function ψ_1 and closed vortices formed at vorticity field ω_1 at $0 \leqslant x \leqslant 2\pi, 0 \leqslant y \leqslant 2\pi/k$. The magnetic field a_1 formed closed vortices at $0 \leqslant x \leqslant \pi, 0 \leqslant y \leqslant 2\pi/k$ and magnetic current j_1 exhibits zonostrophic structure, In this figure we have a non-zero imaginary part $\mathrm{Im}(p) \neq 0$ and so we have a travelling unstable mode and we lose the symmetry that we had in figure 4.12 (b). In panel (c) the basic equilibrium state is shown with a small amount of perturbation added.

Hence the sausage mode has emerged along the streamlines of flow ψ_1 and strong wavy magnetic lines along the magnetic field a_1.

4.5 Linear stability theory with $k \ll 1$

We discuss the perturbation theory for the horizontal field system as shown in section (3.7) including weak and strong fields in the limit $k \to 0$ while keeping other parameters fixed. We reduce the system and split it into two independent matrix systems giving the two branches of instability involving the flow mode G_0 and the field mode H_0.

The horizontal field equations (4.25-4.31) are truncated involving, $G_0, H_0, G_{\pm 1}, H_{\pm 1}$ and dropping terms involving $G_{\pm 2}, H_{\pm 2}$, with

$$pG_n = \frac{k}{2}\left[\frac{1}{(n-1)^2+k^2} - 1\right] G_{n-1} - \frac{k}{2}\left[\frac{1}{(n+1)^2+k^2} - 1\right] G_{n+1} - \nu(k^2+n^2)G_n$$

$$+\frac{ikB_0}{2\eta}((n-1)^2+k^2-1)H_{n-1}+\frac{ikB_0}{2\eta}((n+1)^2+k^2-1)H_{n+1}+inB_0(k^2+n^2)\ H_n \quad (4.38)$$

$$pH_n = -\frac{k}{2}H_{n-1} + \frac{k}{2}H_{n+1} - \eta(k^2+n^2)H_n + \frac{inB_0}{k^2+n^2}G_n + \frac{ikB_0}{2\eta}\frac{1}{(n-1)^2+k^2}G_{n-1}$$

$$+ \frac{ikB_0}{2\eta}\frac{1}{(n+1)^2+k^2}G_{n+1}. \quad (4.39)$$

We have for $n = 0$

$$pG_0 = -\nu k^2 G_0 - \frac{k}{2}\frac{k^2}{1+k^2}\,G_{-1} + \frac{k}{2}\frac{k^2}{1+k^2}\,G_1 + \frac{ikB_0}{2\eta}\,k^2 H_{-1} + \frac{ikB_0}{2\eta}\,k^2 H_1, \quad (4.40)$$

$$pH_0 = -\eta k^2 H_0 - \frac{k}{2}\,H_{-1} + \frac{k}{2}\,H_1 + \frac{ikB_0}{2\eta}\frac{1}{1+k^2}\,G_{-1} + \frac{ikB_0}{2\eta}\frac{1}{1+k^2}\,G_1. \quad (4.41)$$

and for $n = \pm 1$

$$pG_{\pm 1} = -\nu(1+k^2)G_{\pm 1} \pm \frac{k}{2}\frac{1-k^2}{k^2}G_0 \pm iB_0(1+k^2)H_{\pm 1} + \frac{ikB_0}{2\eta}(-1+k^2)H_0, \tag{4.42}$$

$$pH_{\pm 1} = -\eta(1+k^2)H_{\pm 1} \pm \frac{k}{2}H_0 \pm iB_0\frac{1}{1+k^2}G_{\pm 1} + \frac{ikB_0}{2\eta}\frac{1}{k^2}G_0. \tag{4.43}$$

This system corresponds to taking $G_1 = -G_{-1}, H_1 = -H_{-1}$. We now express these equations in terms of $G_\pm$, $H_\pm$ with

$$G_\pm = \tfrac{1}{2}(G_1 \pm G_{-1}), \quad H_\pm = \tfrac{1}{2}(H_1 \pm H_{-1}); \tag{4.44}$$

we rescale $G_0 = k^2 G_0'$ by divided equation 4.40 by k^2, we obtain 4.45, and rescale other quantities $G_- = G_-'$, $H_+ = H_+'$, $p = p'$, $\eta = \eta'$, $\nu = \nu'$ and we set $\tilde{B}_0 = B_0/\eta$. The equations decompose into two uncoupled systems. The first system includes only G_0 on the large scale

$$pG_0' = -\nu' k^2 G_0' + k(1+k^2)^{-1}G_-' + ik\tilde{B}_0 H_+', \tag{4.45}$$

$$pG_-' = -\nu'(1+k^2)G_-' + \tfrac{1}{2}k(1-k^2)G_0' + iB_0'(1+k^2)H_+', \tag{4.46}$$

$$pH_+' = -\eta'(1+k^2)H_+' + iB_0'(1+k^2)^{-1}G_-' + \tfrac{1}{2}ik\tilde{B}_0 G_0', \tag{4.47}$$

while the second involves only H_0 on the large scale,

$$pH_0' = -\eta' k^2 H_0' + kH_-' + ik\tilde{B}_0\,(1+k^2)^{-1}\,G_+', \tag{4.48}$$

$$pH_-' = -\eta'(1+k^2)H_-' - \tfrac{1}{2}kH_0' + iB_0'(1+k^2)^{-1}G_+', \tag{4.49}$$

$$pG_+' = -\nu'(1+k^2)G_+' + iB_0'(1+k^2)H_-' + \tfrac{1}{2}ik\tilde{B}_0(-1+k^2)H_0', \tag{4.50}$$

These two branches are treated using the eigenvalue perturbation theory. Then, we use binomial expansion

$$1+k^2 \approx 1, \quad \frac{1}{k^2}-1 \approx \frac{1}{k^2}, \quad \frac{1}{1+k^2}-1 = 1-k^2+k^4-\cdots-1 \approx -k^2 \tag{4.51}$$

The term "large scale" means for: G_0, H_0 we have e^{iky} wave vector $(0,k)$ and the wavenumber is $k \ll 1$. While the term "small scale" means: for $G_\pm, H_\pm$ we have $e^{\pm ix+iky}$, wavevectors $(\pm 1, k)$ and the length of the wavevector is $\sqrt{1+k^2} \approx 1$.

4.5.1 Flow or G_0 branch

We now return to the first system with equations (4.45–4.47), which includes a dominant large-scale flow in G_0, so we define this as the *flow branch* or G_0, and dropped the primes with

$$M = \begin{pmatrix} -\nu k^2 & k(1+k^2)^{-1} & ik\tilde{B}_0 \\ \frac{1}{2}k(1-k^2) & -\nu(1+k^2) & iB_0(1+k^2) \\ \frac{1}{2}ik\tilde{B}_0 & iB_0(1+k^2)^{-1} & -\eta(1+k^2) \end{pmatrix}, \quad \boldsymbol{v} = \begin{pmatrix} G_0 \\ G_- \\ H_+ \end{pmatrix}. \tag{4.52}$$

We expand M and use (4.51), to give:

$$M_0 = \begin{pmatrix} 0 & 0 & 0 \\ 0 & -\nu & iB_0 \\ 0 & iB_0 & -\eta \end{pmatrix}, \quad M_1 = \begin{pmatrix} 0 & 1 & i\tilde{B}_0 \\ \frac{1}{2} & 0 & 0 \\ \frac{1}{2}i\tilde{B}_0 & 0 & 0 \end{pmatrix}, \quad M_2 = \begin{pmatrix} -\nu & 0 & 0 \\ 0 & -\nu & iB_0 \\ 0 & -iB_0 & -\eta \end{pmatrix}. \tag{4.53}$$

Figure 4.14 shows that M_0 incorporates small-scale Alfv́en waves between G_-, H_+ as for large-scale flow G_0, due to weak diffusion, these waves are damped.

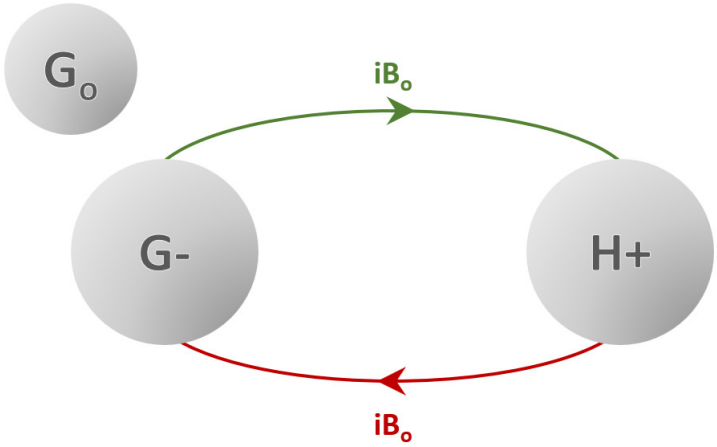

Figure 4.14: Schematic of the matrix M_0

Figure 4.15 shows that M_1, the Alfv́en waves drive the flow G_0 and the flow drives the Alfv́en waves giving the possibility of instability. There is a coupling between G_- & H_+ in matrix M_2, similar to figure 4.14 of M_0 with a crucial difference in the sign, and therefore no need for a schematic picture.

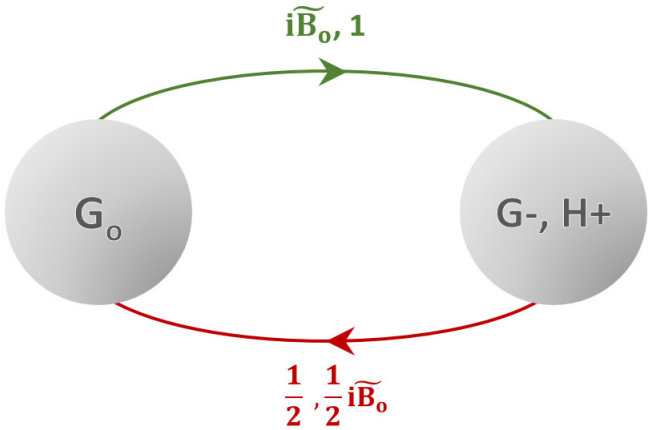

Figure 4.15: Schematic of the matrix M_1

The inverse of the non-trivial 2×2 block of M_0 is

$$\begin{pmatrix} -\nu & iB_0 \\ iB_0 & -\eta \end{pmatrix}^{-1} = \Delta \begin{pmatrix} -\eta & -iB_0 \\ -iB_0 & -\nu \end{pmatrix}, \quad \Delta^{-1} = \nu\eta + B_0^2, \tag{4.54}$$

where Δ is the inverse of the appropriate determinant. We solve (3.56) in order of k.

From equation (3.59) we obtain the first correction of growth rate p and take

$$p_0 = 0, \quad \boldsymbol{v}_0 = (1,0,0)^T, \quad \boldsymbol{w}_0 = (1,0,0), \quad \boldsymbol{v}_0\boldsymbol{w}_0 = 1. \tag{4.55}$$

At next order, we use (3.64) and have

$$M_1\boldsymbol{v}_0 = (0, \tfrac{1}{2}, \tfrac{1}{2}i\tilde{B}_0)^T, \quad p_1 = \frac{\boldsymbol{w}_0 M_1 \boldsymbol{v}_0}{\boldsymbol{w}_0\boldsymbol{v}_0} = 0. \tag{4.56}$$

We now solve (3.60) for $\boldsymbol{v}_1$, to obtain

$$(M_0 - p_0 I)\boldsymbol{v}_1 = -M_1\boldsymbol{v}_0, \tag{4.57}$$

To find $\boldsymbol{v}_1$ we solve

$$\begin{pmatrix} -\nu & iB_0 \\ iB_0 & -\eta \end{pmatrix}^{-1} = \frac{1}{\nu\eta + B_0^2}\begin{pmatrix} -\eta & -iB_0 \\ -iB_0 & -\nu \end{pmatrix} \tag{4.58}$$

$$\boldsymbol{v}_1 = \Delta \begin{pmatrix} -\eta & -iB_0 \\ -iB_0 & -\nu \end{pmatrix}\begin{pmatrix} -\frac{1}{2} \\ -\frac{i\tilde{B}_0}{2} \end{pmatrix} \tag{4.59}$$

$$\boldsymbol{v}_1 = \Delta \begin{pmatrix} \frac{1}{2}\eta - \frac{B_0\tilde{B}_0}{2} \\ \frac{iB_0}{2} + \frac{i\tilde{B}_0\nu}{2} \end{pmatrix} \tag{4.60}$$

and thus obtain

$$\boldsymbol{v}_1 = \tfrac{1}{2}\Delta(0, \eta - \tilde{B}_0 B_0, iB_0 + i\nu\tilde{B}_0)^T. \tag{4.61}$$

Here we have used the inverse (4.54) to find a solution for $\boldsymbol{v}_1$. We could add on an arbitrary multiple of $\boldsymbol{v}_0$ but this would only change the (irrelevant) normalisation of the eigenvector $\boldsymbol{v}$ in our calculation; any solution is acceptable.

Finally at $O(k^2)$ we find from (3.65) the second growth rate p_2 with

$$p_2 = \frac{\boldsymbol{w}_0 M_1 \boldsymbol{v}_1}{\boldsymbol{w}_0\boldsymbol{v}_0} + \frac{\boldsymbol{w}_0 M_2 \boldsymbol{v}_0}{\boldsymbol{w}_0\boldsymbol{v}_0}, \qquad \boldsymbol{w}_0\boldsymbol{v}_0 = 1 \tag{4.62}$$

$$\boldsymbol{w}_0 M_1 \boldsymbol{v}_1 = \begin{pmatrix} 1 & 0 & 0 \end{pmatrix} \begin{pmatrix} 0 & 1 & i\tilde{B}_0 \\ \frac{1}{2} & 0 & 0 \\ \frac{1}{2} i\tilde{B}_0 & 0 & 0 \end{pmatrix} \frac{1}{\nu\eta + B_0^2} \begin{pmatrix} 0 \\ \frac{\eta}{2} - \frac{1}{2} B_0 \tilde{B}_0 \\ \frac{iB_0}{2} + \frac{i\nu\tilde{B}_0}{2} \end{pmatrix}$$

$$\boldsymbol{w}_0 M_1 \boldsymbol{v}_1 = \begin{pmatrix} 1 & 0 & 0 \end{pmatrix} \frac{1}{\nu\eta + B_0^2} \begin{pmatrix} \frac{\eta}{2} - \frac{B_0\tilde{B}_0}{2} - \frac{B_0\tilde{B}_0}{2} - \frac{\tilde{B}_0^2\nu}{2} \\ 0 \\ 0 \end{pmatrix}$$

$$\boldsymbol{w}_0 M_1 \boldsymbol{v}_1 = \frac{1}{\nu\eta + B_0^2}(\frac{\eta}{2} - B_0\tilde{B}_0 - \frac{\tilde{B}_0^2\nu}{2}), \qquad \boldsymbol{w}_0 M_2 \boldsymbol{v}_0 = -\nu$$

$$p_2 = \frac{\frac{1}{2}}{\nu\eta + B_0^2}(\eta - 2B_0\tilde{B}_0 - \nu\tilde{B}_0^2) - \nu \tag{4.63}$$

Now we have, by stating that $\tilde{B}_0 = B_0/\eta$, this gives

$$p = p_2 k^2 + \cdots = \left[\tfrac{1}{2}\Delta(\eta - 2B_0^2/\eta - B_0^2\nu/\eta^2) - \nu\right]k^2 + \cdots, \tag{4.64}$$

with the Prandtl number $P = \nu/\eta$, we substitute $\eta = \frac{\nu}{P}$ into equation 4.63 & we obtain instability threshold for B_0, we have:

$$p_2 = \frac{\frac{1}{2}}{\frac{\nu^2}{P} + B_0^2}(\frac{\nu}{P} - \frac{2PB_0^2}{\nu} - \frac{\nu P^2 B_0^2}{\nu^2}) - \nu \tag{4.65}$$

and we set $p_2 = 0$ to find:

$$0 = \frac{\frac{1}{2}}{\frac{\nu^2}{P} + B_0^2}(\frac{\nu}{P} - \frac{2PB_0^2}{\nu} - \frac{P^2 B_0^2}{\nu}) - \nu \tag{4.66}$$

$$0 = \frac{\frac{1}{2}}{\frac{\nu^2}{P} + B_0^2}(\frac{\nu}{P} - \frac{(2+P)PB_0^2}{\nu}) - \nu \tag{4.67}$$

$$\frac{\nu}{P} - \frac{(2+P)PB_0^2}{\nu} = 2\nu(\frac{\nu^2}{P} + B_0^2)$$

which gives

$$\frac{1}{P} - \frac{(2+P)PB_0^2}{\nu^2} = 2(\frac{\nu^2}{P} + B_0^2)$$

$$\frac{1}{P} - \frac{2\nu^2}{P} = \frac{(2+P)PB_0^2}{\nu^2} + 2B_0^2$$

Finally, we obtain:

$$B_0^2 = \frac{\frac{1}{P} - \frac{2\nu^2}{p}}{(\frac{(2+P)P}{\nu^2} + 2)}, \qquad B_0^2 = \frac{\nu^2(\frac{1-2\nu^2}{P})}{(2+P)P + 2\nu^2}, \qquad B_0^2 = \frac{\nu^2}{P}\frac{1-2\nu^2}{2\nu^2 + (2+P)P}. \tag{4.68}$$

The threshold for instability with $p_2 = 0$ for $P = 1$ into equation 4.68, we obtain :

$$B_0^2 = \frac{\nu^2(1-2\nu^2)}{2\nu^2 + 3} \tag{4.69}$$

This formula shows a good agreement for the lower branch in figure 4.5(b). For $B_0 = 0$ we obtain the Meshalkin and Sinai (1961) result in $\nu_c = 1/\sqrt{2}$, and this formula indicates how hydrodynamic instability is suppressed by the magnetic field.

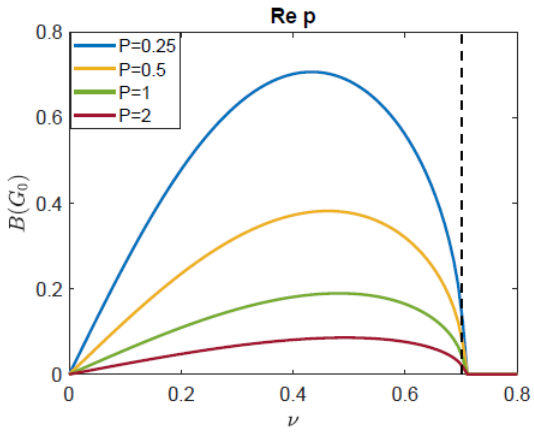

Figure 4.16: Instability growth rate of flow branch G_0 for different values of Prandtl number $P = (0.25, 0.5, 1, 2)$.

4.5.2 Field or H_0 branch

In the second system of equations (4.70–4.72), the large-scale field H_0 is present and we define this as the *field branch* or H_0 and drop the primes.

$$pH_0' = -\eta' k^2 H_0' + kH_-' + ik\tilde{B}_0 (1+k^2)^{-1} G_+', \tag{4.70}$$

$$pH_-' = -\eta'(1+k^2)H_-' - \tfrac{1}{2}kH_0' + iB_0'(1+k^2)^{-1}G_+', \tag{4.71}$$

$$pG_+' = -\nu'(1+k^2)G_+' + iB_0'(1+k^2)H_-' + \tfrac{1}{2}ik\tilde{B}_0(-1+k^2)H_0', \tag{4.72}$$

We write the system as $M\boldsymbol{v} = p\boldsymbol{v}$ with

$$M = \begin{pmatrix} -\eta k^2 & k & ik\tilde{B}_0(1+k^2)^{-1} \\ -\frac{1}{2}k & -\eta(1+k^2) & iB_0(1+k^2)^{-1} \\ \frac{1}{2}ik\tilde{B}_0(-1+k^2) & iB_0(1+k^2) & -\nu(1+k^2) \end{pmatrix}, \quad \boldsymbol{v} = \begin{pmatrix} H_0 \\ H_- \\ G_+ \end{pmatrix}. \quad (4.73)$$

We expand M and use (4.51), to give:

$$M_0 = \begin{pmatrix} 0 & 0 & 0 \\ 0 & -\eta & iB_0 \\ 0 & iB_0 & -\nu \end{pmatrix}, \quad M_1 = \begin{pmatrix} 0 & 1 & i\tilde{B}_0 \\ -\frac{1}{2} & 0 & 0 \\ -\frac{1}{2}i\tilde{B}_0 & 0 & 0 \end{pmatrix}, \quad M_2 = \begin{pmatrix} -\eta & 0 & 0 \\ 0 & -\eta & -iB_0 \\ 0 & iB_0 & -\nu \end{pmatrix}. \quad (4.74)$$

Figure 4.17 shows that M_0, a small scale Alfv́en waves in the coupling of G_+, H_-, and there is a large scale Alfv́en waves in the field H_0.

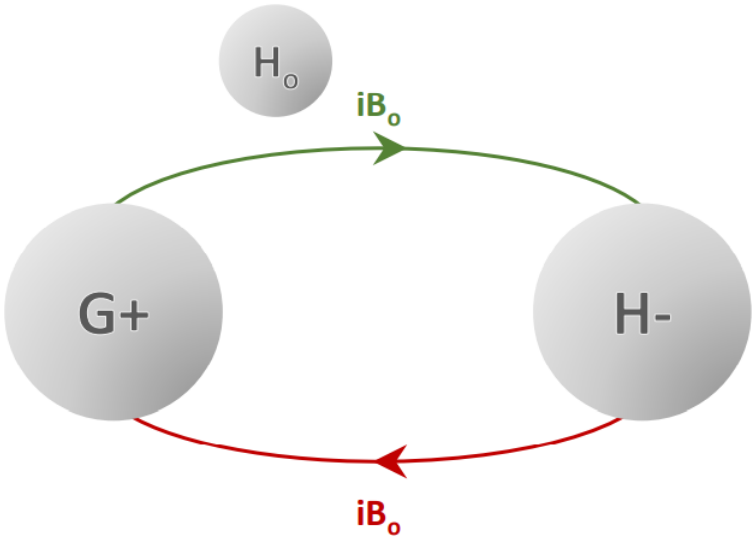

Figure 4.17: Schematic of the Matrix M_0.

Figure 4.18 shows that M_1, the Alfv́en waves G_+, H_- drive the field H_0 and the field drive the Alfv́en waves. so there is instability here between these coupling. There is a coupling between G_+ & H_- in matrix M_2, similar to figure 4.17 of M_0 , therefore, and no need for a plotting scheme.

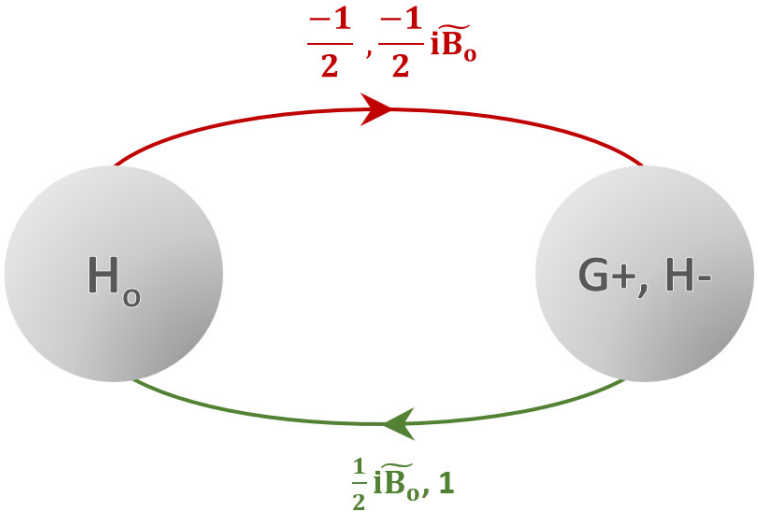

Figure 4.18: Schematic of the Matrix M_1.

The inverse of the 2×2 block of matrix M_0 is given as in (4.54) with ν and η interchanged and the same Δ. The calculation proceeds as before. At leading order in the eigenvalue problem (3.58) we take the same solution as that given in (4.55). At first order, from equations 3.59, 3.64 we have

$$p_0 = 0, \quad p_1 = 0, \quad M_1 \boldsymbol{v}_0 = (0, -\tfrac{1}{2}, -\tfrac{1}{2} i\tilde{B}_0)^T. \tag{4.75}$$

we solve (3.60) for $\boldsymbol{v}_1$ as

$$(M_0 - p_0 I)^{-1} = -\begin{pmatrix} -\eta & iB_0 \\ iB_0 & -\nu \end{pmatrix}^{-1} = \frac{1}{\nu\eta + B_0^2} \begin{pmatrix} -\nu & -iB_0 \\ -iB_0 & -\eta \end{pmatrix}$$

$$(M_0 - p_0 I)^{-1} = \Delta \begin{pmatrix} -\nu & -iB_0 \\ -iB_0 & -\eta \end{pmatrix} \begin{pmatrix} \frac{1}{2} \\ \frac{i\tilde{B}_0}{2} \end{pmatrix}$$

$$(M_0 - p_0 I)^{-1} = \Delta \begin{pmatrix} -\frac{\nu}{2} & +\frac{B_0 \tilde{B}_0}{2} \\ -\frac{iB_0}{2} & -\frac{iB_0}{2} \end{pmatrix}$$

Then

$$\boldsymbol{v}_1 = \tfrac{1}{2}\Delta(0, -\nu + \tilde{B}_0 B_0, -2iB_0)^T. \tag{4.76}$$

At the next order (3.65) yields the growth rate p_2 and from 4.62, we obtain:

$$\boldsymbol{w}_0 M_1 \boldsymbol{v}_1 = \begin{pmatrix} 1 & 0 & 0 \end{pmatrix} \begin{pmatrix} 0 & 1 & i\tilde{B}_0 \\ -\frac{1}{2} & 0 & 0 \\ -\frac{1}{2} i\tilde{B}_0 & 0 & 0 \end{pmatrix} \frac{1}{\nu\eta + B_0^2} \begin{pmatrix} 0 \\ -\frac{\nu}{2} + \frac{B_0\tilde{B}_0}{2} \\ \frac{-iB_0}{2} - \frac{iB_0}{2} \end{pmatrix}$$

$$\boldsymbol{w}_0 M_1 \boldsymbol{v}_1 = \begin{pmatrix} 1 & 0 & 0 \end{pmatrix} \frac{1}{\nu\eta + B_0^2} \begin{pmatrix} -\frac{\nu}{2} + \frac{B_0\tilde{B}_0}{2} + \frac{B_0\tilde{B}_0}{2} + \frac{B_0\tilde{B}_0}{2} \\ 0 \\ 0 \end{pmatrix}$$

$$\boldsymbol{w}_0 M_1 \boldsymbol{v}_1 = \frac{1}{\nu\eta + B_0^2} (\frac{3B_0\tilde{B}_0}{2} - \frac{\nu}{2})$$

$$p_2 = \frac{\frac{1}{2}}{\nu\eta + B_0^2} (\frac{3B_0^2}{\eta} - \nu) - \eta, \qquad \boldsymbol{w}_0 M_2 \boldsymbol{v}_0 = -\eta \tag{4.77}$$

by stating that $\tilde{B}_0 = B_0/\eta$, , this gives

$$p = p_2 k^2 + \cdots = \left[\tfrac{1}{2}\Delta(-\nu + 3B_0^2/\eta) - \eta\right] k^2 + \cdots , \tag{4.78}$$

$$p = \left(\frac{P}{2\nu} \frac{-\nu^2 + 3B_0^2 P}{\nu^2 + B_0^2 P} - \frac{\nu}{P} \right) k^2 + \cdots . \tag{4.79}$$

We substitute Prandtl number $\eta = \nu/P$ in equation (4.77), we obtain instability threshold at general Prandtl number

$$0 = \frac{\frac{1}{2}}{\nu\eta + B_0^2} (\frac{3B_0^2}{\eta} - \nu) - \eta, \tag{4.80}$$

$$= \frac{\frac{1}{2}}{\frac{\nu^2}{P} + B_0^2} (\frac{3PB_0^2}{\nu} - \nu) - \frac{\nu}{P}, \tag{4.81}$$

This gives,

$$\frac{2\nu}{P} (\frac{\nu^2}{P} + B_0^2) = (\frac{3PB_0^2}{\nu} - \nu), \tag{4.82}$$

and so,

$$\frac{\nu^2}{P} + B_0^2 = \frac{3P^2 B_0^2}{2\nu^2} - \frac{P}{2}, \tag{4.83}$$

$$B_0^2 (1 - \frac{3p^2}{2\nu^2}) = -\frac{P}{2} - \frac{\nu^2}{P}, \tag{4.84}$$

Finally, we obtain:

$$B_0^2 = \frac{\nu^2}{P}\,\frac{P^2+2\nu^2}{3P^2-2\nu^2}\,. \tag{4.85}$$

The threshold of instability is given by $p_2 = 0$ for $P = 1$ into equation (4.85), we obtain:

$$B_0^2 = \frac{\nu^2(1+2\nu^2)}{3-2\nu^2} \tag{4.86}$$

This formula shows a good agreement for the field branch in figure 4.5(b). and this formula indicates how hydrodynamic instability is enhanced by increasing the magnetic field. We note that for fixed P, $B_0 \to \infty$ with

$$\nu \to \nu_c, \qquad \nu_c = P\sqrt{3/2}. \tag{4.87}$$

For confirmation of this, figure 4.19 (a,b) shows the magnetic field threshold for different Prandtl numbers. the expression in 4.87 which is $\nu \simeq 1.2$ for $P = 1$ provides evidence of good agreement between theory and numerical calculations. Details will be discussed in the following section.

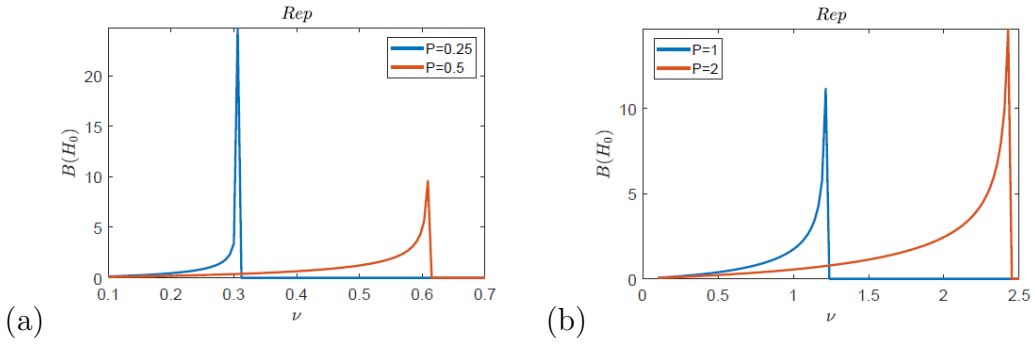

(a) (b)

Figure 4.19: Instability threshold for field branch H_0 with varying Prandtl number $P = (0.25, 0.5, 1, 2)$.

4.6 Discussion

We compare the theory & numerics for different values of the magnetic diffusivity η and Prandtl number P, the kinematic viscosity ν and magnetic field B_0. Figures 4.20 and 4.21 show the comparison between theoretical plots and numerical plots for various Prandtl numbers generated using leading eigenvalues and plotting software,

in the Matlab framework. Here panels (a,c) show the instability growth rate as a function of (ν, B_0)-plane. These instabilities are shown by colour plots and the white lines of the threshold $\mathrm{Re}\, p = 0$ are identical to the thresholds for the flow branch G_0 and field branch H_0 in panels (b,d). Both panels clearly show threshold behaviour that agrees with theoretical curves.

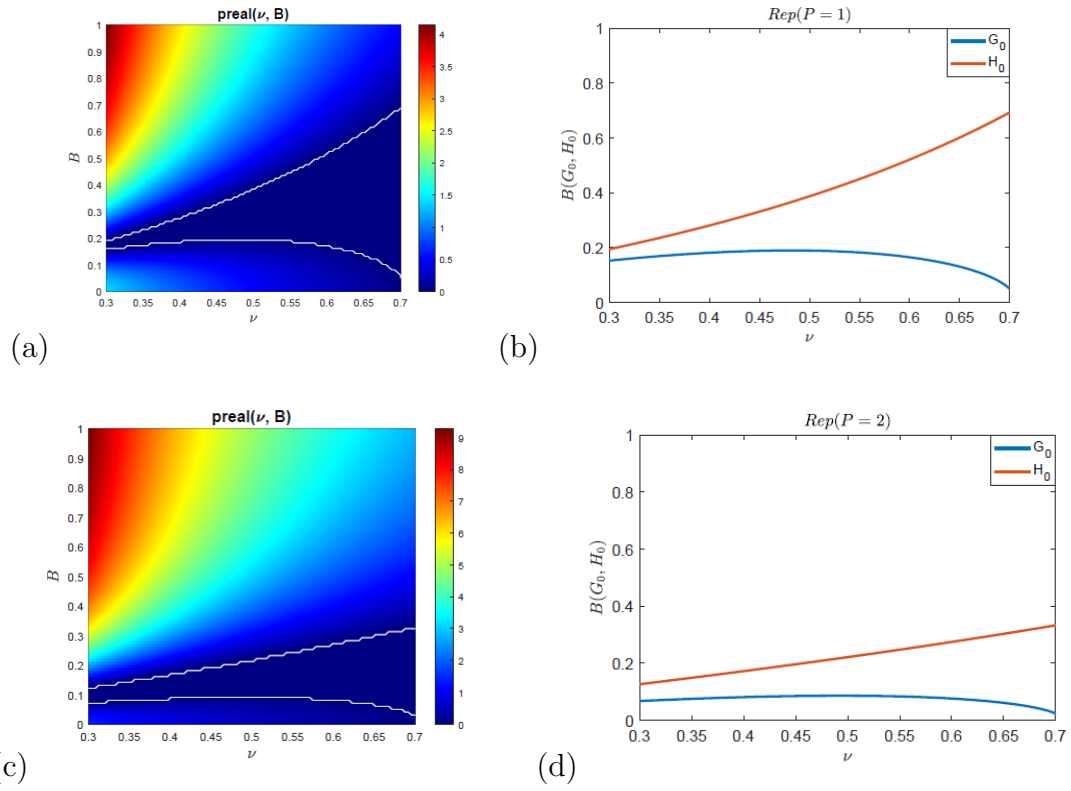

Figure 4.20: The maximum of growth rate as a function of (B_0, ν), Panels (a,b) shows $P = 1$, panels (c,d) shows $P = 2$.

Figure 4.20 shows the instability structure at $P = 1$ determined by the contour white lines $\mathrm{Re}\, p = 0$ in panel (a) and identical to the solid curves in panel (b), we have the field branch (red curve) H_0 from equation (4.85) and the flow branch (blue curve) G_0 from equation (4.69). Panel (c,d) shows instability at large Prandtl number $P = 2$, the field branch H_0 dominates, which suppresses the flow branch G_0. For comparison, we have taken the panel 4.20 (d) on the same scale as the panel (c). The *flow branch* G_0 start at $\nu = 0.7$, and the *field branch* (red curve) occurs below $B = 0.2$. We take the maximum growth rate over all the values of k to show the flow and field branches in panels (a,c) and we find that at a fixed value of Prandtl number, and as $B_0 \to 0$, we obtain the threshold of the flow branch:

$$\nu \to \nu_c, \qquad \nu_c = \frac{1}{\sqrt{2}}, \tag{4.88}$$

This viscosity value in equation (4.88) is valid for any value of Prandtl number as $B_0 \to 0$ and is identical to the (black dashed) in figure 4.16. The viscosity value in field branch H_0 in equation 4.89 is identical as far as the asymptote's curves of the figure 4.19(b). We have taken the figures 4.19 (a,b) on another scale to show the reader the agreement between the field branches H_0 and the instability threshold in equation (4.89). As $B_0 \to \infty$, we have $\nu \to \nu_c$

$$P = 1 \to \nu_c = \sqrt{\frac{3}{2}} \simeq 1.2, \qquad P = 2 \to \nu_c = \sqrt{6} \simeq 2.4 \tag{4.89}$$

For $\nu > \nu_c$ in equation (4.89) the viscosity is large enough to stabilise the system for any magnetic field strength B_0, no matter how strong.

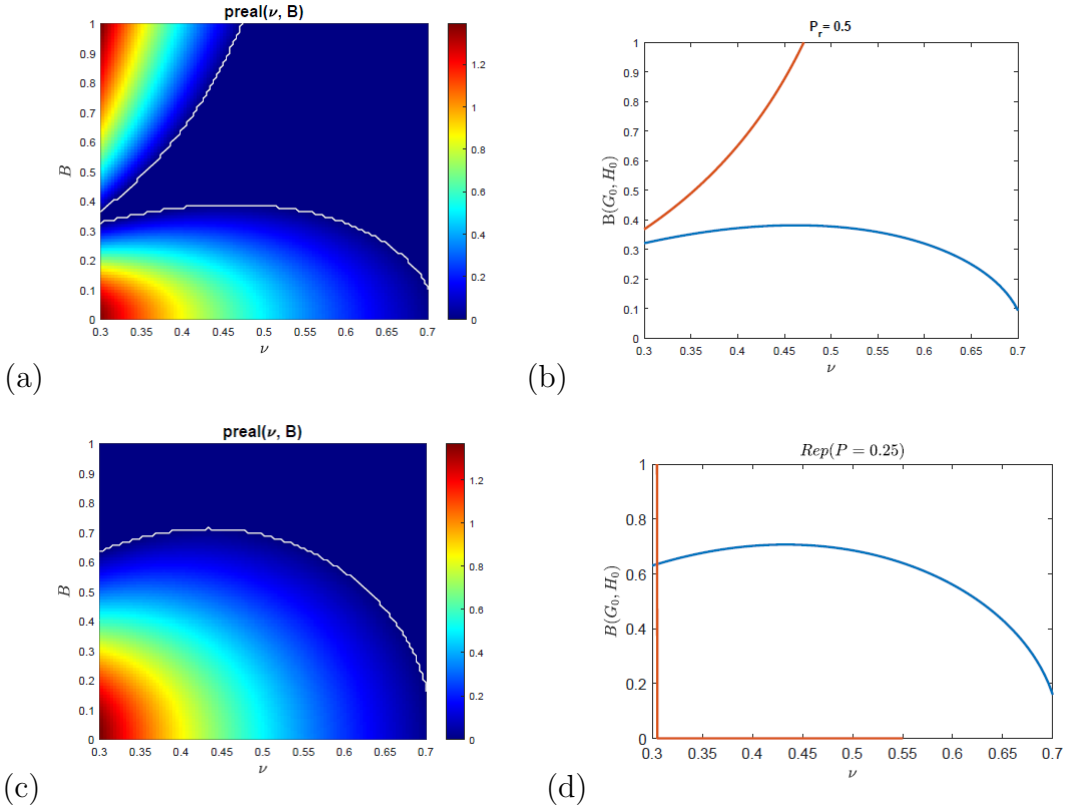

Figure 4.21: The maximum of growth rate as a function of (B_0, ν) for small Prandtl number, (a,b) shows $P = 0.5$, (c,d) shows $P = 0.25$.

Figure 4.21 shows instability at $P = 0.5$ in panels (a,b) where the flow branch G_0 dominates and ends up to $B = 0.3$. Panel (c,d) shows the instability at $P = 0.25$ the

flow branch is dominant and the field branch H_0 vanishes. We take the maximum growth rate over all values of k to show the flow and field branches in panels (a,c) and we find that at a fixed value of Prandtl number, the viscosity values of *field branch* H_0 in equation (4.90) are identical to the field branches H_0 in figure 4.19 (a).

$$P = 0.5, \rightarrow \nu_c = \sqrt{\frac{3P^2}{2}} \simeq 0.61, \qquad P = 0.25, \rightarrow \nu_c = \sqrt{\frac{3}{32}} \simeq 0.31 \tag{4.90}$$

For $\nu < \nu_c$ there is instability for a sufficiently strong magnetic field in equation (4.90)

4.7 Conclusion

In this chapter we have discussed the following results:

- We discussed instability behaviour with a horizontal magnetic field. By using the driving of a fundamental hydrodynamic structure and establishing the basic equilibrium state, we found a growth rate given by the linear system shown in equations (4.25 - 4.31).
- Numerical results show two types of instability, hydrodynamic instability is partly suppressed by the weak magnetic fields, and the other instability occurs at the strong magnetic field as shown in the figures 4.5, 4.6.
- The instability structure for the perturbation eigenfunctions has been described for each of the two branches of instability presented in this chapter (see section 4.4).
- Our study reveals a third type of oscillatory instability which occurs at a Prandtl number $P > 1$ and strong magnetic field (see figures 4.6 (c,d), 4.8). The system keeps the same instability structure at $P = 1$ with changes in the field branch occurring as we reduce a Prandtl number $P < 1$ in section (4.3.3).
- We have confirmed our numerical results by using perturbation theory in the limit $k \rightarrow 0$. The theory gives an analytical approximation for the growth rate

and instability threshold of the flow branch (4.69), and the field branch (4.85), which is in excellent agreement with a wide range of our results.

5. MHD stability:

Floquet wavenumber $\ell \neq 0$

5.1 Introduction

The Floquet wavenumber or Bloch wave concept was first proposed by Felix Bloch in 1929 to describe electron conduction in crystals. Therefore, it is known by a variety of names: when applied to ordinary differential equations, it is known as the Floquet theory (or the Lyapunov-Floquet theorem), used to solve linear differential equations with periodic coefficients. Jones and Gilbert (2014) studied the kinematic dynamo action in ABC flow for high magnetic Reynolds number. They used different representations of the numerical problem and reduced the scale of the problem to distinct branches of eigenvalues and eigenfunctions of magnetic fields. They used a Bloch wavenumber formulation to allow fields of arbitrary scale.

This chapter considers the underlying structure of the growth rate in chapters 3- 4 as a basis for our analysis. We identified possible instability configurations and specified the parameters space (ν, η, B_0) at which the growth rate shows growth or decay for fields that are 2π- periodic in x. Hence, we need to compare them directly to growth rate structures predicted by Floquet theory. The stability analysis method based on the Floquet theory provides solutions to linear dynamic systems with periodic functions and a large scale in x. Therefore, the motivation of this chapter is to address the linear MHD Kolmogorov flow by considering the natural extension to our investigation with Floquet wavenumber ℓ. We verify our results by applying perturbation theory and show a good agreement. The chapter concludes with a brief

summary of the major findings.

5.2 Formulating the problem using a Floquet wavenumber

We begin with a formulation of the problem in terms of a general Floquet wavenumber and solve numerically by imposing Floquet wave ℓ in a x- direction $0 < x < 2\pi/\ell$ along with a wavenumber k in y-direction $0 < y < 2\pi/k$. In our numerical scheme, we derive the growth rate p with a Floquet wave and draw comparisons between our previous results at $\ell = 0$ in chapters 3-4 and $\ell \neq 0$ in this chapter. By using Fourier expansions involving the Floquet wavenumber ℓ we define a large-scale flow small wavenumber and magnetic field as follows:

$$\boldsymbol{u} = e^{pt+iky} \sum_{n=-\infty}^{\infty} \boldsymbol{u_n} \;\; e^{i(\ell+n)x} \tag{5.1}$$

$$\boldsymbol{B} = e^{pt+iky} \sum_{n=-\infty}^{\infty} \boldsymbol{b_n} \;\; e^{i(\ell+n)x} \tag{5.2}$$

The Floquet wavenumber is used to determine the scale of the fluid flow and magnetic field along the x direction in the range of restriction $-0.5 < \ell \leqslant 0.5$.

We observed that adding ℓ affects hydrodynamic instability by allowing more possibility of instability (detailed in chapter 2), without considering the magnetic field strength. In this chapter, we investigate a possible instability by adding the Floquet wavenumber in the range $-0.5 < \ell \leqslant 0.5$, we have $0 < y < 2\pi/k$ and for $\ell > 0$ we take $0 < x < 2\pi/\ell$, we use boundary conditions in x and y. Then, we introduce the vertical and horizontal magnetic fields and choose the magnetic field strengths and viscosity values corresponding to the previous results to see the effect of ℓ on the onset instability. We solve the eigenvalue problem numerically by filling the matrix M involving Floquet wavenumber ℓ and using the Matlab framework.

5.3 Numerical methods

The analytical and numerical solution has been done at large-scale flow & field (small wavenumbers) by calculating the eigenvalue p of the growing or decaying eigenmode (see chapters 3-4). The same numerical approaches can be used with $\ell \neq 0$ by replacing any coefficient of n with $\ell + n$ wherever it appears. This method has the advantage of avoiding lengthy code rewriting and eliminating the need to reexamine parameter values for eigenvalue convergence (i.e. lower resolution). The Fourier mode indices for the large-scale magnetic problem remain unchanged. There are still six Fourier modes, by including the general mode of $(\ell + n)$ to the vertical field equation (3.52), we obtain

$$a_n = \frac{-k}{2} + \frac{k}{2}\left(\frac{1}{((n+\ell)-1)^2+k^2}\right), \quad b_n = -\nu((n+\ell)^2+k^2), \quad c_n = \frac{k}{2} - \frac{k}{2}\left(\frac{1}{((n+\ell)+1)^2+k^2}\right),$$

$$d_n = ikB(k^2+(n+\ell)^2), \quad e_n = \frac{-k}{2}, \quad f_n = -\eta(k^2+(n+\ell)^2), \quad g_n = \frac{k}{2}, \quad h_n = \frac{iBk}{k^2+(n+\ell)^2} \tag{5.3}$$

and in the horizontal field equation (4.35), we find :

$$a_n = \frac{-k}{2} + \frac{k}{2}\left(\frac{1}{((n+\ell)-1)^2+k^2}\right), \quad b_n = -\nu((n+\ell)^2+k^2), \quad c_n = \frac{k}{2} - \frac{k}{2}\left(\frac{1}{((n+\ell)+1)^2+k^2}\right)$$

$$g_n = inB(k^2+(n+\ell)^2), \; d_n = \frac{ikB}{2\eta}(-1+((n+\ell)-1)^2+k^2)),$$

$$f_n = \frac{ikB}{2\eta}(-1+((n+\ell)+1)^2+k^2)), \quad e_n = \frac{-k}{2}, \quad r_n = -\eta(k^2+(n+\ell)^2), \quad s_n = \frac{k}{2},$$

$$t_n = \frac{iBk}{2\eta[((n+\ell)-1)^2+k^2]}, z_n = \frac{inB}{k^2+(n+\ell)^2}, \quad w_n = \frac{ikB}{2\eta[(n+\ell)+1)^2+k^2]}. \tag{5.4}$$

The array N, which has indices from $-N$ to N. The entries will range from $-N+\ell$ at index $-N$ to $N+\ell$ at index N. We take the original (full) code and replace any

references to n that are not part of the array index with $\ell + n$. If $\ell = 0$, the entries in each of these vectors will have the same value as their index, otherwise identical to the original problem. This gives a discrete set of eigenvalues with a dependence $p(k, \ell, \nu, B_0, P)$ in general, and the real part of the growth rate is unchanged on the replacement $(k, \ell) \to (-k, -\ell)$ due to the imaginary part give symmetry for the wavenumbers. In fact, they appear to be symmetric under the $(k, \ell) \to (-k, -\ell)$, see figure 5.1(a,b).

Finding the growth rate is now more computationally expensive as we need to maximize over k & ℓ. To simplify things, we split the complex growth rate p into its real and imaginary parts such that $p = p_r + ip_i$ and reconstruct any range of x for a two-dimensional Floquet wave. During one period of the Floquet wave, we rebuild the field in $0 < x < 2\pi/\ell$. In our numerical solution, for a given N, the $(4N+2)\times(4N+2)$ matrix is set up in Matlab, and an eigenvalue p with maximum real part is calculated. For a given parameter set $\mathrm{Re}\, p_{\max}(\nu, B_0, P) = \max_{k,\ell} \mathrm{Re}\, p(k, \ell, \nu, B_0, P)$ with the maximum taken over the grid of k, ℓ values in some results.

5.4 Vertical magnetic field with $\ell \neq 0$

In this section, we consider instability with a vertical magnetic field and Floquet wavenumber ℓ present in the system. We reconstruct the growth rate and confine our attention to $-0.5 < \ell \leqslant 0.5$, and present in the original domain $0 \leqslant x \leqslant \frac{2\pi}{\ell}$, $0 \leqslant y \leqslant \frac{2\pi}{k}$. We investigated the instability of growth rate as a function of (ν, B_0) with $\ell = 0$ and found the reduction of instability by the magnetic field (see figure 3.4 chapter 3). In this section, we look for instability with $\ell \neq 0$. It is possible to look for instability at the wavenumbers (ℓ, k) in the (x, y)-direction, and find the growth rate p, as a function of $(k, \ell, \nu, \eta, B_0)$ parameter space as shown in figure 5.1.

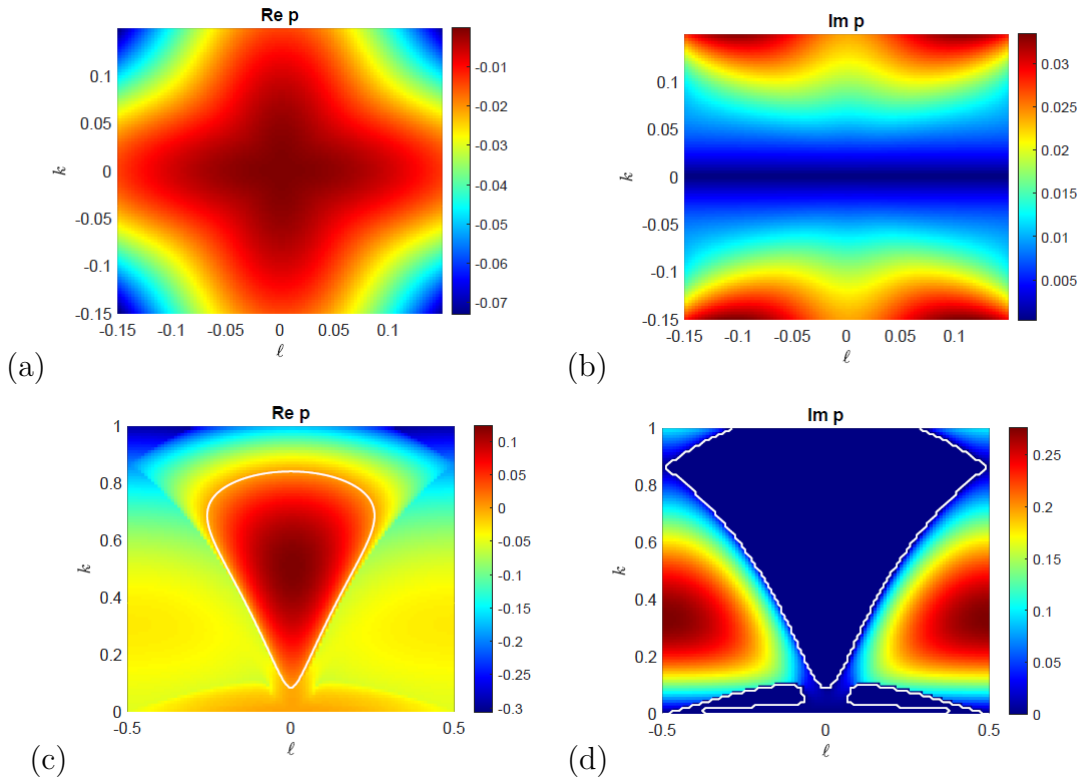

Figure 5.1: Colour plots of the linear growth rate, p as a function of wavenumbers (ℓ, k) for $P = 1$, and $B_0 = 0.2$. Panels (a,b) show $\nu = 0.6$, and panels (c,d) show $\nu = 0.2$.

We plot the growth rate with the wavenumbers (ℓ, k) varied independently at weak field $B_0 = 0.2$. Panel (a,b) indicates stability at $\nu = 0.6$ with a negative growth rate appearing in the colour bar, hence introducing ℓ doesn't change the system, where the viscosity is high enough to prevent the instability and the white line disappears allowing Alfvén waves to dominant in both panels (a,b). We found unstable mode at the same viscosity value $\nu = 0.6$ in the hydrodynamic case with $\ell = 0$ in figure 2.1, while introducing a weak magnetic field leads to suppression of this instability in figure 3.4. Therefore, $\ell \neq 0$ does not change the system in this case.

We observed instability by reducing the viscosity value from $\nu = 0.6$ to $\nu = 0.2$ as shown in panels (c,d), we obtain a *jewel* of instability in the real part $\mathrm{Re}\, p$ in panel (c) associated with zero frequency (dark blue) in the imaginary part $\mathrm{Im}\, p$ in panel (d). This *jewel* of instability also appears for a strong magnetic field (detailed in section 5.4.2, figure 5.3), we change the range of k an ℓ to see the occur figure. In the four panels shown in figure 5.1, the growth rate has mirror symmetry along the

wavenumber axes (k, ℓ). Thus, we can say that the system consists of a quartet of wavenumbers (k, ℓ). We conclude that increasing ℓ from zero has only a stabilising effect in the vertical field case. In the next section, we will discuss the vertical field case further, and the theory might be extended to incorporate $\ell \neq 0$, details in section 5.4.2.

5.4.1 Vertical magnetic field with (ν, B_0)-plane and $\ell \neq 0$

One of the most important results is looking for instability by varying the viscosity and increasing the magnetic field gradually. Section 3.4 show the suppression of instability by vertical magnetic field with $\ell = 0$ chapter 3. The hydrodynamic threshold is observed at $\nu_c = 1/\sqrt{2} \simeq 0.7$, details in the hydrodynamics chapter 2. This instability threshold also is visible in the vertical field with $\ell = 0$.

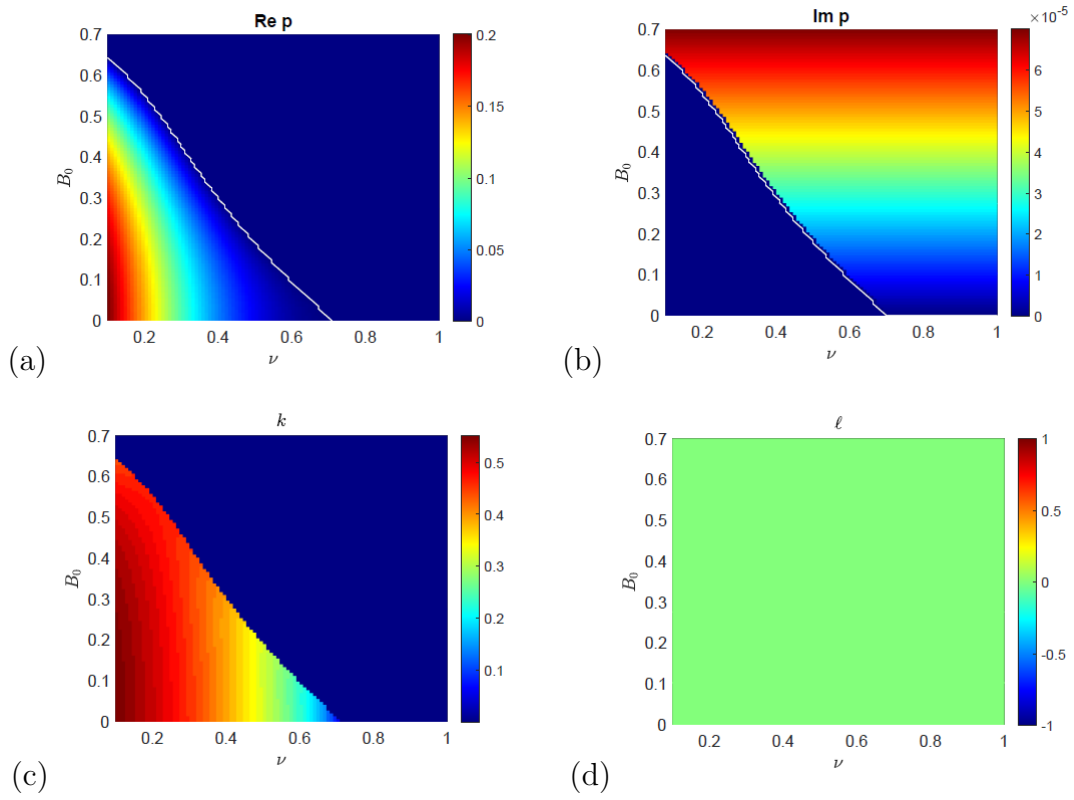

Figure 5.2: Instability of growth rate p for vertical field plotted as a function of (ν, B_0)-plane for $P = 1$, and $\ell \neq 0$. Instability threshold determined by the contour white line $\mathrm{Re}\, p = 0$. Panels (a,b) show $\mathrm{Re}\, p$ and $\mathrm{Im}\, p$, respectively. Panels (c,d) show the wavenumbers (k, ℓ) respectively.

The suppression of instability is shown in figure 5.2, this instability is observed in three panels (a) $\mathrm{Re}\, p$,(b) $\mathrm{Im}\, p$ and plot of k in panel (c), and determined by the

contour white line $\mathrm{Re}\, p = 0$, which interests the $B_0 = 0$ axis at $\nu = 0.7$. However, panel (d) shows that the mode with maximum $\mathrm{Re}\, p$ occurs at $\ell = 0$. By introducing the Floquet wavenumber $\ell \neq 0$ in the vertical field, the instability structure remains unchanged.

5.4.2 Vertical field linear theory with $\ell \neq 0, k \ll 1$

The perturbation theory from section 3.7.1 can be extended to incorporate the Floquet wavenumber $\ell \neq 0$. This can be done in the case of a vertical field. We calculate an approximate growth rate valid for $k \to 0$. Having ℓ non-zero seems to have only suppressed the instability as shown in section 5.4.1. In this section, we apply the theory for a strong vertical field for $P < 1$ and $\ell \neq 0$. The analytical results are given in Appendix A.

The growth rate p_{21} informs us about the instability as k increases from 0, but to find out how the growth rate decreases, we would need to calculate p_{22}. Analysis gives equation (A.60) which is reproduced here by rescaling $\ell' = k/\ell$:

$$p_{21} = \frac{\Delta}{4(1+\ell^2/k^2)}[\eta(1-3\ell^2/k^2)-\nu(1+\ell^2/k^2)-4\ell^2/k^2\Delta\nu(\eta+iB_0')^2+4\ell^2/k^2\Delta\eta(\nu-iB_0')iB_0'] \tag{5.5}$$

$$p_{21}k^2 = \frac{\Delta k^2}{4(k^2+\ell^2)}[\eta(k^2-3\ell^2)-\nu(k^2+\ell^2)-4\ell^2\Delta\nu(\eta+ikB_0)^2+4\ell^2\Delta\eta(\nu-ikB_0)ikB_0] \tag{5.6}$$

The second term of equation (5.6) comes from the full growth rate $p_2 = p_{21} + p_{22}$ at the usual p_2 equation calculation, however, it might be worthwhile to put the p_{22} term numerically to see how the theory works.

$$p_{22}k^2 = -\frac{1}{2}(\eta+\nu)(k^2+\ell^2) \tag{5.7}$$

Comparison between the numeric and theoretical results is shown in Figure 5.3, where the instability growth rate is a function of (ℓ, k) at small Prandtl number $P = 0.5$ and varying the strong magnetic field strength ($B_0 = 2, 4, 6$). The left column represents the numerical results, while the right column represents the theoretical results. The

agreement is excellent at the strong field of B_0; the jewels of stability in both panels appear to be aligned as B_0 increases, which confirms our analysis. For example, figure 5.3 shows growth rates in the (ℓ, k)-plane for strong field $B_0 = 2$ in panels (a) and (b). We can see clearly a large island of instability in both panels, where the growth rates decreased for $\ell \neq 0$ and the most unstable mode observed at $\ell = 0$ determined by the contour white line $\mathrm{Re}\, p = 0$.

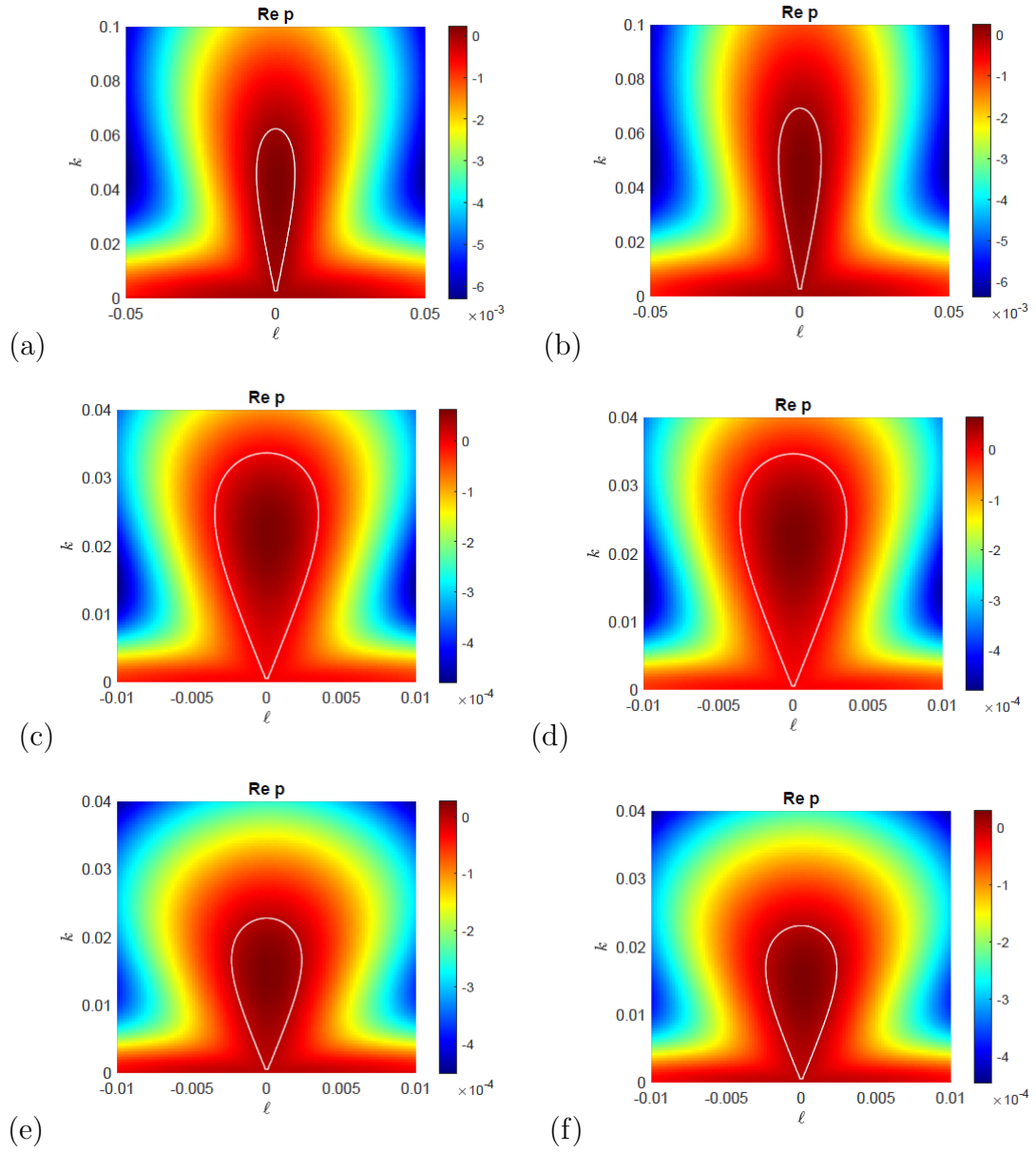

Figure 5.3: Colour plots of the growth rate of $\mathrm{Re}\, p$ at $P = 0.5$ calculated from equation 5.6, and $\eta = 2\nu$ with varying B_0. Panels (a, b) $B_0 = 2$, panels (c, d) $B_0 = 4$, (e, f) panels $B_0 = 6$.

5.5 Horizontal magnetic field with $\ell \neq 0$

We consider the horizontal field with $\ell \neq 0$. The results in chapters 4 have been taken for zero Floquet wavenumber $\ell = 0$. Adding $\ell \neq 0$, allows more freedom of instability to take up the scale $2\pi/k$ in the y-direction and $2\pi/\ell$ in the x-direction. It turns out that instabilities can occur for $\ell \neq 0$ even when the system is stable for $\ell = 0$, in the case of horizontal field (unlike the situation for vertical field). Figure 5.4 shows instability plotted at wavenumbers (ℓ, k)-plane for weak field $B_0 = 0.2$ and different values of viscosity corresponding to stability at $\ell = 0$. Panels (a,b) show a region of instability taking a 'butterfly' structure, determined by the white contour line $\mathrm{Re}\, p = 0$ associated with the imaginary part $\mathrm{Im}\, p$ showing zero frequency in panel (b). The most unstable modes have been observed at $(\ell, k) = (0.05, 0.1)$ marked by a white square in panel (a). Here, the field destabilizes the system, and we can see clearly a similar instability emerges at $(\ell, k) = (0.05, -0.1)$ and at $(\ell, k) = (-0.05, 0.1)$.

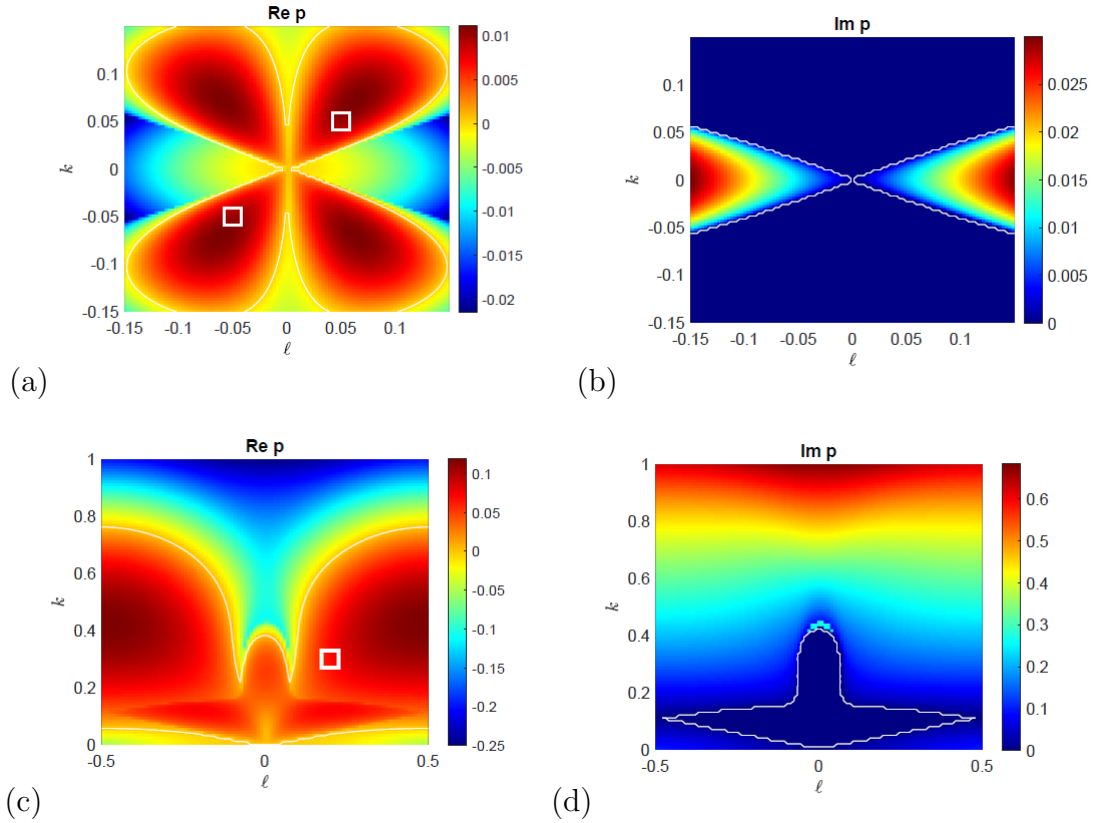

Figure 5.4: Colour plots of instability growth rate,p, as a function of the wavenumbers (ℓ, k) for $B_0 = 0.2$. Panels (a,b) show instability at $\nu = 0.6$, and panels (c,d) show instability at $\nu = 0.2$.

Instability structure can also be observed with low viscosity $\nu = 0.2$ as shown in panels (c,d) for $\ell = 0$ and $\ell \neq 0$. An example of the most unstable mode is represented by the white square in panel (c) at $(\ell, k) = (0.2, 0.3)$. We can see clearly at $\ell = 0$ there is a small island of instability appears associated with zero frequency in the imaginary part $\mathrm{Im}\, p$ in panel (d). This island of instability corresponds to the flow branch G_0 as shown in figure 4.5(a). We generated figure 5.4 by fixing the values (ν, B_0) and varying the wavenumbers (ℓ, k). We let $p_{\max}(\nu, B_0, \eta)$ be the corresponding maximum growth rate p. Then, we include the appropriate imaginary part (zero or positive) to obtain $p_{\max}$ as the complex instability growth rate with maximum growth rate.

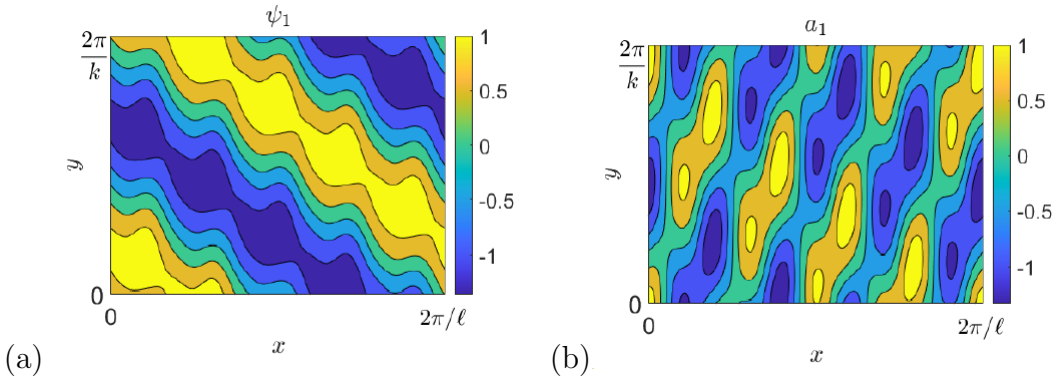

Figure 5.5: A typical unstable mode, with $\ell = 0.2, k = 0.2, \nu = \eta = 0.2, B_0 = 0.2$; (a) shows the stream function ψ_1 and (b) the vector potential a_1

An example of unstable mode for $\ell \neq 0$ in figure 5.5 at $B_0 = 0.2, \nu = \eta = 0.2$ and $k = 0.2$ corresponding to the square in figure 5.4(c) indicating the unstable mode. Panel (a) shows oblique instability in the perturbation stream function ψ_1. The perturbation magnetic field a_1 exhibits oblique zonostrophic instability with small systematic vortices along the magnetic lines in panel (b) for $0 \leqslant x \leqslant 2\pi/\ell, \quad 0 \leqslant y \leqslant 2\pi/k$.

5.5.1 Horizontal magnetic field in (ν, B_0)-plane and $\ell \neq 0$

Having investigated the individual effects of low and high viscosity and weak magnetic field on two-dimensional fluid, we now extend our results in section (5.5) by varying the parameter values of (ν, B_0), then take the maximisation over a finite range

of k-values, ℓ-values including $\ell = 0$, typically at 50×50 resolution in the range $0 < k < 1$ and $-0.5 < \ell \leqslant 0.5$. Compared with figure 4.5 (b) which uses identical parameter ranges to show instabilities with ℓ constrained to be zero.

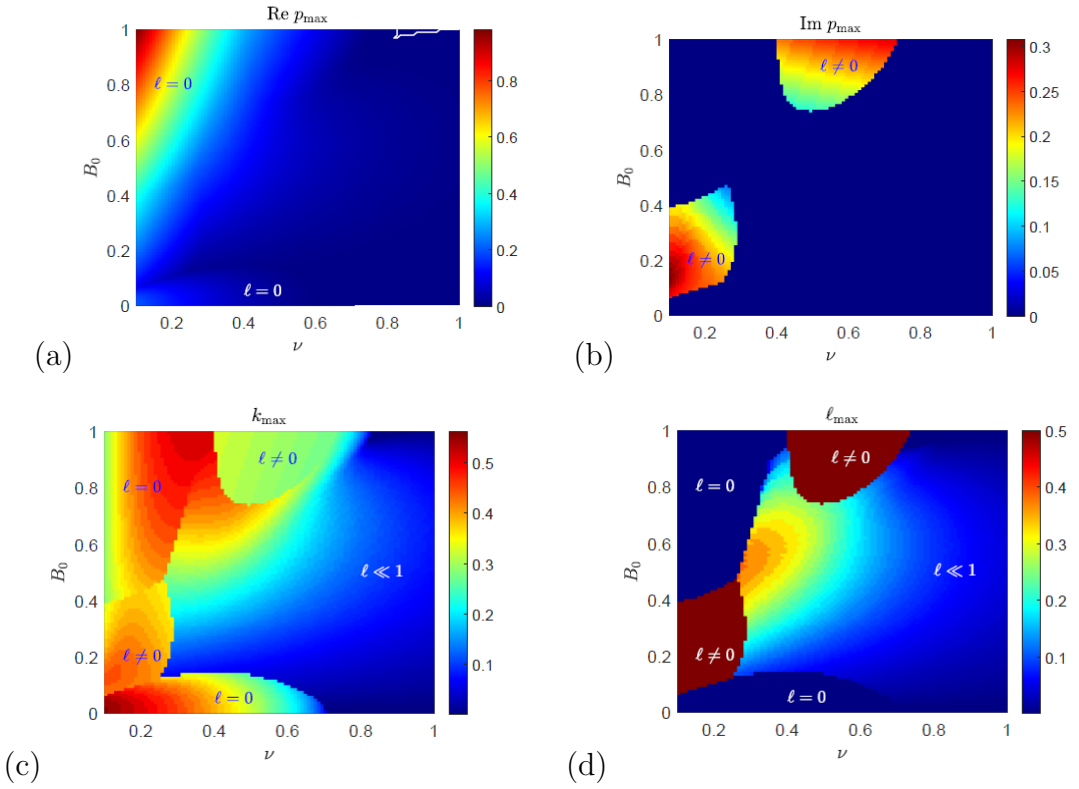

Figure 5.6: Instability growth rate $\mathrm{Re}\, p_{\max}$ for horizontal field plotted as a function in the (ν, B_0) plane for $P = 1$, $\ell \neq 0$. Panels (a,b) show $\mathrm{Re}\, p_{\max}$ and $\mathrm{Im}\, p_{\max}$, respectively. The maximising values of $k_{\max}$ and of $\ell_{\max}$ are shown in panels (c,d) respectively.

Figure 5.6 illustrates the structure of instability in the four panels: (a,b) the real and imaginary parts of the growth rate $p_{\max}$, and (c,d) the maximising values $k_{\max}$ and $\ell_{\max}$. First, we can see that the visible white curve in panel (a) is reduced to a small triangle at the top right corner of the panel 5.6(a) as compared to 4.5(b). The purely hydrodynamic instabilities are suppressed by increasing B_0, and the flow and field branches are not really visible now in panel (a) compared with figure 4.5(a). This region demonstrates $\ell = 0$ as the dominant mode and remains prominent in flow and field branches indicated by $\ell = 0$ in figure 5.6(a), evident in panel (c,d) showing $k_{\max}$, with $\ell_{\max}$. Panels (c,d) show that there are two islands of instability attached to the field branch marked by $\ell \neq 0$ and has a constant value at $\ell_{\max} = 0.5$, which also with non-zero frequency in $\mathrm{Im}\, p$ in panel (b) indicating instabilities with 4π periodicity in x.

There is a transition strongly visible in panel (d) in the yellow region with $\ell_{\max} \neq 0$, as well as this transition appearing in $k_{\max} \neq 0$. Therefore, we have a wide area of instability in panel 5.6(a) indicated by $\ell \ll 1$. These modes show small values of $k_{\max}$ and $\ell_{\max}$ and have low growth rates. As a result, these modes depend on the presence of $\ell \neq 0$, where this region was stable in the previous panel 4.5(a). As a result of this region, the white curve in panel 5.6(a) has been pushed to the top right corner for a small area of stability. To gain a better understanding of this new region of instability for $\ell = 0$, please refer to section (5.5.3) for the theory in $\ell \ll 1, k \ll 1$. discussed in Appendix (B). Finally, figures 5.2-5.6 with $\ell = 0$ and $\ell \neq 0$ are fundamentally different in terms of instability structure and magnetic field direction. The linear stability problem is further complicated if there is a Floquet wavenumber ℓ and magnetic field B_0 in the system. We also compared these calculations with Manfroi and Young (2002) results, who studied the hydrodynamic instability with β-plane at the large-scale structure and with Floquet wavenumber $\ell \neq 0$ and they found the most unstable modes occur at $k, \ell \neq 0$.

5.5.2 Horizontal linear theory with $\ell \neq 0, k \ll 1$

We present the horizontal field theory for the case of Floquet wavenumber $\ell \neq 0$ where this can enhance instability even though at $\ell = 0$ we can refer to instability structure in section 4.3.1. We will only use first-order perturbation theory due to the complexity of the system. To give the reader a comprehensive understanding of how the theory works, we summarize the major conclusions with a simple example of a double eigenvalue perturbation problem before moving on to the details of the theory of the approximation. We begin by double eigenvalues with a family of eigenvectors, to gain analytical results (see Appendix B).

The growth rate p informs us about the instability as k increases from 0, but to find out how the growth rate decreases, we would need to calculate p_2, which is too complicated to do here. We will add the viscosity suppression term to p_2 to

provide a qualitative sense of the growth rate. Analysis gives equation B.64 which we reproduce here as:

$$p = \pm B_0 \ell \left[\frac{k^2}{\ell^2 + k^2} \frac{\nu\eta + 2\eta^2 - B_0^2}{\eta^2(\nu\eta + B_0^2)} - 1 \right]^{1/2} - \tfrac{1}{2}(\nu + \eta)(k^2 + \ell^2) + O(k^2, \ell^2). \quad (5.8)$$

The second term of equation (5.8) comes from the M_2 matrix at the usual p_2 equation calculation. In this section, it would be very messy to find the full p_2 equation, but it is worth putting the partial p_2 term numerically to see how the theory works.

We gain the equation only going to first order matrix M_1, but it reveals an instability that crucially relies on having a non-zero Floquet wave number ℓ, with ℓ and k to be small. If we fix the parameters value ν, P and B_0 we can consider the growth rate p_2 as a function in the (ℓ, k) plane. Furthermore, by setting the quantity inside the square root to zero we observe the instability threshold determined by the black contour lines shown in figure 5.7

$$\frac{k^2}{\ell^2} = \frac{\eta^2(\eta\nu + B_0^2)}{\nu\eta + 2\eta^2 - \nu\eta^3 - B_0^2(1 + \eta^2)} = \frac{\nu^2(\nu^2 + PB_0^2)}{\nu^2(P^2 + 2P - \nu^2) - PB_0^2(\nu^2 + P^2)} \quad (5.9)$$

For instability at general points in the (ν, B_0) plane, we need the first term of the equation (5.8) to be positive for some values of k, ℓ. This amounts to the condition,

$$B_0^2 < \frac{\eta(\nu + 2\eta - \eta^2\nu)}{1 + \eta^2} = \frac{\nu^2(P^2 + 2P - \nu^2)}{P(\nu^2 + P^2)}\,. \quad (5.10)$$

We obtain the threshold equation (5.10) by setting the denominator of equation (5.9) to zero, as $\frac{k}{\ell} \to \infty$, we obtain the instability threshold in the (ν, B_0) plane at $\ell \neq 0$. The contour lines in equation (5.9) become vertical at this point, and the region of instability disappears.

For $P = 1$ and from equation (5.10) the instability is cut off at $\nu = \sqrt{3}$ and requires

$$\nu < \sqrt{P(2 + P)} \quad (5.11)$$

Numerical experimentation shows that for ν less than this value, the region of instability in the wavenumber ℓ, k plane becomes small as B_0 tends to zero. The maximum magnetic field for the $\ell \neq 0$ instability we found by taking the maximum B_0 over ν^2 (details in Appendix B). The maximum occurs at

$$\nu^2 = -P^2 + \sqrt{2P^3(1+P)} \tag{5.12}$$

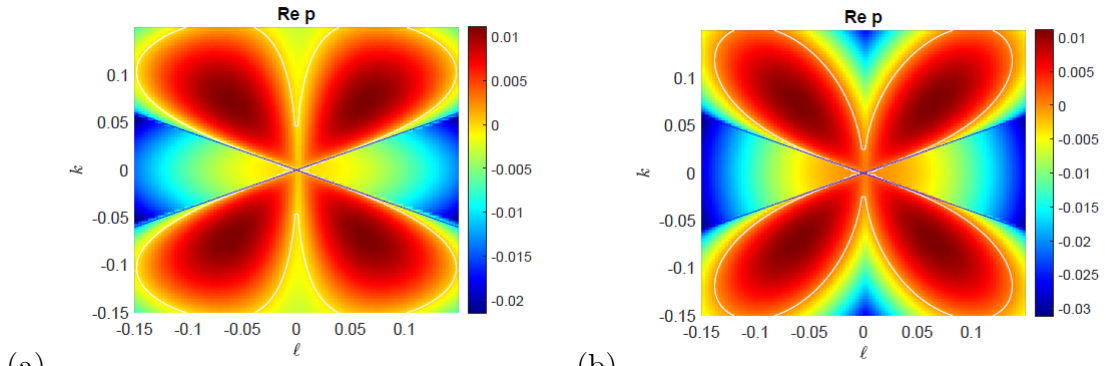

(a) (b)

Figure 5.7: Instability growth rate p for the horizontal field as a function of the wavenumbers (ℓ, k) for $\nu = \eta = 0.6$, $(P = 1)$, with $B_0 = 0.2$. Panel (a) shows numerical results, and panel (b) shows the approximation growth rate calculated from (5.8). In both panels, the black contour line emerging from the origin is from the formula (5.9).

Figure 5.7, shows the growth rate obtained numerically plotted as a function of the (ℓ, k)-plane for $B_0 = 0.2$ and $\nu = \eta = 0.6$ at the same parameters value in figure 4.5(a) to stability for $\ell = 0$, the point $(\nu, B_0) = (0.6, 0.2)$ laying to the stable region (dark blue), but unstable for $\ell \neq 0$ from figure 5.6(a). The growth rate colour plot in figure 5.7 (a) shows instability occurring for all (ℓ, k) points lying inside the region taking a *butterfly* structure, outlined by the white lines $\mathrm{Re}\, p = 0$. At the origin, these curves are tangential to the vertical axis $\ell = 0$, which confirms that modes with $\ell = 0$ are stable for any k. Here, the maximum growth rate of instability occurs when $(\ell, k) = (0.05, 0.05)$. The straight black lines in both panels are given by (5.9) and are tangential to the white curves at the origin, showing good agreement. The agreement between the two panels (a) and (b) is excellent near the origin, otherwise is only qualitative as we might expect. This is because the term $-\frac{1}{2}(\nu + \eta)(k^2 + \ell^2)$ is included in (5.8) which would have a further stabilising effect in this case, we can clarify this as one of many which would appear by using perturbation theory at order

k^2, ℓ^2.

5.5.3 Growth rate at $\ell \neq 0$

In this section, we first recall instability growth rate as a function of (ν, B_0)-plane with $\ell = 0$ and varying the magnetic field strength and viscosity values as shown in figure 5.8 (a) comparing with the theoretical threshold of instability in panel (b). We observe the suppression of the purely hydrodynamic instability as in figure 4.5(a). However, as B_0 is increased another branch of instability emerges and shows increasing growth rates, determined by the white line of instability threshold $\mathrm{Re}\, p = 0$.

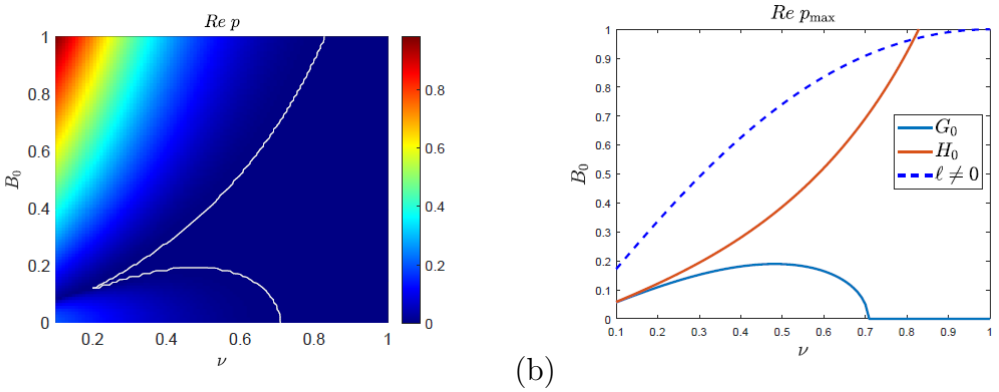

(a) (b)

Figure 5.8: Instability growth rate p as a function of (ν, B_0) for varying values of ν and the strength of magnetic field B_0. Panel(a) shows a colour plot as a function of (ν, B_0), panel (b) shows the theoretical curve of instability calculated from equation (4.69) for the flow branch (blue) and from 4.85 for the field branch (red), and the dashed blue line from equation 5.10 for $\ell \neq 0$.

Panel (b) shows the plot of two branches of instability, the flow branch G_0 indicated by blue and the field branch H_0 indicated by red, we also see a new branch of instability with non-zero Floquet wavenumber $\ell \neq 0$ branch indicated by the blue dashed curve. This curve comes from the theoretical approximation (5.10) and below this curve, the system becomes unstable to $\ell \neq 0$ modes.

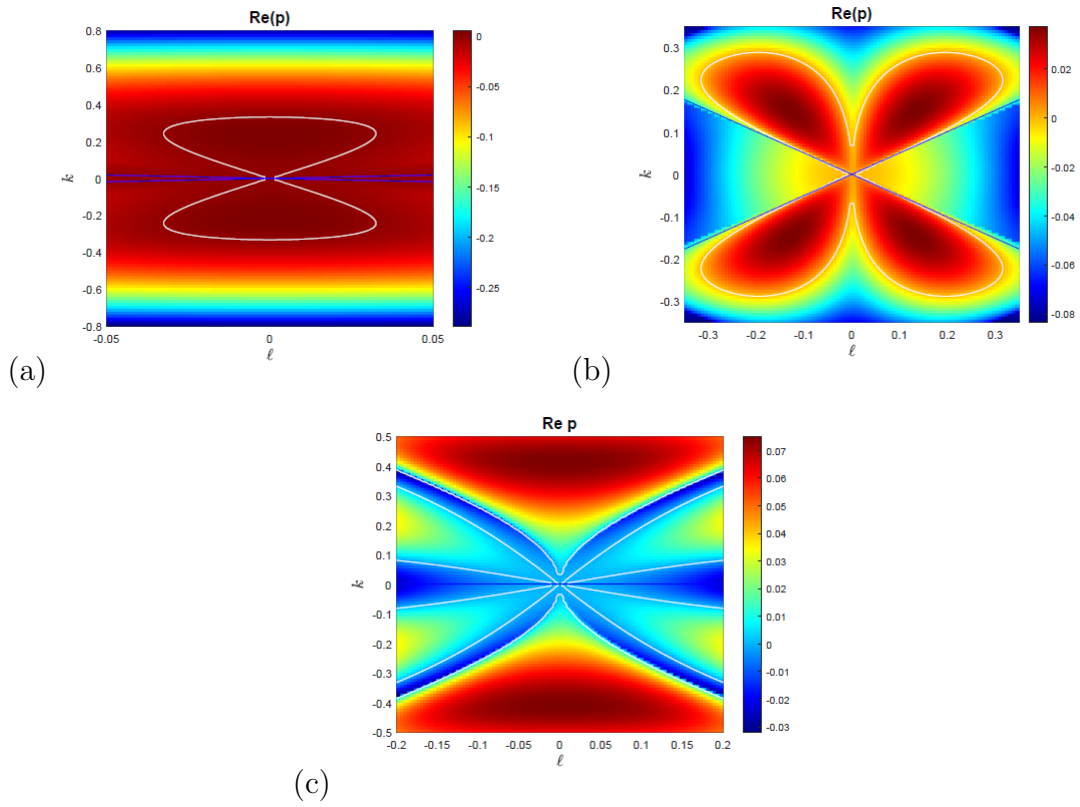

Figure 5.9: Instability growth rate p as a function of wavenumbers (ℓ, k) for $\nu = 0.6$ and varying strength of magnetic field B_0, (a) hydrodynamic case $B_0 = 0$, (b) $B_0 = 0.4$, (c) strong field at $B_0 = 1$.

To better understand the behaviour of the blue dashed branch in figure 5.8(b), we plot a colour plot for the fixed value of viscosity $\nu = 0.6$ and varying magnetic field from weak to strong strength. Figure 5.9(a) shows the hydrodynamic instability $B_0 = 0$ corresponding to the region below the flow branch G_0 (solid blue) in figure 5.8 (b) and confirming the instability determined by the white contour line for $\ell = 0$ in 5.8(a), we can see clearly the region of instability appearing for $\ell = 0$ and $\ell \neq 0$ and outlined by the white contour line $\mathrm{Re}\, p = 0$.

We observed again a "butterfly" of instability for $B_0 \neq 0$, particularly at $B_0 = 0.4$ in panel 5.9(b) corresponding to field branch H_0 (red) in 5.8(b) below $\ell \neq 0$ branch. This figure shows a similar instability structure to figure 5.7 but with different magnetic field strengths and different scales of wavenumbers (ℓ, k). However, we observed instability for a strong field at $B_0 = 1$ indicated by the red region in 5.9(c), while we found the stable mode indicated by the blue region in 5.9(c).

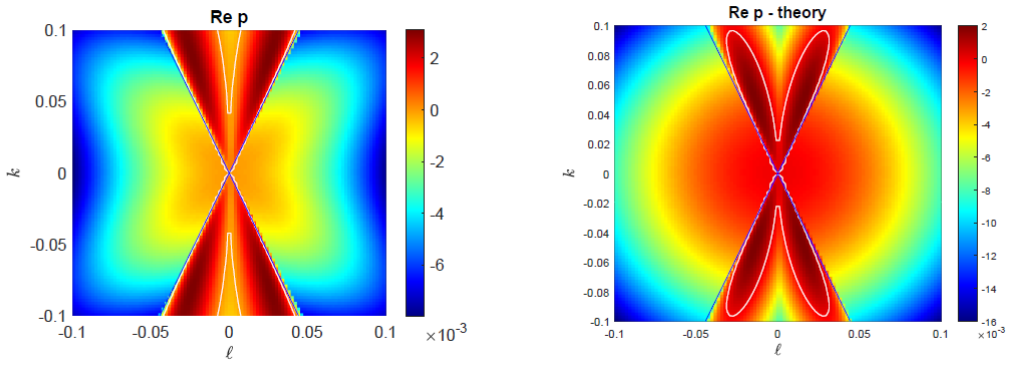

(a) (b)

Figure 5.10: Instability growth rate p as a function of wavenumbers (ℓ, k) for $\nu = 0.8, B_0 = 0.9$. Panel (a) shows the numerical growth rate, and panel (b) shows approximate growth rates calculated from equation (5.8).

Figure 5.10 shows the instability growth rate as a function of the wavenumbers in the (ℓ, k) plane for $\nu = 0.8, B_0 = 0.9$, corresponding to the peak of the triangle region between field branch H_0 (red) and $\ell \neq 0$ (dashed blue) branch, at strong field $B_0 = 0.9$ in figure 5.8(b), which can also seen in figure 5.6(a). Panel (a) shows the numerical growth rate, and panel (b) shows the approximate growth rate obtained from equation (5.8). We can see clearly the butterfly of instability becomes narrow compared with figure 5.9(b), due to a high viscosity and strong field. The theory still works near the origin as we discussed in the previous figure 5.7. Our investigation in this figure shows that the region between flow branch G_0 and field branch H_0 is unstable and as we reduced the magnetic field strength to be close to the flow branch G_0 (blue) in figure 5.9 (a) and we found the instability vanishes. Meanwhile, as we increase the magnetic field more than $B_0 > 0.9$ the instability also vanishes even with non-zero Floquet wavenumber $\ell \neq 0$. Hence, we can consider the instability occurring at $0 < B_0 \leqslant 0.9$.

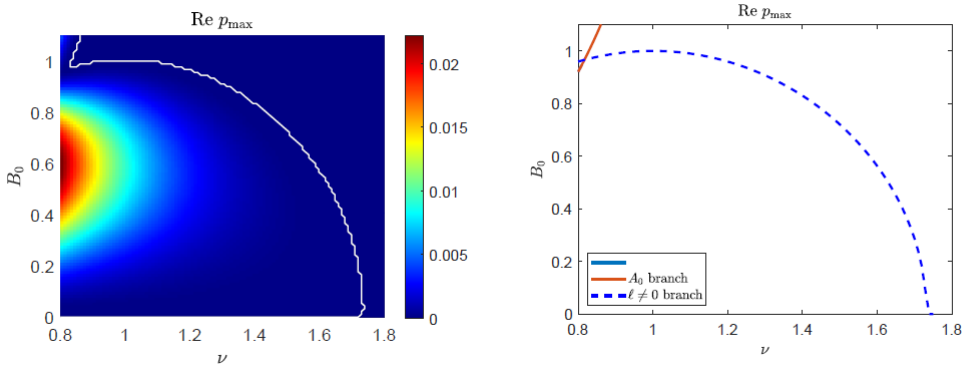

Figure 5.11: (a) Instability growth rate p_{max} plotted in the $(\nu; B0)$ plane with $P = 1$, and $\ell \neq 0$; (b) shows thresholds 4.85 for $\ell = 0$ (red) and B.65 for $\ell \neq 0$ (blue dashed).

To further confirm this analysis, figure 5.11 shows similar information to figure 5.8(b), but over a large scale, I had to adjust the (k, ℓ) ranges a lot to get the figure for the paper Algatheem, Gilbert and Hillier (2023). We observe that the flow branch (blue) G_0 vanishes and the field branch (red) shrinks and appears as a small triangle at the top of the panel (b). While the dashed line extended to reach, $\nu = \sqrt{3} \approx 1.73$ associated with the white contour line in panel (a), we found the instability below the white line, above this line the system is stable. There is a clear agreement between this and the numerical results in panel (a). The dashed curve in panel (b) shows the thresholds in B.65.

5.6 MHD instability with general angle γ, and $\ell \neq 0$

We look for instability of the MHD system for general angle γ, in a range between vertical and horizontal fields $0 < \gamma < \pi/2$, where γ represents the angle between the field and the y axis. As indicated in the schematic figure 5.12, the angle $\gamma = 0$ refers to a vertical field, while $\gamma = \pi/2$ refers to a horizontal field.

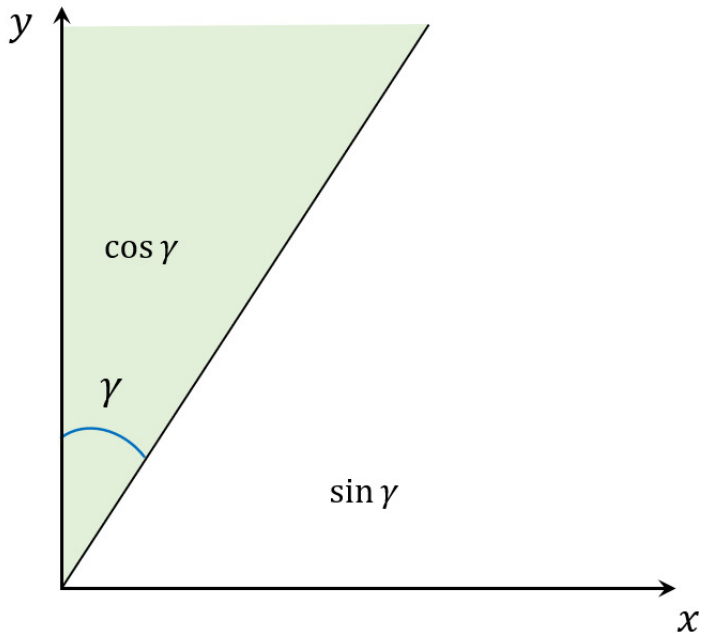

Figure 5.12: Schematic illustrating the angle γ located between the field and y-axis (indicated by the light green shading).

A combination of a general basic state equilibrium from vertical and horizontal fields is given by

$$\boldsymbol{B_0} = (A_{0y}, -A_{0x}), \quad A_0 = -B_0 x\cos\gamma + (B_0 y - \frac{B_0}{\eta}\sin x)\sin\gamma, \quad g = 2\nu\cos x + \frac{B_0^2}{\eta}\cos x. \tag{5.13}$$

where $\cos\gamma$ refers to the vertical component and $\sin\gamma$ refers to the horizontal component. By substituting the basic state above (5.13), then solving the linear equations (3.29–3.30) and using Fourier expansion equations (3.37-3.40), we found an infinite system of equations is obtained with zero Floquet wavenumber $\ell = 0$. We obviously incorporate the growth rate equations of the vertical field (A.1 -A.2) and horizontal field (B.7 - B.8), and adding sin γ times any terms coming from the horizontal equation and adding $\cos\gamma$ times any terms coming from the vertical equations, we obtain:

$$\begin{aligned} pG_n =& \frac{k}{2}\left[\frac{1}{(n-1)^2+k^2} - 1\right] G_{n-1} - \frac{k}{2}\left[\frac{1}{(n+1)^2+k^2} - 1\right] G_{n+1} - \nu(k^2+n^2)G_n \\ &+ \frac{ikB_0\sin\gamma}{2\eta}\left(-1 + ((n-1)^2+k^2)\right) H_{n-1} + \frac{ikB_0\sin\gamma}{2\eta}\left(-1 + (n+1)^2+k^2)\right) H_{n+1} \\ &+ ikB_0\cos\gamma(k^2+n^2)H_n + inB_0\sin\gamma(k^2+n^2)H_n. \end{aligned} \tag{5.14}$$

$$pH_n = -\frac{k}{2}H_{n-1} + \frac{k}{2}H_{n+1} - \eta(k^2+n^2)H_n + \frac{inB_0\sin\gamma}{k^2+n^2}G_n + \frac{ikB_0\sin\gamma}{2\eta}\frac{1}{(n-1)^2+k^2}G_{n-1}$$
$$+\frac{ikB_0\sin\gamma}{2\eta}\frac{1}{(n+1)^2+k^2}G_{n+1} + \frac{ikB_0\cos\gamma}{k^2+n^2}G_n. \tag{5.15}$$

Thus, we have a linear system of equations for the flow G_n & and the field H_n, and numerical solutions with variation in the angle γ by using the Matlab framework will be presented in the next sections.

5.6.1 MHD with (ℓ, k)-plane and $\gamma = \pi/4$

To give a more global picture of instability for a general magnetic field we show instability at a specific angle γ where we found the most unstable mode at $\gamma = \pi/4$. Figure 5.13 shows instability at weak field $B_0 = 0.2$ and different values of viscosity ν. We observed that the instability structure for $\gamma = \pi/4$ is similar to instability for $\gamma = \pi/2$ in figure 5.4. Panels (a,b) show instability at $\nu = 0.6$, with a "red fan" of instability outlined by the white contour line and emerge from the origin at $(\ell, k) = 0$. The most unstable modes occur at $\ell \neq 0$. Reducing the viscosity to $\nu = 0.2$ allows more possibility of instability as shown in panels (c,d), the red fan of instability becomes wider to show the instability associated with zero frequency in panel (b). We eventually lose the symmetry for $\gamma \neq 0$, particularly at $\pi/4$ in comparison with figure 5.4.

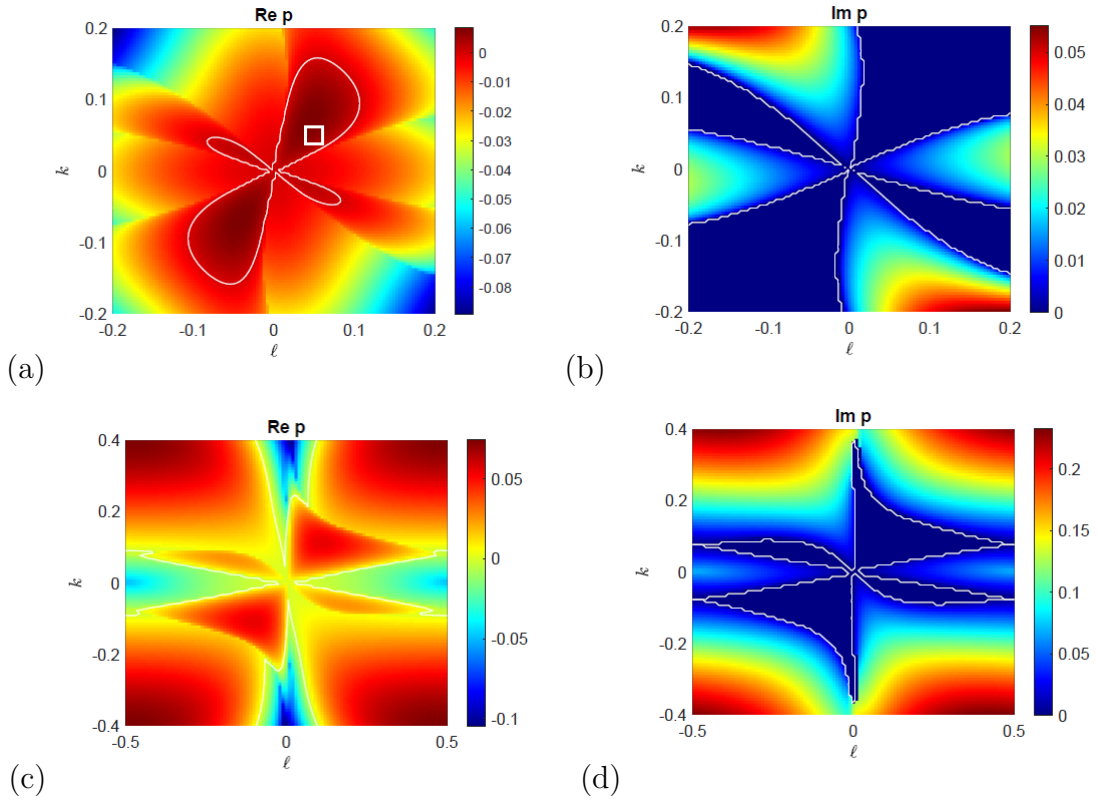

Figure 5.13: Colour plots of the linear growth rate, p , as a function of wavenumbers (ℓ, k) for $\gamma = \pi/4, B_0 = 0.2$. Panels (a,b) show instability at $\nu = 0.6$, and panels (c,d) show instability at $\nu = 0.2$.

An example of the most unstable mode is marked by a white square at $(\ell, k) = (0.05, 0.05)$ in panel (a), associated with zero frequency in panel (b). Alfvén waves are observed at $\ell = 0$ in the imaginary part $\mathrm{Im}\, p$ in panel (b). While Alfvén waves are observed at $\ell \neq 0$ in panel (d). Thus, having $\ell \neq 0$ destabilizes the system, looking for panels (a,c).

5.6.2 MHD instability with $0 < \gamma < \pi/2$

In this section, we look for instability using the combination of vertical and horizontal fields by variation of the angle γ in the range of $0 < \gamma < \pi/2$, and the effect of the magnetic field strength can be more easily compared. Previously we investigated the instability for vertical magnetic field at $\gamma = 0$ in chapter 3 and for horizontal field at $\gamma = \pi/2$ in chapter 4. In this study, we investigate the instability in the intermediate case within the range $0 < \gamma < \pi/2$. As $\gamma \to \pi/2$ we obtained two branches of instability referring to a horizontal field structure in figure 4.3.1(b), while the field

branch shrinks and vanishes as we reduce $\gamma \to 0$ and the flow branch dominates refer to vertical field structure as shown in figure 5.14(e).

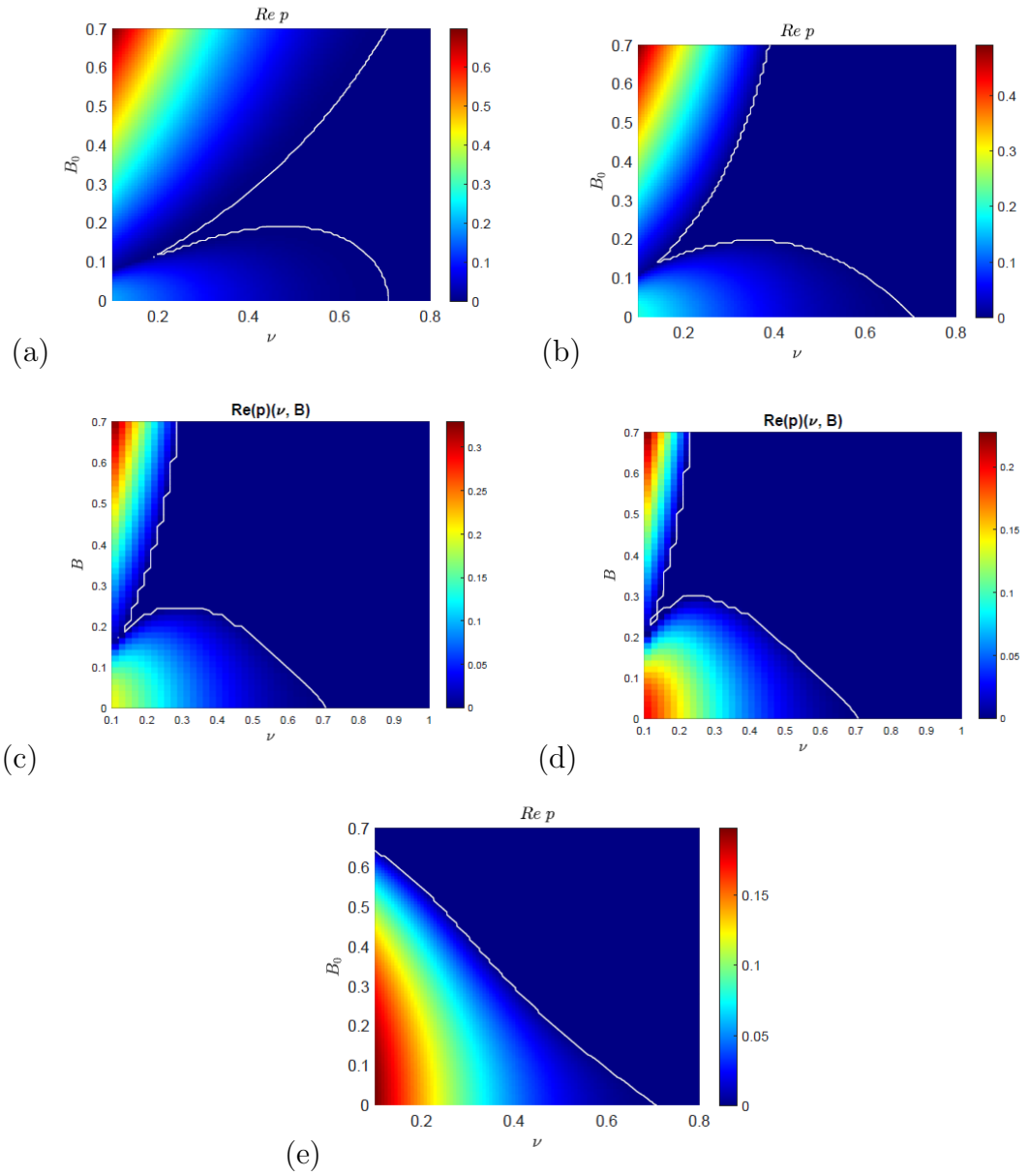

Figure 5.14: Colour plots of the linear growth rate of $\mathrm{Re}\, p$, as a function of (ν, B_0) for (a) $\gamma = \pi/2$ (horizontal magnetic field), (b) $\gamma = \pi/4$, (c) $\gamma = \pi/6$, (d) $\gamma = \pi/8$, (e) $\gamma = 0$ (vertical magnetic field). The instability threshold is outlined by the white contour line $\mathrm{Re}\, p = 0$.

Figure 5.14 shows instability growth rate as a function of (ν, B_0) with changes in the angle γ in the range $0 < \gamma < \pi/2$, with calculations performed at zero Floquet wavenumber $\ell = 0$. Panels (a,b) show instability at $\gamma = \pi/2, \gamma = \pi/4$ respectively. The two branches of instability are formed and we may refer to the horizontal field case as shown in figure 4.5(b), where the flow branch is suppressed by a weak magnetic field in both panels. There is a small change at the field branch H_0, in which panel

(a) shows the contour white line along the vertical axis and corresponding the value $\nu = \simeq 0.7$ for $B_0 = 0.7$, while panel (b) shows the contour white line slightly shrunk and corresponds to the value $\nu \simeq 0.5$ for $B_0 = 0.7$. A significant change occurs in panels (c,d), particularly at $\gamma = \pi/6, \gamma = \pi/8$, where the field branch H_0 shrinks and the flow branch G_0 continuously grows. The most unstable region is observed when $\nu \longrightarrow 0$. Once we reduce the $\gamma \to 0$, the field branch of instability vanishes reducing to the vertical field result at $\gamma = 0$, as shown in panel (e).

5.7 Linear theory with angle γ and $k \ll 1$

Having investigated the vertical field at $\gamma = 0$ in chapter 3 and the horizontal field at $\gamma = \pi/2$ in chapter 4, here we apply the theory with a combination of the vertical field and horizontal field which can give complicated theoretical calculations even with $\ell = 0$. To consider angles γ for which the numerics and theory agree, (see Appendix C) for analytical results.

The growth rate p informs us about the instability as k increases from 0 with $\alpha = ickB_0,\ \beta = isB_0$, where $c = \cos\gamma, s = \sin\gamma$ and if we set out $s = 0$ we get vertical field growth rate C.38. Analysis gives equation C.39 which reproduce here as:

$$p_2 k^2 = \frac{k^2}{4\eta^2} \frac{(\eta - \nu)(\eta^2 + s^2 B_0^2)[\nu\eta + (\nu + \eta)ickB_0 + s^2 B_0^2]}{[\nu\eta + (\nu + \eta)ickB_0 + s^2 B_0^2]^2 - 4s^2 c^2 k^2 B_0^4} - \frac{1}{2}(\nu + \eta)k^2 \qquad (5.16)$$

The second term of equation (5.16) comes from the M_2 matrix at the usual p_2 equation calculation. To explain instability at general points in the (ν, B_0) plane, we take p_2 over a common denominator & set $k = 0$

$$p_2 = \frac{1}{4\eta^2} \frac{(\eta - \nu)(\eta^2 + s^2 B_0^2)(\nu\eta + s^2 B_0^2)}{(\nu\eta + s^2 B_0^2)^2} - \frac{1}{2}(\nu + \eta) \qquad (5.17)$$

over common numerator

$$= \frac{1}{4\eta^2}\frac{(\eta-\nu)(\eta^2+s^2B_0^2)-2\eta^2(\nu+\eta)(\nu\eta+s^2B_0^2)}{\nu\eta+s^2B_0^2} \tag{5.18}$$

set the numerator to zero

$$(\eta-\nu)(\eta^2+s^2B_0^2) = 2\eta^2(\nu+\eta)(\nu\eta+s^2B_0^2) \tag{5.19}$$

we use the Prandtl number as the expression $P=\nu/\eta$, this amounts to the condition

$$B_0^2 = \frac{2\nu^4(1+P)-P(1-P)\nu^2}{P(1-P)s^2P^2-2\nu^2(1+P)Ps^2} \tag{5.20}$$

we obtain the instability threshold at $\ell=0$ and by setting the numerator of equation (5.20) to zero, as $B_0\to 0$ and at a fixed value of the Prandtl number, we obtain the quadratic expression of ν for the general Prandtl number.

$$2\nu^4(1+P) = P(1-P)\nu^2, \qquad \nu^4 = \frac{P(1-P)\nu^2}{2(1+P)} \tag{5.21}$$

$$\nu^2 = \frac{P(1-P)}{2(1+P)}, \qquad \nu = \sqrt{\frac{P(1-P)}{2(1+P)}} \tag{5.22}$$

For the Prandtl number $P=1$, and $B_0\to 0$ we obtain the same instability threshold of the vertical field in equation (3.109)

$$P=0.5 \Rightarrow \qquad \nu_c = \frac{1}{\sqrt{12}} \simeq 0.28 \tag{5.23}$$

For confirmation of the theory expression in 5.22 and the curves in figure 5.15 for small Prandtl numbers. The instability threshold in (5.23) for $P=0.5$ provides evidence of a good agreement of the theory calculations with the blue curve at $\nu=0.28$. While, as $B_0\to\infty$ and by setting the denominator of equation (5.20) to zero, and assuming $s=1$ which gives the vertical field, we obtain the straight curves along the vertical axes B_0, the blue curve around $\nu=0.14$ for $P=0.25$, and the red curve around $\nu=0.2$ for $P=0.5$.

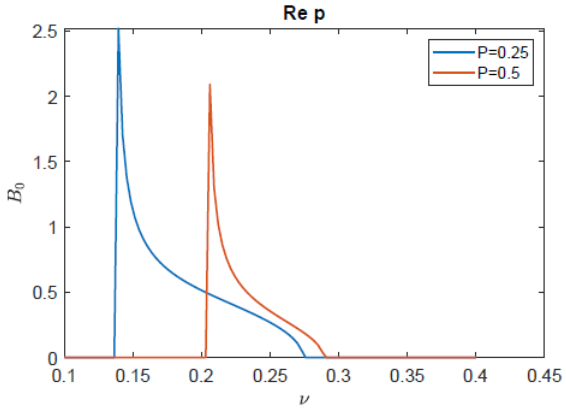

Figure 5.15: Instability threshold for small Prandtl numbers $P = 0.25, 0.5$ obtained analytically from the expression 5.20, $s = 1$.

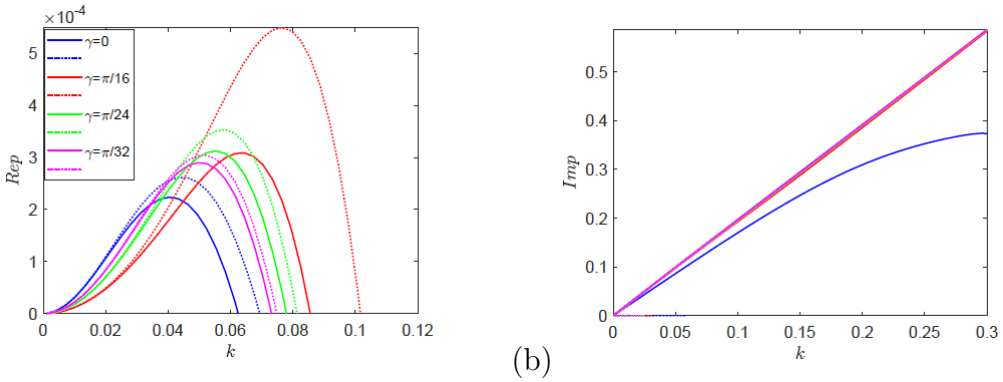

(a) (b)

Figure 5.16: Instability growth rate as a function of k with variation of small angle γ for $P = 0.5$, $\nu = 0.2, B_0 = 2$, (a) $\mathrm{Re}\, p$ (b) $\mathrm{Im}\, p$. The solid lines are obtained numerically, while the dotted lines in panel (a) are the analytical expressions given in expression (5.16).

Figure 5.16 shows instability growth rate as a function of wavenumber k with an arbitrary choice of the angle γ. Panels (a, b) show $\mathrm{Re}\, p$ and the imaginary part $\mathrm{Im}\, p$ respectively. We can see clearly that as we increase the angle γ the curves grow. These theoretical lines are observed at the strong magnetic field $B_0 = 2$ and small Prandtl number $P = 0.5$. We noticed that at $\gamma = 0$ which is the vertical field, the theory works nicely, and increasing γ makes it much more unstable because the growth rate goes up. So changing γ has a quite strong effect and makes the system less stable. Numerical curves have overlapping frequencies as shown in panel (b), the blue curve is only $\gamma = 0$, while the red curve includes all other values of γ which give overlapping curves in figure 5.16(b). The excellent agreement between the numerical results and theoretical lines, determined by the white contour lines $\mathrm{Re}\, p = 0$ are shown in the following figures.

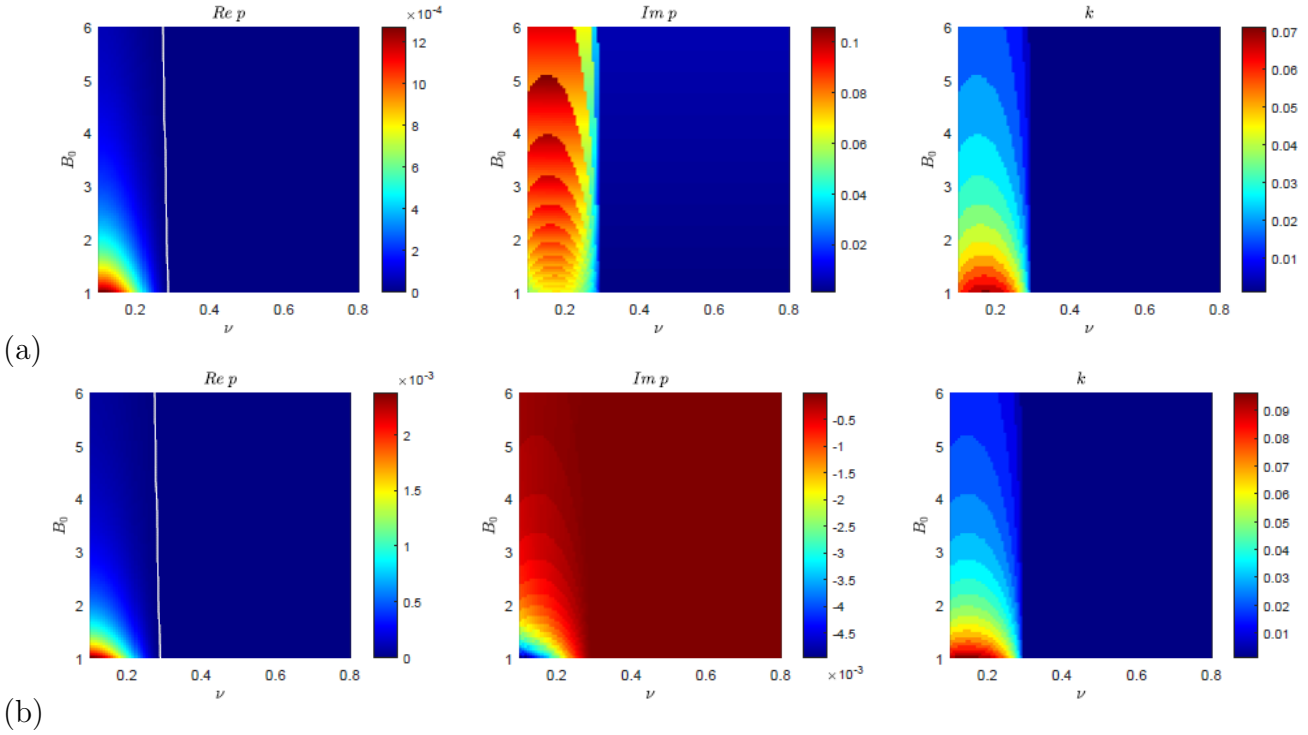

Figure 5.17: Colour plot of instability growth rate as a function of (ν, B_0) at $\gamma = 0$ and $P = 0.5$. Panel (a) show the numerical computation of the growth rate, and panel(b) shows the theoretical threshold determined by the white line $\mathrm{Re}(p) = 0$ from equation (5.16).

Figure 5.17 shows the instability growth rate as a function of (ν, B_0), with small Prandtl number $P = 0.5$ and $\gamma = 0$ corresponding to the vertical field case (see figure 3.15), Panels (a,b) shows numerical companion and approximate growth rate coming from equation (5.16), the white contour line for both panels corresponding to the theoretical curve (blue) in figure 5.16(a). We can see clearly there are oscillatory regions in the imaginary part $\mathrm{Im}\, p$ that have a small growth rate of instability in panel (b), these oscillatory regions also occur in the plot of k in both panels.

A similar agreement can be seen in figure 5.18 for $\gamma = \pi/24$ corresponding to the theoretical line (green) in figure 5.16(a). As γ increases we obtain the similar white contour lines roughly at $\nu = 0.28$ in the real part of both panels (a,b). We can see clearly that the theory shows good agreement at small values of $\gamma \to 0$.

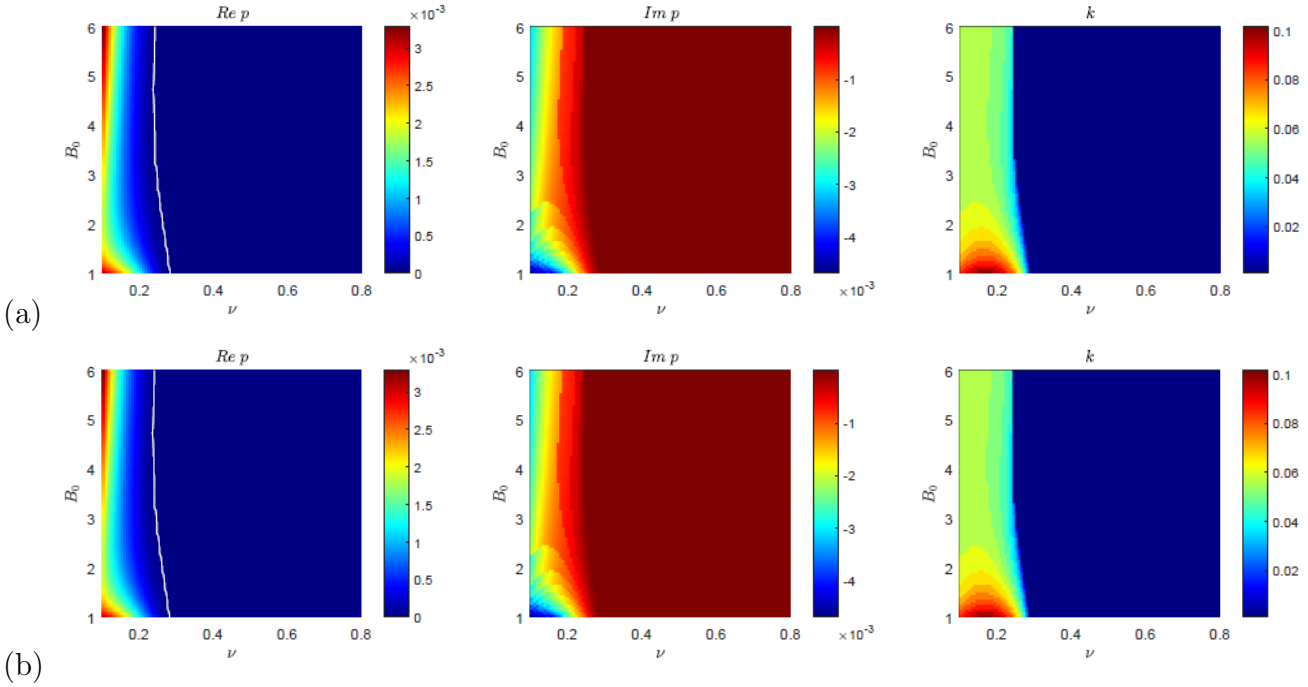

Figure 5.18: Colour plot of instability growth rate as a function of (ν, B_0) at $\gamma = \pi/24$ and $P = 0.5$. Panel (a) show the numerical computation of the growth rate, and panel(b) shows the theoretical threshold determined by the white line $\mathrm{Re}(p) = 0$ from equation (5.16).

5.8 Conclusion

We briefly present the key results of this chapter as follows:

- We compare the numerical results for $\ell = 0$ in the vertical and horizontal fields in chapters (3,4) and $\ell \neq 0$ in this chapter and found that there is no significant difference in the structure at the large-scale vertical field, where introducing a Floquet wavenumber $\ell \neq 0$ has no effect on the system. However, we observe more freedom of instability for the horizontal field, shown on the (k, ℓ) wavenumbers plots (see figure 5.4, 5.6).

- We verify numerical results with perturbation theory at $k \to 0$ in vertical field section 5.4.2 and horizontal field section 5.5.2 and found the appropriate scale for Floquet wavenumber ℓ. We found a good agreement between the theory and numerics in both field directions determined by the threshold of instability, see equation (5.9) and figures (5.7-5.3).

- Section 5.5.3 shows a good agreement between growth rates obtained numeric-

ally at $\ell = 0$ and the approximation growth rates for $\ell \neq 0$ in the flow branch and field branch in figure 5.8 and also the agreement of ℓ branch between numerical and theoretical results at $\ell \neq 0$ in figure 5.11. While increasing or reducing the magnetic field strength B_0 further leads to the instability vanishing, particularly at $\nu = 0.8$ (see figure 5.10), the theory works at Prandtl number $P = 1$.

- We investigate instability at different angles $0 < \gamma < \pi/2$ and $\ell = 0$. and found numerical and theoretical results in section (5.7), We also found the theory only works at small values as $\gamma \to 0$, otherwise disagrees e.g. as $\gamma \to \pi/2$.

6. Non-linear evolution: two-dimensional incompressible hydrodynamic flow

6.1 Introduction

In our previous study, we investigated the characteristics of zonostrophic instability of sinusoidal, incompressible flows with finite viscosity across a wide range of parameters in a linear regime. The natural progression is now to investigate the nonlinear evolution of HD and MHD systems. We begin by presenting the background state and nonlinear equations of Kolmogorov flow, showing the hydrodynamic branch of instability (Meshalkin and Sinai, 1961) in chapter 2. Next, we focus on an unstable mode, which occurs at a small value of viscosity and that is determined by the instability threshold in the hydrodynamic chapter (2), and then we present a magnetic field that will be explained in the next chapters. We review the linear numerical results that we obtained compared with nonlinear evolution over time. The purpose of this chapter is to provide an overview of the dynamics in the purely hydrodynamic system with time evolution. Finally, we conclude with a short discussion of the potential relevance of our results for hydrodynamic systems.

6.2 Non-linear simulation: implementation & testing

6.2.1 Hydrodynamic evolution:

We start with a brief discussion of the nonlinear hydrodynamic system of Kolmogorov flow. Our numerical solution for the hydrodynamic case is performed on partial differential equations, which are defined in terms of the vorticity and stream function, we set $\boldsymbol{B} = \boldsymbol{0}$ in the governing equation (6.1) representing the hydrodynamic system. Firstly, we solve the nonlinear equations using the Dedalus programming language (Burns et al., 2020). Then we examine whether the critical value of the inverse Reynolds number in the linear phase affects the development or decay determined by the growth rate. Once the instability has been initiated, the non-linear phase of the instability determines how the system will evolve. These processes are usually observed in astrophysical observations as discussed in Hillier and Polito (2018) and Klaassen and Peltier (1985) for the evolution of Kelvin–Helmholtz instability.

6.2.2 Mathematical formulation and numerical methods

We consider the hydrodynamic case with $B_0 = 0$; we also consider $L = 2\pi/k$ as the flow scale in the y-direction. Our investigation of the nonlinear evolution is carried out numerically using the Dedalus framework to solve the two-dimensional incompressible HD equations by time-stepping as follows:

$$\partial_t \omega + \mathcal{J}(\omega, \psi) = \nu \nabla^2 \omega + g, \tag{6.1a}$$

$$\omega = -(\frac{\partial^2}{\partial x^2} + \frac{\partial^2}{\partial y^2})\psi = -\nabla^2 \psi \tag{6.1b}$$

where ψ is the stream function and ω is the vorticity; g is the forcing; ν is dimensionless viscosity. All the fields are functions of (x, y, t). The basic state of the flow takes the form :

$$\boldsymbol{u_0} = (0, \sin x), \qquad \Psi_0 = \cos x, \qquad \omega_0 = \cos x, \qquad g = \nu \cos x. \tag{6.2}$$

The divergence-free conditions are automatically satisfied, $\nabla \cdot \boldsymbol{u} = 0$, and the set of equations (6.1) leads to:

$$\partial_t \omega + \underbrace{\partial_x \omega . \partial_y \Psi - \partial_y \omega . \partial_x \Psi}_{\mathcal{J}(\omega,\Psi)} = \nu \nabla^2 \omega + g. \tag{6.3}$$

To solve equation (6.3) in Dedalus we must separate the linear terms in LHS & the nonlinear terms in RHS, as described in Burns et al. (2020), we obtain:

$$\partial_t \omega - \nu(\partial_x^2 \omega + \partial_y^2 \omega) - g = \mathcal{J}(\psi, \omega). \tag{6.4}$$

We can calculate the kinetic energy (E_k), and the enstrophy (Ω), followed by the perturbation kinetic energy (PE_k), and the perturbation enstrophy (Ω_p). The non-linear terms transfer energy between the velocity components and do not affect the total energy in any way. From this point, we use the perturbation energy in our simulation to better understand the non-linear evolution. We acknowledge that the system is stable if the perturbation quantities decay and tend to zero as time tends to infinity. While, if the perturbation quantities are growing, we can say that the system is unstable.

The stream function & vorticity field of the eigenmodes can be used to estimate their kinetic energy (E_k) & enstrophy (Ω); the kinetic energy can be described as the integral of the square of the velocity as :

$$E_k = \frac{1}{2} \int \int (u^2 + v^2)\, dxdy \qquad = \frac{1}{2} \int \int (\Psi_y^2 + \Psi_x^2)\, dxdy \tag{6.5}$$

The enstrophy corresponds to the vorticity squared, which is

$$\Omega = \frac{1}{2} \int \int \omega^2 dxdy, \qquad \omega_0 = \cos x \tag{6.6}$$

We can obtain the perturbation energy equations by subtracting the basic state of

the flow from the total energy

$$\boldsymbol{u}_{perturbation} = \boldsymbol{u} - \boldsymbol{u_0}, \qquad \boldsymbol{u_0} = (0, \sin x), \quad \boldsymbol{u} = (u, v), \quad \boldsymbol{u_0} = (0, v_0) \tag{6.7}$$

Perturbation kinetic energy (PE_k) is defined by:

$$PE_k = \frac{1}{2}\int\int (u^2 + (v - v_0)^2)\, dxdy \qquad = \frac{1}{2}\int\int (\Psi_y^2 + (-\Psi_x - \sin x)^2)\, dxdy \tag{6.8}$$

Perturbation Enstrophy (Ω_p) is defined by:

$$\Omega_p = \frac{1}{2}\int\int (\omega - \omega_0)^2 dxdy = \frac{1}{2}\int\int (\omega - \cos x)^2 dxdy, \tag{6.9}$$

where $\boldsymbol{u_0}, \omega_0$ are the basic state for velocity and vorticity fields and $\omega - \omega_0$ is the perturbation vorticity.

6.3 Outline approach of Dedalus implementation

Dedalus is a flexible framework for solving partial differential equations with a pseudo-spectral code, including generalized eigenvalue problems. This code was further developed, optimised and used by other authors, see, for example, Fraser, Cresswell and Garaud (2022); Vasil (2015). The eigenvalue problem is solved by spectrally discretizing the spatial domain and evolving the coefficients as coupled ordinary differential equations. Runge-Kutta methods are utilized for implicit time-stepping of linear terms and explicit time-stepping of nonlinear terms. Nonlinear equations (6.1) can be entered in plain text in Dedalus. The arbitrary boundary conditions and initial conditions are also entered in plain text. Further explanation can be found in Burns et al. (2020).

The linear equations are transformed into finite-dimensional matrices and vectors, with entries given by their Fourier series expansion coefficients. Since Dedalus only solves formally first-order differential equations, the fields relevant to the present

system, for example, include not just ω and ψ, but also their derivatives in x and y. To input the equation into Dedalus, we define the domain size as

$$0 < x < 2\pi, \qquad 0 < y < 2L_y\pi, \tag{6.10}$$

The perturbation depends on y-direction as e^{iky}. From this point, we take $L_y = 2$ at present, which means the k values take the form $k = \frac{n}{L_y}$, where $n = 1, 2, 3, ...$ Our results in the linear regime show instability at large-scale flow particularly at $k = 0.5$ which corresponds to $L_y = 2$. From this point, we simulate $L_y = 2$ in all non-linear simulations in this thesis.

6.3.1 Code structure

Dedalus framework reflects the mathematical objects that are encountered when posing and solving a PDE system. Here we solve a vorticity stream function formulation (6.1). We begin by specifying the spatial domain achieved by creating a Basis and domain, we discretize each dimension over a specified interval and form a Domain object as the direct product of these bases, as we have a periodic function in sin and cos. Hence, we construct a 2D periodic domain, in x and y, as the direct product of two Fourier bases, we set nx and ny for the resolution as shown in Dedalus code in figure 6.1:

```
# Bases: names, modes, intervals
x_basis = de.Fourier('x', nx, interval=(0, 2*np.pi))
y_basis = de.Fourier('y', ny, interval=(0, 2*np.pi*Ly))
domain  = de.Domain([x_basis, y_basis], grid_dtype='float')
```

Figure 6.1: Domain and bases type

Next, we implement the equations within this domain. Dedeuls cannot work directly with the second-order derivatives, so we set them in the form (e.g. ψ_y is the first derivative of ψ, but $d_y(\psi_y)$ is the second derivative of ψ). This is done by creating a Problem object, a user-defined initial value problem,(IVP) scheme. We select the time-stepping method to integrate the nonlinear equations, where the Runge Kutta integration is available in this scheme. The equations (6.1) are then added to the

problem. The last equation in the problem shown in Dedalus codes (6.2) is expressed mathematically by $\partial_t g = 0$, where the forcing $g = \nu \cos x$ is time-independent.

```
# Problem: domain and variables
problem = de.IVP(domain, variables=['om','omx','omy','psi','psix','psiy','go','psixx','psiyy'])
#parameter
problem.parameters['nu'] = nu
#Vorticity equation
problem.add_equation("dt(om) - nu*dx(omx)-nu*dy(omy) - go =-omx*psiy+omy*psix")
problem.add_equation("om+dx(psix)+dy(psiy)+1e-6*psi=0")
#First-order reduction
problem.add_equation("omx - dx(om) = 0")
problem.add_equation("omy - dy(om) = 0")
problem.add_equation("psix - dx(psi) = 0")
problem.add_equation("psiy - dy(psi) = 0")
problem.add_equation("psiyy - dy(psiy) = 0")
problem.add_equation("psixx - dx(psix) = 0")
problem.add_equation("dt(go)= 0")
```

Figure 6.2: Governing equations apply as Problems set in Dedaus framework

The temporal integration method (RK443) is determined by implementing the solver state as shown in Dedalus code 6.3, which determines the following three criteria: we terminate the simulation time by the `solver.stop − sim − timeattribute`, then we use the `solver.stop − wall − timeattribute` to terminate simulations before hard time limits, which allows for clean termination and possible post-processing before the job is automatically terminated, we set the iteration count to infinity by the `solver.stop − iterationattribute`. Then we use the initial value solver class to determine the initial values of the variables. The initial variables of the vorticity field ω and stream function ψ can be easily accessed from the solver state by transforming to the grid space ('g') in x and y.

```
# Build solver
solver = problem.build_solver('RK443')
logger.info('Solver built')

# Set integration limits
solver.stop_sim_time = final_time
solver.stop_wall_time = np.inf
solver.stop_iteration = np.inf
```

```
# Set fields and local grid
x   = domain.grid(0)
y   = domain.grid(1)
om  = solver.state['om']
psi=solver.state['psi']
omx = solver.state['omx']
omy = solver.state['omy']
go  = solver.state['go']
psix = solver.state['psix']
psiy = solver.state['psiy']
psixx = solver.state['psixx']
psiyy= solver.state['psiyy']
```

Figure 6.3: Integration solving an initial value problem.

As a final step, we create the main loop directly with an integer number of iterations associated with the final simulation time and time step, which allows arbitrary data interactions as the integration takes place. We first write the perturbation and total energy of the flow and write the basic state of vorticity and stream function as shown in Dedalus code 6.4. Then, we calculate the energy quantities over the domain size using the numerical grid spacing which is expressed numerically by the form $(dx, dy) = (2\pi/n_x, 2\pi L_y/n_y)$ where $L_y = 2$ corresponds to the wavenumber $L_y = 1/k = 0.5$, we call this "darea" in Dedalus as its the area of differential elements. Here (n_x, n_y) are numerical grid sizes. For example:

$$E_k = \frac{1}{2}\int\int[(\psi_x)^2 + (\psi_y)^2]dxdy, \tag{6.11}$$

where the integral $\int$ is refers to numerical summation by the Dedalus command $[sum(sum)]$ as seen in equation (6.12)

$$E_k = \frac{1}{2}\sum\sum[(\psi_x)^2 + (\psi_y)^2]dxdy. \tag{6.12}$$

In this method, we specify the timestep 'dt', then calls the specified integration routine to update the system.

```
# Setup storage
om.set_scales(1)
om_list = [np.copy(om['g'])]
t_list = [solver.sim_time]
#Basic state
u0y=np.sin(x)
om0=np.cos(x)
darea = (2*np.pi / nx) * (2*np.pi*Ly / ny)
#Kinetic energy equation
KE_list = [sum(sum(np.square(psix['g'])+np.square(psiy['g'])))*darea*0.5]
PKE_list = [sum(sum( np.square(psiy['g'])+ np.square(-psix['g']-u0y) ))*darea*0.5]
#Enstrophy equation
enstrophy_list = [sum(sum(np.square(om['g'])))*darea]
Penstrophy_list = [sum(sum(np.square(om['g']-om0)))*darea]
```

```
dt =0.01
#Main loop checking stopping criteria
while solver.ok:
    #set forward
    solver.step(dt)
    if solver.iteration % 5== 0:
        om.set_scales(1)
        om_list.append(np.copy(om['g']))
        t_list.append(solver.sim_time)
        #Perform some analysis
        print(solver.sim_time)
        KE_list.append(sum(sum(np.square(psix['g'])+np.square(psiy['g'])))*darea*0.5)
        PKE_list.append(sum(sum( np.square(psiy['g']) + np.square(-psix['g']-u0y) ))*darea*0.5)
        enstrophy_list.append(sum(sum(np.square(om['g'])))*darea)
        Penstrophy_list.append(sum(sum(np.square(om['g']-om0)))*darea)
    if solver.iteration % 5 == 0:
        print('Completed iteration {}'.format(solver.iteration))
```

Figure 6.4: Main loop of time

The initial conditions are set up for stream function ψ and the force g which is expressed by Dedalus numerically by "go" as shown in Dedalus code in figure 6.5 with a small appropriate perturbation value. Our initial perturbations are small enough to allow linear growth before nonlinear interactions become significant.

```
# Set initial conditions
x,y=domain.grids(scales=1)
om.set_scales(1)
go.set_scales(1)
psi['g'] = np.cos(x)+0.0*np.cos(y/Ly)+0.1*(0.1*np.sin(y/Ly)+0.5*np.cos(y/Ly))
go['g']  = nu*np.cos(x)
psi.differentiate('x', out=psix);
psi.differentiate('y', out=psiy);
psix.differentiate('x',out=psixx);
psiy.differentiate('y',out=psiyy);
om['g']=-psixx['g']-psiyy['g'];
om.differentiate('x', out=omx);
om.differentiate('y', out=omy);
```

Figure 6.5: Initial conditions of perturbation, where $L_y = 2$

.

6.3.2 Numerical methods: computation of linear results using time integration

We expand our previous results in the hydrodynamic linear theory chapter 2 by performing numerical simulations over time. We select a typical viscosity value that allows instability to occur. The concept of reducing the value of ν to determine the most unstable mode is very critical to understand as it indicates what Fourier mode will grow in a system most rapidly. For this investigation, we focus on zero magnetic fields $B_0 = 0$, where we use linear growth rates and eigenfunctions are only small perturbations. We then consider several values of ν ranging from $0.01 < \nu < 0.5$.

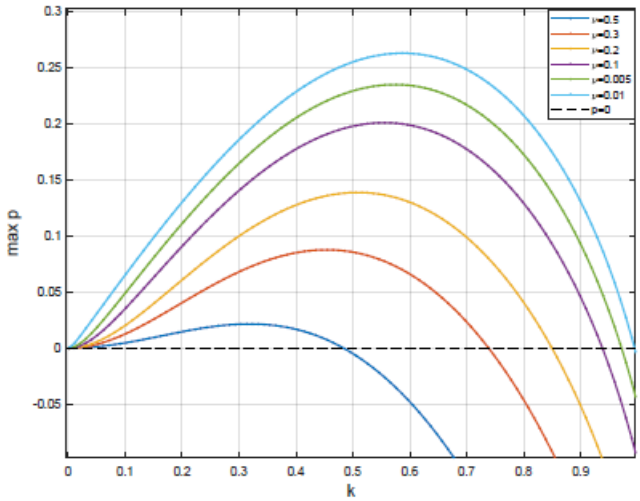

Figure 6.6: Instability growth rate $\mathrm{Re}\, p_{\max}$ at different wavenumbers k shown for a range of ν, $B_0 = 0$. This figure is similar to figure 2.1 with a reduction of viscosity values.

Our findings in chapter 2 show that the most unstable mode occurs at $k < 1$ and $\nu < 0.7$ as shown in figure 2.1. It is possible to determine at which wavenumber k exhibits the largest growth rate, and the $\mathrm{Re}\, p_{\max}$ must be greater than 0. Figure 6.6 shows the region of instability for $\nu = 0.2$ (yellow curve) above the black dashed lines $\mathrm{Re}\, p = 0$. The maximum growth rate occurs at $k = 0.5$. However, for $\nu = 0.5$ (dark blue curve) located below the black dashed lines $\mathrm{Re}\, p = 0$, wavenumber $k = 0.5$ is now stable (though there is instability for smaller k.

We have performed numerical simulations by considering a domain that is periodic in x and y with length $L_y = 2\pi/k$ in y, which supports one of the wavelengths of

the instability with wavenumber k. These techniques allow us to find growing modes at large scales. These simulations use a value of $\nu = 0.2$ and length scale $L_y = 2$, the vertical scaling of the eigenfunction is $1/k$.

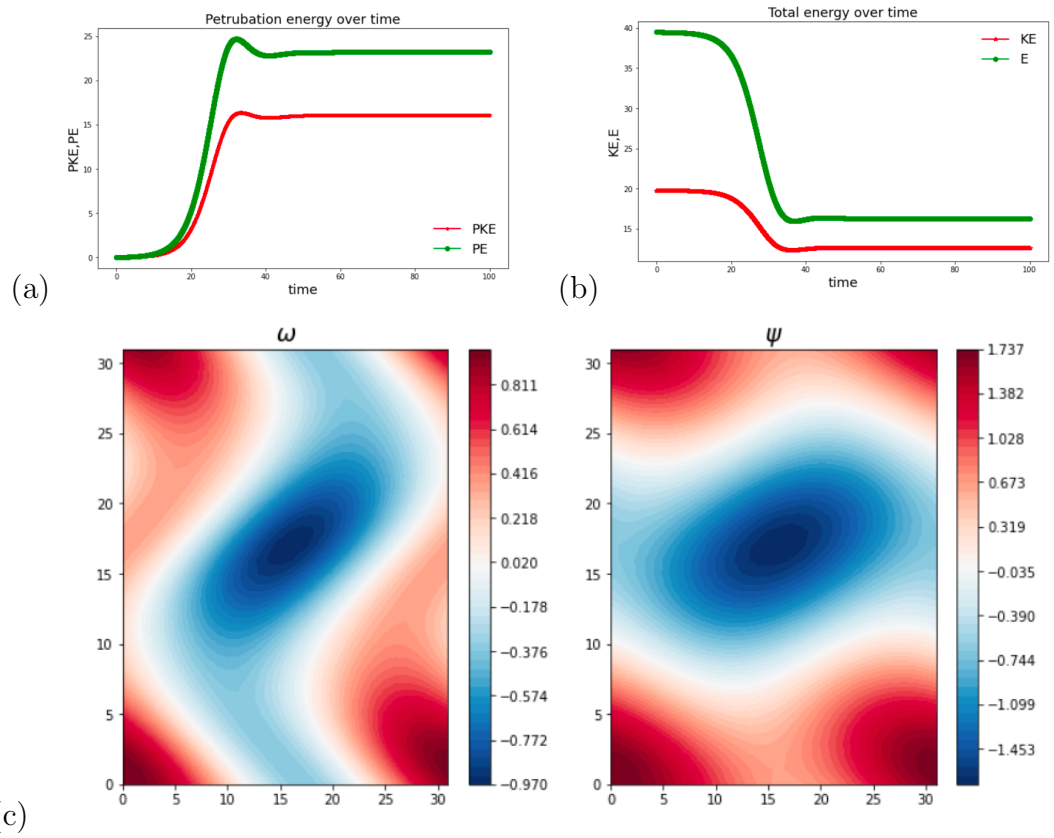

Figure 6.7: HD simulation over time for $\nu = 0.2$ run up at $t = 100$ (red curve = E_k green curve = Ω_p), (a),(b) perturbation and total energy, (c) full vorticity field ω and streamlines of flow Ψ. Note that enstrophy E, PE in panels (a,b) is Ω, Ω_p in the text .

We show first in figure 6.7 a time series of the domain integrated perturbation and total energy. We show the total energy of flow & enstrophy (E_k, Ω) in panel (b) from equations (6.5), and perturbation energy of flows & enstrophy (PE_k, Ω_p) in panel (a) from equation (6.8). We see that the perturbation energy in panel (a) is growing initially from $t = 0$ to $t = 40$, and then the energy saturates at the final time $t = 100$. In panel (b), the total energy decays initially from $E_k = 20$ to $E_k = 15$ at $t = 20$ and $\Omega_p = 40$ to $\Omega_p = 20$ at $t = 40$, then kinetic energy has a steady state at the final time $t = 100$. Panel (c) shows plots of ψ & ω run up to $t = 100$. We observed a large vortex formed in our periodic domain in the plot of ω. The streamlines ψ are physically arranged to exhibit a systematic flow similar to Roberts flow between $\psi = 1.737$ and $\psi = -1.453$ as described in Plunian and Rädler (2002).

6.4 Hydrodynamic simulations

In this section, we will verify the accuracy of our simulation by performing a convergence test prior to running and investigating the nonlinear evolution of hydrodynamic instability. We specify a time step of $dt = 0.01$. Thus, we did a convergence test by decreasing the time step to $dt = 0.005$ in order to obtain more accurate results. Figure 6.8 explores simulations with varying time steps.

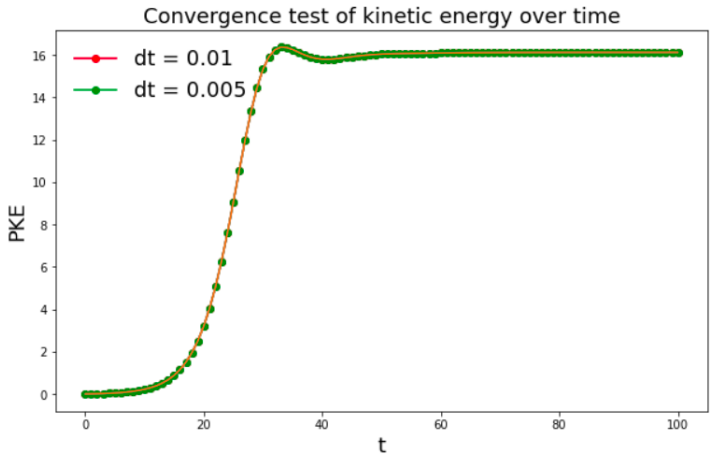

Figure 6.8: Convergence test of kinetic energy run up to $t = 100$ for $\nu = 0.2$ for resolution 50×50 and we vary the time step. $dt = 0.01$ is represented by the red curve and $dt = 0.005$ is represented by the green curve. The green curve completely overlaps the red one.

We found the same kinetic energy for different time steps as shown in figure 6.8, we can see clearly that a time step of $dt = 0.01$ (red curve) is a sufficiently small timestep because decreasing it further doesn't affect the kinetic energy. We observe both curves overlap in figure 6.8 which gives us confidence that our choice of time step leads to a well-resolved simulation. We also increased the resolution to 100×100, for which we observed the same energy behaviour and both curves overlapped as well.

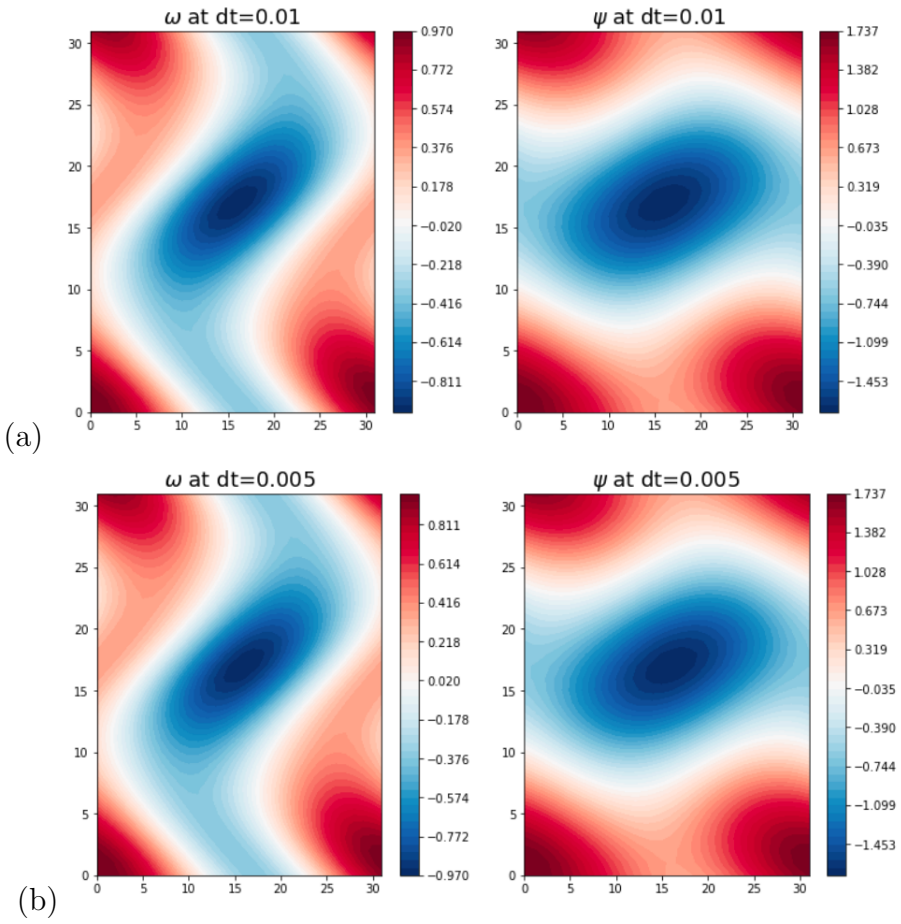

Figure 6.9: Vorticity field ω (left) & streamlines ψ (right) for $\nu = 0.2$ run up to $T = 100$ (a) run at $dt = 0.01$, (b) run at $dt = 0.005$. The domain is supposed to be $0 < x < 2\pi$, $0 < y < 4\pi$.

We can also be looking at the kinetic energy & enstrophy evolution corresponding to vorticity ω & stream function ψ of flow plots. For example, figure 6.7 shows a run at $dt = 0.01$. By reducing the time step and computing the variation between each time step, we obtain a small difference between the kinetic energy (5×10^{-3}), indicating our runs are accurate and well-resolved. We also verify our codes by reducing the final time and computing the variation between each time step, we obtain a small difference between the vorticity field and stream function (below 10^{-6}). Figure 6.9 shows a simulation of vorticity & stream function is run to $t = 100$ for $\nu = 0.2$ and different time steps. Panel (a) shows a simulation run at $dt = 0.01$, and panel (b) shows a simulation run at $dt = 0.005$. We can see clearly both panels have the same instability behaviour. As a result, whenever we reduce the timestep the simulations are well-converged. From this point, we run our simulations in this chapter at a fixed value of timestep $dt = 0.01$.

Throughout the simulation in this thesis, we encountered some errors from Dedalus. We received an error message stating that the factor is "exactly singular". It is possible to remove these errors in many ways. Suppose we have the vorticity function $\omega = -\nabla^2\Psi$, and we code this using:

```
problem.add_equation("om+dx(psix)+dy(psiy)=0")
```

As we perform the Fourier transform of the above, we should keep in mind that the ω_{mn} gives modes of

$$\omega = \sum e^{imx+iny}\,\omega_{mn}, \qquad \Psi = \sum e^{imx+iny}\,\Psi_{mn}. \tag{6.13}$$

Therefore, in a transformed routine, all the coefficients of wavenumbers satisfy

$$\omega = -\nabla^2\Psi, \qquad \omega_{mn} = (m^2+n^2)\Psi_{mn}, \qquad \Psi_{00} = \frac{\omega_{00}}{0} \tag{6.14}$$

Even though $\omega_{00} = 0$ (no mean vorticity), this dividing by zero in Dedalus and give an error message. In order to overcome this problem we set $\Psi_{00} = 0$. We can artificially set that value to zero as follows; we make a small change by replacing $\omega = -\nabla^2\Psi$ by $\omega = -\nabla^2\Psi + 10^{-6}\Psi$. Adding a constant to Ψ will result in almost the same flow $\boldsymbol{u} = (\Psi_y, -\Psi_x)$, which is expressed mathematically as

$$\omega_{mn} = (m^2+n^2+10^{-6})\Psi_{mn},$$

So that

$$\omega_{00} = 10^{-6}\Psi_{00}, \qquad \Psi_{00} = \frac{\omega_{00}}{10^{-6}} = \frac{0}{10^{-6}} = 0.$$

This minor change enables Dedalus to solve for Ψ, and it makes negligible difference to all modes (m,n) except $(m,n) = (0,0)$. Similarly, the pressure in the Navier-Stokes equation represents the isotropic part of the stress tensor. It is determined up to an arbitrary constant value. For an incompressible fluid that is, adding an arbitrary constant to the pressure $(p \to p + p_0)$ at all locations throughout the flow field still

enables it to satisfy the NS equation.

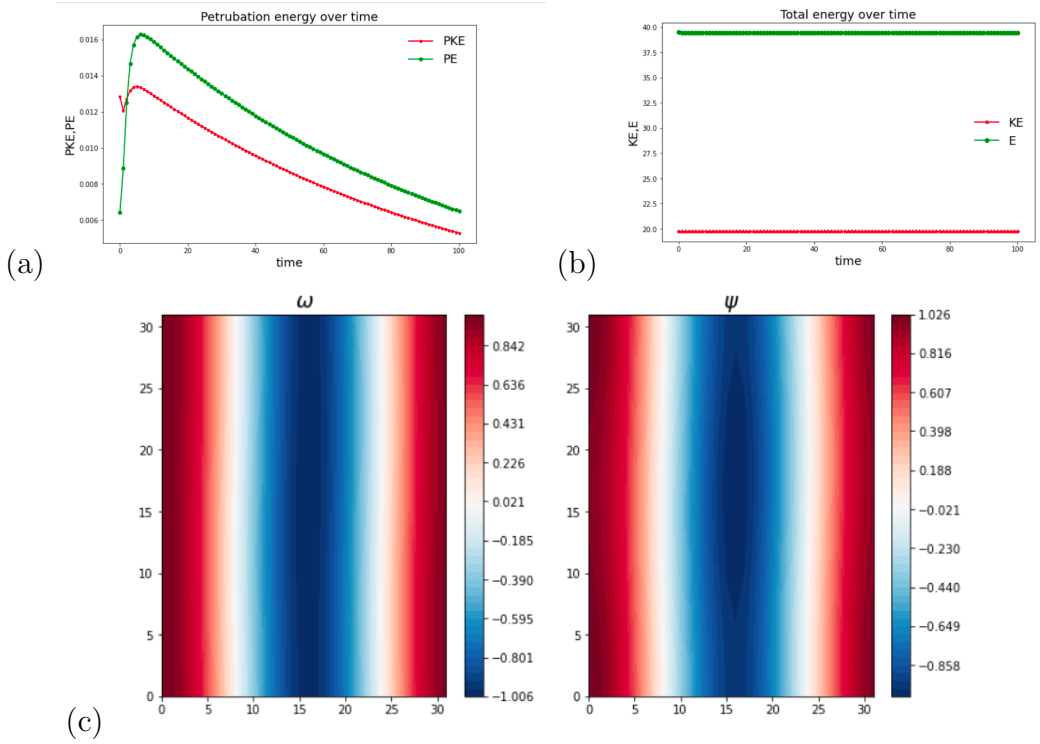

Figure 6.10: HD simulation over time for $\nu = 0.5$ run up at $T = 100$ (red curve = E_k green curve = Ω_p), (a),(b) perturbation and total energy & enstrophy, (c),(d) full vorticity field ω and streamlines of the flow Ψ. Note that enstrophy E, PE in panels (a,b) is Ω, Ω_p in the text.

Figure 6.10 shows a simulation run up to $t = 100$ for $\nu = 0.5$, corresponding to the dark blue curve in figure 6.6. which implies a decay mode located below the black dashed line $\mathrm{Re}\, p = 0$. Panels (a),(b) show the computation of energy over time; we can see clearly that the perturbation energy decays between $t = 20$ to $t = 100$ and loss of about 15 % in panel (a), comparable with perturbation energy in figure 6.7(a). This indicates that the Reynolds number significantly affects of the dynamics. These energy losses are shown in qualitative results of full vorticity & stream function in both panels (c),(d), which show the basic state after the perturbation has died away. A test run at a higher resolution indicates that this energy loss is due to the choice of viscosity ν and not from the runs being under-resolved.

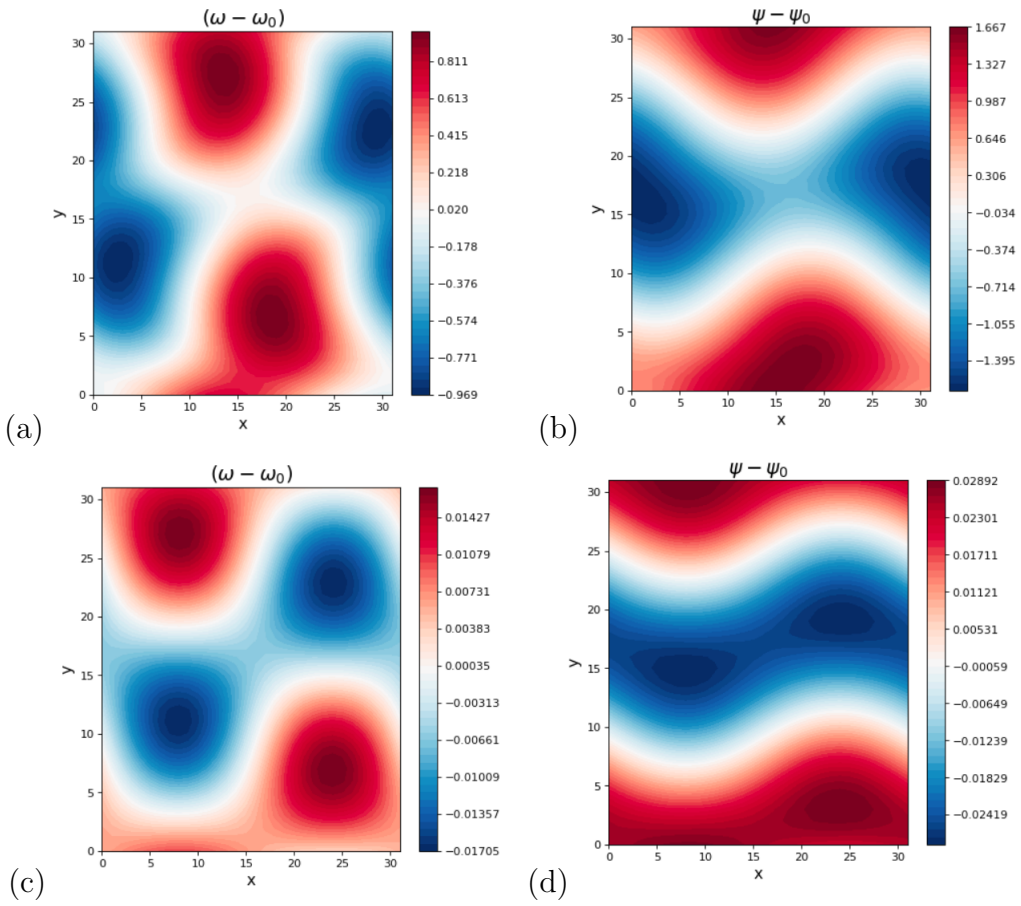

Figure 6.11: Snapshots of the perturbation flow, vorticity field $\omega - \omega_0$ and stream function $\psi - \psi_0$ from equations (6.8-6.9) run up to $t = 100$, where (a),(b) show $\nu = 0.2$, (c),(d) show $\nu = 0.5$, the left panels shows the vorticity field and the right panels shows the streamlines of the flow.

The simulation in figure 6.11 shows the perturbation flow pattern with positive & negative vortices formed at $t = 100$; we have one wavelength $L_y = 2$ of our domain. Panels (a,b) show the unstable mode at $\nu = 0.2$ (see figure 6.7), the velocity changes dramatically, which ultimately results in the disruptions of the vortices which may emerge in different forms by increasing simulation time . Panels (c,d) shows a stable situation at $\nu = 0.5$, (see figure 6.10), the perturbation energy of the flow is dying away, and energy is extracted due to the viscous forces; this phenomenon happens as a consequence of increasing the value of viscosity $\nu = 0.5$. If we look at panels (a,b) in figure 6.11 and combine them with the basic state of flow in figure 6.10 (c,d) we obtain the fields of figure 6.7 (c,d).

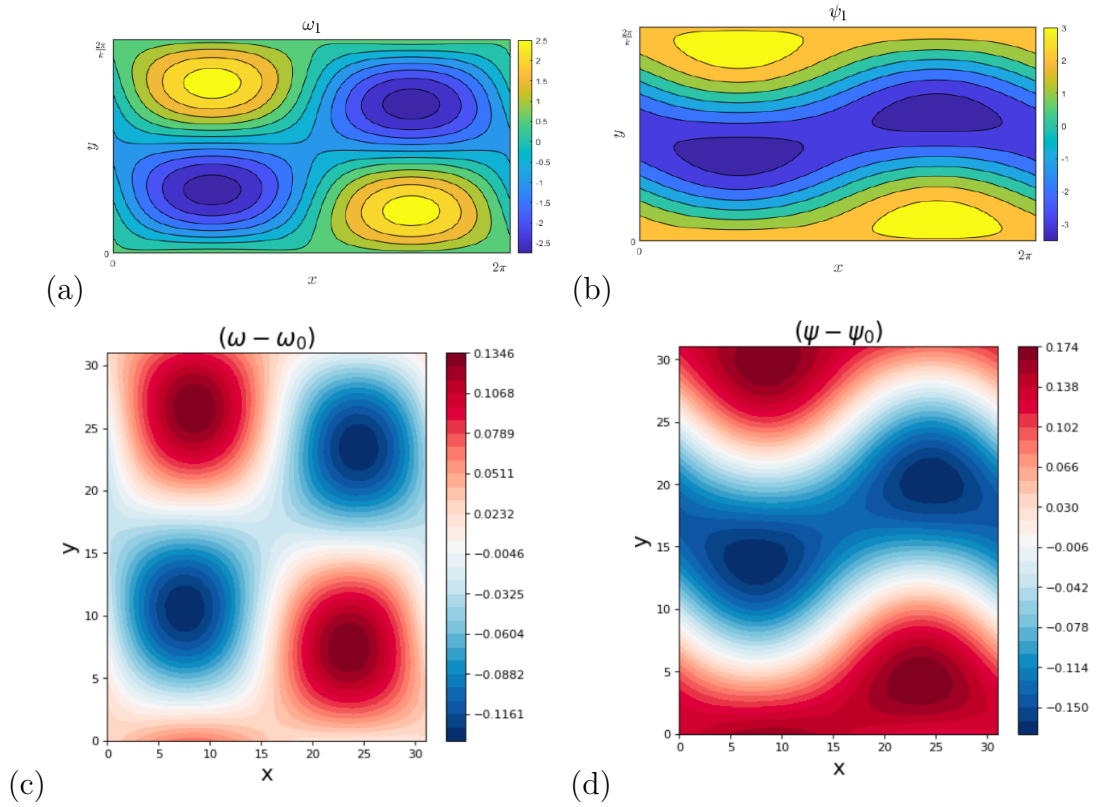

Figure 6.12: Perturbation of both vorticity field (right) and stream function (left) for $\nu = 0.2$. Panels (a,b) show linear regime for $k = 0.5$, and panels (c, d) show nonlinear simulation for $L_y = 2$ run up to $t = 10$.

Figure 6.12 shows snapshots of comparison between the linear result and the nonlinear simulation. We run the simulation at the resolution $(N_x, N_y) = (32, 32)$, as well as $\nu = 0.2$. There is an unstable wavenumber $k = 0.5$ associated with the linear Fourier mode in panels (a,b). Thus, we initiate the Fourier mode during the simulation by setting the domain size as $L_y = 2$ in panels (c,d). To make a good comparison, we consider the perturbation vorticity & stream function from the linear calculation as shown in chapter 2 in panels (a, b) and compare with simulation 6.11 (a,b) by reduce the simulation time from $t = 100$ to $t = 10$ in figure 6.12 (c,d).

Our simulation indicates that the vorticity and stream functions in panels (c,d) are similar to the instability pattern in linear panels (a, b), where the vorticity eigenfunction is derived from linear theory. Initially, only ω needs to be specified, since the first timestep involves an inversion that determines the corresponding stream function ψ. Panels (c,d) show the vortices at an early time $t = 10$ in the plot of ω in panel (c), and zonostrophic instability is growing linearly as shown in the plot

of ψ in panel (d). The small values in the colour bar indicate small perturbations. The similarity between these panels gives us confidence that the linear phase is long enough for the perturbations to adjust to the optimal configuration, despite not using the exact eigenfunction at the beginning of the simulation.

6.5 Hydrodynamic evolution with $\ell \neq 0$

In chapter 2, we investigated linear instability for wavenumbers (k, ℓ), where ℓ is the Floquet wave number in the x direction. We have conducted nonlinear simulations where the domain is large enough to support two vortices at $L_y = 2$. We observed that the periodic vortices form at $t = 10$ where the instability starts to saturate at $t = 30$. We also need to run simulations at double wavelengths and look for nonlinear evolution with additional wavelengths in the x direction. Our domain is also capable of supporting a mode corresponding to $\ell = 0.5$. We run the simulation at a resolution of $N^2 = 50$, and the same viscosity value $\nu = 0.2$ as shown in figure 6.6.

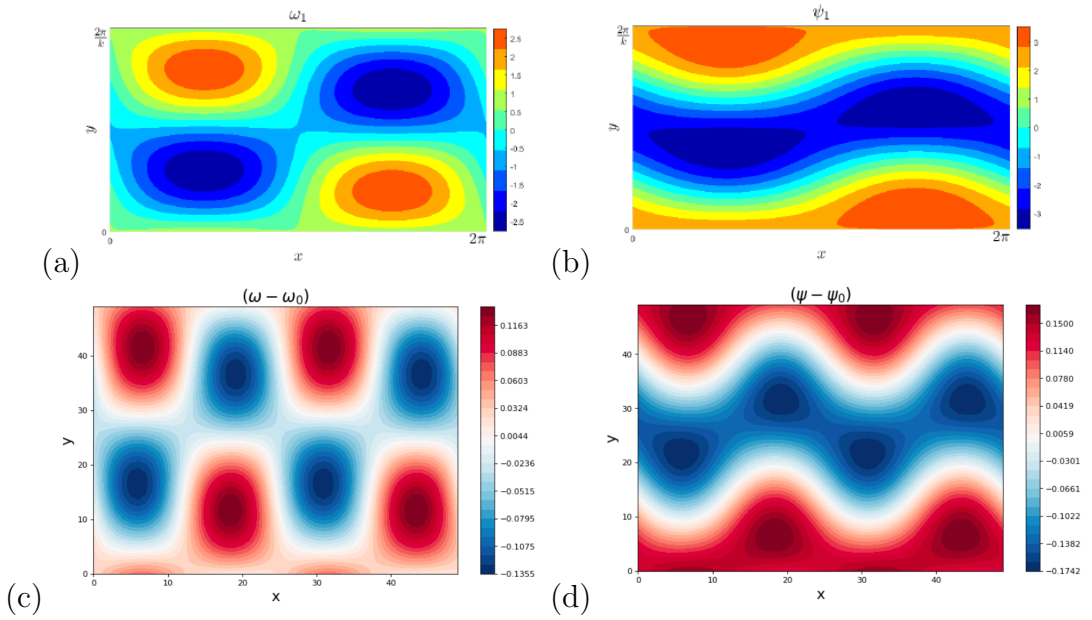

Figure 6.13: Perturbation of both vorticity field (right) and streamlines (left) at $\nu = 0.2$. Panels (a,b) show linear phase at $k = 0.5, \ell = 0$, and panels (c,d) show nonlinear simulation at $(k, \ell) = (0.5, 0.5)$, $(L_x, L_y) = (2, 2)$, run up to $t = 10$.

We can now compare the linear & non-linear results. Panels (a,b) show a linear system run for $\ell = 0, k = 0.5$ where the most unstable mode occurs at $\ell = 0$, panels

(c,d) show the non-linear simulation at $(L_y, L_x) = (2, 2)$, to make a good comparison between both figures we run the simulation at $t = 10$. We observed that there is the symmetry of perturbation vorticity between panels (a,c), where (a) has two positive & negative vortices at $L_y = 2, L_x = 1$, at $\ell = 0$, but (c) shows four positive & negative vortices at $\ell = 0.5, L_x = 2$. The perfect symmetry between the left and right sides of (c) implies that this is an $\ell = 0$ mode. Panels (b,d) show symmetry between the streamlines of flow ψ in both linear & nonlinear results; where the flow lines bend due to underlying Kolmogorov flow and generate small vortices with different signs.

We have used Floquet wavenumber ℓ to gain a better understanding of the instability's behaviour and allow nonlinear dynamics to occur at large scales in both x and y and allow further Fourier modes in the system. Moreover, if we initialize instability with non-zero amplitudes and larger time simulations, the vortices can merge, leading to an energy cascade. The next section will provide more details.

6.6 Energy considerations at large-scale

The concept of energy cascade is usually described in two dimensions in terms of "eddies", although recent attempts have been made to better define the concept by utilizing wavelets. Fundamentally, an eddy is a region in a fluid that behaves coherently (Frisch, 1995). In Fourier space, an inverse cascade is observed with the dominant excited wavenumber shifting to smaller and smaller wavenumbers. While in real space, the energy is transferred. In 2D Kolmogorov flow, we always have an inverse cascade. Energy likes to gather at a large scale during the dynamics of two-dimensional instability at late times, leading to an inverse cascade,(Legras, Villone and Frisch, 1999). Here, we present a schematic 6.14 to describe the inverse energy cascade process. We investigate the inverse energy cascade in a finite large box in x and y.

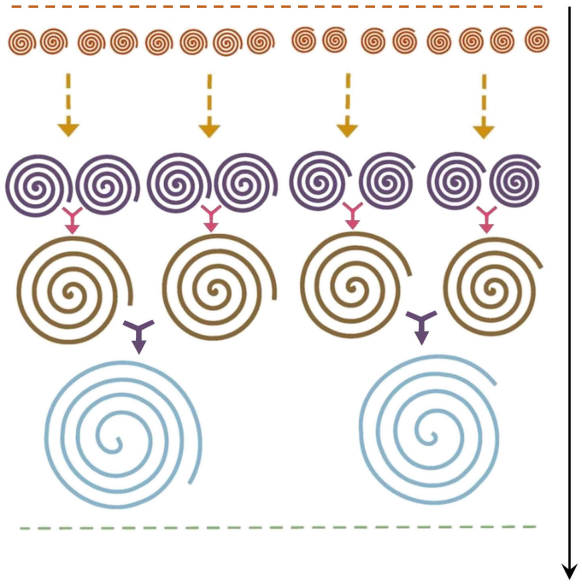

Figure 6.14: Energy cascade in Kolmogorov flow. The energy transfers from small eddies to large eddies.

We take a sample of Kolmogorov flow and calculate the total energy and perturbation energy. Figure 6.14 shows eddies going from small to large, the largest eddies have the most energy and the smallest eddies have very little energy in comparison and this is referred to as an energy cascade. Kolmogorov divided energy cascades into three regions, the production of eddy transfers energy from small scale to large scale and then we have a dissipation phase. Furthermore, each of these three areas has a very different behaviour, in the production phase, the behaviour of instability depends only on the kinetic energy and the dissipation rate, in the transfer phase only depends on the size of the eddy and again the dissipation rate and in the dissipation phase it depends on the viscosity of the flow and again the dissipation rate.

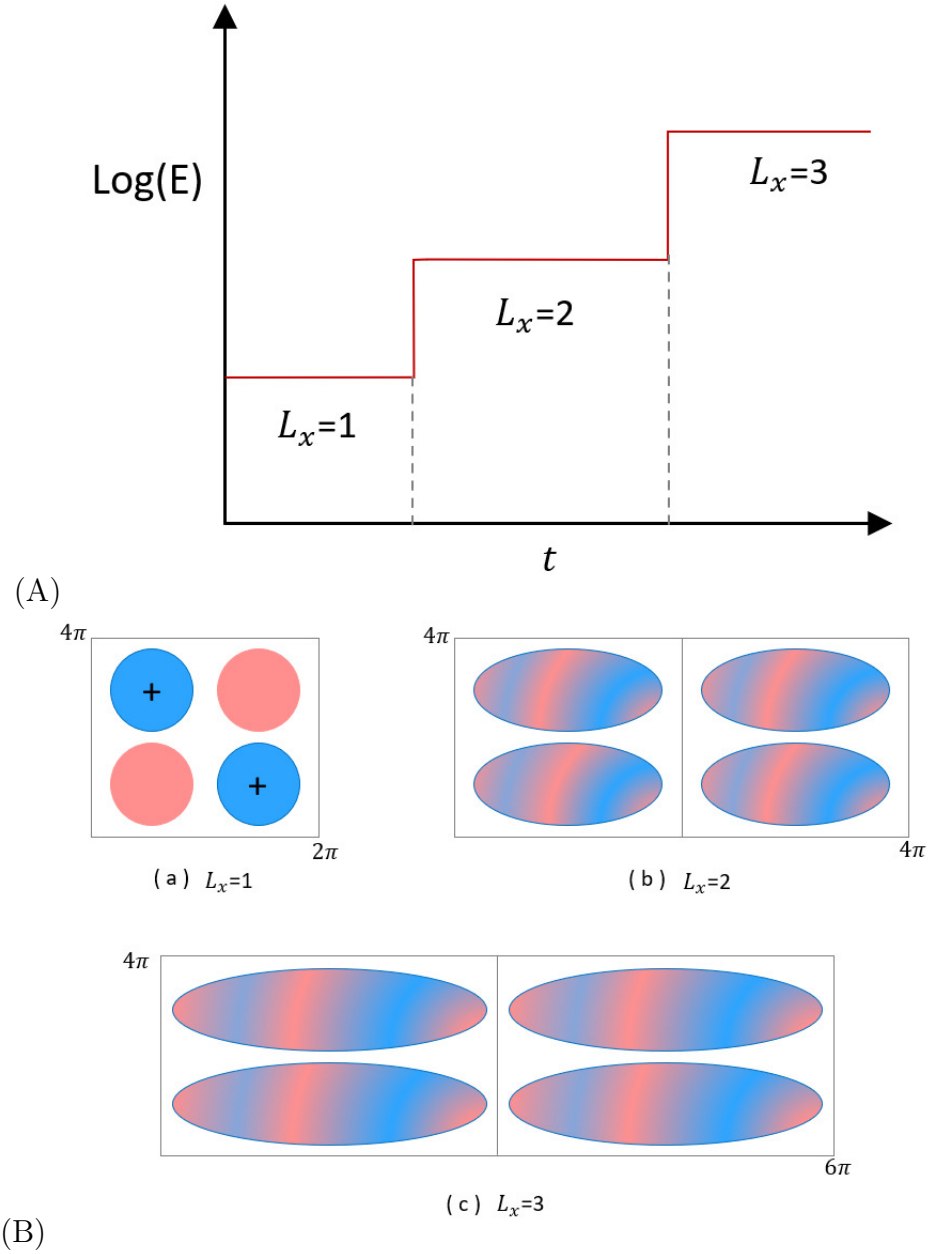

Figure 6.15: The instability energy cascade is depicted schematically in the following diagram. (A) Energy cascade process by fixing the wavelength in y-direction $L_y = 2$ and increasing the wavelength in x-direction. (B) eddies at large scale domain illustrates that the eddies of $L_x = 1$ in panel (a), eddies of $L_x = 2$ in panel (b) and eddies of $L_x = 3$ in panel (c). These eddies merge with increasing the simulation time to show the energy cascade process at a large scale of instability.

We plot the energy cascade as a log scale as shown in figure 6.15 (A) and then instead of small to large eddies in figure 6.14. We change the wavelength to increase the box size in the x-direction $L_x = 1/\ell$ where $\ell = 1/2, 1/3, ...$ Note that in simulation the box size $L_x \times L_y$ is fixed & only ℓ changes. In comparison with figure 6.15 (B). we can see clearly at $L_y = 2$, the box size is double in y-direction. We have two vortices with different signs marked by different colours as shown in panel (a), the blue is

positive and the red is negative and this is the initial case at $t = 0$. Panel (b) shows at $L_x = 2$, the vortices start to merge with $\ell = 1/2$ and the box size is doubled in x along with y-direction by $4\pi \times 4\pi$, and at $L_x = 3$ the box size increase further in x-direction and the domain becomes $6\pi \times 4\pi$ giving the large $\ell = 1/3$ structure as shown panel (c). We consider this process as the inverse energy cascade.

In this section, we are naturally interested in the kinetic energy of fluid flow and how it is transported between different length scales. An inverse cascade is a multi-step process that leads to larger scales. In this chapter, we will only explore one or two steps of this process.

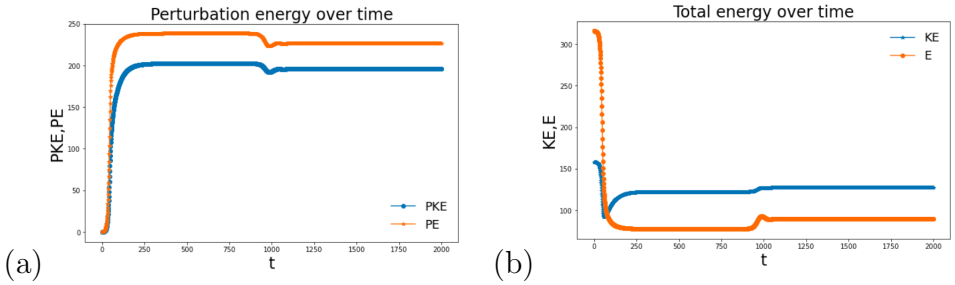

(a) (b)

Figure 6.16: Simulation of kinetic energy (blue) & enstrophy (orange) at $\nu = 0.2, (x, y) = (4\pi, 4\pi)$ run up to $t = 2000$. Panel (a) evolution of perturbation energy, panel (b) evolution of total energy. An inverse cascade is observed from $t = 1000$ to $t = 2000$. Note that enstrophy E, EP in panels (a,b) are Ω, Ω_p in the text.

We consider hydrodynamic simulation in a large domain $(x, y) = (4\pi, 4\pi)$ as shown in figure 6.16 with the same parameter values described in figure 6.7. The kinetic energy evolution is found at wavenumbers $k = 0.5, \ell = 0.5$ corresponding to wavelengths $L_y = 2, L_x = 2$. Panel (a) shows the kinetic energy & enstrophy growing initially between $t = 0$ to $t = 250$, then takes a quasi-static state from $t = 250$ to $t = 750$, and eventually evolves from $t = 1000$ to $t = 2000$ creating energy cascade. In panel (b) the kinetic energy dissipates initially from $E_k = 150$ to $E_k = 100$ between $t = 0$ to $t = 200$ then the system becomes a steady state resulting in the energy being constant from $t = 250$ to $t = 1000$. Then the energy evolves to create the inverse cascade as shown in figure 6.18

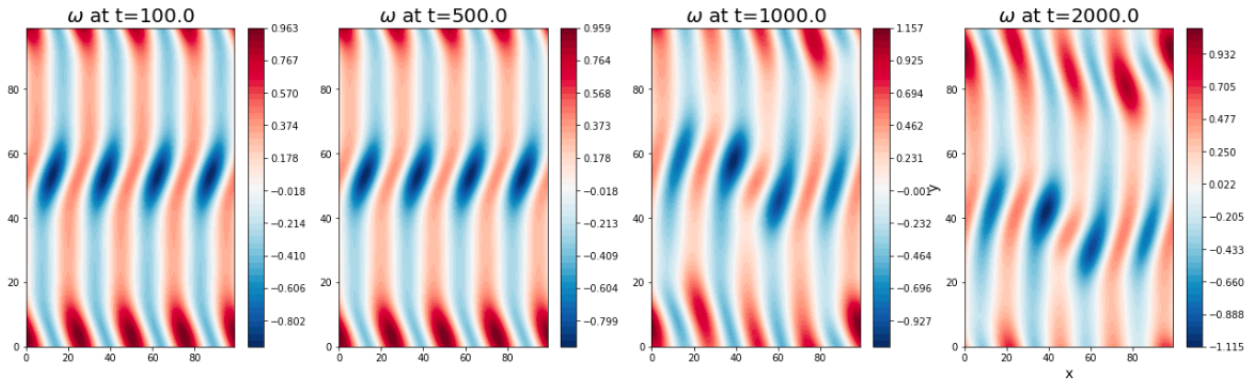

Figure 6.17: Vorticity field ω at $\nu = 0.2$, $(x, y) = (4\pi, 4\pi)$ run up to $t = 2000$, start and end up with small eddy interacting and continues along the four simulation times.

Figure 6.17, shows the vorticity field run up to $t = 2000$, this evolution begins and ends up forming smaller eddies located in the centre of flow lines. This behaviour was observed during the simulation time due to the differential in $\omega = -\nabla^2\psi$. This phenomenon also happens evidently for constant energy, referring to figure 6.16 panel (b) where the total energy goes to constant behaviour between $t = 250$ to $t = 750$. Eventually, there is a balance between sources and sinks.

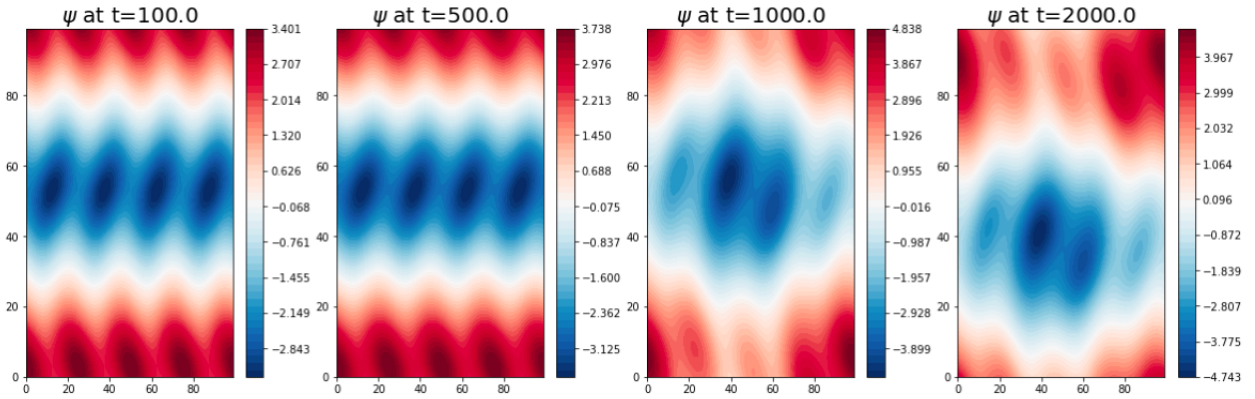

Figure 6.18: Inverse cascade of stream function ψ at $\nu = 0.2, (x, y) = (4\pi, 4\pi)$ run up to $t = 2000$, start with small eddy, a large eddy made from many interacting smaller eddies at a later time $t = 2000$.

By looking at figure 6.18, we show the kinetic energy cascade occurring at viscosity $\nu = 0.2$ and large domain size $(x, y) = (4\pi, 4\pi)$. The kinetic energy is prominent in figure 6.16 panel(b) between $t = 250$ to $t = 750$, The small eddies are limited by the viscous effect at the smallest length scale in $t = 100, t = 500$ as shown in figure 6.18. The energy cascade transfer proceeds from small to large scales as shown at $t = 2000$.However, the emergence of this inverse cascade is slow, since the initial

state is 2π periodic, the emergence of the $\ell = 0.5$ mode is delayed

6.7 Conclusion

Nonlinear numerical simulations of a two-dimensional HD system have shown different types of flow behavior. The following are some of our findings:

- The Dedalus framework has been implemented for HD equations, including nonlinear terms. We have run the simulation with different inverse Reynolds numbers estimated from the hydrodynamic linear chapter 2.
- The large-scale HD zonostrophic instability leads to the growth of zonal jets see figure 2.2. Thus, the linear results can be confirmed through numerical simulation, which we set out in this chapter (see figure 6.12).
- We have confirmed the similarity between our linear and non-linear simulations at large domain size, with double wavelengths L_x, L_y in section 6.5. These symmetries can also exist on a single wavelength $L_y = 1/k$ for $\ell = 0$ in figure 6.12.
- In 2D Kolmogorov flow, kinetic energy inverse cascade is observed at large domain size as forming large-scale structures as seen in section 6.6.

In the next two chapters, we will investigate the magnetohydrodynamic extension of this current system. We consider the purely hydrodynamic simulation in this chapter as a basis for seeing what is the effect of the magnetic field, which will be studied in the next two chapters.

7. Nonlinear MHD evolution: vertical field

7.1 Introduction

We have investigated linearly stable and unstable modes with an initially uniform magnetic field aligned with the Kolmogorov flow. This chapter develops the investigation thereby analyzing 2D, nonlinear incompressible MHD simulations with finite resistivity and viscosity computed with the Dedalus framework, along with some linear calculations for comparison. The field strength and resistivity are varied to explore different regimes of magnetic activity, focusing more on the weak-field regime than the strong-field regime for its closer correspondence to the familiar hydrodynamic case. These instabilities are relevant to important astrophysical processes, for example, in the solar dynamo responsible for generating the magnetic field of the Sun.Tobias, Diamond and Hughes (2007) investigated a local 2D β-plane model and found that a weak toroidal magnetic field modified angular momentum transport in the lower tachocline. Three types of MHD can be considered in advance:

- MHD effects are "strong", so this case is linearly stable and a non-linear regime might also be stable (e.g., suppression of instability in case of vertical field or we can get tearing mode instabilities, *field branch* for horizontal field).
- MHD effects are 'weak', and the evolution is much like the hydrodynamic case but modified by the field.
- There are some different situations in which a fluid motion can grow with MHD feedback; this may be particularly relevant when there is a small Prandtl

number and a strong vertical magnetic field. Therefore, the non-linear evolution in this case needs a large domain with double wavelengths in (L_x, L_y). More details will be in the numerical simulation section (7.3.3).

7.1.1 Mathematical formulation:

Numerical simulations are conducted by solving the nonlinear equations numerically using the Dedalus framework, and details regarding this system are given for the pure hydrodynamics in chapter (6). We do not intend to repeat them in the present section. Instability evolution is expected to be affected by the Lorentz force parameterized by the magnetic field's strength B_0, the magnetic diffusivity η, and the viscosity ν. Looking at the equation of motion, nonlinear terms exist for both the velocity and the Lorentz force. Also, magnetic field strength and diffusivity are the only parameters mediating the interaction between flow and field. The vertical MHD equations are shown in chapter 3 with more details. Here we express these equations with non-linear terms and then solve them numerically in the Dedalus framework.

The basic state of a vertical magnetic field is taken to be:

$$\boldsymbol{B_0} = (0, B_0), \qquad A_0 = -B_0 x, \qquad J_0 = -\nabla^2 A_0 = 0. \tag{7.1}$$

Then we set

$$\boldsymbol{B} = \boldsymbol{B_0} + \boldsymbol{b}, \qquad A = A_0 + a, \qquad J = J_0, \tag{7.2}$$

The vorticity equation is

$$\partial_t \omega + \mathcal{J}(\omega, \Psi) = B_0 \partial_y J + \mathcal{J}(J, a) + \nu \nabla^2 \omega + g. \tag{7.3}$$

To solve 7.3 using Dedalus, we must separate the linear & non-linear terms.

$$\partial_t \omega - \nu(\partial_x(\omega_x) + \partial_y(\omega_y)) - B_0 \partial_y J - g = \underbrace{J_x a_y - J_y a_x}_{\mathcal{J}(J,a)} - \underbrace{\omega_x \Psi_y + \omega_y \Psi_x}_{\mathcal{J}(\omega,\Psi)} \tag{7.4}$$

Our fields satisfy the vector potential or induction equation:

$$\partial_t a + \underbrace{a_x \Psi_y - a_y \Psi_x}_{\mathcal{J}(a,\Psi)} - B_0 \Psi_y = \eta \nabla^2 a \tag{7.5}$$

To solve (7.5), using Dedalus, we must separate the linear & non-linear terms.

$$\partial_t a - \eta \nabla^2 a - B_0 \Psi_y = - \underbrace{a_x \Psi_y + a_y \Psi_x}_{\mathcal{J}(a,\Psi)}, \tag{7.6}$$

Here Ψ is the stream function; ω is the vorticity; B_0 is the strength of the magnetic field; J is the magnetic current; A_0 is a magnetic equilibrium.

The stream function and magnetic vector potential can be used to compute the kinetic energy (E_k) and magnetic energy (ME), given in this non-dimensionalization by

$$ME = \int \int \frac{1}{2}((a_y)^2 + (B_0 - a_x)^2)\, dxdy \tag{7.7}$$

We can obtain the perturbation energy by subtracting the basic state from the total energy; the basic state of the vertical magnetic field in (7.1) takes the form:

$$\boldsymbol{B} = (0, B_0) + (a_y, -a_x) = (A_y, -A_x) \tag{7.8}$$

$$\boldsymbol{B} = (a_y, B_0 - a_x) = (A_y, -A_x) \tag{7.9}$$

By substituting (7.8) into (7.7), we obtain the perturbation magnetic energy:

$$PME = \int \int \frac{1}{2}((a_y)^2 + (a_x)^2)\, dxdy \tag{7.10}$$

We check the numerical routines by comparing the results with the linear calculations from the linear chapter 3, which is approved by linear theory. Furthermore, by setting the magnetic field parameter $B_0 = 0$ to zero, we are able to retrieve the hydrodynamic equations. This clearly indicates how well the numerical routine performed by comparing the hydrodynamic simulation with the magnetic similar

implementation of the magnetic field and gives reasonable confidence that our simulation is well resolved.

7.1.2 Dedalus implementation

We have now included the vertical magnetic equations in the Dedauls framework, by creating a Problem object representing the initial value problem (in this case, a magnetic problem, IVP) with three principal parameters defined by domain (η, ν, B_0) as shown in Dedalus code (7.1).

```
#Problem: domain and variables
problem = de.IVP(domain, variables=['om','omx','omy','psi','psix','psiy','go','psixx','psiyy','A','J',
                                                                    'Ax','Ay','Axx','Ayy','Jx','Jy'])
#Parameters
problem.parameters['nu'] = nu
problem.parameters['eta'] = eta
problem.parameters['B0'] = B0
#Vorticity equation
problem.add_equation("dt(om) - nu*dx(omx)-nu*dy(omy) - go -B0*Jy= -omx*psiy+omy*psix +Jx*Ay-Jy*Ax")
problem.add_equation("om+dx(psix)+dy(psiy)+1e-6*psi=0")
#magnetic vector potential equation
problem.add_equation("dt(A) - eta*(dx(Ax)+dy(Ay))-B0*psiy= -Ax*psiy+Ay*psix ")
problem.add_equation("J+dx(Ax)+dy(Ay)= 0")
#First-order reduction
problem.add_equation("omx - dx(om) = 0")
problem.add_equation("omy - dy(om) = 0")
problem.add_equation("psix - dx(psi) = 0")
problem.add_equation("psiy - dy(psi) = 0")
problem.add_equation("psiyy - dy(psiy) = 0")
problem.add_equation("psixx - dx(psix) = 0")
problem.add_equation("Ax - dx(A)=0")
problem.add_equation("Ay - dy(A) = 0")
problem.add_equation("Axx - dx(Ax)=0")
problem.add_equation("Ayy - dy(Ay) = 0")
problem.add_equation("Jy - dy(J) = 0")
problem.add_equation("Jx - dx(J) = 0")
problem.add_equation("dt(go)= 0")
```

Figure 7.1: Governing equation solving numerically.

The MHD problem is also solved by iteratively applying the temporal integration scheme (IVP schemes) to advance the solution in time as shown in Dedalus code 7.2. We create the main loop that directly allows for arbitrary data interactions as the integration occurs. The equations (7.3 - 7.5) are then added to the problem, we also add the magnetic energy (ME) & perturbation magnetic energy (PME) and compare with kinetic energy and enstrophy in section 6.3.1.

```
# Setup storage
om.set_scales(1)
om_list = [np.copy(om['g'])]
t_list = [solver.sim_time]
u0y=np.sin(x)
om0=np.cos(x)
darea = (2*np.pi / nx) * (2*np.pi*L / ny)
KE_list = [sum(sum(np.square(psix['g'])+np.square(psiy['g'])))*darea*0.5]
PKE_list = [sum(sum( np.square(psiy['g'])+ np.square(-psix['g']-u0y) ))*darea*0.5]
enstrophy_list = [sum(sum(np.square(om['g'])))*darea]
Penstrophy_list = [sum(sum(np.square(om['g']-om0)))*darea]
ME_list = [sum(sum( np.square(Ay['g']) + np.square(B0-Ax['g']) ))*darea*0.5]
PME_list = [sum(sum( np.square(Ay['g'])+ np.square(Ax['g']) ))*darea*0.5]
```

```
dt =0.01
while solver.ok:
    solver.step(dt)
    if solver.iteration % 100== 0:
        om.set_scales(1)
        om_list.append(np.copy(om['g']))
        t_list.append(solver.sim_time)
        print(solver.sim_time)
        KE_list.append(sum(sum(np.square(psix['g'])+np.square(psiy['g'])))*darea*0.5)
        PKE_list.append(sum(sum( np.square(psiy['g']) + np.square(-psix['g']-u0y) ))*darea*0.5)
        # print(KE_list)
        enstrophy_list.append(sum(sum(np.square(om['g'])))*darea)
        Penstrophy_list.append(sum(sum(np.square(om['g']-om0)))*darea)
        ME_list.append(sum(sum( np.square(Ay['g']) + np.square(B0-Ax['g']) ))*darea*0.5)
        PME_list.append(sum(sum( np.square(Ay['g']) + np.square(Ax['g']) ))*darea*0.5)
    if solver.iteration % 100 == 0:
        print('Completed iteration {}'.format(solver.iteration))
```

Figure 7.2: Main loop of time

The initial conditions have been defined in the grid space ('g') by the initial value Solver object, which has been constructed by the Problem object. We set up the initial conditions for stream function ψ, magnetic field A and the force g which is expressed by Dedalus numerically as "go" as shown in Dedalus code figure 7.3. Therefore, we can add an appropriate perturbation value. As we saw previously, $\Psi = \cos x$ on the x axis for the basic state & so we add the arbitrary perturbation; a variation on the box scale can then be obtained by changing the axis to y and putting in $\cos(\frac{y}{L})$. Initially, we set the perturbation magnetic field a to zero, where the basic vertical field $A_0 = -B_0 x$; this technique reveals the vertical magnetic field at $t = 0$.

```
# Setup a sine wave
x,y=domain.grids(scales=1)
om.set_scales(1)
go.set_scales(1)
psi['g'] = np.cos(x)+0.0*np.cos(y/Ly)+0.1*(0.1*np.sin(y/Ly)+0.5*np.cos(y/Ly))
go['g']  = nu*np.cos(x)
A['g'] =0; #vertical field basic state
J['g']=0;
```

Figure 7.3: Initial conditions, where $L_y = 2$ for Prandtl number $P = 1$ and varies for $P = 0.5$. see table 7.2

7.2 Numerical considerations

The linear instability for a uniform magnetic field has been well-studied in chapter 3. We incorporate the MHD equations considered here with time evolution developed by the Dedalus framework (see section 7.1.2). In the nonlinear hydrodynamic chapter 6, we have investigated the kinetic energy & enstrophy and showed the effect of viscous force on the kinetic energy through energy dissipation or conservation. This chapter considers magnetic energy evolution over time, where the non-linear system is now linked with Lorentz's force and magnetic diffusivity η which has a significant effect on the non-linear evolution. We observed a growing mode in linear regimes with double diffusion (see section 3.5.1), thereby motivating us to investigate this mode with nonlinear evolution. The initial perturbations in simulations are small enough to allow a phase of linear growth before nonlinear interactions become relevant.

Description	**Parameters**	**Typical values**
Magnetic field strength	B_0	$0 \leqslant B_0 \leqslant 0.7$
Viscosity	ν	0.2
Magnetic diffusivity	η	0.2, 0.4
Box length (x)	$2\pi L_x$	2, 4
Box length (y)	$2\pi L_y$	2, 10
Number of grid point	N	$32^2 \leqslant N^2 \leqslant 50^2$
Time step	dt	0.01
wavenumber in y-axis	k	$0.5, (L_y = 2)$
wavenumber in x-axis	ℓ	$0.5, (L_x = 2)$

Table 7.1: This table shows the parameter values involved in finding numerical solutions. The third column presents the typical values/ranges for each of these parameters.

Table 7.1 shows a list of parameter values used in our simulation; we keep the purely hydrodynamic simulation of our system at roughly $\nu = 0.2$ as a typical value and employ Fourier modes e^{inx} & e^{iky} in the x, y directions. Our simulation domain size is $2\pi L_x \times 2\pi L_y$. The simulations presented in this chapter use a resolution of $N_x \times N_y = 32^2$. Increasing the domain size requires an increase in the number of grid points $N_x \times N_y = 50^2$. We run our simulation to the magnetic field strengths $B_0 < 0.7$; otherwise, the growth rate will vanish. Keeping the timestep at 0.01, with convergence tests performed at the small timestep values by checking that changes

in spectral energy with the resolution are minimal between different runs.

7.2.1 Linear modes & nonlinear effects

We begin by considering linear modes derived from eigenvalue calculations obtained by 2D incompressible MHD equations as shown in section (7.1.1) before describing the subsequent nonlinear stages. Our nonlinear simulations have the background flow and magnetic field in equation (3.31). The unstable mode with a positive growth rate is observed for wavenumbers ranging from $0 < k < 1$ as long as the B_0 lies between the threshold $0 < B_0 < 0.7$. The growth rate of the growing mode is plotted against vertical wavenumber k for various values of B_0 (see figure 3.2). Hence, we ran simulations at weak magnetic field strength $B_0 = 0.1$ and strong magnetic field strength $B_0 = 0.5$ and varied the viscosity values to find the most unstable mode.

Figure 7.4 shows the growth rate of instability for fixed field strength and varying viscosity values. We can see clearly that the most unstable mode yellow curve for $\nu = 0.3$ and outlined by the dashed red curve gives the maximum growth rate at $k = 0.5$, above the threshold $\mathrm{Re}\, p = 0$ the black dashed curve in panel (a). By increasing the magnetic field strength $B_0 = 0.5$ in panel (b) and looking at the maximum growth rate $k = 0.5$, we observe the most unstable mode (red curve) for $\nu = 0.2$ above the threshold $\mathrm{Re}\, p = 0$ (black dashed). Hence, the values in the comparison (stable versus unstable) are almost the same values but with different magnetic field strengths. We can see clearly that the magnetic field stabilizes the growth rate at $\nu \geqslant 0.2$ with the curves below the threshold (black dashed) line $\mathrm{Re}\, p = 0$ in both panels.

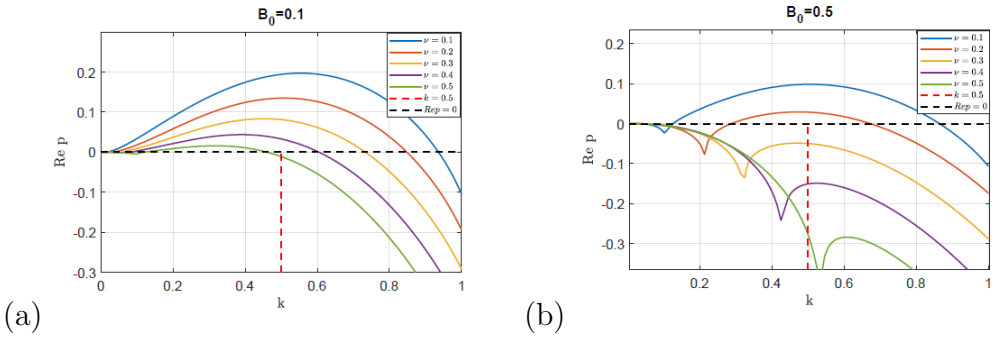

Figure 7.4: Instability growth rate showing $\mathrm{Re}\, p$ against wavenumber k for variety of ν, where $\nu = \eta$. Panel (a) at $B_0 = 0.1$, panel (b) at $B_0 = 0.5$. The black dashed line is the instability threshold at $\mathrm{Re}\, p = 0$; these figures are similar to figure 3.2 in chapter 3 but with different field strengths.

In the following subsections, we present direct numerical simulations consistent with findings from the linear stability analysis to find a saturated state dominated by steady state. We are not concerned with performing a comprehensive scan of the parameter space, but rather with providing some validation to the linear instability analysis and determining, at least qualitatively, how this unstable mode saturates. We perform multiple simulations for values of B_0 and ν. Particularly, L_y and L_x may be varied independently while B_0 and ν remain fixed as shown in figure 7.5.

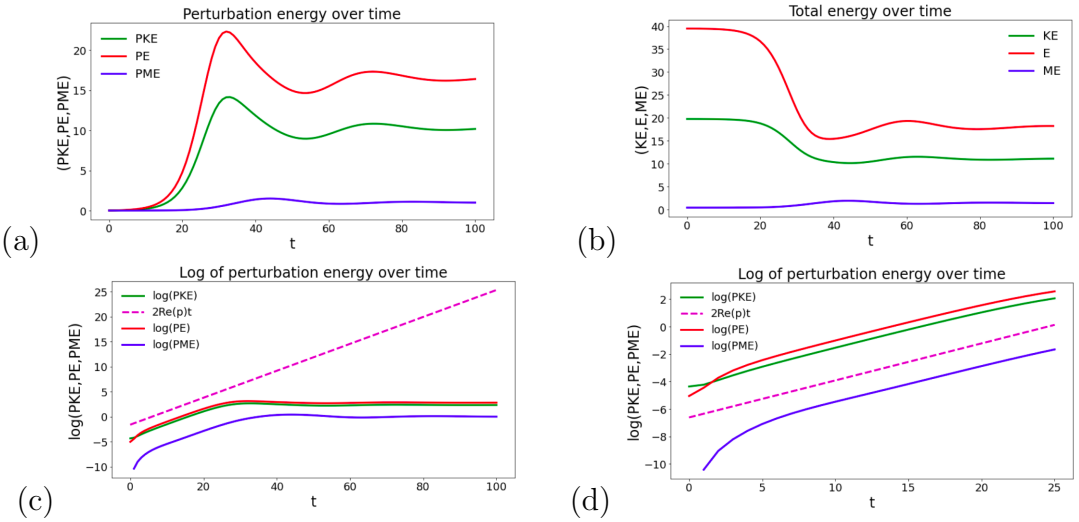

Figure 7.5: Simulation of kinetic energy, enstrophy and magnetic energy run at $t = 100$ and wavelengths $L_y = 2, L_x = 1$ for $\nu = \eta = 0.2, B_0 = 0.1$. Panels (a,b) show perturbation and total energy over time, and panels (c,d) show perturbation energies alongside the linear growth rate of the most unstable mode determined by (magenta dashed lines) $E \propto e^{2pt}$ with $\mathrm{Re}\, p = 0.1348$. Note that E, EP in the figures are Ω, Ω_p in the text.

Figure 7.5 shows the kinetic energy and enstrophy evolution over time for $\nu = 0.2, B_0 = 0.1$; this is similar to the hydrodynamic simulation in figure 6.7 (a,b). The

magnetic field is now incorporated into the system, we also plot the magnetic energy (blue curve). We run the simulation at $\nu = 0.2$, and $B_0 = 0.1$, which corresponds to the unstable mode (yellow curve) in figure 7.4(a). Panels 7.5(a,b) show the perturbation and total energy grow exponentially, then saturate before $t = 100$. A close inspection of the kinetic energy E_k plotted in panels (c,d) shows a linear scale (dashed magenta); by measuring the perturbation quantities to be approximately $(PE_k, \Omega_p, PM) \propto e^{2pt}$, in panel (c). We plot the perturbation kinetic energy & enstrophy for a shorter period up to $t = 25$ to ensure that the linear scale matches the linear evolution displayed in panels (d). We found a good agreement in the growth rate between linear matrix codes and non-linear simulations. The value of the $\mathrm{Re}\, p$ that comes from the linear matrix code is $\mathrm{Re}(p) = 0.1348$.

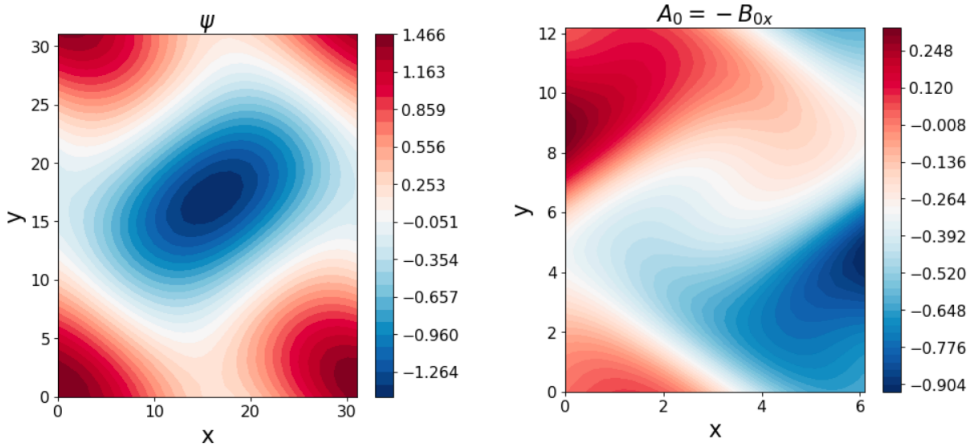

Figure 7.6: MHD simulation shows streamlines of flow ψ in panel and magnetic field lines A run up to $t = 100$.

Figure 7.6 shows the streamlines of the flow ψ corresponding to the simulation shown in figure 7.5. The saturation of kinetic energy occurs before the final time of simulation particularly at $t = 40$, as shown in figure 7.5. The streamlines ψ are physically arranged to exhibit systematic vortices similar to Roberts flow between $\psi = 1.466$ and $\psi = -1.264$ as shown in figure 7.6. The magnetic field lines in the plot of A correspond to weak $B_0 = 0.1$ and have little effect on the flow. Our simulation shows that the instability evolution is not significantly different to the hydrodynamic simulations shown in chapter 6, where the streamlines of flow ψ form a Robert flow structure (see figure 6.7). It is evident that the kinetic energy (green) is significantly stronger in both panels 7.5 (a,b) and is observed to be greater than the magnetic

energy (blue).

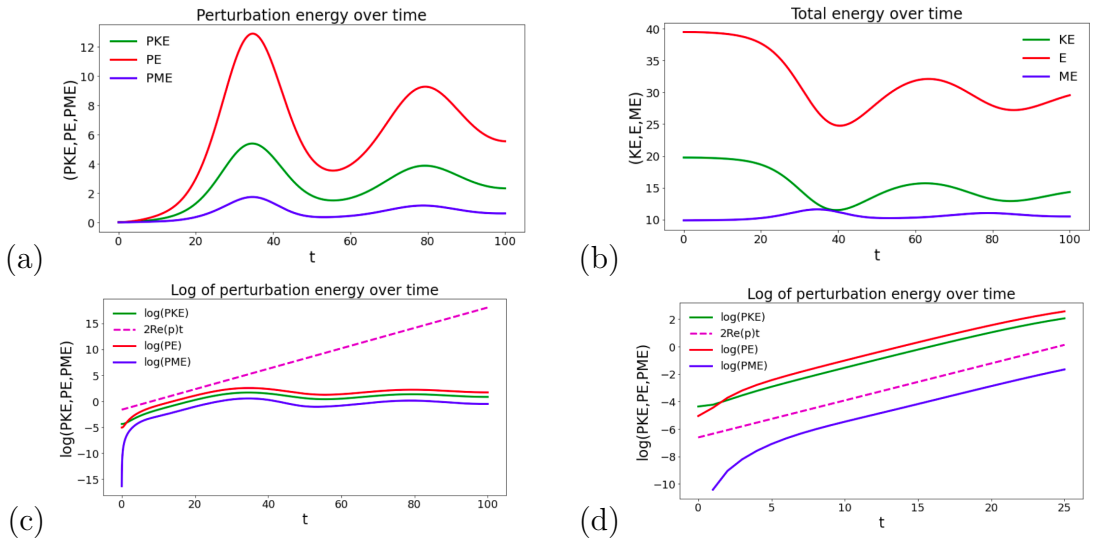

Figure 7.7: Kinetic energy & enstrophy and magnetic energy in a run up to $t = 100$ and wavelengths $L_y = 2, L_x = 1$ for $\nu = \eta = 0.1, B_0 = 0.5$. Panels (a,b) show perturbation and total energy over time, and panels (c,d) show perturbation energies alongside the linear growth rate of the most unstable mode determined by (magenta dashed lines) $E \propto e^{2pt}$ with $\mathrm{Re}\, p = 0.0983$. Note that E, EP in the figures are Ω, Ω_p in the text.

We implement a simulation for another strength of magnetic field $B_0 = 0.5$ as shown in figure 7.7, the simulation is run up to $t = 100$ for $\nu = \eta = 0.1$ corresponding to unstable modes (blue curve) in figure 7.4(b). These parameter values show the most unstable mode in the linear analysis at $k = 0.5$ which is linked to our choice of L_y. We can see clearly that the perturbation and total energy in panels (a,b) show damped oscillations and the magnetic energy (blue) is weaker than the kinetic energy. Panels (c,d) show the logarithm of perturbation energy agreeing with the linear scale (dashed magenta) from $t = 0$ to $t = 40$ as shown in panel (c), and the perturbation energy also agrees with the linear scale (dashed magenta) as shown in panel (d), to better understand the linear behaviour we run the simulation up to a short time $t = 25$.

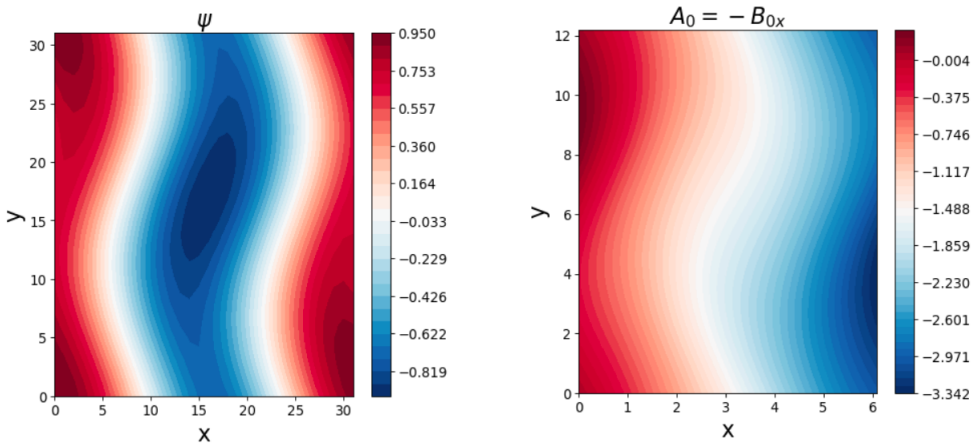

Figure 7.8: MHD simulation of streamlines of flow ψ in panel (a) and magnetic field lines A in panel (b).

Figure 7.8 shows the wavy streamlines of flow ψ where the magnetic field affects the flow by bending the flow lines. Magnetic lines A show a wave-like structure. We can see clearly that the kinetic energy is still growing in 7.7 (a,b) requiring a longer simulation time, details will be in the next section 7.3.1.

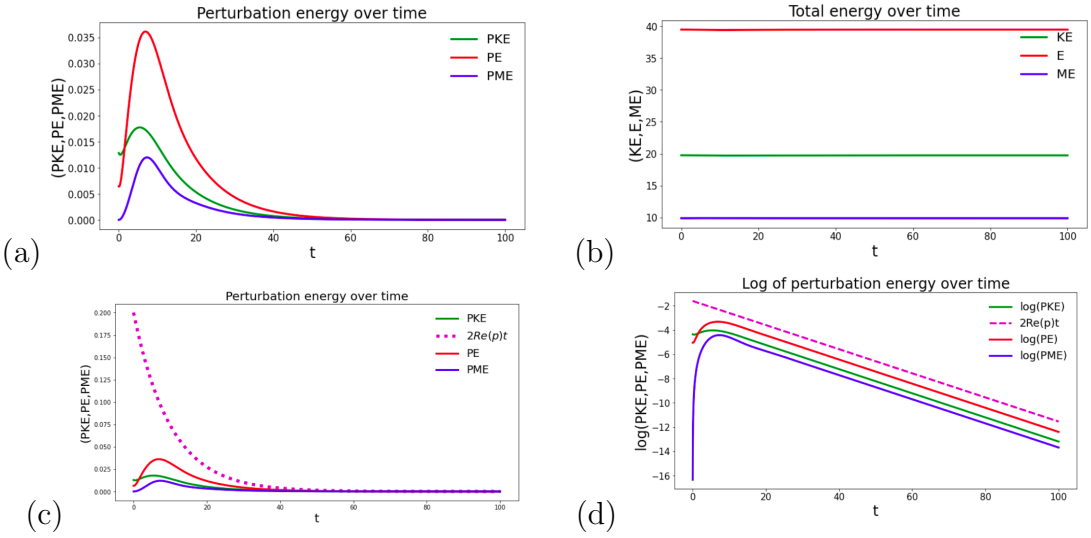

Figure 7.9: Kinetic energy & enstrophy and magnetic energy in a run up to $t = 100$ for $\nu = 0.3, B_0 = 0.5$. Panels (a,b) show perturbation and total energy & enstrophy over time, Panels (c,d) Perturbation energy & enstrophy are shown alongside the linear growth rate indicated by magenta dashed lines $E \propto e^{(2pt)}$ with $p = -0.0497$.

Figure 7.9 shows energy dissipation for the parameter values $B_0 = 0.5, \nu = 0.3$ corresponding to a decaying mode (green curve) in figure 7.4 (b), below the threshold (dashed black) $\mathrm{Re}\, p = 0$. Panel (a) shows kinetic energy & enstrophy, and magnetic energy dissipates more quickly, while in panel (b), the total energy demonstrates a steady state behavior. A simulation run at a higher resolution indicates that

this energy loss is due to the choice of viscosity value $\nu = 0.3$ and not from the runs being under-resolved. For completeness, we investigated the kinetic energy & enstrophy by linear scale (dashed magenta) as shown in panels (c,d) and found a good agreement with other energy curves. Our observation shows that the linear analysis has a negative growth rate $\mathrm{Re}\, p = -0.0497$, evidence of a decaying mode .

Figure 7.10 shows that the streamlines of flow ψ and magnetic lines A run at the same parameter values of figure 7.9 Both panels display a stable behaviour, with straight streamlines of flow ψ and uniform magnetic field lines A.

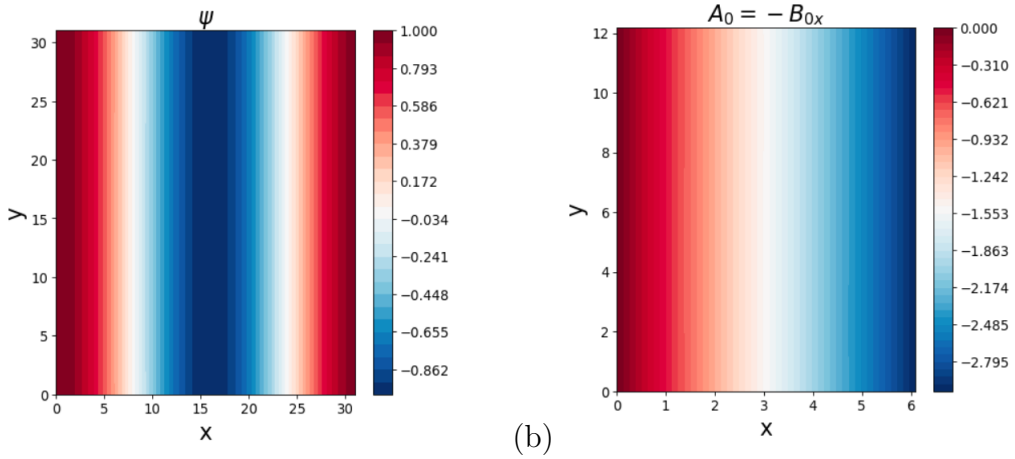

(a) (b)

Figure 7.10: MHD simulation run at the same parameter values and $t = 100$ as figure 7.9. Panel (a) shows streamlines of flow ψ, panel (b) shows magnetic field lines A.

7.3 MHD simulation effect of Prandtl number

We have investigated linear instability with varying Prandtl numbers with an initially uniform magnetic field with finite viscosity and magnetic diffusivity and found two families of instability in chapter 3. The first one corresponds to the usual hydrodynamic branch (Meshalkin and Sinai, 1961) and occurs when the Prandtl number $P = 1$ is unity, while the second one is observed at a strong magnetic field and $P < 1$. The nonlinear dynamics of both of these instabilities will be discussed in the following subsections.

In this section, we present a direct numerical simulation of non-linear evolution

for these instabilities, where the first family of instability is observed at $P = 1$ and saturates in a quasi-steady state similar to the hydrodynamic case identified by Meshalkin and Sinai (1961), whereas the second one at $P < 1$ requires further investigation based on its linear growth rate. Consequently, the parameter values for simulation with a small Prandtl number have been chosen and their ranges are provided in table 7.2

parameter	values
B_0	0.1, 0.5, 0.7
L_y	2, 4, 6, 10
t	300, 500, 1000
ν	0.3
P	≤ 1
$N_x \times N_y$	32×32
	50×50 otherwise

Table 7.2: Typical physical parameter values employed in our investigation for the vertical magnetic field, particularly at small Prandtl numbers.

The physical parameters in the table 7.2 are used in the numerical simulation for $P < 1$; the typical values/ranges of each of these parameters are given in the second column. The size of our numerical grid, N, depends on domain size and is determined on a case-by-case basis. Each simulation has been taken on a sufficiently fine grid to ensure that it is fully resolved.

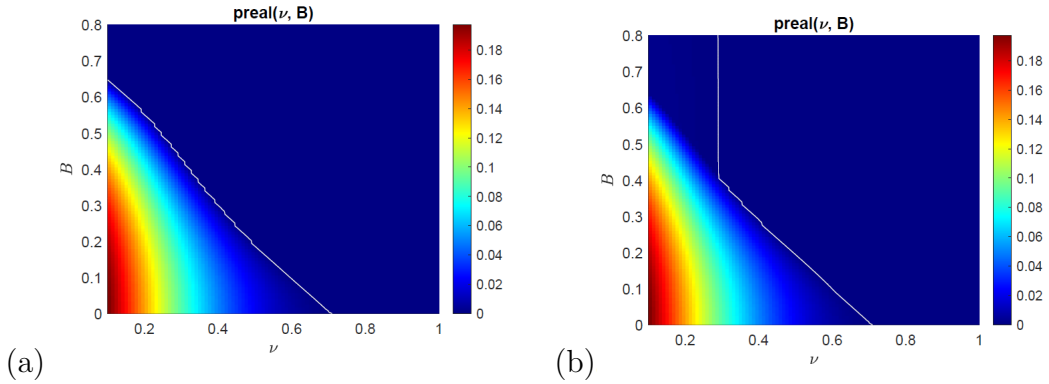

(a) (b)

Figure 7.11: Colour plot of maximum growth rate as a function of (ν, B_0) where in panel (a) $P = 1$, panel (b) $P = 0.5$. Red indicates a fast-growing mode, while blue indicates a zero growth rate.

Figure 7.11 shows the linear growth rate plotted at different values of the Prandtl number. Panel (a) shows a magnetic field suppresses the fastest growth rate at

$P = 1$, Panel (b) shows a new instability appears with Prandtl number $P < 1$, (more details of the linear theory discussed in chapter 3). We mention this figure again to remind the reader the differences between Prandtl numbers and to easily link with the simulations in this section. From this point, we conducted simulations for $P = 1$ and $P < 1$ in the following subsections in 7.3.1.

7.3.1 MHD simulation at $P = 1$

There are some results that need further investigation in section 7.2.1, (e.g, figures 7.7-7.5). Our investigation is based on $P = 1$, where the dissipation terms have the same values $\nu = \eta$. To gain a comprehensive understanding of the scope of this simulation, we have run our simulation for as long as possible for relatively large-scale domain size. Thus, we reveal that the instability tends to be a steady state, and the energy tends to be a constant. Obviously, we observed a saturation of instability when we run the simulation for a longer time. This simulation refers to the hydrodynamic simulation performed for a weak field $B_0 = 0.1$.

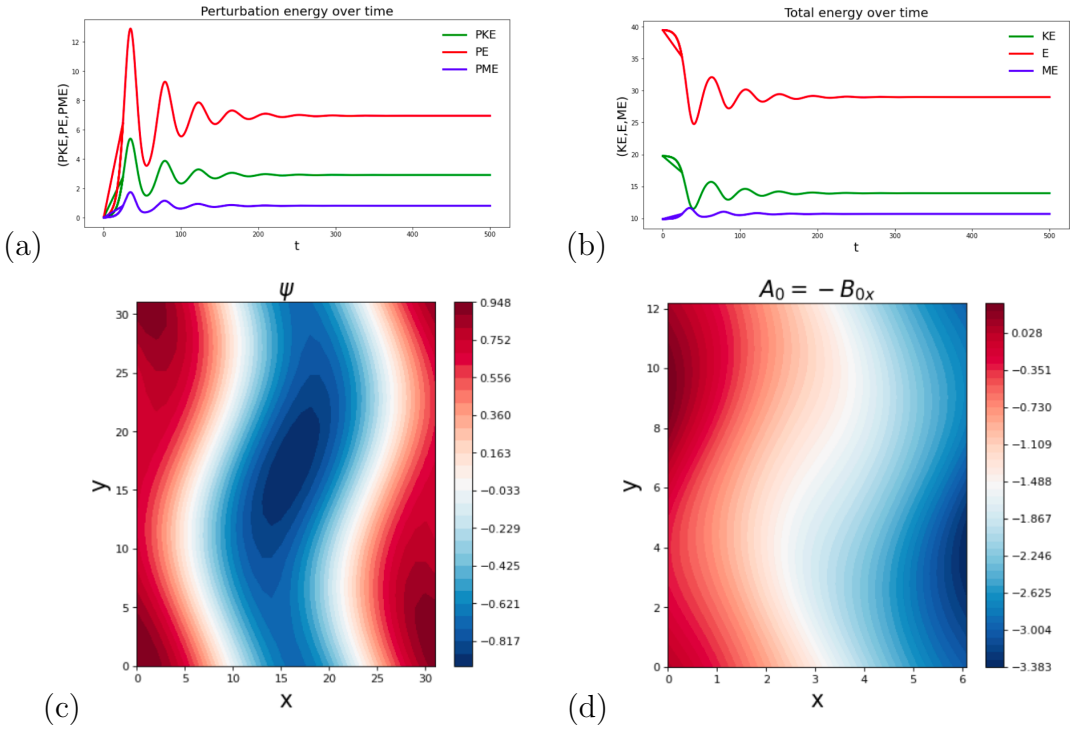

Figure 7.12: Simulation corresponding to figure 7.7 run up at $t = 500$ for $B_0 = 0.5$ and $\nu = 0.1$, panels (a,b) show the perturbation and total energy, panels (c,d) show the streamlines of flow Ψ and the magnetic lines $A = -B_0 x + a$.

We simulate the same parameter values of figure 7.7, $\nu = \eta = 0.1, B_0 = 0.5, P = 1$

with increasing simulation time from $t = 100$ to $t = 500$. We can see clearly that the perturbation and total energy in panels (a,b) initially begin with a transient from $t = 0$ to $t = 100$, then they settle from $t = 200$ to a later time, the kinetic energy (green) is strong and observed above the magnetic energy (blue). Panels (c,d) show a wavy streamlines of flow ψ with a small vortex located in the center, and the magnetic lines are bent by the flow lines . The instability behaviour in both panels is similar to figure 7.7 (c,d).

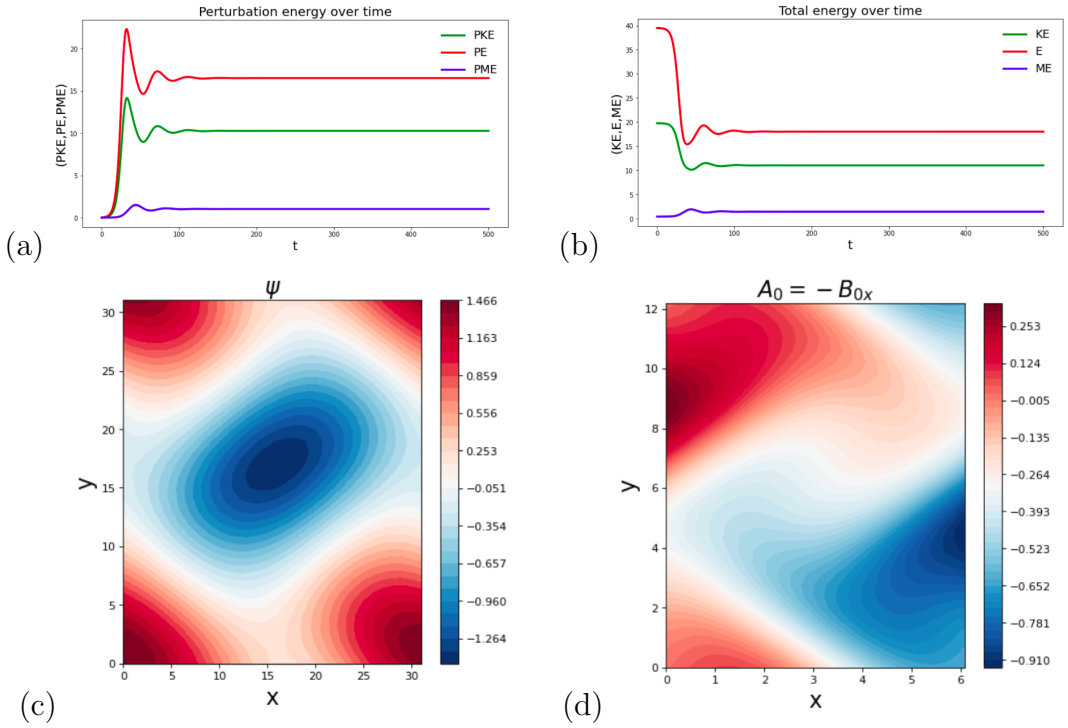

Figure 7.13: Simulation corresponding figure 7.5 run up at $t = 500$ for $B_0 = 0.1, \nu = 0.2$. Panels (a,b) show the perturbation and total energy, and Panels (c,d) show streamlines of flow Ψ and magnetic field lines $A = -B_0 x + a$.

Figure 7.13 shows a simulation at the same parameter values of figure 7.5, with $\nu = 0.2, B_0 = 0.1$ with increasing the simulation time from $t = 100$ to $t = 500$. We can see clearly that the perturbation and total energy has a transition from $t = 0$ to $t = 100$ then saturates to a later time. The kinetic energy (green) is strong and observed above the magnetic energy (blue).

Our simulation of figures 7.12 and 7.13 shows the same instability behaviour as figures 7.7 and 7.5, although implemented at different magnetic field strengths $B_0 = 0.5$ and

$B_0 = 0.1$. We also observed that the energy tends to be constant with increasing simulation time in both figures, even with different magnetic field strengths. The difference is observed in streamlines of flow and magnetic field lines. A systematic vortex formed in figure 7.13 (c) at $B_0 = 0.1$, the hydrodynamic case modified by the weak field and the viscosity values remain identical to the hydrodynamic case simulation 6.7, whereas there are wave-like streamlines in figure 7.12 (c) at $B_0 = 0.5$, the flow more modified by the magnetic field $B_0 = 0.5$ and suppress the jets of pure hydrodynamic instability.

7.3.2 MHD simulation comparing with linear mode

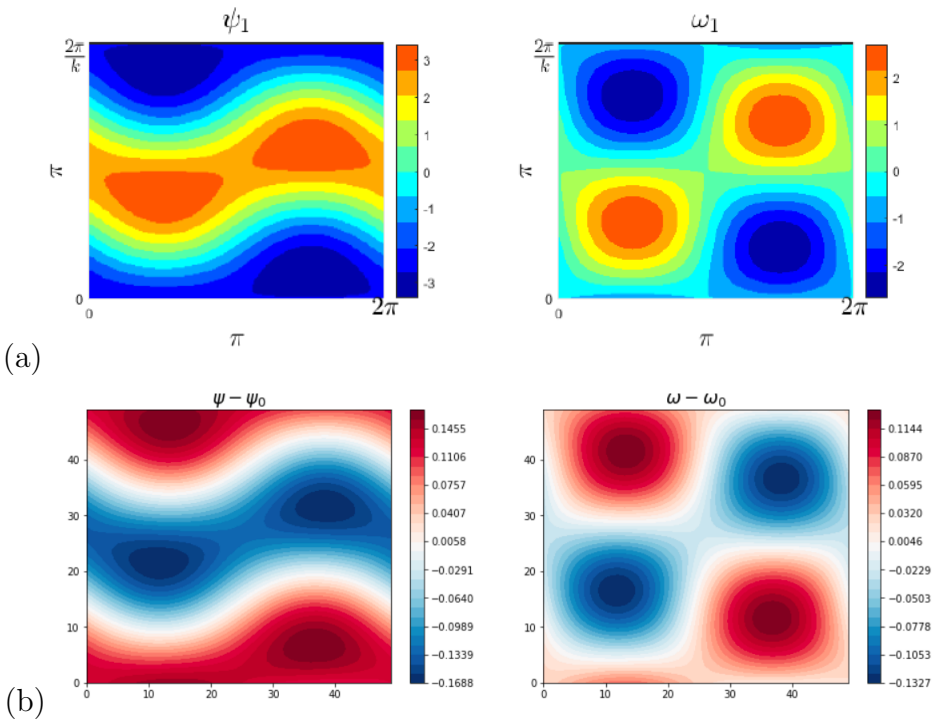

Figure 7.14: Simulation of vorticity field ω (right) and stream function ψ (left) for $\nu = 0.2$ and $B_0 = 0.1$. Panels (a, b) show linear results at $k = 0.5$, and panels (c,d) show nonlinear simulation at $L_y = 2$, run up to $t = 10$.

Figure 7.14 shows snapshots of comparison between the linear result and the nonlinear simulation. We run the simulation at $\nu = 0.2, B_0 = 0.1$, the domain size is $(x, y) = (2\pi, 4\pi)$, and the resolution is $(N_x, N_y) = (50, 50)$. Thus, we initiate the Fourier mode during simulation by setting the domain size as $L_y = 2$ in panel (b). To make a good comparison, we consider the perturbation vorticity & stream function

from the linear calculation as shown in chapter 3 and compare with simulation 7.5(b) by reducing the simulation time from $t = 100$ to $t = 10$.

The non-linear simulation indicates that the vorticity and stream functions in panel (b) are similar to the linear instability pattern in panel (a), where the vorticity eigenfunction is derived from linear theory see figure 2.2. Panel (b) shows the vortices at an early time $t = 10$ in the plot of ω, and zonostrophic instability is growing linearly as shown in the plot of ψ. The small values in the colour bar indicate small perturbations. These panels resemble the nonlinear hydrodynamic figure 6.12 but are modified by a weak field $B_0 = 0.1$, This confirms that the linear phase is sufficiently long for perturbations to exhibit appropriate instability behaviour.

7.3.3 MHD simulation at $P < 1$

Having investigated the linear instability at $P < 1$ in chapter 3 and verified by perturbation theory in section 3.7.1, we need to determine how this instability evolves in non-linear evolution. Hence, we begin using the Dedalus framework and varying the Prandtl number independently with the parameter values $B_0 = 0.7, \eta = 2\nu, P = 0.5$ shown in figure 7.11 (b). We run the simulation of the domain size of $(x, y) = (2\pi, 2\pi L_y)$ and resolution $N^2 = 32$ resolution of Fourier modes in the x and y directions. We can see clearly more decay occurs for the value $k = 0.5$ (blue dashed) below the threshold $\mathrm{Re}\, p = 0$ (red dashed horizontal line) in figure 7.15, so we look for positive growth rate at smaller k, which requires a bigger value of L_y, but this doesn't help to reach saturation level as we see in figures 7.16-7.18.

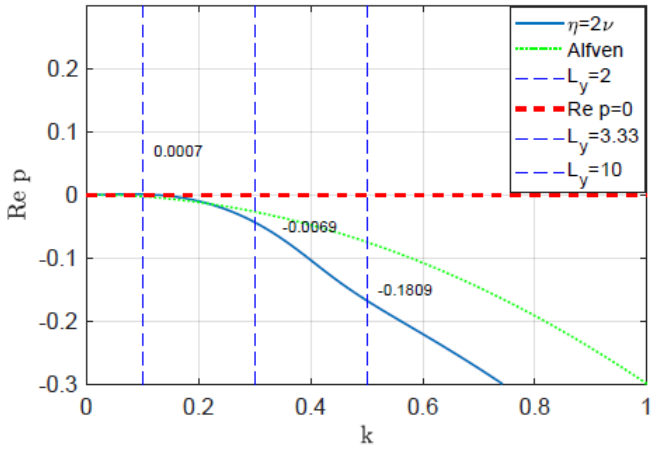

Figure 7.15: Growth rate as afunction of wavenumber k for $\nu = 0.2, \eta = 0.4, B_0 = 0.7$. The (blue solid line) is obtained numerically by solving linear equations (3.100), while the (dotted green) is the Alfvén wave decay rate from (1.70). The vertical (blue dashed) gives the three values of large-scale wavenumber k, and the horizontal (red dashed) is the threshold of instability $\mathrm{Re}\, p = 0$.

Figure 7.15 shows the instability growth rate against the wavenumber k outlined by the (blue dashed vertical line) represent three values of wavenumber $k = 0.3, k = 0.5, k = 0.1$. In this figure, we obtain a decay mode (solid blue) showing below the instability threshold of the horizontal (red dashed) with damping Alfvén waves (green dotted). We can see clearly there are negative growth rates corresponding to the value of $k = 0.3$ and $k = 0.5$ representing that there is damped oscillatory behaviour as shown in figure 7.16 at these two values. To better understand the instability dynamics we run our simulation at a positive growth rate with $k = 0.1$ and $L_y = 10$ as $L_y = 1/k$ as shown in figure 7.18.

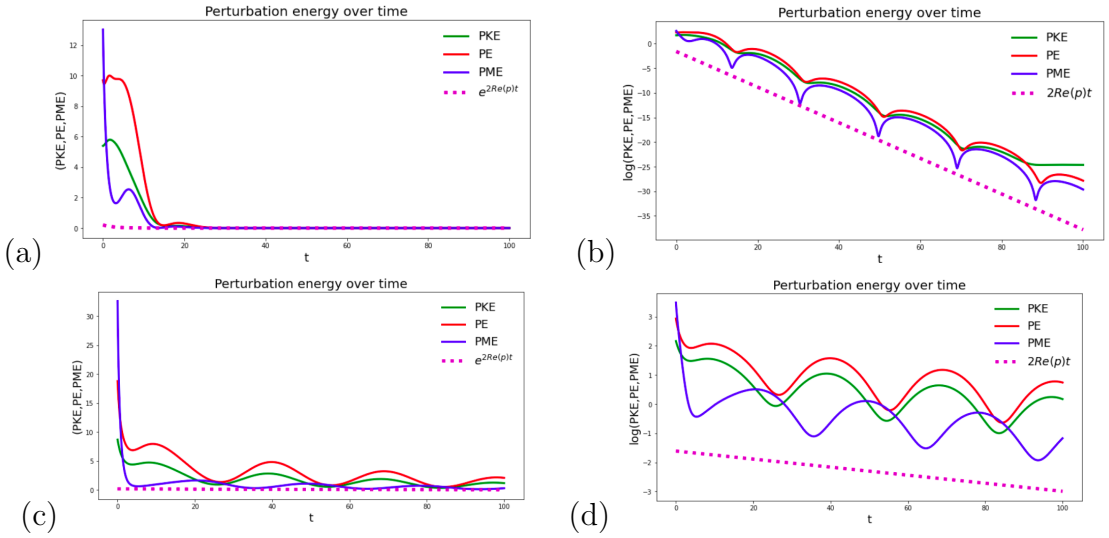

Figure 7.16: MHD simulation run up to $t = 100$ with $B_0 = 0.7, \nu = 0.3, P = 0.5$, panels (a,b) perturbation energy at $L_y = 2$, the linear scale determined by (magenta dashed) at $p = -0.1809 + 0.2361i$, Panel (c,d) perturbation energy at $L_y = 3$, the linear scale determined by (dashed magenta) at $p = -0.0069 + 0.1070i$.

Figure 7.16 shows the perturbation kinetic energy & enstrophy and magnetic energy in panels (a,c) and the logarithm of perturbation energy proportional to the linear growth rate shown in panels (b,d). We run the simulation at $L_x = 1$, then first look at $L_y = 2$ in panels (a,b), then $L_y = 3$ in panels (c,d). We can see clearly that the logarithm of perturbation energy has a damped oscillatory evolution that agrees with the linear scale (dashed magenta) in both panels. We observed that repeating the simulation for increased wavelength L_y resulted in the amplitude gradually increasing for each simulation from $\mathrm{Re}\, p = -0.1809$ to $\mathrm{Re}\, p = -0.0069$, respectively.

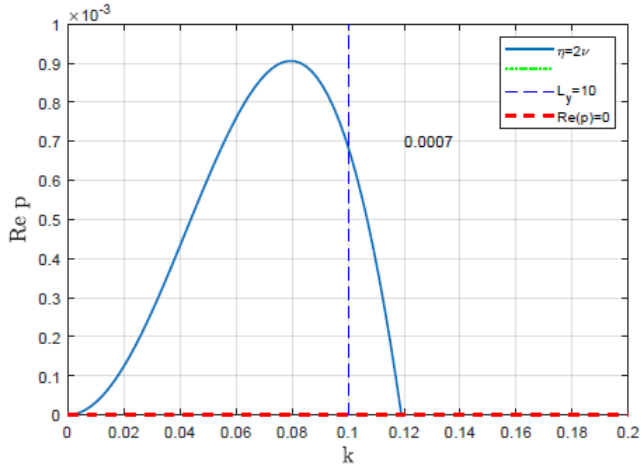

Figure 7.17: Instability growth rate against the wavenumber k derived from figure 7.15 shows that the growth rate (solid blue) above $\mathrm{Re}\, p = 0$ (red dashed), the positive growth rate determined by the vertical (blue dashed) at $k = 0.1$.

Having investigated the instability with an increase in the domain size and found that the oscillatory mode dies away, we now perform the simulation using the same parameter values and the initial conditions as in figure 7.16, with $(x, y) = (2\pi, 20\pi)$ and $L_x = 1, L_y = 10$, corresponding to $k = 0.1$ (blue dashed vertical line) in figure 7.17, which is represent the positive growth rate $\mathrm{Re}\, p = 0.0007$ above the threshold (red dashed horizontal line). From this point, we are able to run the simulation at this positive growth rate at 3 different simulation times up to $t = 100$, $t = 500$, and $t = 1000$. To determine whether this oscillatory damping stops or continues permanently as shown in figure 7.18.

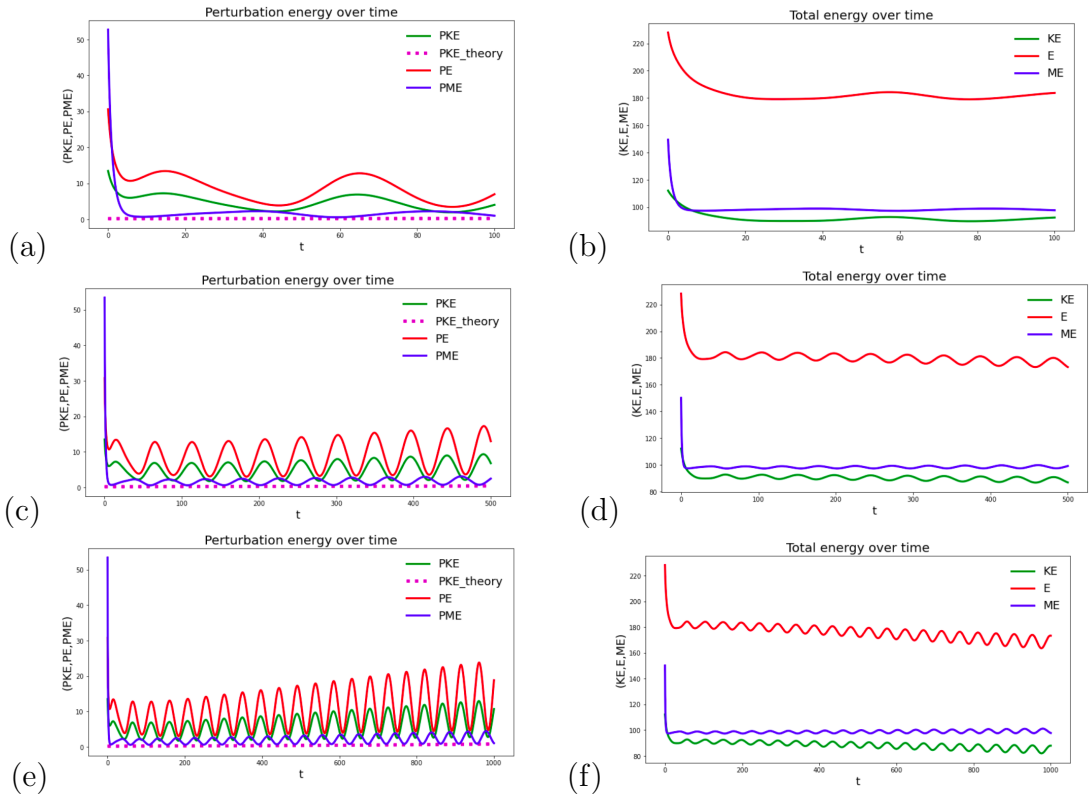

Figure 7.18: MHD simulation perturbation & total energy with $B_0 = 0.7, \nu = 0.2, \eta = 2\nu, L_y = 10$. The linear scale indicated by (dashed magenta) at $p = 0.0007 + 0.0655i$. Panels (a,b) run up to $t = 100$, panels (c,d) run up to $t = 500$, panels (e,f) run up to $t = 1000$.

We can see clearly that the oscillatory behaviour occurs in three panels as shown in figure 7.18. This oscillatory evolution agrees with the linear scale (dashed magenta) and the perturbation fields become stronger as we increase the simulation time to $t = 1000$ as shown in panel (e). The kinetic energy (solid green) is strong in three panels of perturbation energy with a transient observed in magnetic energy (blue)

beginning before the oscillation behaviour of perturbation energy, this transition resulting in the initial conditions. We run the simulation at a strong field $B_0 = 0.7$ and small Prandtl number $P = 0.5$ and at different times. Panels (a,b) show the perturbation and total energy at $t = 100$, panels (c,d) run at $t = 500$, and panels (e,f) run at $t = 1000$.

We conclude that the oscillatory damping behaviour continues with a positive growth rate $p = 0.0007 + 0.0655i$. This oscillatory behaviour resembles more closely the Alfveńic Dubrulle–Frisch modes; (Fraser, Cresswell and Garaud, 2022). We observe that repeating the simulation with increasing simulation time shows strong oscillatory behaviour. This occurs because the non-conservative damping force removes energy from the system. For example, to keep swinging on a playground swing, we must keep pushing which means we need more force to continue to generate oscillatory motion in the presence of damping. However, to achieve the saturation level, we need to run the simulation with a larger box domain size as shown in figure 7.20.

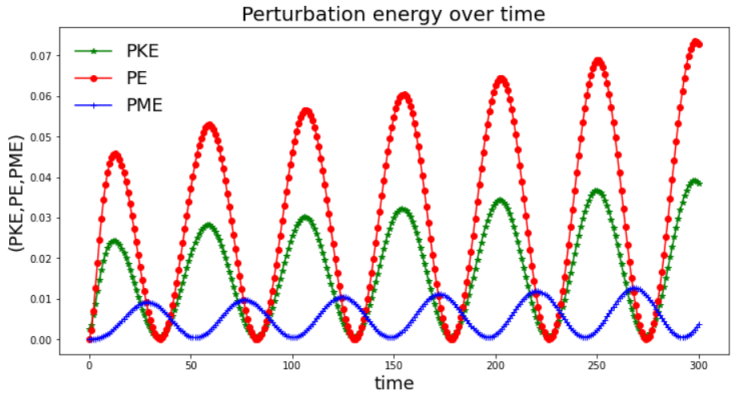

Figure 7.19: Perturbation energy over time run up to $t = 300$ at the same parameter values of figure 7.18.

From figure 7.19, we observe that the growth rate has a frequency $p = 0.0007+0.0655i$; by using a relatively small computational investigation we are able to calculate the frequency of the imaginary part by taking cos frequency since the KE is real, which gives

$$f(t) = e^{p_r t} \cos p_i t \tag{7.11}$$

The energy-like quantity is

$$f^2(t) = e^{2p_r t} \cos^2 p_i t \tag{7.12}$$

so, the perturbation energy varies in time as

$$f^2(t) = e^{2p_r t} \frac{1}{2}(1 + \cos 2p_i t) \tag{7.13}$$

and has a $2p_i$ frequency component. Where E_k, ME are the kinetic energy and magnetic energy, Ω is the enstrophy, we can compute the simulation time up until $t = 300$ as we have a larger domain size in y, $(x, y) = (2\pi, 10\pi)$. By using the imaginary part p_i we obtain :

The time at 2π

$$t = \frac{2\pi}{2p_i} \simeq \frac{3.14 \times 2}{2 \times 0.0655} = \frac{1}{0.02} \simeq 50, \tag{7.14}$$

The time at 4π

$$t = \frac{4\pi}{2p_i} \simeq \frac{3.14 \times 4}{2 \times 0.0655} = \frac{1}{0.01} \simeq 100, \tag{7.15}$$

The time at 6π

$$t = \frac{6\pi}{2p_i} \simeq \frac{3.14 \times 6}{2 \times 0.0655} = \frac{1}{0.007} \simeq 150. \tag{7.16}$$

We can see clearly that the curve starts with zero for both kinetic energy (green) and magnetic energy (blue) and then the kinetic energy (green) shows the period of the oscillations seen in the first period π, particularly at $t \simeq 50$, also at the second period 2π at $t \simeq 100$. Similarly, we can calculate the other times of simulation as we found oscillation in the kinetic energy and magnetic energy with frequency the twice imaginary part of the growth rate $\mathrm{Im}\, p$ over time as shown in equation (7.11).

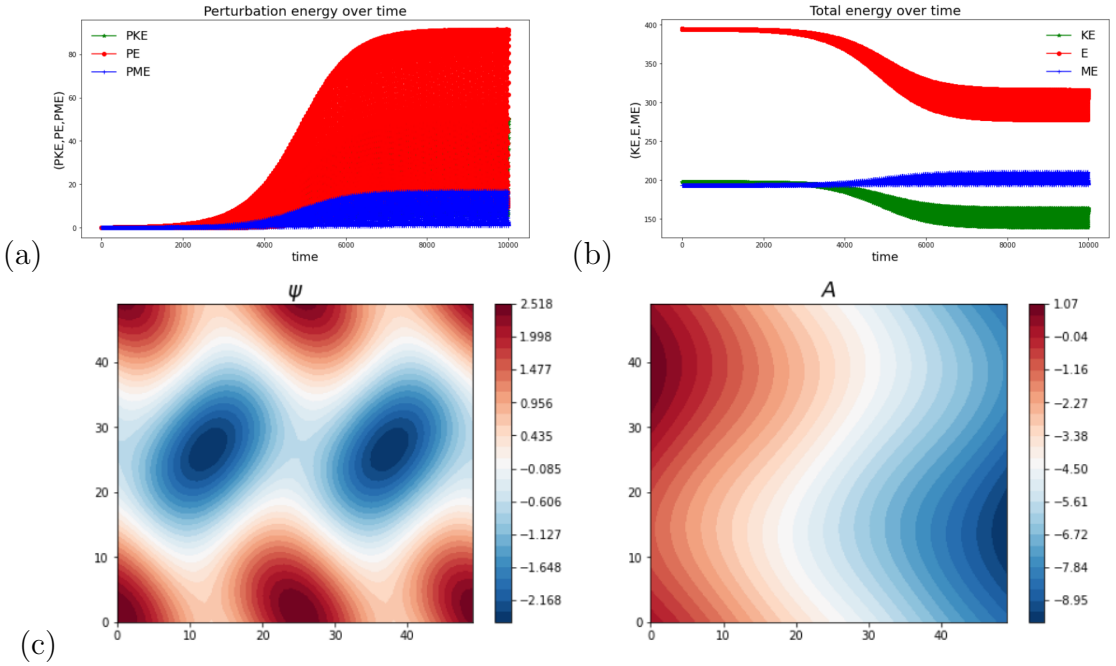

Figure 7.20: MHD simulation run up to $t = 10000$, at domain size $(x, y) = (4\pi, 20\pi)$ for $B_0 = 0.7, \nu = 0.2, \eta = 2\nu$, panels (a,b) perturbation & total energy and enstrophy over time, (c) streamlines of flow ψ and magnetic lines $A = -B_0 x + a$.

Upon investigation of the instability structure and relative growth rate of the flow and field in the nonlinear regime, we find that they are qualitatively different from those of the linear modes computed in chapter 3, and really hard to achieve the saturation level at a single wavelength. Our previous simulation 7.18 shows that the oscillatory behaviour & growth does not stop as we increase the simulation time due to a small growth rate of linear instability. From this point, we run the simulation at the same parameter values of figure 7.18 and double wavelengths in $L_x = 2$ and $L_y = 10$, (where the Floquet wavenumber is present in the system) as shown in figure 7.20, we obtained the saturation of instability at $t = 10000$ as shown in panel (a), and we can see clearly that the enstrophy (red) is strong and above the magnetic energy (blue) in both panels (a,b). However, we observed that two vortices located in the centre of the streamlines of the flow ψ result from the double wavelength in the x-direction $L_x = 2$, and the magnetic lines show a wavy behaviour dominated by vertical field.

(a)

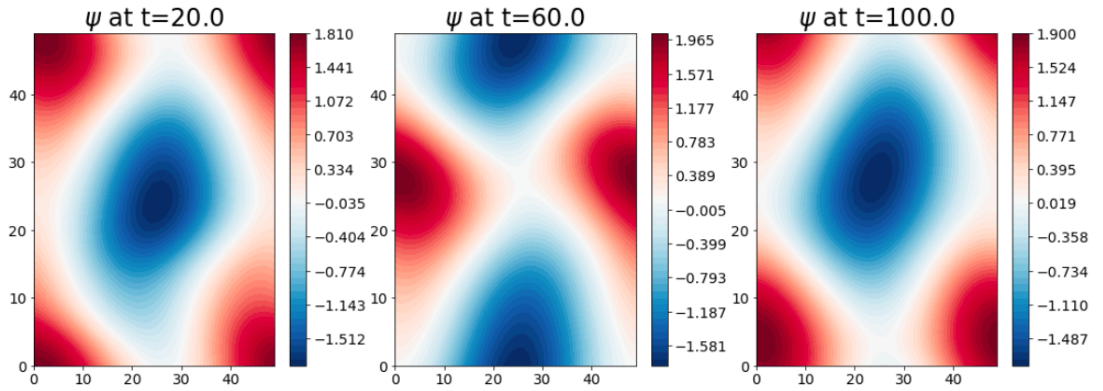

(b)

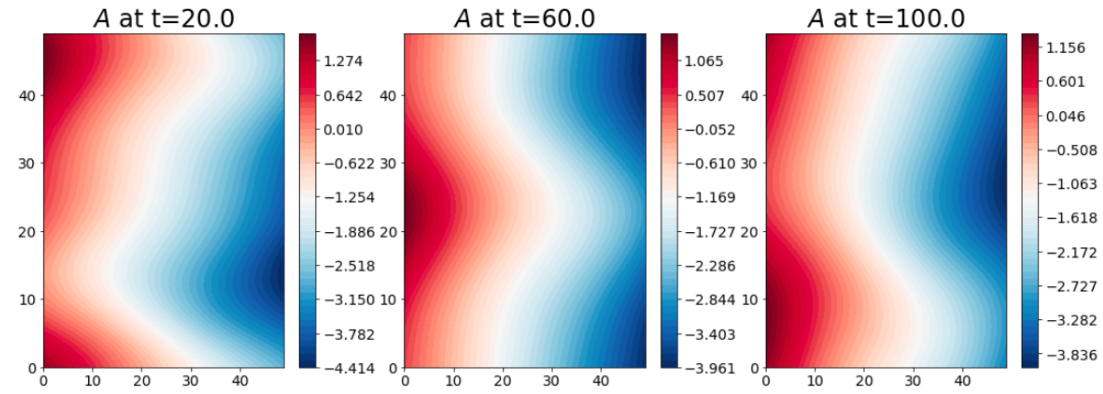

Figure 7.21: Snapshots of streamlines of flow & magnetic field lines run up to $t = 100$ and the same parameter values of figure 7.18 for $B_0 = 0.7, \nu = 0.2, \eta = 2\nu$, Panel (a) streamlines of flow evolution ψ, panel (b) magnetic field lines A.

Snapshots of the stream function & magnetic field are shown in figure 7.21. The linear growth rate has a positive value that can be observed as periodic pairs of unstable waves that propagate with increasing simulation time, as shown in panel (a). The phenomenon is further underlined by the negative eddy viscosity of periodic shear flows, as identified by Dubrulle and Frisch (1991). In the plot of ψ, the system exhibits the periodic vortices at $t = 20$ then the original vortex breaks down in ψ at $t = 60$. Eventually, the system goes back to periodic vortices at $t = 100$ as the kinetic energy is constant. Similarly, the magnetic lines are bent by the flow lines showing a wavy magnetic field $A = -B_0 x + a$ as shown in panel (b), giving the same instability behaviour in the three times implemented.

7.4 MHD inverse cascade: vertical field

In fully developed 2D turbulence, in the mathematical limit of zero viscosity, energy is not dissipated and is dynamically transferred to large scales creating the inverse

cascade. (Boffetta and Ecke, 2012).

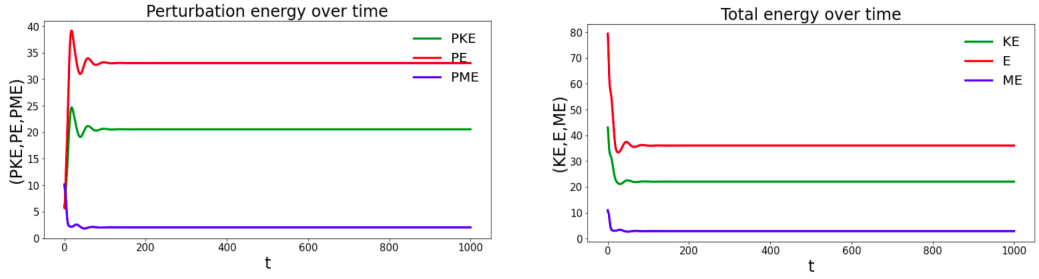

Figure 7.22: Simulation of kinetic energy (green) & enstrophy (red) and magnetic energy (blue), domain size $(x, y) = (4\pi, 4\pi)$ run up to $t = 1000$, for $\nu = 0.2, B_0 = 0.1$. Panel (a) evolution of perturbation energy, panel (b) evolution of total energy.

Compared with the hydrodynamic inverse cascade in section 6.6, we implement simulation at the same parameter values and weak magnetic field $B_0 = 0.1$. This simulation required a shorter time to reach saturation, resulting in the magnetic field present in the system, unlike the hydrodynamic case in figure 6.6 which needed a long run to reach saturation. Figure 7.22 shows the evolution of perturbation & total energy over time in panels (a,b); the energy starts with transient then tends to a steady state to the final time $t = 1000$; we run the simulation at large domain size $(x, y) = (4\pi, 4\pi)$, and weak magnetic field $B_0 = 0.1$.

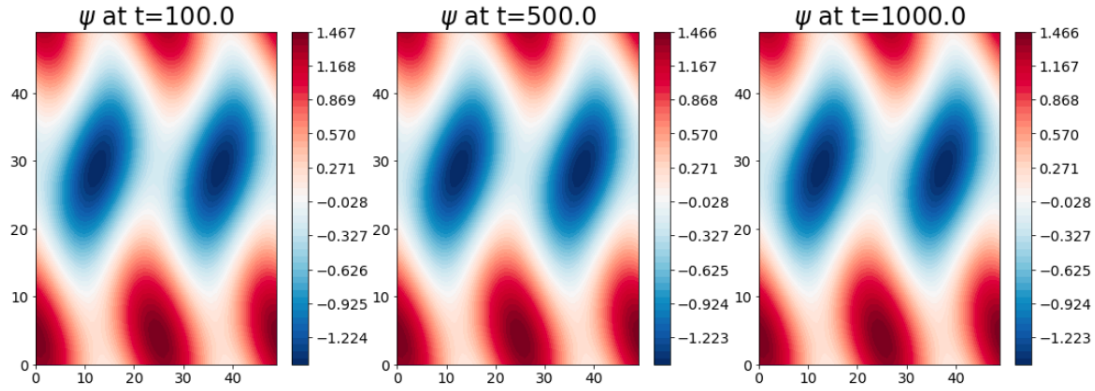

Figure 7.23: Kinetic energy cascade of stream function ψ at $\nu = 0.2$, $(x, y) = (4\pi, 4\pi)$ run up to $t = 1000$, arrested by weak magnetic field $B_0 = 0.1$

Figure 7.23 shows that kinetic energy inverse cascade is arrested by weak magnetic field $B_0 = 0.1$. The domain size is enough to support two vortices formed in the centre of flow with different signs; as we increased the simulation time, we received the same instability behaviour, resulting in the magnetic field halting the energy to transfer. Figure 7.24 illustrates the evolution of the magnetic field over time; the

same behaviour is observed each time, where, the weak field interacts with the flow to create this pattern.

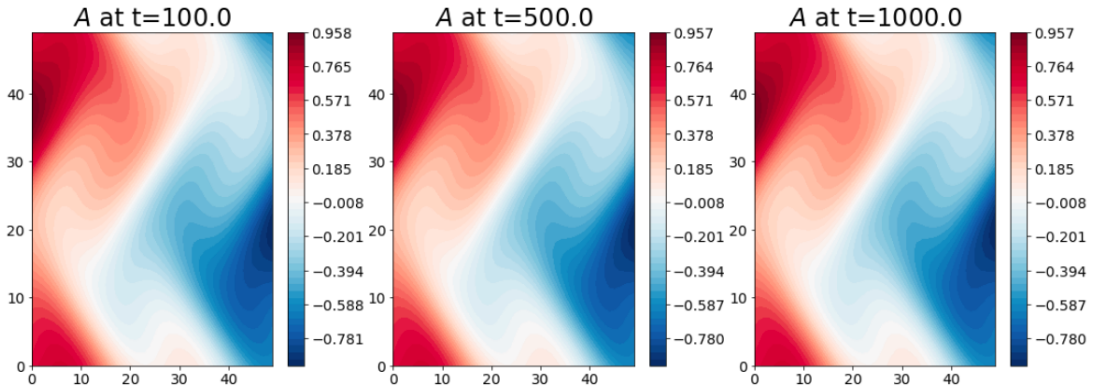

Figure 7.24: Snapshots of magnetic energy over time run at the same parameter values in the above figures.

Simulations show that the inverse cascade is arrested by a weak magnetic field $B_0 = 0.1$ as the flow becomes more dominated by Alfvén waves. The relevant analogy is shown in Legras, Villone and Frisch (1999) shows that the inverse cascade of structures to large scales in y is arrested by the β effect. In addition, Bradshaw (1973) has suggested that the cascade "arrest" occurs when the flow character transitions from strongly nonlinear and turbulent to weakly nonlinear and wave-dominated. It is possible to determine precisely what threshold of B prevents the cascade from occurring by varying B and finding the limit of the magnetic field to arrest the inverse cascade. However, even weak magnetic fields are sufficient to arrest the cascade.

7.5 Conclusion

The following points summarize the main results of this chapter:

- We run our simulations with different magnetic field strengths. The Dedalus framework is similar to that given in the hydrodynamic case in chapter 6 with Lorentz force present in the system.

- Direct numerical simulation is presented in the MHD system by tracking the linear growth rate; we pay attention to linear unstable modes rather than stable

modes as we look for non-linear evolution.

- A simulation with a weak magnetic field appears to be relevant to approximate hydrodynamics provided that ν is small enough to permit the instability in section 7.3.1. We found the saturation at a single wavelength L_y, and the flow field has formed a large-scale structure, similar to the hydrodynamic case.

- For a strong magnetic field B_0, The magnetic field suppresses the flow lines (through the Lorentz force). However, a small value of magnetic Prandtl number $P < 1$ enhances instability linearly and shows oscillatory behaviour non-linearly. Simulations become challenging to resolve this behaviour at single wavelength L_y. We get saturation at $L_y = 10$ and large domain sizes as shown in section 7.3.3.

- In 2D MHD, the vertical magnetic field has arrested the energy cascade; even for weak magnetic fields, the energy transfer stops to at large-scale flow as seen in section 7.4.

In the following chapter, we will discuss some simulations in which a horizontal magnetic field is present.

8. Nonlinear MHD evolution: Horizontal field

The linear instability affected by horizontal magnetic field has been studied in detail (see chapter 4). Two families of instability were identified, the flow branch with a weak magnetic field, and the magnetic field branch with an arbitrarily strong magnetic field. In this chapter, we extend our investigation to explore the non-linear evolution and solve the two-dimension MHD equations using the Dedalus framework. Furthermore, we will investigate the nonlinear evolution in the presence of non-zero Floquet wavenumber ℓ and varying Prandtl numbers.

8.1 Mathematical formulation

We implement simulations of two-dimensional incompressible flow with a horizontal magnetic field into the Dedalus framework similar to those adopted for the linear horizontal chapter 4 with non-linear terms. We do not intend to repeat these results in this section. In this case, instability evolution is influenced by a Lorentz force parameterized by the strength of the magnetic field B_0 with a sinusoidal vertical field component coming from the external force as shown in section 4.2 which gives more details. Here we express these equations with non-linear terms and then solve them numerically by the Dedalus framework. We have

$$\partial_t \omega + \mathcal{J}(\omega, \Psi) = B_0 J_x + \mathcal{J}(J, a) + \nu \nabla^2 \omega + g. \tag{8.1}$$

To solve equation (8.1) using Dedalus, we must separate linear & non-linear terms

$$\partial_t \omega - \nu \nabla^2 \omega - B_0 J_x - g = -\mathcal{J}(\omega, \Psi) + \mathcal{J}(J, a) \tag{8.2}$$

Our field satisfies the vector potential equation or induction equation:

$$\partial_t a - \eta \nabla^2 a - B_0 \Psi_x = \underbrace{-a_x \Psi_y + a_y \Psi_x}_{\mathcal{J}(a,\Psi)} \tag{8.3}$$

To gain a comprehensive understanding of the flow and magnetic field, the total energy is decomposed into kinetic energy and magnetic energy. The kinetic energy & enstrophy have been discussed in the non-linear hydrodynamic chapter (see equations (6.5-6.6), and the perturbation kinetic energy & enstrophy in equations (6.8-6.9). The magnetic energy takes a different form in the horizontal field as the basic equilibrium state is different in both fields.

The magnetic energy (ME) in a horizontal field takes the form

$$ME = \frac{1}{2} \int \int (B_x^2 + B_y^2) dx dy \tag{8.4}$$

for the total field; the magnetic field takes the form:

$$A = B_0 y + a \qquad \boldsymbol{B} = (B_0 + a_y, -a_x), \tag{8.5}$$

and the basic state of the magnetic field takes the form

$$A_0 = B_0 y - \frac{B_0}{\eta} \sin x \qquad \boldsymbol{B_0} = (B_0, \frac{B_0}{\eta} \cos x), \tag{8.6}$$

We can obtain the perturbation magnetic energy by subtracting the basic state from equation (8.6) from the total field equation (8.5), to obtain

$$PME = \text{energy of the (Total magnetic field} - \text{basic state of magnetic field)} \tag{8.7}$$

$$PME = \frac{1}{2}\int\int\left[(B_x - B_0)^2 + (B_y - \frac{B_0}{\eta}\cos x)^2\right]dxdy \tag{8.8}$$

By using the total field, then substituting into equation (8.8), we obtain:

$$\boldsymbol{B} = (B_x, B_y) = (B_0 + a_y, -a_x) \tag{8.9}$$

$$PME = \frac{1}{2}\int\int\left[(B_0 + a_y - B_0)^2 + (-a_x - \frac{B_0}{\eta}\cos x)^2\right]dxdy \tag{8.10}$$

then calculate the corresponding energy

$$PME = \frac{1}{2}\int\int\left[(a_y)^2 + (-a_x - \frac{B_0}{\eta}\cos x)^2\right]dxdy \tag{8.11}$$

To verify the numerical routines, we compare the hydrodynamic simulation in chapter 6 with the magnetic field implementation in this chapter by setting the magnetic field parameter $B_0 = 0$ to zero which refers to the hydrodynamic results and indicating how well the numerical routine that we performed. We also compare the linear calculations supported by linear theory in the chapter 4, with nonlinear simulation in this chapter, which provides a reasonable level of confidence that the simulation performed is well resolved.

8.2 Dedalus implementation

We use the Dedalus framework with the same approach used for of the hydrodynamic and vertical field problems in section 6.3.1. The Dedalus framework is set up using the Fourier bases and periodic domain as set out in (6.1). The horizontal magnetic field equations in section 8.1 are introduced with the problem object and integrated with the initial value problem scheme (RK443) using the same time integration step as in hydrodynamic and vertical field problems.

```
# Problem:domain and variables
problem = de.IVP(domain, variables=['om','omx','omy','psi','psix','psiy','go','psixx','psiyy','A','J',
                                                                    'Ax','Ay','Axx','Ayy','Jx','Jy'])
#Parameters
problem.parameters['nu'] = nu
problem.parameters['eta'] = eta
problem.parameters['B0'] = B0
#Vorticity equation
problem.add_equation("dt(om) - nu*dx(omx)-nu*dy(omy) - go -B0*Jx=-omx*psiy+omy*psix+ Jx*Ay-Jy*Ax")
problem.add_equation("om+dx(psix)+dy(psiy)+1e-6*psi=0")
#Magnetic vector potential equation
problem.add_equation("dt(A) - eta*(dx(Ax)+dy(Ay))-B0*psix= -Ax*psiy+Ay*psix ")
problem.add_equation("J+dx(Ax)+dy(Ay)= 0")
#First-order reduction
problem.add_equation("omx - dx(om) = 0")
problem.add_equation("omy - dy(om) = 0")
problem.add_equation("psix - dx(psi) = 0")
problem.add_equation("psiy - dy(psi) = 0")
problem.add_equation("psiyy - dy(psiy) = 0")
problem.add_equation("psixx - dx(psix) = 0")
problem.add_equation("Ax - dx(A)=0")
problem.add_equation("Ay - dy(A) = 0")
problem.add_equation("Axx - dx(Ax)=0")
problem.add_equation("Ayy - dy(Ay) = 0")
problem.add_equation("Jy - dy(J) = 0")
problem.add_equation("Jx - dx(J) = 0")
problem.add_equation("dt(go)= 0")
```

Figure 8.1: Governing equations solved numerically.

We created the main loop to allow arbitrary data interactions throughout the time integration process. We also add the magnetic energy (8.4) and the perturbation magnetic energy (8.11), while the perturbation kinetic energy and the enstrophy have been implemented into the system since the hydrodynamic problem in section 6.3.1.

```
# Setup storage
om.set_scales(1)
om_list = [np.copy(om['g'])]
t_list = [solver.sim_time]
u0y=np.sin(x)
om0=np.cos(x)
a0x=-(B0/eta)*np.cos(x)
B0y=B0*y
darea = (2*np.pi/ nx) * (2*np.pi*Ly / ny)
KE_list = [sum(sum(np.square(psix['g'])+np.square(psiy['g'])))*darea*0.5]
PKE_list = [sum(sum( np.square(psiy['g'])+ np.square(-psix['g']-u0y) ))*darea*0.5]
PKEtheory_list=[np.exp(2*(...)*solver.sim_time)*0.2]
enstrophy_list = [sum(sum(np.square(om['g'])))*darea]
Penstrophy_list = [sum(sum(np.square(om['g']-om0)))*darea]
ME_list = [sum(sum( np.square(B0+Ay['g']) + np.square(Ax['g']) ))*darea*0.5]
PME_list = [sum(sum( np.square(Ay['g'])+ np.square(-Ax['g']+a0x) ))*darea*0.5]
```

```
dt =0.01
while solver.ok:
    solver.step(dt)
    if solver.iteration % 100== 0:
        om.set_scales(1)
        om_list.append(np.copy(om['g']))
        t_list.append(solver.sim_time)
        print(solver.sim_time)
        KE_list.append(sum(sum(np.square(psix['g'])+np.square(psiy['g'])))*darea*0.5)
        PKE_list.append(sum(sum( np.square(psiy['g']) + np.square(-psix['g']-u0y) ))*darea*0.5)
        PKEtheory_list.append(np.exp(2*(...)*solver.sim_time)*0.2)
        enstrophy_list.append(sum(sum(np.square(om['g'])))*darea)
        Penstrophy_list.append(sum(sum(np.square(om['g']-om0)))*darea)
        ME_list.append(sum(sum( np.square(B0+Ay['g']) + np.square(Ax['g']) ))*darea*0.5)
        PME_list.append(sum(sum( np.square(Ay['g']) + np.square(-Ax['g']+a0x) ))*darea*0.5)
    if solver.iteration % 100 == 0:
        print('Completed iteration {}'.format(solver.iteration))
```

Figure 8.2: Main loop of time.

Then we add the initial conditions for ψ and the force ('go'). The initial conditions of the variables have been set through the initial value Solver built for each Problem and can be set in the grid space ('g'). The flow field is the basic state plus a small perturbation. The magnetic field here has a similar structure to the basic state but is different. We see it relax to the basic state early in the runs with some distance from the basic state as shown in Dedalus code (8.3).

```
# Setup a sine wave
x,y=domain.grids(scales=1)
om.set_scales(1)
go.set_scales(1)
psi['g'] = np.cos(x)+0.0*np.cos(y/Ly)+0.1*(0.1*np.sin(y/Ly)+0.5*np.cos(y/Ly))
go['g']  = (B0**2/eta)*np.cos(x)+nu*np.cos(x)
A['g'] =-(B0/eta)*np.sin(x)  #horizontal field basic state
J['g']=0;
```

Figure 8.3: Initial conditions of the flow ψ and horizontal magnetic field A.

8.3 Nonlinear behaviour & linear theory

We begin by comparing the linear analysis introduced in chapter 4 with the non-linear evolution of instability in the presence of the horizontal magnetic field, where the initial linear phase of instabilities has been computed by the perturbation theory in section 4.5. All the non-linear calculations in this chapter are initialized by adding a small perturbation to the equilibrium state defined in section 8.3.

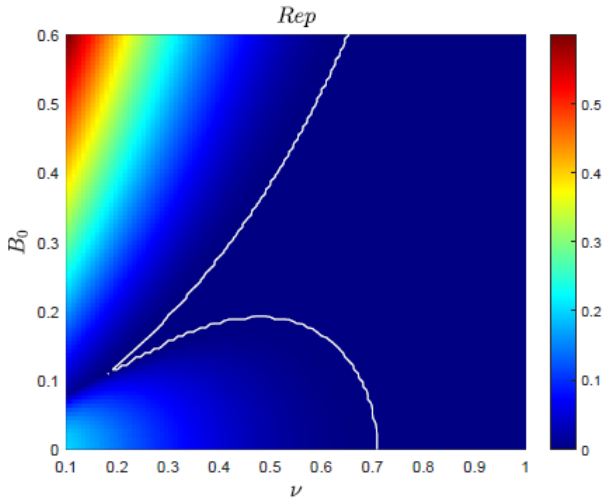

Figure 8.4: Instability growth rate of the $\mathrm{Re}\, p$ as a function of (ν, B_0) for $P = 1$. An explanation of the figure has been given in chapter 4.

Throughout this section, we remind the reader of the linear results and check the operation of the non-linear simulations in this chapter. We consider the linear results in figure 8.4 as a basis for simulations in this chapter determined by three magnetic field strengths, the weak field $B_0 = 0.1$ gives hydrodynamic instability (Meshalkin and Sinai, 1961). The strong field $B_0 = 0.5$ gives the magnetic field instability, and the intermediate case between these two instabilities $B_0 = 0.2$ gives a stable mode at $\nu < 0.3$ (more details discussed in chapter 4). For simplicity, the Prandtl number here is fixed to be unity. We are interested in how these stable and unstable modes evolve in a non-linear regime and how this varies with magnetic field strength B_0. Before constructing the non-linear evolution for figure 8.4, we plot the real part of the growth rate $\mathrm{Re}\, p$ against the wavenumber k to gain a better understanding of instability behaviour based on the linear results. Figure 8.5 displays three magnetic

field strengths, as selected from figure 8.4. As a result, we vary the viscosity value in order to identify the most unstable mode. We maintain the viscosity at $\nu = 0.3$ in order to allow the system to be unstable for $B_0 = 0.1, B_0 = 0.5$.

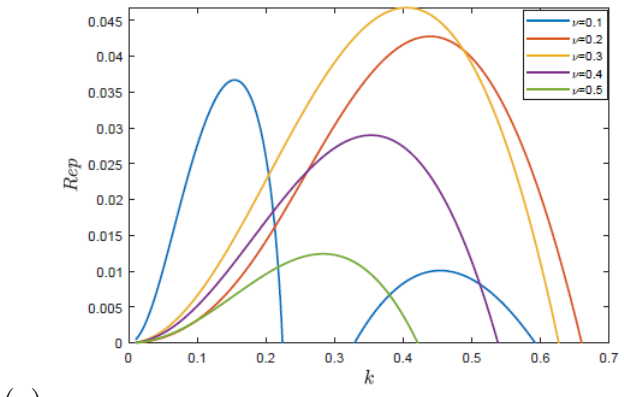

(a)

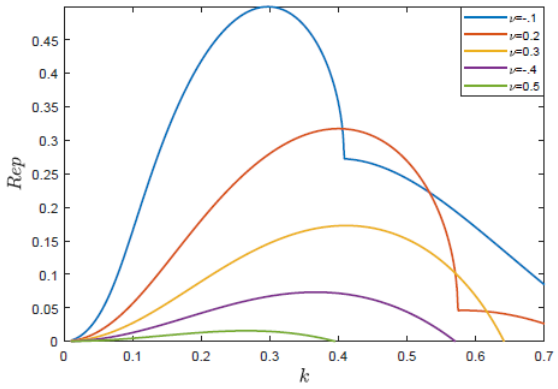

(b)

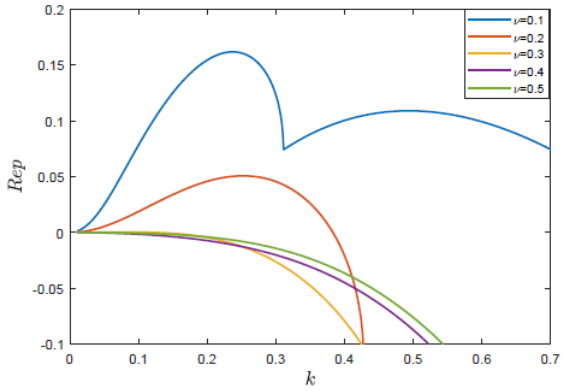

(c)

Figure 8.5: Linear growth rate showing $\mathrm{Re}\, p$ against k for various values of ν. Panel (a) unstable mode at $B_0 = 0.1$, panel (b) unstable mode at $B_0 = 0.5$, panel (c) stable & unstable modes at $B_0 = 0.2$.

Panel (a) shows that the instability for weak magnetic field $B_0 = 0.1$ corresponding to the flow branch of instability shown in figure 8.4, considered as the hydrodynamic branch, Meshalkin and Sinai (1961). This instability is observed at all the values of

viscosity ν but more clearly at small values (e.g. $\nu = 0.2$, red solid curve). Panel (b) shows instability for strong magnetic field $B_0 = 0.5$ corresponding to the field branch of instability shown in figure 8.4, where instability is observed at small values of viscosity, (e.g. at $\nu = 0.1$, blue solid curve). Panel (c) shows the intermediate case at $B_0 = 0.2$ in figure 8.4, the system is stabilised, roughly at the value $\nu = 0.3$ and subsequently higher. These values correspond to the region outside the instability threshold outlined by the white contour line $\mathrm{Re}\, p = 0$. Whereas, the system destabilises at two values of viscosity $\nu = 0.1, \nu = 0.2$ corresponding to the region inside the white curve $\mathrm{Re}\, p = 0$ as shown in figure 8.4.

8.4 MHD simulation

Our simulation is based on the periodic domain $2\pi L_x \times 2\pi L_y$ with a y-directed flow that varies sinusoidally in x, and a horizontal magnetic field in the x-direction. We run the simulation at the principal parameters, (ν, η, B_0) varying independently and used different initial conditions from the case of a vertical magnetic field. A quantitative analysis is conducted by considering the evolution of total energy and perturbation energy over time. This study also presents snapshots of the stream function of ψ and the total magnetic field $A = B_0 y + a$ at various times to illustrate the behaviour of the instability and to determine the saturation level.

Description	**Parameters**	**Typical values**
Strength of magnetic field	B_0	$0 \leqslant B_0 \leqslant 0.5$
Viscosity	ν	0.3
Magnetic diffusivity	η	0.2, 0.4
Box length (x)	$2\pi L_x$	1, 2
Box length (y)	$2\pi L_y$	2, 4
Number of grid point	N	$32^2 \leqslant N^2 \leqslant 50^2$
Time step	dt	0.01
Wavenumber in y-axis	k	$0.5, (L_y = 2)$
Wavenumber in x-axis	ℓ	$0.5, (L_x = 2)$

Table 8.1: Shows the parameters used to calculate numerical solutions. The third column presents the typical values/ranges of each of these parameters.

Table 8.1 shows a list of parameters used in our simulations; we keep the viscosity value fixed at $\nu = 0.3$ as we found unstable modes at this value. The simulations presented here use a resolution of $N_x \times N_y = 50^2$. Increasing the domain size requires an increase in the number of points in our numerical grid. In this chapter, we also run the simulation at magnetic field strength up to $B_0 = 0.5$. However, we observed that increasing the strength of the magnetic field (e.g. $B_0 = 0.7, B_0 = 1$) results in an unstable mode, as shown in figure 8.4, but we found that $B_0 = 0.5$ has better performance. We keep the time step at 0.01, with convergence tests performed at smaller time step values by checking that changes in spectral energy with the resolution are minimal between different runs.

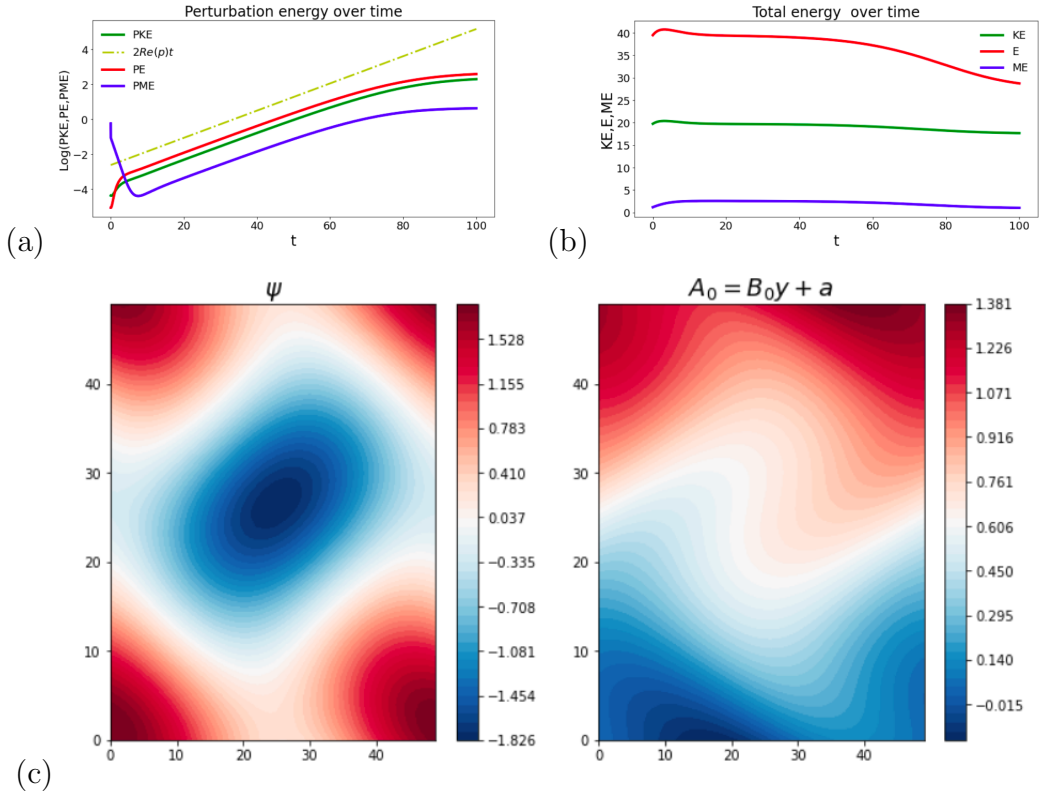

Figure 8.6: Kinetic energy & enstrophy and magnetic energy run up to $t = 100$ for $\nu = \eta = 0.3, B_0 = 0.1$ and wavelengths $L_y = 2, L_x = 1$. Panels (a,b) show perturbation and total energy over time, and Panel (c) shows streamlines of flow Ψ, and magnetic lines $A_0 = B_0 y + a$. Perturbation energies are shown alongside the linear growth rate agrees with yellow dashed lines $E \propto (2pt)$ with $p = 0.0389 - 0.0000i$.

Figure 8.6 shows a simulation corresponding to the yellow curve $\nu = 0.3$ of the weak field $B_0 = 0.1$ in figure 8.5 (a) and also represents the flow branch of instability in figure 8.4. Panels (a,b) show the perturbation energy growing over time and the total

energy tends to a steady state over the simulation time. We ran the simulation at a weak field $B_0 = 0.1$ and domain size $(x, y) = (2\pi, 4\pi)$ and found a result similar to the hydrodynamic simulation in figure 6.7. We can see clearly the perturbation energy agrees with the linear scale (dashed yellow) at positive growth rate $\mathrm{Re}\, p = 0.0389$; the linear scale agrees with the linear evolution when the perturbation energy is simulated at time $t = 80$ and after that disagrees during the nonlinear-evolution. We observe that for small B_0 the stretching effect of the magnetic field on the vortices is negligible compared to the rate at which they are bent out by the background flow as shown in panel (c). Similar to the case of purely hydrodynamic flow, we can observe that the flow motion organizes the vortices into roughly Robert flow across the periodic domain as shown in the plot of ψ in figure 6.7(c).

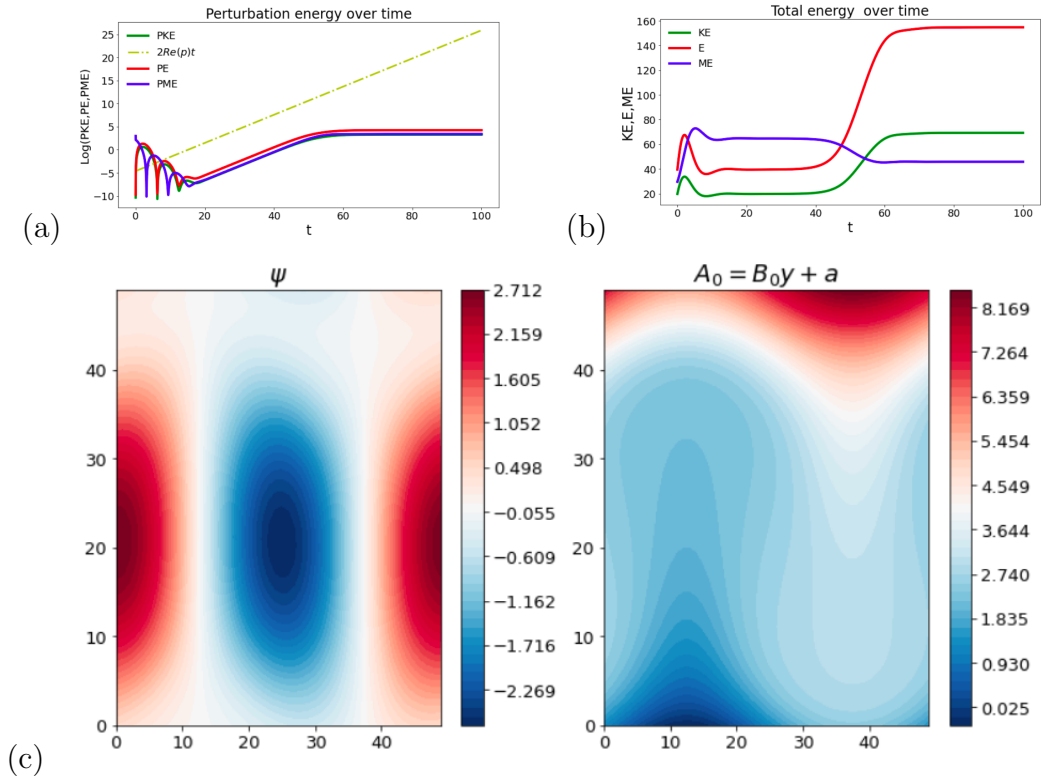

Figure 8.7: Kinetic energy & enstrophy and magnetic energy over time run up to $t = 100$ for $\nu = \eta = 0.3, B_0 = 0.5$ and wavelengths $L_y = 2, L_x = 1$. Panels (a,b) show perturbation and total energy over time, Panels (c,d) streamline flow Ψ and magnetic lines $A_0 = B_0 y + a$. Perturbation energies are shown alongside the linear scale (yellow dashed line) $E \propto (2pt)$ with $p = 0.1524 + 0.0000i$.

Another simulation is run with a strong magnetic field $B_0 = 0.5$ shown in figure 8.7 corresponding to the yellow curve in figure 8.5 (b) and also represents the field branch of instability in figure 8.4. Panels (a,b) show the perturbation & total energy

over time run up to $t = 100$; the energy starts with a decaying oscillation from $t = 0$ to $t = 20$, then growing linearly from $t = 20$ to $t = 40$ in agreement with the linear scale (yellow dashed), and eventually the energy tends to a steady state at a later time. We can see clearly in panel (b) that the magnetic energy (blue) is greater than the kinetic energy (green) from $t = 0$ to $t = 60$, then the energy is extracted from the magnetic field. Here we take $L_y = 2, L_x = 1$, the wavelength for small wavenumbers $k = 0.5, \ell = 0$. There is an initial period when the system relaxes to the basic state before becoming unstable as shown in figure 8.7 (a). We use different initial conditions as shown in figure 8.8.

In panel (c), we see the Lorentz force working to modify the vortices created by the body force. The magnetic field breaks the vortex into two vortices as shown in the streamlines of the flow ψ. We also note that, when a strong field is introduced, Alfvén waves are generated in the system which creates tearing mode behaviour in the plot of A. The positive region of magnetic potential A corresponding to negative regions of ψ. The tearing mode instability has also been studied in Boldyrev and Loureiro (2018) as well as parasitic modes for magnetorotational instabilities, the latter involving a basic state of both sinusoidal magnetic and flow fields (e.g. Pessah, 2010).

```
# Setup a sine wave
x,y=domain.grids(scales=1)
om.set_scales(1)
go.set_scales(1)
psi['g'] = np.cos(x)
go['g']  = (B0**2/eta)*np.cos(x)+nu*np.cos(x)
A['g'] =-(B0/eta)*np.sin(x)
J['g']=0
# Add a small perturbation to our basic state
A['g']=A['g']       + 0.001*np.exp(0.008*np.sin(y/L)+0.005*np.cos(y/L)- np.cos(x))
psi['g'] = psi['g'] + 0.001*np.exp( np.cos(y/L)+0.6 * np.sin(y/L)+ 0.5*np.sin(x))
```

Figure 8.8: Basic state with small perturbations

We write the initial conditions used for figure 8.7 mathematically as follows:

$$A = -(B_0/\eta)\sin x + 0.001e^{(0.8\sin(y/\ell)+0.5\cos(y/\ell)-\cos(x))} \tag{8.12}$$

$$\psi = \cos x + 0.001e^{(\cos(y/\ell)+0.6\sin(y/\ell)+0.5\sin(x))} \tag{8.13}$$

The initial conditions for ψ & A have the basic state plus a term somewhat arbitrarily chosen to give a general initial perturbation. We observed that the initial kinetic energy and magnetic energy shows an oscillatory damping going to negative logarithm values as shown in figure 8.7.

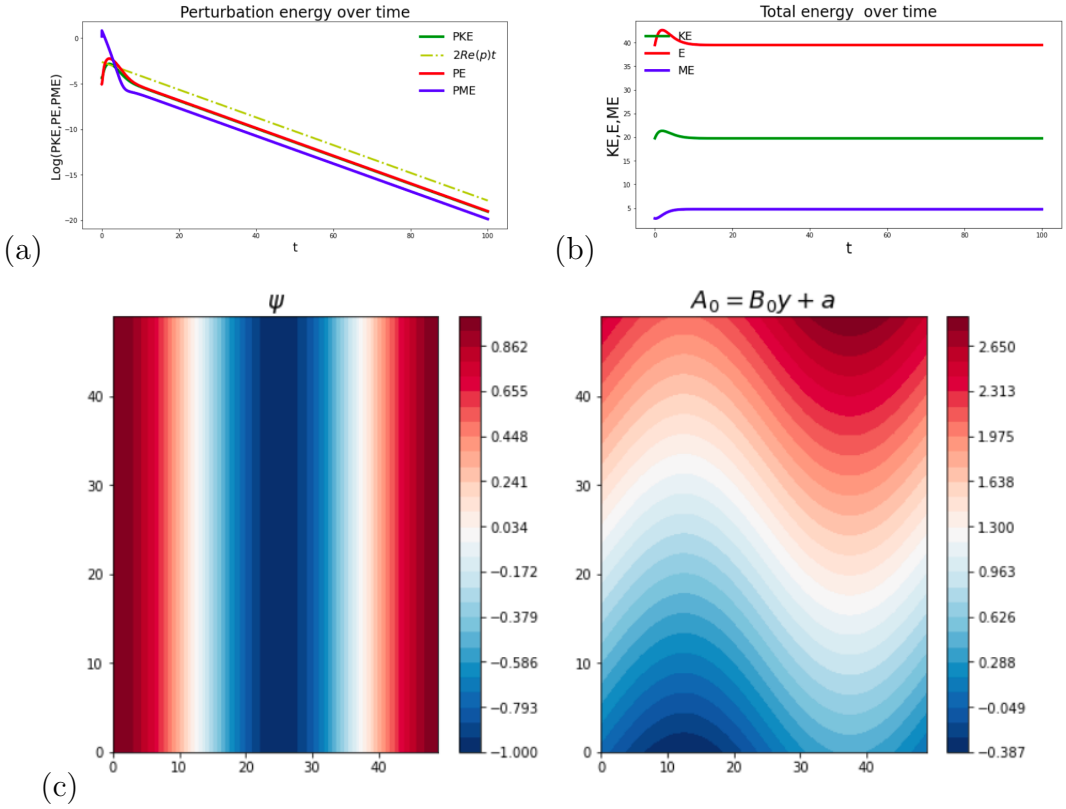

Figure 8.9: Kinetic energy & enstrophy and magnetic energy run up to $t = 100$ for $\nu = \eta = 0.5, B_0 = 0.2$ and wavelength $L_y = 2, L_x = 1$. Panels (a,b) show perturbation and total energy over time, panels (c,d) streamlines of flow ψ, magnetic lines $A = B_0 y + a$, Perturbations energies are shown alongside the linear growth rate indicated by (yellow dashed line) $E \propto (2pt)$ with $p = -0.0762 - 0.0000i$.

Figure 8.9 shows a simulation corresponding to the decay mode (solid green) in figure 8.5(c) and represents the region between the two families of instability in figure 8.4. Panels (a,b) show kinetic energy and enstrophy, and magnetic energy at the largest scale dissipates more quickly, while the total energy tends to a steady state behaviour. The simulation runs up to $t = 100$ with the parameter values $B_0 = 0.2, \nu = 0.5$. We change the value of viscosity here to see the stability behaviour as we increase ν, This parameter value indicates that the energy loss is due to the high viscosity, and not to the under-resolving of the runs. To ensure completeness, we compared the decay mode with the prediction value of growth rate $p = -0.0762$ determined by the dashed yellow line in panel (a); this test revealed a

good agreement between the linear calculation and the result from the nonlinear code.

We also observed that the weak initial field pushes the initial perturbation magnetic energy (PME) curve up as shown in figure 8.9 (a). We observe that the vertical axis y shows the exponential decay and the initial perturbation magnetic energy (PME) going to large negative logarithm values. We found that the stretching effect of the magnetic field on the vortices suppressed the streamlines of the flow ψ as shown in panel (c) and bent out by the background flow as shown in the plot of A. Reducing the value of B_0 results in unstable mode, Robert's flow behaviour, as illustrated in figure 8.6(c). We can find an unstable mode at $\nu = 0.2$ (red curve) by changing the wavelength $L_y = 2$ to $L_y = 5$ corresponding to a large scale wavenumber $k = 0.2$ in figure 8.5(c).

8.5 MHD simulation at $P = 1$

Further analysis has been performed for the simulation in section 8.4, quantifying the saturation of instability by increasing the simulation time. We rerun simulation 8.6 and 8.7 at a much larger time t and at the same parameter values and domain size to verify the nonlinear evolution and saturation levels.

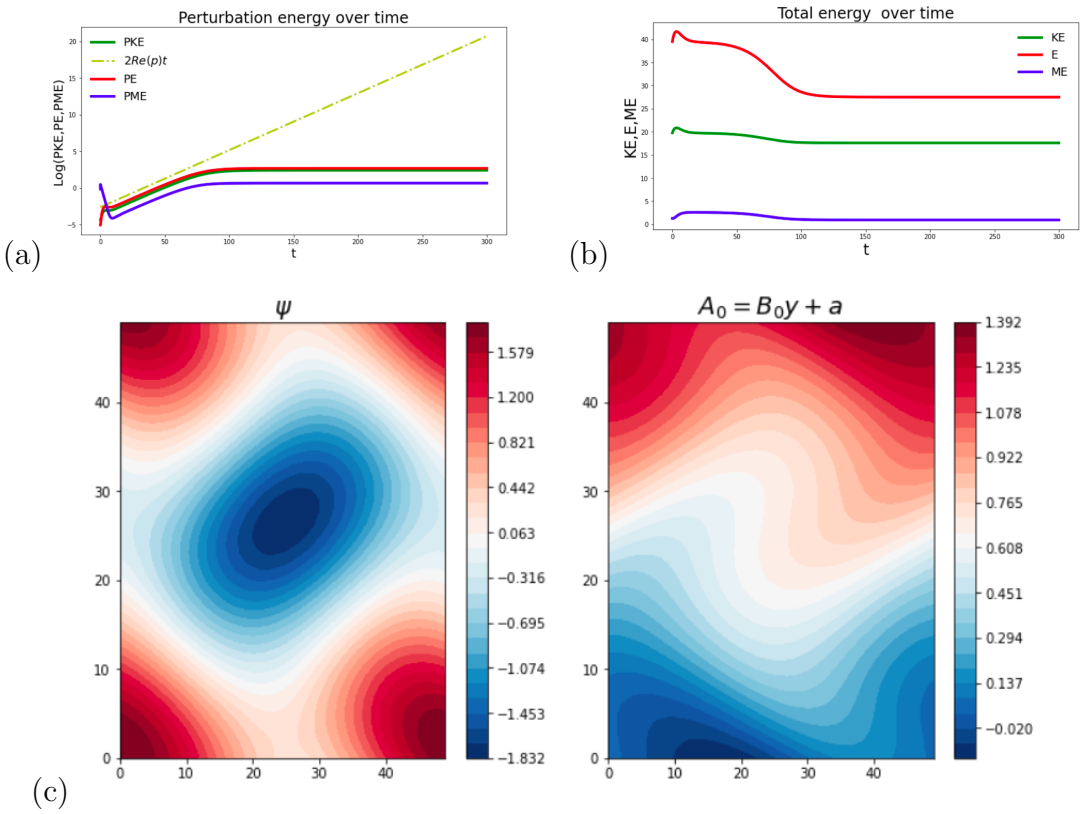

Figure 8.10: Kinetic energy & enstrophy and magnetic energy over time run up to $t = 300$ for $\nu = \eta = 0.3, B_0 = 0.1$ and wavelengths $L_y = 2, L_x = 1$. Panels (a,b) show perturbation and total energy over time, Panels (c,d) streamline flow Ψ, magnetic lines $A = B_0y + a$, Perturbations energies are shown alongside the linear growth rate with (yellow dashed line) $E \propto (2pt)$ with $p = 0.0389 - 0.0000i$.

According to figure 8.10, we run the simulation at the same parameter values in figure 8.6, for $\nu = 0.3$, and weak field $B_0 = 0.1$, where the simulation time has been increased from $t = 100$ to $t = 300$. We observe that the perturbation energy in panel (a) begins with a transient, then agrees with the linear scale (yellow dashed) from $t = 0$ to $t = 100$, and then tends to a steady state at a later time. Panel (b) shows the kinetic energy decays from $t = 0$ to $t = 100$ then tends to a steady state at a later time. We observed that the stretching effect of the magnetic field on the vortices isn't affected by increasing the simulation times as shown in panel (c) where the streamlines of flow ψ take the same Roberts flow pattern in the absence of a strong impact of Lorentz forces leads to a wavy magnetic line in the plot of A. However, panel (c) shows a similarity to the apparently well-structured hydrodynamic case given in Figure 8.6(c) and confirms the same non-linear evolution behaviour in both figures and allows them to reach the saturation level.

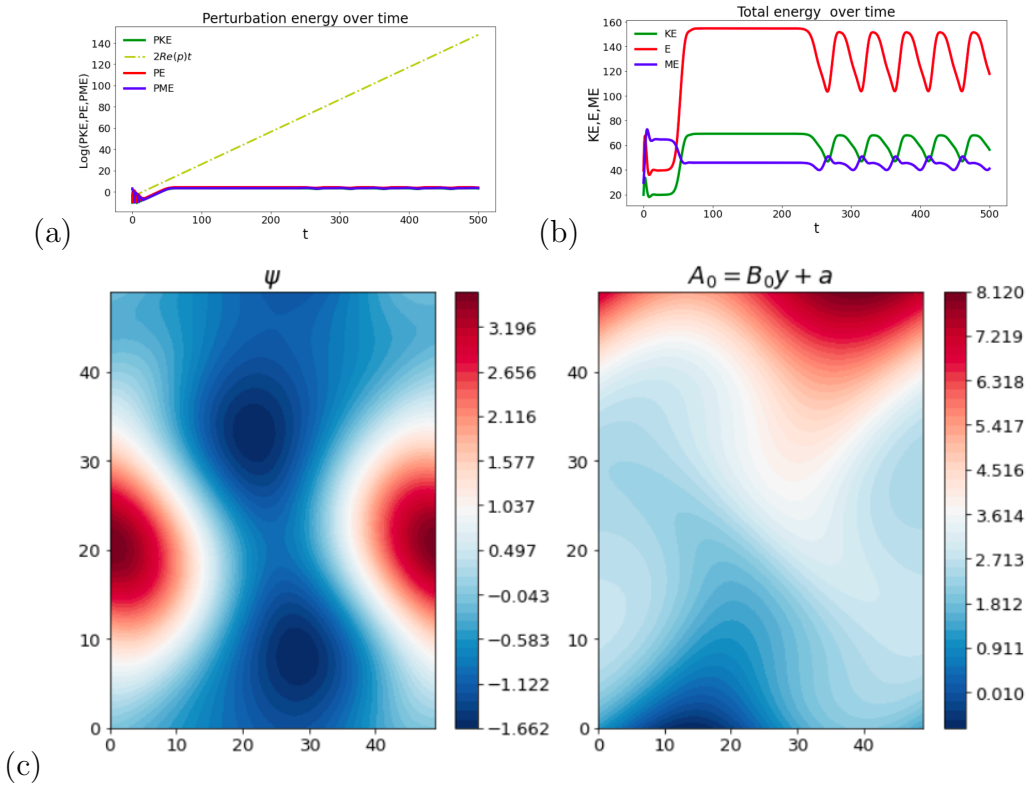

Figure 8.11: Kinetic energy & enstrophy and magnetic energy over time run up to $t = 500$ for $\nu = 0.3, B_0 = 0.5$. Panels(a,b) show perturbation and total energy over time, Panel (c,d) streamline of flow Ψ, magnetic field lines $A = B_0 y + a$, Perturbation energies are shown alongside the linear growth rate determined by (yellow dashed line) $exp(2pt)$ with $p = 0.1524 + 0.0000i$.

Figure 8.11 shows a simulation with $\nu = 0.3$, and a strong field $B_0 = 0.5$ similar to the simulation in figure 8.7, with a longer run to $t = 500$. We can see clearly that the total energy begins with a quasi-steady state from $t = 0$ to $t = 100$, then oscillatory behaviour from $t = 300$ to $t = 500$. However, the perturbation energy in panel (a) shows similar behaviour to figure 8.7 (a) and exhibits oscillatory behaviour from $t = 100$. We can not see this oscillation clearly due to the logarithmic axis. We observed an initial agreement between linear scale (yellow dashed) and linear instability evolution from $t = 0$ to $t = 100$. The instability behaviour in panel (c) changes with increasing the simulation time. The tearing mode instability in the plot of A becomes wavy magnetic lines in panel (c), while the vortices in the streamlines of flow ψ merge and become periodic vortices with different signs. We run the simulation at the same domain size and the wavelengths $L_y = 2, L_x = 1$ as we found the instability and the agreement between the linear calculation and linear scale at this value.

8.6 MHD simulation: Prandtl number

In this section, we will discuss a number of important topics. We first remind the reader of the linear stability in the presence of a horizontal magnetic field and varying Prandtl number from low e.g. $P = 0.5$ to larger e.g. $P = 2$ values in chapter 4. We observed two branches of instability present at small Prandtl number $P = 0.5$; see figure 4.6 (a,b). We also observed an oscillatory mode attached to the field branch at larger Prandtl number $P = 2$, particularly at $\nu = 0.1$, and in the range $0.04 < B_0 < 0.14$, visible in the $k_{\max}$ plot in figure 4.6(d). Our motivation in this section is to understand how this instability develops over time and show the instability behaviour with varying Prandtl numbers.

parameter	values
B_0	0.1, 0.2, 0.5
L_y	2, 4
t	100, 300, 500
ν	0.2
P	$1, 0.5, 2$
$N_x \times N_y$	32×32
	50×50 otherwise

Table 8.2: Typical parameter values employed in our investigation for the horizontal magnetic field and $P < 1$, $P > 1$.

We run our simulation at the specific parameter values as shown in the table 8.2; where the typical values/ranges of each of these parameters are given in the second column. These parameter values are not determined randomly but depend on our findings in the linear instability regime (see figure 8.12). The magnetic field strength choices correspond to figure 8.5, and the viscosity indicates the most unstable mode for each magnetic field strength as shown in figure 8.5. The simulation domain size is increased properly with the wavelength values and the Prandtl number values in the table depend on our findings for the linear results in figure 8.12.

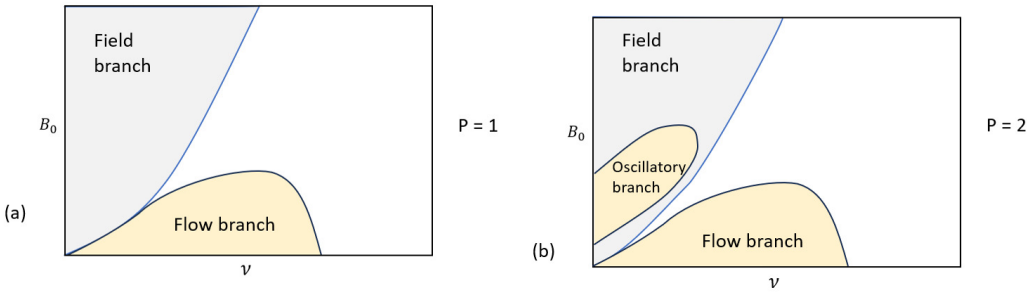

Figure 8.12: Schematic of the maximum growth rate as a function (B_0, ν), panel (a) shows $\mathrm{Re}\, p$ at $P = 1$, panel (b) shows $\mathrm{Re}\, p$ at large Prandtl number $P = 2$.

Figure 8.12 shows a schematic diagram of the instability growth rate for varying Prandtl numbers. Panel (a) shows instability at $P = 1$ and panel (b) shows instability at large Prandtl number $P = 2$. Further explanation and discussion are given in chapter 4. We refer to figure 4.6 to remind the reader of our linear results and the effect of varying the Prandtl number in the linear regime before studying the non-linear evolution. In this section, we haven't run simulations at much larger or smaller values of the Prandtl number. We highlight our simulations at two choices of Prandtl numbers $P = 0.5$ and $P = 2$. A review of figure 8.12 will allow the reader to gain a clear understanding of Prandtl number differences, as well as being easy to link to the simulations provided in this section.

8.6.1 MHD simulation at large Prandtl number, $P = 2$

Our observation shows that linear instability is driven at a larger Prandtl number $P = 2$ and wavenumber $k = 0.5$ corresponding to the oscillatory branch in figure 8.12(b); we need to determine how this oscillatory mode saturates. We run the simulation up to $t = 500$, with resolution $N^2 = 50^2$ and domain size $(x, y) = (2\pi, 4\pi)$ with box size $L_y = 2$ along the y-axis, and $L_x = 1$ along the x-axis, the scale in y-direction taking the form $L_y = 1/k, k = 0.5$. For a better understanding of the evolution of this oscillatory mode, we always go back to the linear analysis and identify the value at which it becomes unstable.

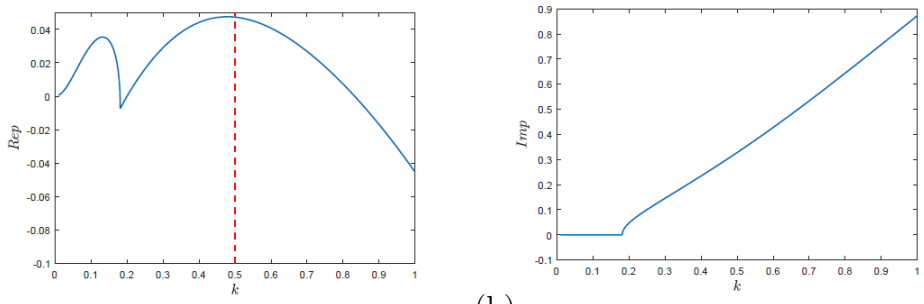

(a) (b)

Figure 8.13: instability growth rate for the maximum $\mathrm{Re}\, p$ against k with $\nu = 0.15, B_0 = 0.1, P = 2$, (a) $\mathrm{Re}\, p$, (b) $\mathrm{Im}\, p$, with $p = 0.0473 + 0.3279i$, the red dashed line indicates the most unstable mode at $k = 0.5$.

Figure 8.13 shows the instability growth rate with the parameter values corresponding to a yellow island of instability in figure 8.12 (b) visible at $\nu = 0.15, B_0 = 0.1$. The red dashed line in figure 8.13 (a) indicates the most unstable mode at small wavenumber $k = 0.5$, this oscillatory mode has a frequency in the imaginary part $\mathrm{Im}\, p$ appearing in panel (b). Essentially, the large Prandtl number causes the oscillatory behaviour attached to the magnetic field branch of instability with non-zero imaginary part.

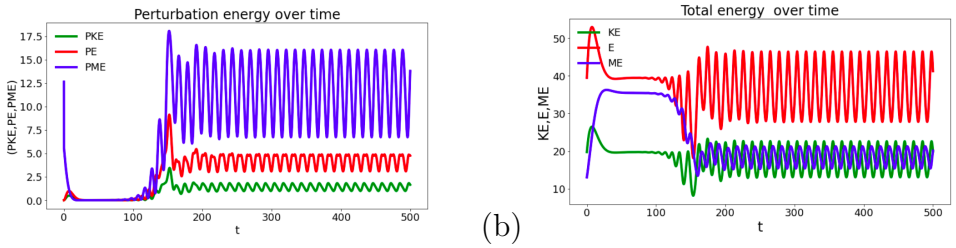

(a) (b)

Figure 8.14: Kinetic energy & enstrophy and magnetic energy run up to $t = 500$ and $L_y = 2, L_x = 1$ for $P = 2$, $\nu = 0.15, B_0 = 0.1$. Panels (a,b) show perturbation and total energy & enstrophy over time, with a positive growth rate $p = 0.0473 + 0.3279i$ shown in figure 8.13.

Figure 8.14 shows perturbation and total energy over time. Panels (a,b) show a quasi-steady state from $t = 0$ to $t = 200$ and exhibit an oscillatory behaviour from $t = 200$ to a later time in both panels, where magnetic energy (blue) is strong and greater than the kinetic energy (green) in both panels.

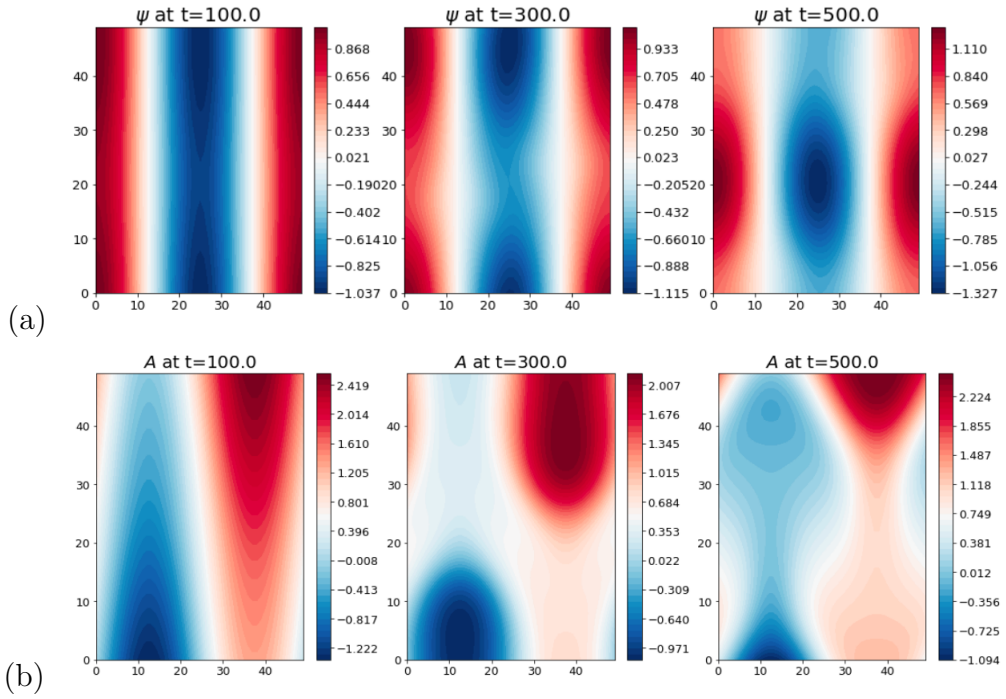

Figure 8.15: Streamline of flow Ψ, and magnetic field lines $A = B_0 y + a$.

Figure 8.15 illustrates snapshots of streamlines ψ and magnetic lines A reflecting the oscillatory behaviour shown in figure 8.14. There are straight streamlines of flow at $t = 100$ that result in a quasi-steady state in panel 8.14(a), while at $t = 300$ there are two parallel vortices seen clearly in the plot of A and a small vortex in the plot of ψ. At $t = 500$, large vortices can be seen in the streamlines of flow, however, they are blended into the A plot leading to wavy magnetic lines.

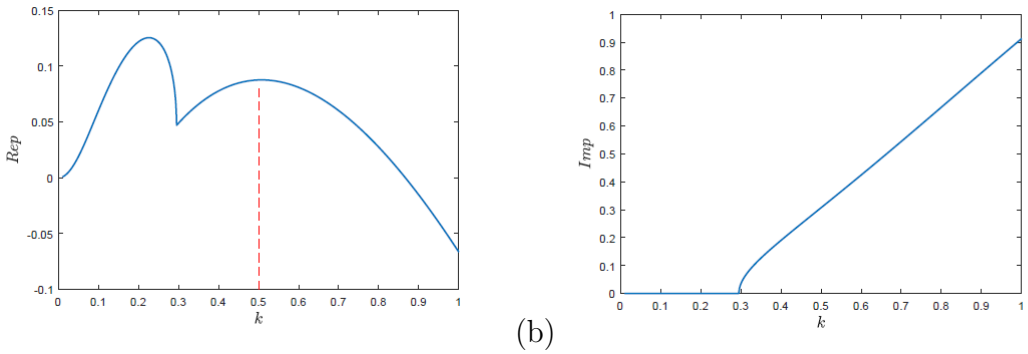

Figure 8.16: Instability growth rate of $\mathrm{Re}\, p$ against wavenumber k, for $P = 2$, and $\nu = 0.2, B_0 = 0.2$, with positive growth rate $p = 0.0876 + 0.3072i$, panel (a) $\mathrm{Re}\, p$, panel (b) $\mathrm{Im}\, p$.

We also look at instability corresponding to the magnetic field branch (grey region)in figure 8.12 (b) at the parameter values $\nu = 0.2, B_0 = 0.2$, and small wavenumber $k = 0.5$ outlined by the dashed red line indicated the most unstable mode as shown

in figure 8.16 (a). This instability has two peaks the second peak correspond to non-zero imaginary part $\mathrm{Im}\, p$ appearing in panel 8.16(b). While the first peak has zero imaginary part. This instability is also associated with the orange curve in figure 4.4, and chapter 4.

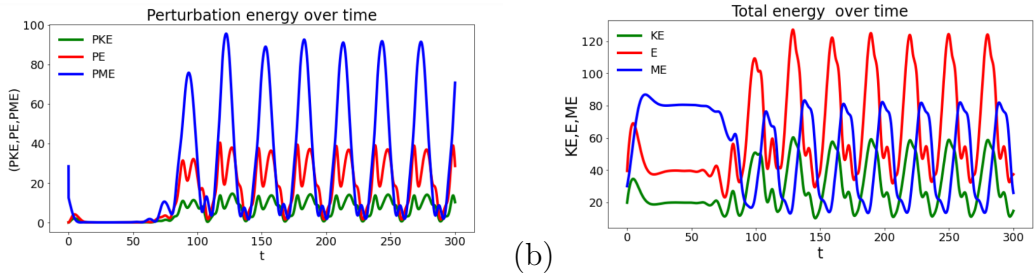

(a) (b)

Figure 8.17: Kinetic energy & enstrophy and magnetic energy over time run up to $t = 300$ for $\nu = 0.2, B_0 = 0.2, P = 2$. Panels (a,b) show perturbation and total energy & enstrophy over time, $L_y = 2, L_x = 1$, with linear positive growth rate $p = 0.0876 + 0.3072i$ comes from figure 8.16.

We can see clearly that the energy exhibits a quasi-steady state from $t = 0$ to $t = 100$ in panels (a,b), then the oscillatory behaviour from $t = 150$ to a later time. The magnetic energy (blue) is strong in both panels (a,b) showing greater than the kinetic energy (green). Similar examples can be found in Kobayashi, Gürcan and Diamond (2015) for zonal flow in plasma. Generally speaking, this type of effect appears quite frequently in fluid dynamics and convection and is known as a relaxation oscillation, especially in the limit where the oscillatory peaks become quite widely separated. Hence, there is a clear phase where instability is excited (the peak) and then a longer period (the decaying piece) where the system behaves stably - then the process repeats.

(a)

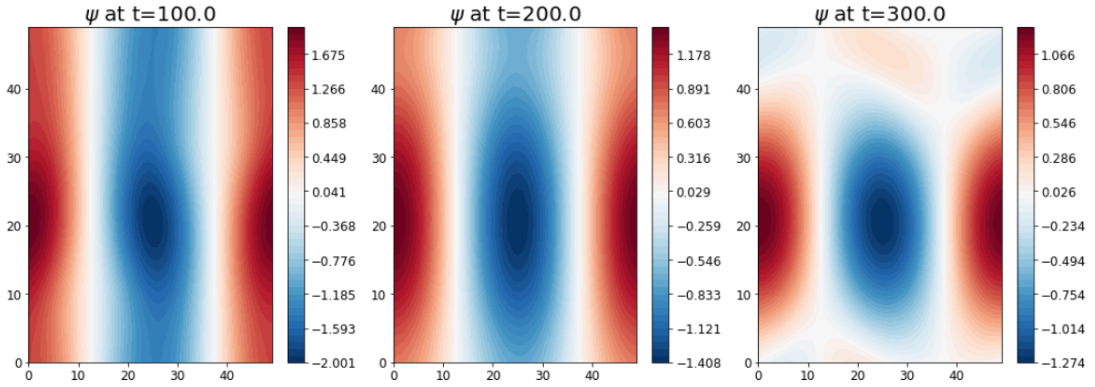

(b)

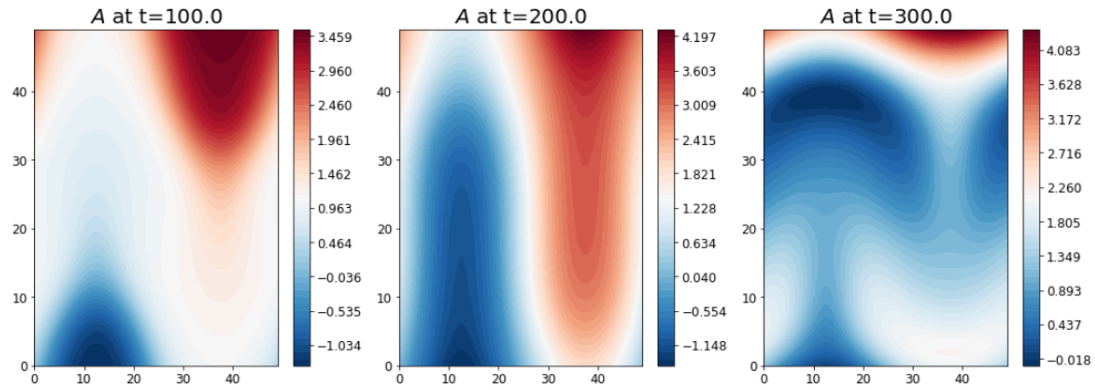

Figure 8.18: Snapshots of streamline of flow Ψ, and magnetic lines $A = B_0 y + a$.

It can be seen in figure 8.18 that the system tends to form a tearing mode in the plot of A that gradually merges to the same size permitted by the simulation domain in panel (b). This is broadly consistent with the simulation presented in figure 8.7 for $P = 1$ and $B_0 = 0.5$. Panels (a,b) show snapshots of streamlines ψ and magnetic lines A corresponding to perturbation & total energy in figure 8.17 (a,b). There are the straight streamlines of ψ at $t = 100$ referring to a quasi-steady state in figure 8.17, whereas at $t = 200$ and $t = 300$ the oscillatory behaviour with strong magnetic energy (blue) leads to a strong wavy line and tearing mode at a later time in the plot of A 8.18(b) and the periodic vortices in figure 8.18(a). We also observed that the kinetic & magnetic energy oscillate together over time leading to deformations of the vortices in figure 8.18 (a).

8.6.2 MHD simulation at small Prandtl number, $P = 0.5$

Linear stability analysis shows the same instability structure for $P = 1$ appearing with a small Prandtl number $P = 0.5$ (see section 4.3.1 panel (a)). In this section, we need to see the instability evolution at a small Prandtl number $P = 0.5$. To understand the instability behaviour we refer back to the linear results by determining the unstable mode with a positive growth rate shown in figure 8.19.

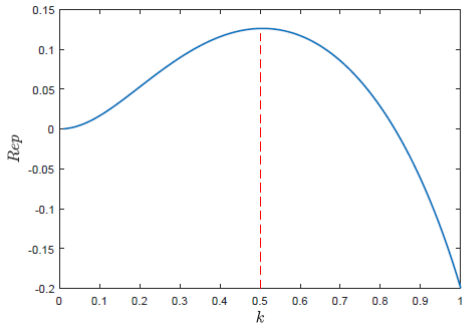

Figure 8.19: Instability growth rate for $\mathrm{Re}\, p$ against k for small Prandtl number $P = 0.5, \nu = 0.5\eta, \eta = 0.2$, and weak field $B_0 = 0.1$. Red dashed shows unstable mode of the value $p = 0.1260 + 0.0000i$ at $k = 0.5$.

First, we plot the growth rate against the wavenumber k for the parameter values $P = 0.5$ and weak field $B_0 = 0.1$ corresponding to the flow branch of instability in scheme 8.12(a). The red dashed line indicates an unstable mode at small wavenumber $k = 0.5$ associated with zero imaginary part $\mathrm{Im}\, p = 0$.

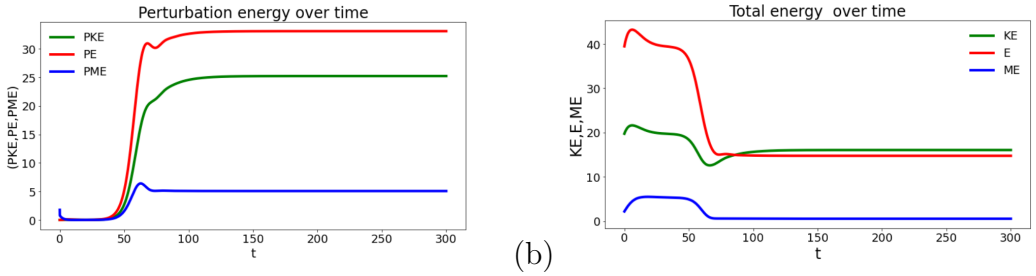

(a) (b)

Figure 8.20: Kinetic energy & enstrophy and magnetic energy over time, run up for $t = 300$ and $P = 0.5, B_0 = 0.1$. Panels (a,b) show perturbation and total energy & enstrophy over time.

For this purpose, we run a simulation with a domain size of $(x, y) = (2\pi, 4\pi)$, and wavelengths of $L_x = 1, L_y = 2$, and simulation time runs up to $t = 300$. Figure 8.20 shows that the perturbation energy has a quasi-steady state initially from $t = 0$ to $t = 50$ then growing from $t = 50$ to a later time, while the total energy decays

initially from $t = 0$ to $t = 50$, the kinetic energy (green) decay from $E_k = 20$ to $E_k = 15$ at $t = 50$ then both panels have a steady state at the final time, we can see clearly the kinetic energy (green) is strong and weak magnetic energy (blue) showing lower levels in both panels. Comparing with figure 8.17 we can see that the system no longer exhibits time-dependent behaviour where the total energy gradually going to steady state over time.

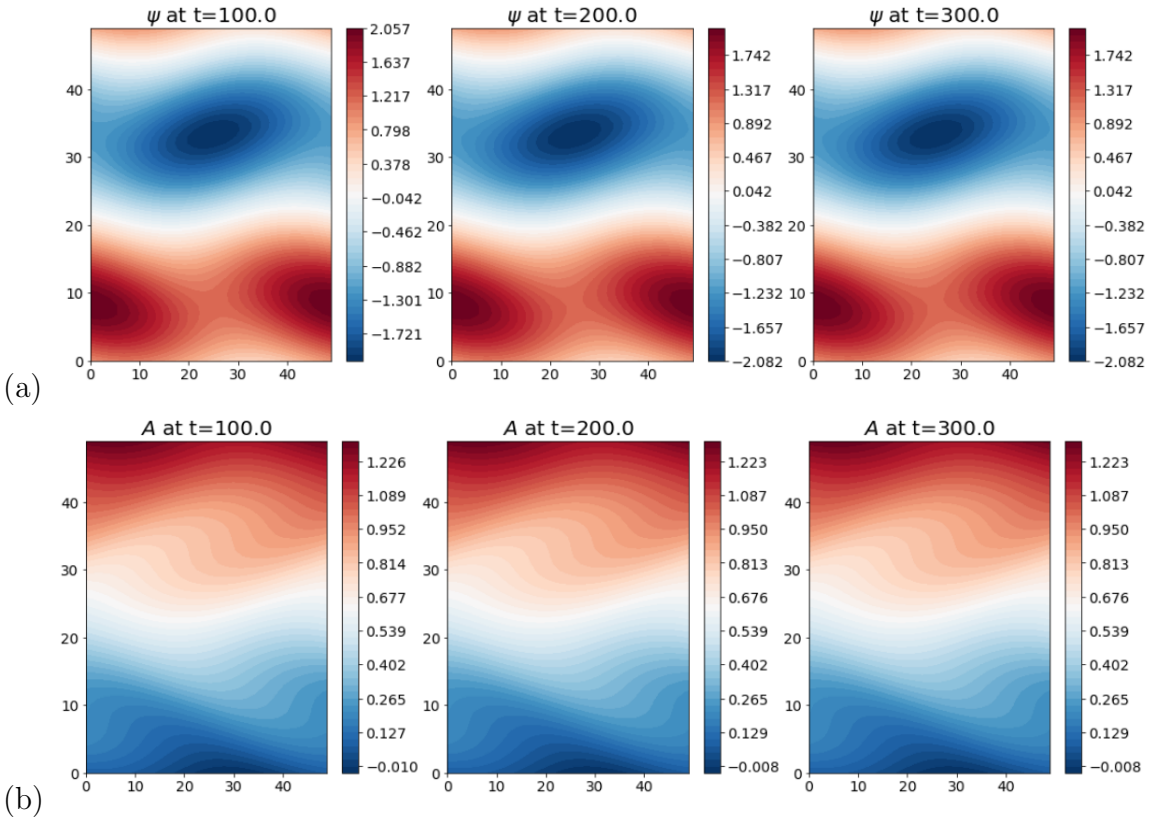

(a)

(b)

Figure 8.21: (a) Snapshots of a streamline of flow Ψ, and (b) magnetic field lines $A = B_0 y + a$.

We run the simulation with a snapshot of streamlines ψ & magnetic field lines A shown in figure 8.21 corresponding to the total and perturbation energy in 8.20 panels (a,b). We can see clearly large vortices centred in the streamlines of flow ψ along the simulation times, and a wavy horizontal field in the plot of A, As we pointed out, both panels (a,b) in figure 8.21 exhibit the same instability behaviour due to the quasi-stationary state from $t = 100$ to $t = 300$ in figure 8.20(a,b).

8.7 MHD simulation at Floquet wavenumber $\ell \neq 0$

The linear analysis shows that the instability is enhanced by Floquet wavenumber ℓ when the horizontal field is present (see chapter 5). In this section, we run the simulation by increasing the domain size in x-direction from $L_x = 1$ to $L_x = 5$ at large-scale Floquet wave $\ell = 0.2$, associated with the wavelength $L_y = 5$ linked to the large wavenumber $k = 0.2$ in the y-direction, then the domain size becomes $(x, y) = (10\pi, 10\pi)$, we use the parameter values $\nu = 0.2, B_0 = 0.2$ corresponding to the figure 5.4 (c,d). We observed that the effect of the Floquet wavenumber increases the scale in the x-direction and opens up the possibility of other modes of flow in the plot of flow ψ with repeated Kolmogorov flow in the x-direction.

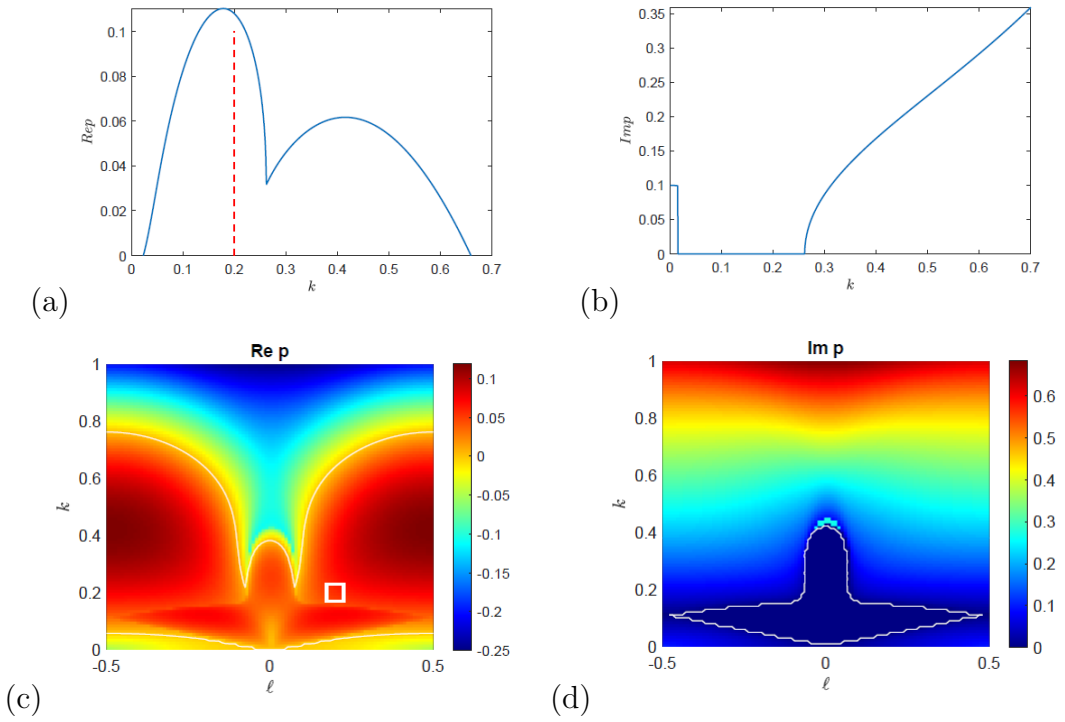

Figure 8.22: Instability of growth rate at $\nu = 0.2, B_0 = 0.2$, and $\ell = 0.2$. Panels (a,b) show $\mathrm{Re}\, p$ against k, the red dashed line corresponds to $k = 0.2$, panels (c,d) show the colour plot of linear growth rate as a function of the wavenumbers (ℓ, k).

To understand the instability behaviour we plot $\mathrm{Re}\, p$ against k for $\nu = 0.2, B_0 = 0.2$ shown in figure 8.22 (a,b), where the red dashed line $k = 0.2$ in panel (a) indicate that the system is unstable at small wavenumbers with zero imaginary part $\mathrm{Im}\, p = 0$ in panel (b). These parameter values correspond to the white square around the

wavenumbers $\ell = 0.2, k = 0.2$ in panel (c).

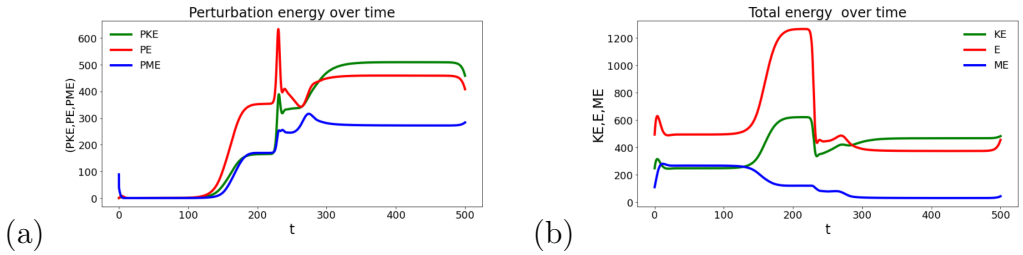

(a) (b)

Figure 8.23: Kinetic energy & enstrophy and magnetic energy over time run up to $t = 500$ and domain size $(x, y) = (10\pi, 10\pi)$ for $P = 1$. Panels (a,b) show perturbation and total energy & enstrophy over time.

Figure 8.23 (a) shows simulation at large domain size $(x, y) = (10\pi, 10\pi)$, and the parameter values $B_0 = 0.2, \nu = 0.2$ corresponding to figure 8.22 (c,d); we can see clearly that the perturbation and total energy exhibit a quasi-steady state from $t = 0$ to $t = 100$, then growing at the peak $t = 200$ then tend to steady state to a later time. We also notice that the magnetic energy (blue) is weak showing a lower level than the kinetic energy in panel (a) while going to steady state in total energy in panel (b) from $t = 100$ to a later time.

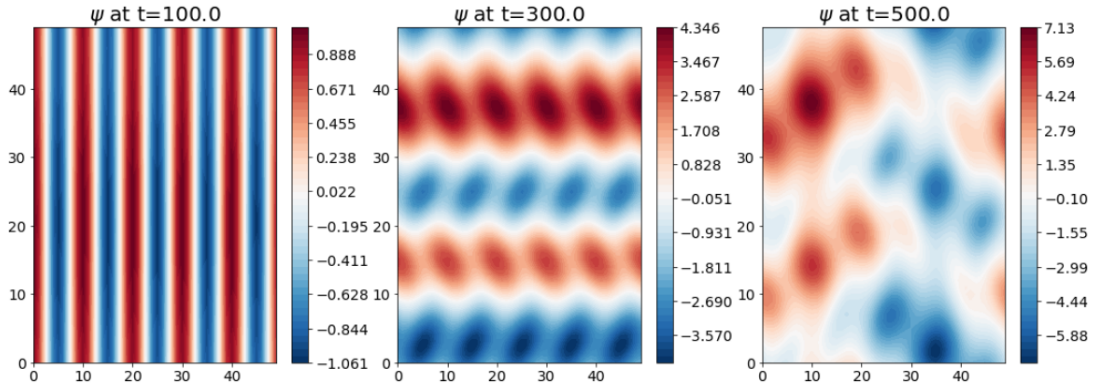

(a)

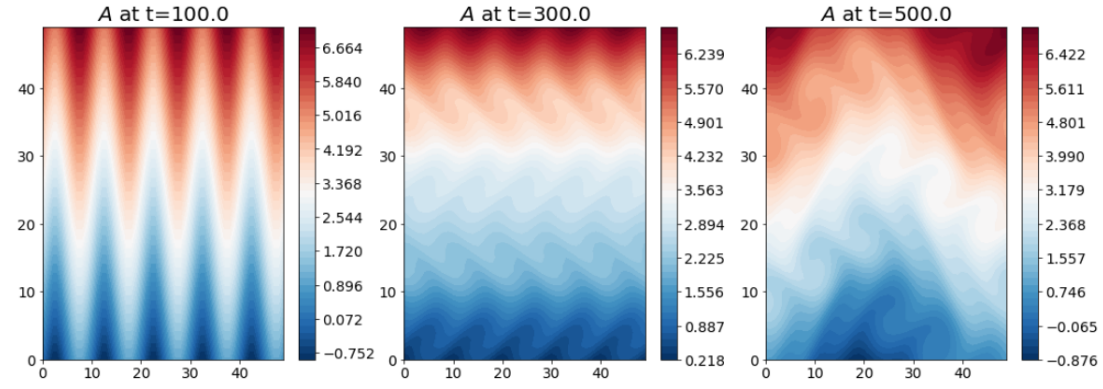

(b)

Figure 8.24: Snapshots of streamlines of flow ψ, and magnetic field lines $A = B_0 y + a$ run at the same parameter values as in figure 8.23.

Figure 8.24 shows snapshots of streamlines ψ and magnetic lines A reflecting the energy behaviour in figure 8.23. We can see clearly at $t = 100$ there are straight streamlines of ψ and magnetic lines of A due to a quasi-steady state in 8.23(a,b). The significant changes appear at $t = 300$ and $t = 500$ in the streamlines of flow ψ due to the energy growing at this time. Hence, the vortices emerge and gather to create a large-scale structure in the plot of ψ showing the nonlinear cascade behaviour.

Here we extend our investigation of non-linear evolution for $P = 1$ by also conducting a simulation for a weak magnetic field $B_0 = 0.2$ and $\nu = 0.6$ and a small wavenumber in the x, y-direction $k = 0.05, \ell = 0.05$ corresponding to the most unstable mode in the butterfly of instability in figure 8.25(c,d). To understand the instability behaviour we plot $\mathrm{Re}\, p$ against k for $\nu = 0.6, B_0 = 0.2$ shown in figure 8.25 (a,b), where the red dashed line corresponding to the value $k = 0.05$ in panel (a) indicate that the system is unstable at small wavenumbers with zero imaginary part $\mathrm{Im}\, p = 0$ in panel (b). These parameter values correspond to the white square around the wavenumbers $\ell = 0.05, k = 0.05$ in panel (c).

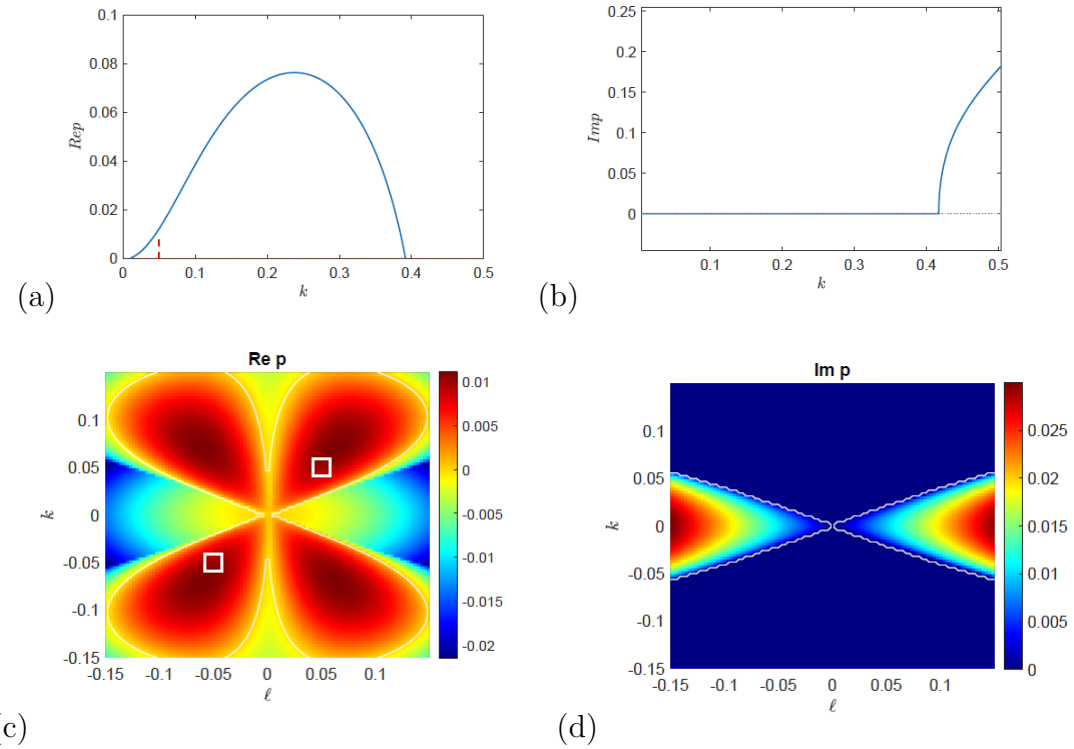

Figure 8.25: Instability of growth rate at $\nu = 0.6, B_0 = 0.2$, and $k = 0.05, \ell = 0.05$. Panels (a,b) show $\mathrm{Re}\, p$ against k, the red dashed line corresponds to $k = 0.05$, panels (c,d) show the colour plot of linear growth rate as a function of the wavenumbers (ℓ, k).

We run the simulation by increasing the domain size in x-direction $L_x = 20$ linked to the large-scale Floquet wavenumber $\ell = 0.05$, associated with the wavelength $L_y = 20$ linked to the small wavenumber $k = 0.05$ in the y-direction. Then the domain size becomes $(x, y) = (40\pi, 40\pi)$ and we also increase the resolution to $N^2 = 100$. Figure 8.26 shows perturbation and total energy over time, run at $t = 1000$ for the parameter values $\nu = 0.6, B_0 = 0.2$ corresponding to the figure 5.4 (c,d). Both panels exhibit a quasi-steady state between $t = 0$ and $t = 800$, then a growing energy to later times, the magnetic energy (blue) showing greater than the kinetic energy (green) in panel (a), while in panel (b) the energy has reached a steady state. Here we altered k along with ℓ as we chose a specific point from figure 8.25 at $(k, \ell) = (0.05, 0.05)$, then see the instability behaviour at this point. The results of this simulation are very tentative as the simulation is probably under-resolved. Further work is needed to obtain clear & definite results here.

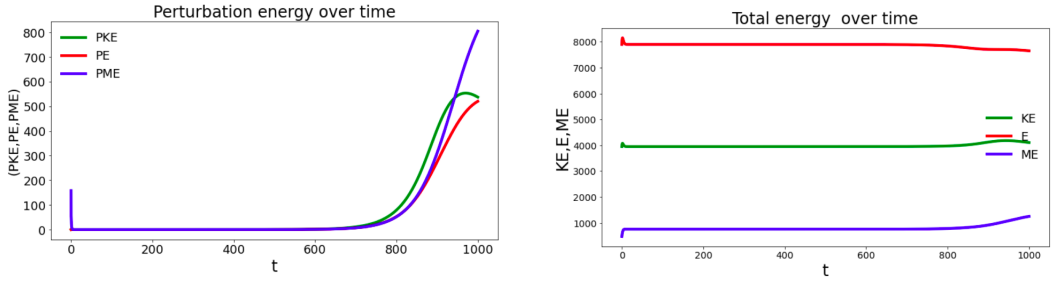

Figure 8.26: Kinetic energy & enstrophy and magnetic energy over time run up to $t = 1000$ and domain size $(x, y) = (40\pi, 40\pi)$ for $P = 1$. Panels (a,b) show perturbation and total energy & enstrophy over time.

Figure 8.27 shows snapshots of streamlines ψ and magnetic lines A reflecting the energy behaviour in figure 8.26. We can see clearly at two first times $t = 100$ and $t = 500$ there are straight streamlines of ψ and horizontal magnetic lines of A due to a quasi-steady state in 8.26 (a,b). The significant changes appear at $t = 1000$ in the streamlines of flow ψ there is a large structure due to the energy growing at a later time. Hence, a large-scale structure is located in the centre of the magnetic lines in the plot of A, as we increase the simulation time we obtain the same large-scale structure behaviour in both panels.

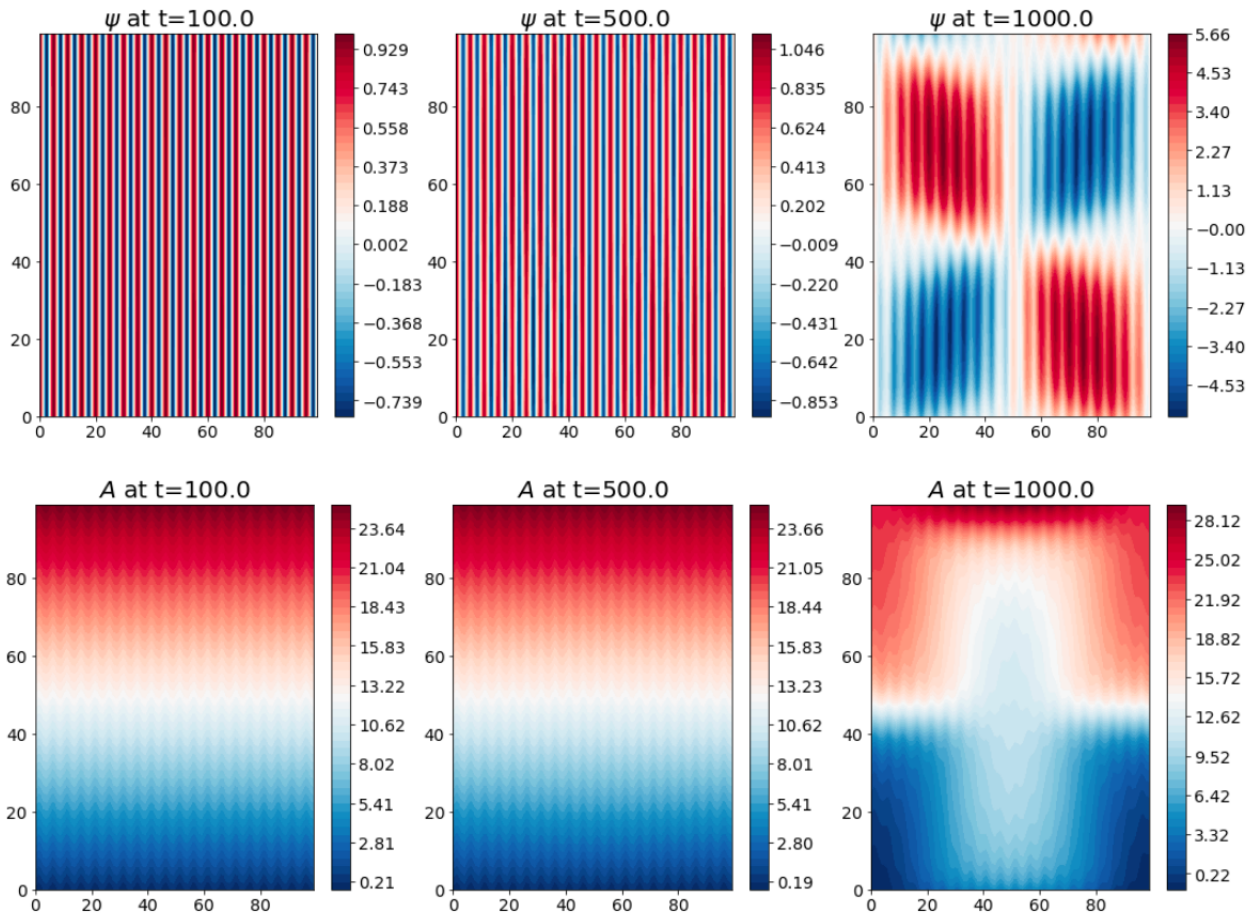

Figure 8.27: Snapshots of streamlines of flow ψ, and magnetic field lines $A = B_0 y + a$ run at the same parameter values as in figure 8.25 (a,b).

8.8 MHD inverse cascade: horizontal field

The history of the inverse cascade in my thesis starts from the hydrodynamic case (chapter 6), where the energy gathers to create a large-scale structure. Our observation is that a uniform vertical magnetic field arrested the inverse cascade as shown in Legras, Villone and Frisch (1999). In this section, we look at the inverse cascade with a horizontal magnetic field which can be weak or strong corresponding to figure 8.4.

8.8.1 Weak magnetic field

For comparison with the hydrodynamic case, we perform simulations using the same parameter values $B_0 = 0.1$ and $\nu = 0.2$ and domain size $(x, y) = (10\pi, 10\pi)$. We run the simulation up to $t = 1000$ as shown in figure 8.28. Panels (a,b) show the

evolution of total energy which initially decays and then quickly exhibits oscillatory behaviour from $t = 200$ to a later time. While the perturbation energy has a steady state initially from $t = 0$ to $t = 200$, then oscillatory behaviour to a later time. in both panels, we observed the kinetic energy (green) is greater than the magnetic energy (blue). The inverse cascade behaviour can be determined by a simulation of streamlines of flow ψ and magnetic lines A (see figures 8.29, 8.30).

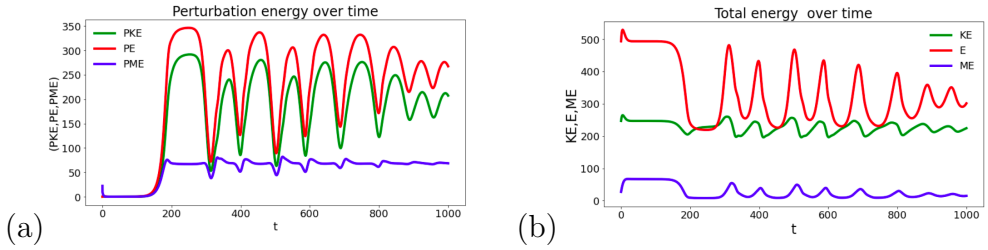

Figure 8.28: Simulation of kinetic energy (green) & enstrophy (red) and magnetic energy (blue), domain size $(x, y) = (10\pi, 10\pi)$ with wavelength $L_x = 5, L_y = 5$ run up to $t = 1000$ for $\nu = 0.2, B_0 = 0.1$, (a) evolution of perturbation energy, (b) evolution of total energy.

The kinetic energy inverse cascades are released by weak magnetic fields $B_0 = 0.1$. There are small vortices formed in the streamlines at $t = 500$ corresponding to the oscillatory behaviour of total energy in figure 8.28(b). Eventually, we observed that these small vortices merge at $t = 1000$ and create a large-scale structure in the plot of ψ.

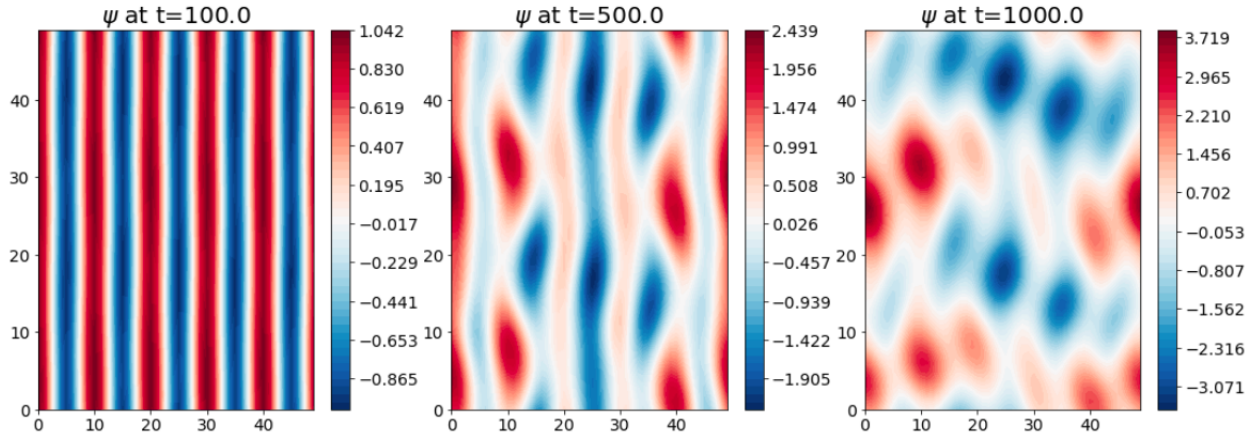

Figure 8.29: Kinetic energy cascade of stream function ψ run up the same parameter values of figure 8.28, enhanced by a weak magnetic field $B_0 = 0.1$.

Figure 8.30 shows snapshots of magnetic field lines corresponding to the evolution of the perturbation energy in figure 8.28 (a). At $t = 100$ there is a wavy magnetic line, where the wavelength in x-direction forms another mode in the flow lines as in

section 8.7. This behaviour corresponds to the initial quasi-steady state in figure 8.28 (a) and at the other two times we find the emergence of these wavy lines resulting in the magnetic field enhancing the energy transferred to larger scales.

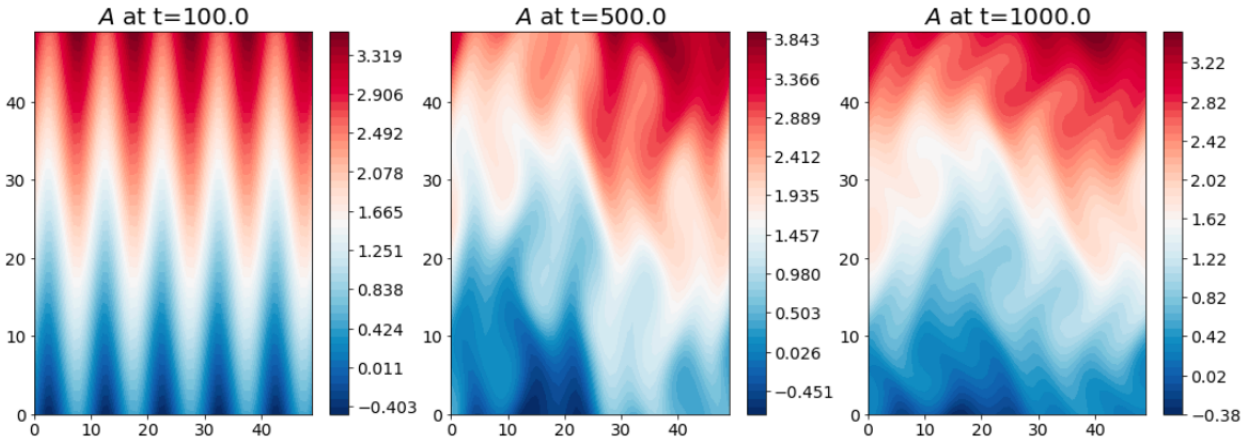

Figure 8.30: Snapshots of magnetic energy over time run at the same parameter values of figure 8.28.

8.8.2 Strong magnetic field

We also performed simulations at a strong magnetic field $B_0 = 0.5$ and $\nu = 0.2$ corresponding to the magnetic field branch in figure 8.12(a) with the domain size $(x, y) = (4\pi, 4\pi)$. We observed that the energy gathers to create a large-scale structure; a similar situation can also be found in section 8.8.1, with a weak magnetic field enhanced the inverse cascade.

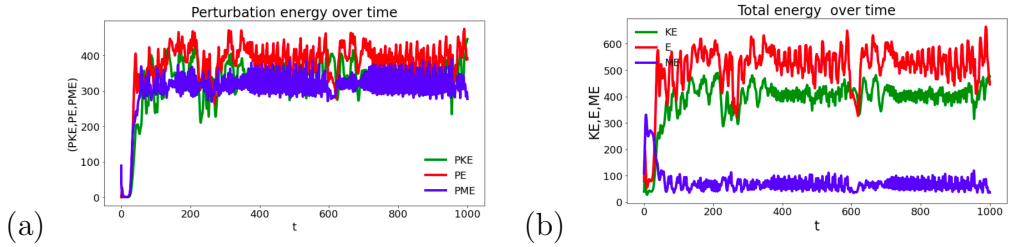

(a) (b)

Figure 8.31: Simulation of kinetic energy (green) & enstrophy (red) and magnetic energy (blue), domain size $(x, y) = (4\pi, 4\pi)$ with wavelength $L_x = 2, L_y = 2$ run up to $t = 1000$, for $\nu = 0.2, B_0 = 0.5$.(a) Evolution of perturbation energy, (b) evolution of total energy.

In figure 8.31, perturbation and total energy are plotted over time in panels (a,b); both panels initially exhibit a transient followed by plenty of oscillations from $t = 200$ to a later time $t = 1000$, the oscillations of kinetic energy (green) appearing greater than magnetic energy (blue) in panel (b). We run the simulation at a double

wavelength $L_x = L_y = 2$. It was not necessary to increase the wavelength where the energy cascade appears at an early stage.

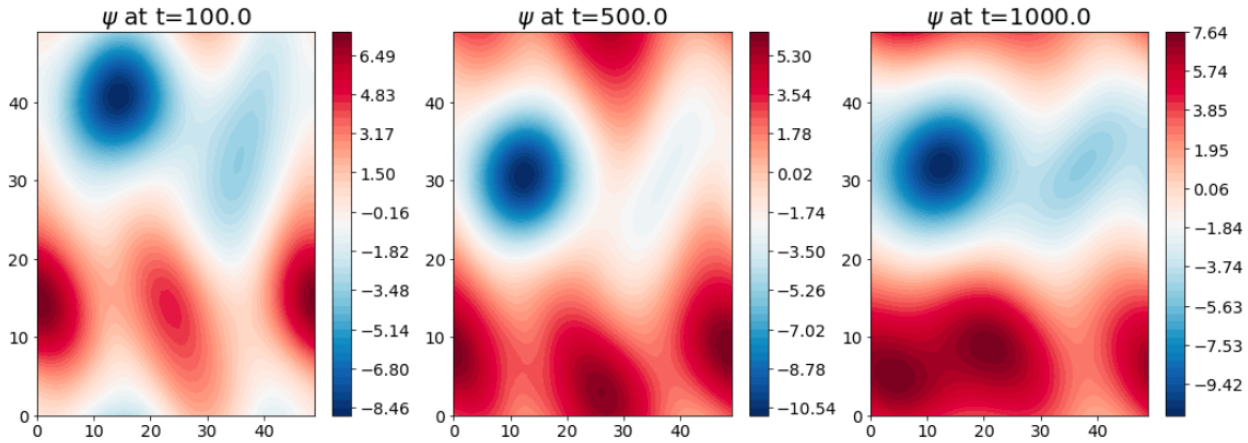

Figure 8.32: Kinetic energy inverse cascade of stream function ψ run at the same parameter values of figure 8.31, the energy cascade evolved for a strong magnetic field $B_0 = 0.5$.

Figure 8.32 shows the snapshots of stream function ψ, We can see clearly at $t = 100$ the system created periodic vortices with a large blue vortex appearing in the streamlines of flow due to an oscillation behaviour in figure 8.31 (b), While at $t = 500$ the energy evolution shows the kinetic energy oscillation is parallel to the magnetic energy oscillation, but with a time shift. As a result, the positive vortices (red) of figure 8.32 merge. The significant change occurs at $t = 1000$ when kinetic energy is strong and the magnetic energy decays, allowing the vortices to form large structures.

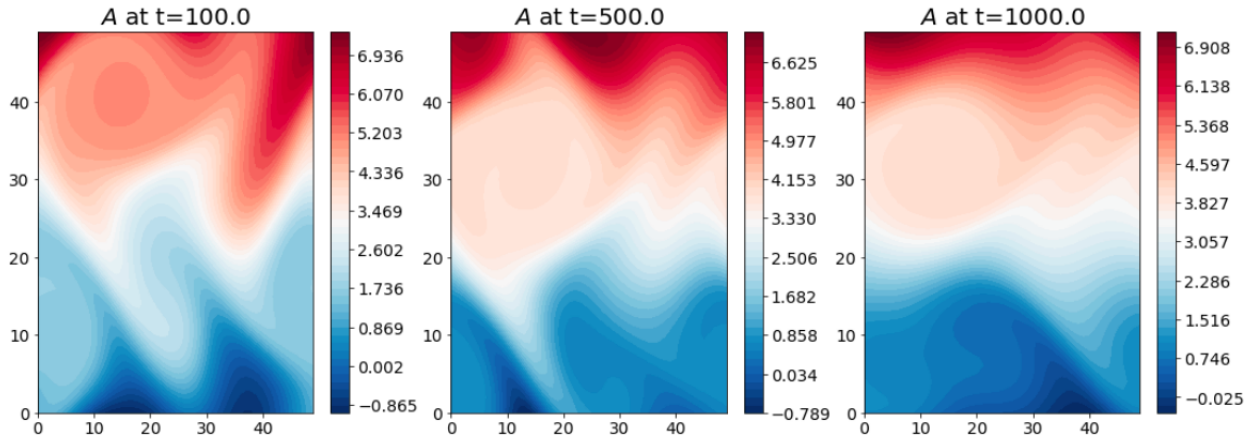

Figure 8.33: Snapshots of magnetic field lines over time run at the same parameter values in the above figures.

As can also be observed in figure 8.33 the magnetic field A, at the three times

selected, there are wavy magnetic lines caused by the oscillation of the magnetic field in 8.31(a). Finally, we conclude that the weak magnetic field contributes to the inverse cascade, while in Figure 8.33, the strong magnetic field generates the inverse cascade at an early stage because the instability grows faster.

8.9 Conclusion

In this chapter, we have discussed the following findings:

- In section 8.3 we have investigated the evolution of unstable modes for weak horizontal fields and found the saturation level compares closely with its hydrodynamic counterpart.

- In section 8.3 we also perform a simulation with a strong horizontal field. As a result, the system exhibited a significant change in the stream function of flow ψ and tearing mode at $P = 1$ in the plot of the magnetic field A as shown in figure 8.7, this tearing mode also exists for $P = 2$ in figure 8.18.

- Consistent with previous work, we implement simulations with a Floquet wavenumber ℓ, which increases the domain size in the x-direction, and for unstable Kolmogorov flow we observed another Fourier mode in the x direction as shown in section 8.7. We have seen that after a quasi-steady state, the system evolves to a chaotic time-dependent state with large-scale vortices seen clearly in the plot of ψ. This is evidence of inverse cascade behaviour in this system.

- The introduction of magnetic fields with a high Prandtl number and small magnetic diffusion produces a relaxation oscillation response (see figure 8.17). This may have implications for research into rotating two-dimensional MHD.

- A horizontal magnetic field causes an inverse cascade, where the energy cascade is enhanced by a weak field in section 8.8.1 and a strong field enhances the energy transfers to a large-scale structure, creating an inverse cascade in section 8.8.2.

- In our simulations, we consider variations of Prandtl numbers particularly at $P = 0.5$ and $P = 2$, and we find that the dynamics of instability differ significantly with the changing of Prandtl numbers. The box sizes for all the simulations take the form $2\pi L_x \times 2\pi L_y$, with the variation of the wavelengths (L_x, L_y) in x and y directions appropriately with simulation time.

9. Conclusion

In this thesis, we have found novel results from analytical theory, numerical methods and computational simulations. This chapter involves a comparison of these results and provides a brief summary of the purely hydrodynamic results and the magneto-hydrodynamics results. We consider some interesting future work and explore some of the results covered in this thesis.

9.1 Hydrodynamics

We have investigated instability on a unidirectional profile with single wavenumber k in classical Kolmogorov flow. General properties on instability from the work of Meshalkin and Sinai (1961) and Manfroi and Young (2002) were reviewed in chapter 2, looking at the unstable Fourier mode formulated by an eigenvalue problem. First, we concentrated on the hydrodynamic problem with no underlying magnetic field.

Kolmogorov flow is characterised by the velocity field profile $\boldsymbol{u_0} = (0, \sin x)$. We note that many of the instabilities seen by us and by other authors can be characterised as involving a negative eddy viscosity term $\nu_E k^2$ or a negative eddy magnetic diffusivity term $\eta_E k^2$ at large scales. The growth rate $p(\ell, k)$ in the case of hydrodynamic flow shows instability at an arbitrary large scale and dependence on the angle α, the angle between the background vorticity gradient and the y-axis and β-effect as shown in figure 2.8. We found an excellent agreement with Manfroi and Young (2002), while we didn't initially find agreement in the case of $\alpha = 0$, we needed to increase the Reynolds number $R > R_c$ to find unstable modes. This was confirmed by including a Floquet wavenumber ℓ in the system as shown in figure 2.4. In agreement with

Meshalkin and Sinai (1961), we determined the instability criterion of inverse critical Reynolds number $\nu_c = 1/\sqrt{2}$ and found the key results of the hydrodynamic problem behind their research.

For nonlinear evolution, analytical and numerical simulation was checked using the Dedalus framework in chapter 6. A fixed value of viscosity was selected to show linear unstable Fourier mode evolution. Despite not using an eigenfunction at the beginning of the simulation, we found a good agreement between linear and non-linear simulation as shown in 6.12 and with Floquet wavenumber in figure 6.13 where the linear phase is long enough for the perturbations to adjust to the optimal growing mode. Simulations show that the inverse cascade of structures to large scales in y is arrested by the β-effect as set out in Frisch, Legras and Villone (1996), while we observed that the vortices gathered and created a Kolmogorov inverse cascade at $\beta = 0$.

9.2 Magnetohydrodynamics

Regarding the MHD effect in this thesis, we consider instability for two magnetic field orientations: *vertical field* aligned with the Kolmogorov flow, and *horizontal field* aligned with the possibility of jet formation. We recognize that this study is somewhat far from the practical application as discussed in chapter 1: the solar tachocline is a more appropriate region to determine the interaction between magnetic fields and waves in a β-plane, e.g. Hughes, Rosner and Weiss (2007). A tachocline may have other physical characteristics, such as stratification, and its origin and persistence are not yet completely understood. However, Diamond et al. (2007) argues that understanding MHD plays an important role in understanding how Alfvén and Rossby waves interact. Our work examines such processes within a linear instability framework & then via nonlinear simulation. We study the coupled MHD system by introducing the Lorentz force to the linear framework, and we observed that the magnetic suppression of instability first discussed by Meshalkin and Sinai

(1961) appears in the vertical and horizontal magnetic field. In terms of the vertical field chapter 3, we discovered the suppression of zonostrophic instability with weak magnetic field and $P = 1$ and $\ell = 0$. In the case of strong magnetic fields and $P < 1$, we have confirmed the numerical results of Fraser, Cresswell and Garaud (2022), although we provide an alternative method of determining the growth rate (3.100) and threshold (3.109). The analytical results with a strong field agree with numerical results. Furthermore, we extend our investigation to find the growth rate of the strong vertical field for $\ell \neq 0$, which we found only reduces the instability determined by threshold 5.6 and found a good agreement between the numerics and theory given in figure 5.3. For weak vertical magnetic fields, we considered this as a method of estimating the field magnitude required to suppress the Kolmogorov instability and magnetic field threshold, as demonstrated in Algatheem, Gilbert and Hillier (2023).

Chapter 4 shows the case of horizontal field, broadly relevant to some studies of jet formation. Similar results are found in Durston and Gilbert (2016) in the presence of shear β-effect and random body forcing. We observe two families of instability, the suppression of the hydrodynamic instability is seen for the flow branch G_0. The threshold for suppression of the growth rate in terms of B_0 is given by (4.69). By increasing the magnetic field strength further branch of instability emerges, the field or H_0 branch. The threshold of magnetic instability is given by (4.85). For small Prandtl number $P < 1$ we obtained the same instability structure. The value of B_0^2 for suppression of the growth rate obtained by maximise B_0^2 over ν from equation 4.68, then amounts to

$$B_0^2 \approx \frac{\eta}{\nu}, \qquad (P \ll 1) \tag{9.1}$$

For large Prandtl number $P > 1$ we obtained an oscillatory mode that appears in the plot of the wavenumber k. This mode is similar to the nearby field branch, so not visible in *Rep* but it is definitely there, as shown in figure 4.6. We have not confirmed this by perturbation theory but we leave this to future research. We simulated this mode and found the system exhibits oscillatory behaviour at weak field strength as shown in figure 8.14, chapter 8.

Introducing the Floquet wavenumber ℓ in x- direction in addition to the wavenumber in y-direction hasn't an effect in the case of the vertical magnetic field. Whereas for the horizontal field, it allows a new branch of instability which we have classified as oblique zonostrophic instability as shown in figure 5.5, chapter 5, in particular. The magnetic field can suppress the hydrodynamic instability subject to the threshold of B_0, the maximum field strength given by equation (B.65) and the threshold of inverse Reynolds number ν_c, the maximum value of ν given by equation (5.12). For Prandtl number $P = 1$, we found instability only at $\nu < 1/\sqrt{2}$ for $\ell = 0$, but the oblique instability is present for the weak magnetic field and non-zero horizontal magnetic field provided $\nu < \sqrt{3}$ in figure 5.11.

For $\ell \neq 0$ and large magnetic field, this instability is again suppressed and by use of the equation (5.12) we obtain:

$$(P \ll 1) \qquad \nu^2 \approx \sqrt{2P^3}, \qquad (P \gg 1) \qquad \nu^2 \approx (\sqrt{2} - 1)P^2 \tag{9.2}$$

In this thesis, we check our results by applying perturbation theory, We fix any value of Prandtl number P and then allow the wavenumbers k and ℓ to tend to zero, other limits may be possible and could be explored using appropriate scaling options. We demonstrated that, at least for the flow profile considered here, instability can occur for an arbitrarily large horizontal magnetic field strength. We employ a matrix eigenvalue perturbation theory as described in this thesis. It is more clear than using another method, such as a multiple-scale formulation, although they are all ultimately equivalent. The underlying mechanism for our instability system from the negative eddy viscosity or negative eddy magnetic diffusivity at large scale of periodic flows described by equation 5.8, except the growth rate $p(\ell, k)$ in the case of the horizontal field show a complex dependence on ℓ and k in 5.9. Instability for $\ell \neq 0$ occurs at a large scale and it cannot be considered as involving a negative eddy diffusivity effect. This happens when we apply the perturbation theory of the limit $k \to 0$, $\ell \to 0$.

We also study the instability of the magnetic field with a general angle γ to the vertical field in chapter 5. Analytical formulas of the threshold of instability are given in equation (5.20). The instability is present provided the Reynolds number is above the threshold, $\nu < \nu_c$, where ν_c is given in (5.22). We investigate instability in the range of $0 < \gamma < \frac{\pi}{2}$ and found the theory works only at small γ, in particular close to the vertical magnetic field we find:

$$P < 1, \qquad \gamma \to 0, \qquad \nu_c \approx 0.28 \tag{9.3}$$

For nonlinear evolution, numerical simulation was specified in the Dedalus framework. The inverse cascade is halted by the presence of a weak vertical magnetic field and the energy rapidly goes to a steady state characterized by the nonlinear interaction of driven Alfveń waves as shown in section 7.4, chapter 7. However, the inverse cascade proceeds in a similar manner to the hydrodynamic case in a weak horizontal field and the vortices merge and saturate at a later time; the final state is essentially identical to that for $B_0 = 0$. We also observe inverse cascade for strong horizontal magnetic fields, referring to the evolution of linear field branch H_0 as shown in section 8.8, chapter 8.

Consistent with previous studies, we implement a simulation for the horizontal magnetic field using the Floquet wavenumber ℓ in section 8, which increases the domain size of the system and provides additional Fourier modes in the x-direction. We observed that the system exhibits a chaotic time-dependent state following the quasi-steady state as shown in section 8.7 and figure 8.23. However, when the Prandtl number is large $P = 2$, the system shows a relaxation oscillation response, as explained in section 8.6.1, and figure 8.17. A strong vertical magnetic field simulation presents a significant challenge for instability structure evolution, particularly at small Prandtl number $P = 0.5$ as shown in section 7.3.3 and figure 7.20. The saturation at a single wavelength $L_y = 4\pi$ could not be established where the growth rate is very small. We obtained the saturation at two wavelengths $(L_y, L_x) = (4\pi, 4\pi)$, and at the simulation time ended at $t = 10000$. Finally, even though we have shown that

2-D modes of instability are the fastest-growing in the linear regime, the saturation of the instability in three dimensions may differ significantly.

9.3 Future research

Future directions are directly linked with the work presented in this thesis. Two of them I consider as postdoctoral research proposals.

- The findings of this thesis may contribute to the exploration and future analysis of the tachocline, the interaction of the magnetic field with the β effect, as well as Rossby waves. We have reproduced the result of Manfroi and Young (2002) using different parameter scalings and found that the Reynolds number $R = R_c$ is in agreement once we account for the different definition of the β-effect values described in equation (2.41) and detailed in chapter 2. We can extend these results to determine the effect of the magnetic field on the system in future research & the interaction between field, Kolmogorov flow, and β-effect.

- The other direction of future research is to explore the instability properties at varying Prandtl number P with the β-plane approximation present in the system. In this case, we can explore the sinusoidal modes that occur in the case of the vertical field at a small Prandtl number as shown in chapter 3 as also discussed by Fraser, Cresswell and Garaud (2022). This mode exists for any magnetic field strength and appears for $P < 1$. The critical value of ν depends on P& the modes have non-zero frequency $\mathrm{Im}\, p \neq 0$ and appear in complex-conjugate pairs at each unstable k. We anticipate that introducing β will affect the system if the angle $\alpha = 0$, where α is the angle between the flow direction and the background vorticity gradient. We also observed an oscillatory behaviour in the case of the horizontal field at a large Prandtl number $P > 1$ as shown in chapter 4. This mode exists for weak magnetic field

strength appears at $P > 1$, and has non-zero frequency $\mathrm{Im}\, P \neq 0$. Thus, these instabilities are found in other periodic shear flows by Fraser, Cresswell and Garaud (2022) but for the vertical field case, whereas we found this mode in the horizontal field, we will discuss in greater detail in future work.

- We propose to study the Kolmogorov flow with both a horizontal magnetic field and the β effect. We observed the formation of jets in the x-direction for zero magnetic fields in chapter 2. We also obtained jet instability at $\beta = 0$ shown in figure 2.2 and we also obtained jets with a fixed value of β in figure 2.6, even though the parameter values of β and α of these results comes from Manfroi and Young (2002). We also found hydrodynamic instability in terms of Rossby waves in section 2.6. The jet structure appears in vertical field cases even with the weak magnetic field, which means the vertical magnetic field doesn't change the structure of the jet; see section 3.5. However, the horizontal magnetic field changes the structure of jets and forms zonostrophic instability observed in the plot of the field lines A. This instability comes from the field branch H_0 (see figures 4.10- 4.12 in section 4.4). These processes are found in Tobias, Dagon and Marston (2011), with varying magnetic field strength and magnetic diffusivity. These authors used non-zero β values and have fixed forcing amplitude while we have fixed Kolmogorov flow, we can present β effect in this case in future to make a good comparison.

- In chapter 5 we introduced a general magnetic field with $\ell = 0$ including a combination of vertical and horizontal magnetic fields, parameterised by the angle γ. We found the theory only works at small γ, though the analysis was complicated, and solved using the Maple framework, detailed in chapter 5 and Appendix C. One future direction can be determined by including the Floquet wavenumber. As we discussed in chapter 5, e.g. figures 5.4, 5.13, the Floquet wavenumber is likely to affect $\gamma = \pi/2$ and $\gamma = \pi/4$. Although the theory does not work in the intermediate region between vertical and horizontal fields, e.g. $\gamma = \pi/8$, we can introduce ℓ with small γ where theoretical and numerical

results are compatible, as shown in figure 5.16.

There is still a lack of clarity, but we predict that ℓ does not affect the growth rate for small γ, thereby obtaining the same instability structure. As indicated in figure 5.1, this prediction is based upon our experiments in the presence of Floquet waves in the vertical field case with $\gamma = 0$. While, $\gamma = \pi/4$ allows more instability. Overall, we observed enhanced instability as the angle $\gamma \to \pi/2$ approached the horizontal field. It is evident that ℓ operates on the horizontal field in accordance with chapter 5, section 5.5. Studying Kolmogorov instability for fields at oblique angles can also be considered a future direction rather than the vertical and horizontal magnetic fields considered here.

- Use of the ideal MHD model could be viewed as a future research direction, where we neglect both viscosity and diffusivity. A study of the vertical magnetic field has been conducted in Fraser, Cresswell and Garaud (2022) and it was discovered that the magnetic field lines are frozen into the flow and forced to move with it, resulting in elastic properties due to the magnetic tension resisting deformation and stiffening the flow. As a result, a magnetic field aligned with a flow is capable of preventing Kelvin–Helmholtz instability from developing. Alternatively, a magnetic field aligned with a possible jet can enhance zonostrophic instability in an ideal MHD since the magnetic field lines bend with fluid flow, as a result of the Alfvén theorem. Therefore, we leave this as future research.

- In this thesis we investigated the results in a very specific problem, the linear instability in 2D incompressible with finite viscosity and resistivity and the non-linear evolution of the instability as a function of time. However, when we consider 3D perturbation in this system, the fastest growing mode is always in 2D as discussed by Fraser, Cresswell and Garaud (2022) in the case of the uniform vertical magnetic field. We do not know what will happen in case of a

horizontal magnetic field where the Fourier expansion will involve the extra wavenumber m in the z-direction $\boldsymbol{u} = \boldsymbol{u}(x) \sum e^{i(ky+\ell x+mz)}$, previously we found adding ℓ in the system allows the possibility of instability, our prediction here is adding the wavenumber m in the z-direction also will bring more freedom and allow more possibility of instability. It is likely that the saturation of the instability will be profoundly different in two and three dimensions. We leave this to future research.

- Inverse cascades often occur in two dimensions. The vortices are perfectly aligned and merge efficiently to create large-scale structures. For 2D instability, we demonstrated remarkable inverse cascade processes at intermediate and long times. Our simulations were typically implemented at small wavenumbers $k = 0.5, \ell = 0.5$ for the hydrodynamic case and for MHD Kolmogorov flows. However, we used some bigger boxes in some simulations to demonstrate a comparison with linear results. Even though we did not use a very large box, we observed a tendency to go from small to large scales. In 3D Kolmogorov flow, energy is cascaded to small scales, Dascaliuc and Grujić (2016).

As a result of MHD, we have obtained an inverse cascade for horizontal fields. The rate at which it occurs depends on the magnetic field strength and direction. One way to address the question of inverse cascades in these systems is to generate an amplitude equation, as does Sivashinsky (1985) for the pure hydrodynamic case. We can explore the evolution & possible inverse cascade governed by the amplitude equation for our system involving horizontal or vertical magnetic fields and using the Dedalus framework numerically.

A. Derivation of vertical field theory with $\ell \neq 0$

Our starting point is given by the equations. (3.68 - 3.69) with n replaced by $n+\ell$, and we consider only the modes $G_0, H_0, G_{\pm 1}, H_{\pm 1}$, we set as the original vertical field problem (see section 3.7.1)

$$pG_n = \frac{k}{2}\left[\frac{1}{((n+\ell)-1)^2+k^2} - 1\right] G_{n-1} - \frac{k}{2}\left[\frac{1}{((n+\ell)+1)^2+k^2} - 1\right] G_{n+1}$$

$$- \nu((n+\ell)^2+k^2)G_n + ikB_0((n+\ell)^2+k^2)H_n. \tag{A.1}$$

$$pH_n = \left[-\frac{k}{2}\right] H_{n-1} + \left[\frac{k}{2}\right] H_{n+1} - \eta(k^2+(n+\ell)^2)H_n + \left[\frac{ikB_0}{k^2+(n+\ell)^2}\right] G_n \tag{A.2}$$

For $n=0$ we have:

$$pG_0 = \underbrace{\frac{k}{2}\left[\frac{1}{(\ell-1)^2+k^2} - 1\right]}_{I} G_{-1} - \underbrace{\frac{k}{2}\left[\frac{1}{(\ell+1)^2+k^2} - 1\right]}_{II} G_1 - \nu(\ell^2+k^2)G_0$$

$$+ ikB_0(\ell^2+k^2)H_0. \tag{A.3}$$

$$I = \frac{k}{2}\left(\frac{1}{(\ell-1)^2+k^2} - 1\right) = \frac{1-(\ell-1)^2-k^2}{(\ell-1)^2+k^2} = \frac{1-(\ell^2-2\ell+1)-k^2}{(\ell^2-2\ell+1)+k^2} \tag{A.4}$$

$$II = \frac{k}{2}\left(\frac{1}{(\ell+1)^2+k^2} - 1\right) = \frac{1-(\ell+1)^2-k^2}{(\ell+1)^2+k^2} = \frac{1-(\ell^2+2\ell+1)-k^2}{(\ell^2+2\ell+1)+k^2} \tag{A.5}$$

$$pH_0 = \left[-\frac{k}{2}\right] H_{-1} + \left[\frac{k}{2}\right] H_1 - \eta(k^2+\ell^2)H_0 + \left[\frac{ikB_0}{k^2+\ell^2}\right] G_0 \tag{A.6}$$

By arranging equations (A.4-A.5), we obtain:

$$pG_0 = \frac{k}{2}\left[\frac{-k^2-\ell^2+2\ell}{k^2+\ell^2-2\ell+1}\right]G_{-1} - \frac{k}{2}\left[\frac{-k^2-\ell^2-2\ell}{k^2+\ell^2+2\ell+1}\right]G_1 - \nu(k^2+\ell^2)G_0 + ikB_0(k^2+\ell^2)H_0, \tag{A.7}$$

$$pH_0 = \frac{-k}{2}H_{-1} + \frac{k}{2}H_1 - \eta(k^2+\ell^2)H_0 + \frac{ikB_0}{k^2+\ell^2}G_0, \tag{A.8}$$

For $n = \pm 1$ we have:

$$pG_1 = \frac{k}{2}\left(\frac{1}{\ell^2+k^2} - 1\right)G_0 - \nu(1+2\ell+\ell^2+k^2)G_1 + ikB_0(1+2\ell+\ell^2+k^2)H_1, \tag{A.9}$$

$$pG_{-1} = -\frac{k}{2}\left(\frac{1}{\ell^2+k^2} - 1\right)G_0 - \nu(1-2\ell+\ell^2+k^2)G_{-1} + ikB_0(1-2\ell+\ell^2+k^2)H_{-1}, \tag{A.10}$$

$$pH_1 = \frac{-k}{2}H_0 - \eta(1+2\ell+\ell^2+k^2)H_1 + \frac{ikB_0}{1+2\ell+\ell^2+k^2}G_1, \tag{A.11}$$

$$pH_{-1} = \frac{k}{2}H_0 - \eta(1-2\ell+\ell^2+k^2)H_{-1} + \frac{ikB_0}{1-2\ell+\ell^2+k^2}G_{-1}. \tag{A.12}$$

By using Taylor expansion for some terms including $\ell = k\ell'$, $\ell \ll 1$ which gives:

$$\frac{-k^2-\ell^2+2\ell}{1+k^2+\ell^2-2\ell} \approx 2\ell - (k^2-3\ell^2) + ... = \quad \to 2k\ell' - k^2(1-3\ell'^2) \tag{A.13}$$

$$\frac{-k^2-\ell^2-2\ell}{1+k^2+\ell^2+2\ell} \approx -2\ell - (k^2-3\ell^2) + ... = -2k\ell' - k^2(1-3\ell'^2) \tag{A.14}$$

The Taylor expansion used is

$$(1+\epsilon)^{-1} = 1 - \epsilon + \epsilon^2 - \cdots \tag{A.15}$$

To obtain equation (A.13) we use

$$(-k^2-\ell^2+2\ell)(1-2\ell+k^2+\ell^2)^{-1} \tag{A.16}$$

$$= (-k^2-\ell^2+2\ell)[1+2\ell+-k^2-\ell^2+(-2\ell+k^2+\ell^2)^2-\cdots] \tag{A.17}$$

$$= (-k^2-\ell^2+2\ell)[1+2\ell-k^2-\ell^2+4\ell^2+\cdots] \tag{A.18}$$

$$= -k^2 - \ell^2 + 2\ell + 4\ell^2 + \cdots, \quad 2\ell - k^2 + 3\ell^2 + \cdots \tag{A.19}$$

$$= 2\ell - (k^2 - 3\ell^2) + \cdots \tag{A.20}$$

Use small $\ell \to 0$ and small $k \to 0$, with $\ell = O(k), \quad \ell = k\ell', \quad \ell' = O(1)$,

$$1 + 2\ell + \ell^2 + k^2 \simeq 1 + 2\ell, \quad 1 - 2\ell + \ell^2 + k^2 \simeq 1 - 2\ell, \tag{A.21}$$

$$\frac{1}{1 + 2\ell + \ell^2 + k^2} \simeq 1 - 2\ell, \quad \frac{1}{1 - 2\ell + \ell^2 + k^2} \simeq 1 + 2\ell. \tag{A.22}$$

Neglect some smaller terms from the equations (A.13 - A.22), we obtain:

$$pG_0 = -\frac{k}{2}(k^2-3\ell^2)G_{-1}+\frac{k}{2}2\ell G_{-1}+\frac{k}{2}(k^2-3\ell^2)G_1+\frac{k}{2}2\ell G_1-\nu(k^2+\ell^2)G_0+ikB_0(k^2+\ell^2)H_0, \tag{A.23}$$

$$pH_0 = -\frac{k}{2}H_{-1} + \frac{k}{2}H_1 - \eta(k^2 + \ell^2)H_0 + \frac{ikB_0}{k^2 + \ell^2}G_0, \tag{A.24}$$

$$pG_1 = \frac{k}{2}\left(\frac{1}{\ell^2 + k^2} - 1\right)G_0 - \nu(1 + 2\ell)G_1 + ikB_0(1 + 2\ell)H_1, \tag{A.25}$$

$$pG_{-1} = -\frac{k}{2}\left(\frac{1}{\ell^2 + k^2} - 1\right)G_0 - \nu(1 - 2\ell)G_{-1} + ikB_0(1 - 2\ell)H_{-1}, \tag{A.26}$$

$$pH_1 = \frac{-k}{2}H_0 - \eta(1 + 2\ell + \ell^2 + k^2)H_1 + \frac{ikB_0}{1 + 2\ell + \ell^2 + k^2}G_1, \tag{A.27}$$

$$pH_{-1} = \frac{k}{2}H_0 - \eta(1 - 2\ell + \ell^2 + k^2)H_{-1} + \frac{ikB_0}{1 - 2\ell + \ell^2 + k^2}G_{-1}. \tag{A.28}$$

We rewrite the equations (A.23 - A.28) in terms of $G_\pm$ and $H_\pm$ with

$$G_\pm = \frac{1}{2}(G_1 \pm G_{-1}), \qquad H_\pm = \frac{1}{2}(H_1 \pm H_{-1}) \tag{A.29}$$

Then we express the equations in terms of $G_0, H_0, G_\pm, H_\pm$

$$pG_0 = k(k^2 - 3\ell^2)G_- + 2\ell k G_+ - \nu(k^2 + \ell^2)G_0 + ikB_0(k^2 + \ell^2)H_0, \tag{A.30}$$

$$pH_0 = kH_- - \eta(k^2 + \ell^2)H_0 + \frac{ikB_0}{k^2 + \ell^2}G_0, \tag{A.31}$$

$$pG_+ = -\nu G_+ - 2\ell\nu G_- + ikB_0H_+ + ikB_0 2\ell H_-, \tag{A.32}$$

$$pG_- = \frac{k}{2}[\frac{1}{\ell^2+k^2}]G_0 - \nu G_- - 2\ell\nu G_+ + ikB_0H_- + ikB_02\ell H_+, \tag{A.33}$$

$$pH_+ = -\eta H_+ - 2\ell\eta H_- + ikB_0G_+ - ikB_02\ell G_-, \tag{A.34}$$

$$pH_- = -\frac{k}{2}H_0 - \eta H_- - 2\ell\eta H_+ + ikB_0G_- - ikB_02\ell G_+. \tag{A.35}$$

we have $\ell \neq 0$ in the problem, so we have ℓ scale as $k \to 0$ in Appendix A. We indicate that the appropriate scaling to gain useful results is

$$G_0 = k^2G_0', \qquad ikB_0 = iB_0', \qquad \ell = k\ell' = O(k), \tag{A.36}$$

So we hold ℓ', B_0' and G_0' constant while $k \to 0$ and follow the usual procedure of making these substitutions, writing the matrix M as the form $M\boldsymbol{v} = p\boldsymbol{v}$:

$$M = \left(\begin{array}{cc|cc|cc} -\nu k^2(1+\ell'^2) & iB_0'(1+\ell'^2) & 2\ell' & 0 & k(1-3\ell'^2) & 0 \\ \frac{iB_0'}{(1+\ell'^2)} & -\eta k^2(1+\ell'^2) & 0 & 0 & 0 & k \\ \hline 0 & 0 & -\nu & iB_0' & -2k\ell'\nu & iB_0'2k\ell' \\ 0 & 0 & iB_0' & -\eta & -iB_0'2k\ell' & -2k\ell'\eta \\ \hline \frac{k}{2(1+\ell'^2)} & 0 & -2k\ell'\nu & iB_0'2k\ell' & -\nu & iB_0' \\ 0 & -\frac{k}{2} & -iB_0'2k\ell' & -2k\ell'\eta & iB_0' & -\eta \end{array}\right), \left(\begin{array}{c} G_0 \\ H_0 \\ G_+ \\ H_+ \\ G_- \\ H_- \end{array}\right) \tag{A.37}$$

By writing the linear system as $M\boldsymbol{v} = p\boldsymbol{v}$, then expanding M give the matrices,

$$M_0 = \left(\begin{array}{cc|cc|cc} 0 & iB_0'(1+\prime\ell^2) & 2\ell' & 0 & 0 & 0 \\ \frac{iB_0'}{(1+\ell^2)} & 0 & 0 & 0 & 0 & 0 \\ \hline 0 & 0 & -\nu & iB_0' & 0 & 0 \\ 0 & 0 & iB_0' & -\eta & 0 & 0 \\ \hline 0 & 0 & 0 & 0 & -\nu & iB_0' \\ 0 & 0 & 0 & 0 & iB_0' & -\eta \end{array}\right), \tag{A.38}$$

Figure A.1 shows that matrix M_0 includes undamped waves, and there are no coupling terms between flow and field G_0, H_0, and damped Alfvén waves in terms of $G_\pm$ and $H_\pm$. So, the Alfvén waves drive the flow and the field and flow drive the Alfvén waves. The only coupling exists between undamped waves G_0 & damped wave G_+.

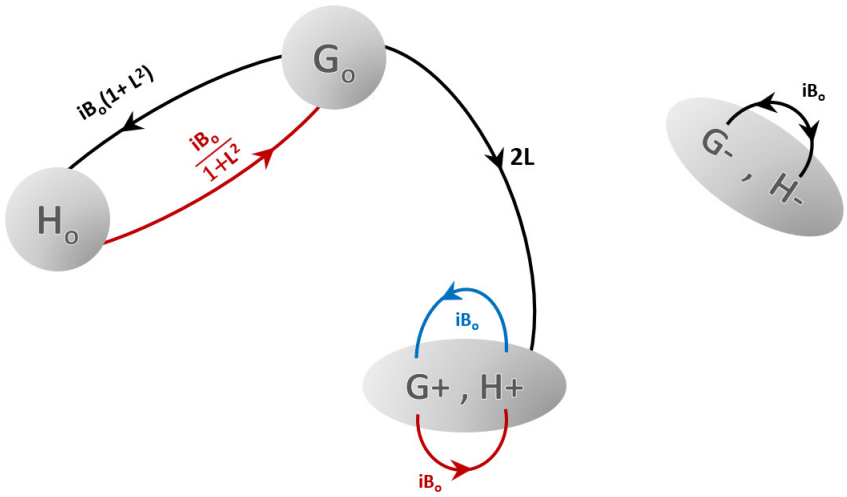

Figure A.1: Schematic of matrix M_0

$$M_1 = \left(\begin{array}{cc|cc|cc} 0 & 0 & 0 & 0 & 1-3\ell'^2 & 0 \\ 0 & 0 & 0 & 0 & 0 & 1 \\ \hline 0 & 0 & 0 & 0 & -2\ell'\nu & 2iB_0'\ell' \\ 0 & 0 & 0 & 0 & -2iB_0'\ell' & -2\ell'\eta \\ \hline \frac{1}{2(1+\ell'^2)} & 0 & -2\ell'\nu & 2i\ell'B_0' & 0 & 0 \\ 0 & -\frac{1}{2} & -2iB_0'\ell' & -2\ell'\eta & 0 & 0 \end{array}\right), \tag{A.39}$$

Figure A.2 shows that matrix M_1 where there is coupling between the flow G_0, and the field H_0 and damped Alfvén waves G_-, H_- So the waves drive the flow and the field, also there is coupling between damped Alfvén waves G_-, H_- and G_+, H_+.

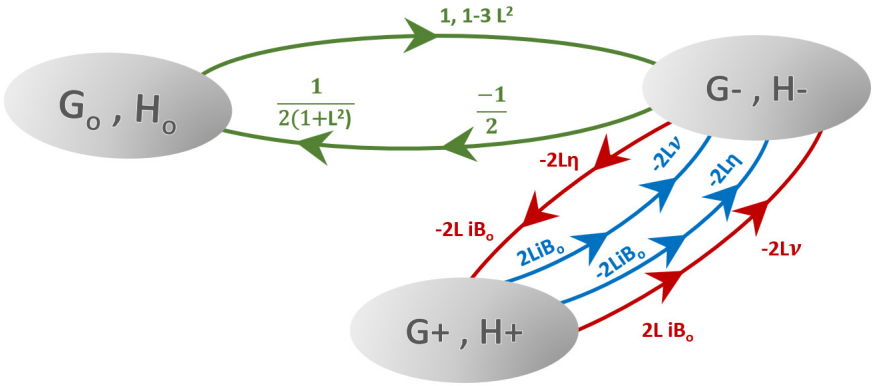

Figure A.2: Schematic of matrix M_1

For an approximate growth rate p we use the expansion (3.58) and solve order by order. At leading order (3.59) we focus on the eigenvalues $p_0 = \pm iB_0'$ of M_0, corresponding to large-scale undamped Alfvén waves. We will focus on the upper sign without loss of generality and take

$$p_0 = iB_0', \quad \boldsymbol{v}_0 = \begin{pmatrix} 1+\ell^2 & 1 & 0 & 0 & 0 & 0 \end{pmatrix}^T, \quad M_0\boldsymbol{v}_0 = \begin{pmatrix} iB_0'(1+\ell'^2) & iB_0' & 0 & 0 & 0 & 0 \end{pmatrix}^T = p_0\boldsymbol{v}_0 \tag{A.40}$$

For the left eigenvector, we try:

$$\boldsymbol{w}_0 = (1, 1+\ell^2, c, d, 0, 0), \quad \boldsymbol{w}_0 M_0 = \begin{pmatrix} iB_0' & iB_0'(1+\ell^2) & 2\ell' - \nu c + iB_0' d & iB_0' c - \eta d & 0 & 0 \end{pmatrix} = iB_0'\boldsymbol{w}_0 \tag{A.41}$$

To satisfy this we need to solve equation A.41 for c and d. We invert the middle part of matrix A.46: look at the block 2×2 corner of field:

$$\begin{pmatrix} -\nu - iB_0' & iB_0' \\ iB_0' & -\eta - iB_0' \end{pmatrix}^{-1} \begin{pmatrix} c \\ d \end{pmatrix} = \begin{pmatrix} -2\ell' a \\ 0 \end{pmatrix}$$

$$\begin{pmatrix} c \\ d \end{pmatrix} = \Delta \begin{pmatrix} -iB_0' - \eta & -iB_0' \\ -iB_0' & -iB_0' - \nu \end{pmatrix} \begin{pmatrix} -2\ell' a \\ 0 \end{pmatrix} \tag{A.42}$$

with the inverse determinant Δ now defined as

$$\Delta^{-1} = \eta\nu + iB_0'(\eta + \nu). \tag{A.43}$$

if $a = 1$, then

$$c = \Delta(iB_0' + \eta)2\ell', \qquad d = \Delta(iB_0' 2\ell') \tag{A.44}$$

we obtain

$$\boldsymbol{w}_0 = (1, 1+\ell'^2, \Delta(iB_0' + \eta)2\ell', \Delta iB_0' 2\ell', 0, 0) \tag{A.45}$$

Here $\boldsymbol{w}_0$ is the left eigenvector as usual, with $\boldsymbol{w}_0(M_0 - p_0) = 0$ and here $\boldsymbol{w}_0\boldsymbol{v}_0 =$

$2(1+\ell'^2)$.

We finding a solution $(M_0 - p_0)(e, b, c.d, e, f)^T = M_1 \boldsymbol{v}_0$, then we obtain:

$$\left(\begin{array}{cc|cc|cc} -iB_0 & iB_0(1+\ell^2) & 2\ell & 0 & 0 & 0 \\ \frac{iB_0}{(1+\ell^2)} & -iB_0 & 0 & 0 & 0 & 0 \\ \hline 0 & 0 & -\nu - iB_0 & iB - 0 & 0 & 0 \\ 0 & 0 & iB_0 & -\eta - iB_0 & 0 & 0 \\ \hline 0 & 0 & 0 & 0 & -\nu - iB_0 & iB_0 \\ 0 & 0 & 0 & 0 & iB_0 & -\eta - iB_0 \end{array}\right) \left(\begin{array}{c} a \\ b \\ c \\ d \\ e \\ f \end{array}\right) = \left(\begin{array}{c} 0 \\ 0 \\ 0 \\ 0 \\ \frac{1}{2} \\ -\frac{1}{2} \end{array}\right) \tag{A.46}$$

Moving to the first order, from (3.64), we find

$$M_1 \boldsymbol{v}_0 = (0, 0, 0, 0, \frac{1}{2}, -\frac{1}{2})^T, \qquad p_1 = 0, \tag{A.47}$$

and multiplying by $\boldsymbol{w}_0$ on the left we find:

$$\boldsymbol{w}_0 M_1 = \left(0 \quad 0 \quad 0 \quad 0 \quad \underbrace{1 - 3\ell^2 - 2\ell\nu c - 2\ell i B_0 d}_{g} \quad \underbrace{1 + \ell^2 + 2\ell i B_0 c - 2\ell\eta d}_{h}.\right) \tag{A.48}$$

We now need to solve (3.60) for $\boldsymbol{v}_1$. To find a solution we clearly need to invert the 2×2 lower right block of $(M_0 - p_0)^{-1} M_1 \boldsymbol{v}_0$ to calculate, we can take $a = b = c = d = 0$ in equation A.46, which gives

$$(M_0 - p_0 I)\boldsymbol{v}_1 = \left(\begin{array}{c} 0 \\ 0 \\ 0 \\ 0 \\ -\frac{1}{2} \\ \frac{1}{2} \end{array}\right) \tag{A.49}$$

We invert just the bottom right of (A.46), which gives:

$$\begin{pmatrix} -\nu - iB_0' & iB_0' \\ iB_0' & -\eta - iB_0' \end{pmatrix}^{-1} \begin{pmatrix} e \\ f \end{pmatrix} = \frac{1}{2} \begin{pmatrix} -1 \\ 1 \end{pmatrix} \tag{A.50}$$

$$\begin{pmatrix} e \\ f \end{pmatrix} = \frac{\Delta}{2} \begin{pmatrix} -iB_0' - \eta & -iB_0' \\ -iB_0' & -iB_0' - \nu \end{pmatrix} \begin{pmatrix} -1 \\ 1 \end{pmatrix} \tag{A.51}$$

$$\begin{pmatrix} e \\ f \end{pmatrix} = \frac{\Delta}{2} \begin{pmatrix} \eta + iB_0' - iB_0' \\ iB_0' - \nu - iB_0' \end{pmatrix} = \frac{\Delta}{2} \begin{pmatrix} \eta \\ -\nu \end{pmatrix} \tag{A.52}$$

with the inverse determinant Δ now defined as

$$\Delta^{-1} = \eta\nu + iB_0'(\eta + \nu). \tag{A.53}$$

Then we look at the second level of the theory p_2 from equation (3.65):

$$p_{21} = -\frac{\boldsymbol{w}_0 M_1 (M_0 - p_0)^{-1} M_1 \boldsymbol{v}_0}{\boldsymbol{w}_0 \boldsymbol{v}_0} \tag{A.54}$$

$$p_{22} = \frac{\boldsymbol{w}_0 M_2 \boldsymbol{v}_0}{\boldsymbol{w}_0 \boldsymbol{v}_0} = -\frac{\nu + \eta}{2}(1 + \ell'^2) \tag{A.55}$$

We calculate p_{21} first:

$$p_{21} = \frac{\Delta}{2} \frac{\begin{pmatrix} g & h \end{pmatrix} \begin{pmatrix} e \\ f \end{pmatrix}}{\boldsymbol{w}_0 \boldsymbol{v}_0} \tag{A.56}$$

$$p_{21} = \frac{1}{2(1 + \ell^2)} \begin{pmatrix} g & h \end{pmatrix} \frac{\Delta}{2} \begin{pmatrix} \eta \\ -\nu \end{pmatrix} \tag{A.57}$$

$$p_{21} = \frac{\Delta}{4(1 + \ell^2)}(\eta g - \nu h) \tag{A.58}$$

by substituting the value of g and h from equation A.48, we obtain:

$$p_{21} = \frac{\Delta}{4(1 + \ell'^2)}(\eta(1 - 3\ell'^2 - 2\ell'\nu c - 2iB_0'\ell' d) - \nu((1 + \ell'^2) + 2\ell' iB_0' c - 2\ell'\eta d).$$

Now we substitute the values of c and d from equation (A.44) :

$$p_{21} = \frac{\Delta}{4(1+\ell'^2)}[\eta(1-3\ell'^2) - \nu(1+\ell'^2) - 4\ell'^2\Delta\nu(\eta + iB_0')^2 + 4\ell'^2\Delta\eta(\nu - iB_0')iB_0']. \tag{A.59}$$

and by using the scaling $\ell' = \ell/k$

$$p_{21}k^2 = \frac{\Delta k^2}{4(1+\ell^2/k^2)}[\eta(1-3\ell^2/k^2) - \nu(1+\ell^2/k^2) - 4(\ell^2/k^2)\Delta\nu(\eta+iB_0')^2 + 4(\ell^2/k^2)\Delta\eta(\nu-iB_0')iB_0']. \tag{A.60}$$

If we put $\ell' = 0$ we gain the vertical field growth rate with $\ell = 0$ as equation (3.99)

$$p_{21} = \frac{\frac{1}{4}(\eta - \nu)}{\nu\eta + iB_0'(\nu + \eta)} \tag{A.61}$$

We keep up the discussion in the main part of the chapter in section 5.5.2

B. Derivation of horizontal field theory with $\ell \neq 0$

We start with an example of double eigenvalue:

$$\text{eigenvalue } \lambda = p_0 = 1, \text{ suppose } M_0 = \begin{pmatrix} 1 & 0 \\ 0 & 1 \end{pmatrix}$$

Consider a general eigenvector for any a or b:

$$\boldsymbol{v}_0 = a \begin{pmatrix} 1 \\ 0 \end{pmatrix} + b \begin{pmatrix} 0 \\ 1 \end{pmatrix} = \begin{pmatrix} a \\ b \end{pmatrix} \tag{B.1}$$

We can apply the theory, and choice of M_1 choosing the entries randomly, taking say

$$M = M_0 + kM_1 = \begin{pmatrix} 1 & k \\ 2k & 1 \end{pmatrix} \tag{B.2}$$

The eigenvalues are then given by

$$\begin{pmatrix} 1-\lambda & k \\ 2k & 1-\lambda \end{pmatrix} = 0, \qquad (1-\lambda)^2 - 2k^2 = 0, \qquad 1-\lambda = \pm k\sqrt{2} \tag{B.3}$$

We have two distinct eigenvalues & eigenvectors

$$\lambda_1 = 1 + k\sqrt{2}, \qquad \begin{pmatrix} 1 \\ \sqrt{2} \end{pmatrix}, \qquad \lambda_2 = 1 - k\sqrt{2}, \qquad \begin{pmatrix} 1 \\ -\sqrt{2}, \end{pmatrix} \tag{B.4}$$

We looking for actual eigenvectors

$$\begin{pmatrix} 1 & 2k \\ k & 1 \end{pmatrix} \begin{pmatrix} c \\ d \end{pmatrix} = (1+k\sqrt{2}) \begin{pmatrix} c \\ d \end{pmatrix} \tag{B.5}$$

$$c + kd = (1+k\sqrt{2})c, \qquad kd = k\sqrt{2}c, \quad c = 1, \qquad d = \sqrt{2}. \tag{B.6}$$

In general, if we start with a double eigenvalue and then add some entries for the matrices, we get two single eigenvalues (B.4). Once these two eigenvalues separate we get two eigenvectors (B.6). We will see the same for the more complicated $\ell = 0$ horizontal field problem.

Our starting point is the equations (B.7-B.8) and we consider only the modes $G_0, H_0, G_{\pm 1}, H_{\pm 1}$, and dropping terms involving $G_{\pm 2}, H_{\pm 2}$, set as in the original horizontal field problem by replacing $n \to n + \ell$, see section 4.5:

$$\begin{aligned} pG_n = {} & \frac{k}{2}\left[\frac{1}{((n+\ell)-1)^2+k^2} - 1\right] G_{n-1} - \frac{k}{2}\left[\frac{1}{((n+\ell)+1)^2+k^2} - 1\right] G_{n+1} - \nu(k^2+(n+\ell)^2)G_n \\ & + \frac{ikB_0}{2\eta}\left[((n+\ell)-1)^2+k^2-1\right] H_{n-1} + \frac{ikB_0}{2\eta}\left[((n+\ell)+1)^2+k^2-1\right] H_{n+1} + \\ & i(n+\ell)B_0(k^2+(n+\ell)^2)\, H_n \end{aligned} \tag{B.7}$$

$$pH_n = -\frac{k}{2}H_{n-1} + \frac{k}{2}H_{n+1} - \eta(k^2+(n+\ell)^2)H_n + \frac{i(n+\ell)B_0}{k^2+(n+\ell)^2}G_n + \frac{ikB_0}{2\eta}\frac{1}{((n+\ell)-1)^2+k^2}G_{n-1}$$

$$+ \frac{ikB_0}{2\eta}\frac{1}{((n+\ell)+1)^2+k^2}G_{n+1}. \tag{B.8}$$

For $n = 0$ we have

$$\begin{aligned} pG_0 = {} & \frac{k}{2}\left[\frac{-k^2-\ell^2+2\ell}{k^2+\ell^2-2\ell+1}\right]G_{-1} - \frac{k}{2}\left[\frac{-k^2-\ell^2-2\ell}{k^2+\ell^2+2\ell+1}\right]G_1 - \nu(k^2+\ell^2)G_0 \\ & + \frac{ikB_0}{2\eta}(k^2+\ell^2-2\ell)H_{-1} + i\ell B_0(k^2+\ell^2)H_0 + \frac{ikB_0}{2\eta}(k^2+\ell^2+2\ell)H_1 \end{aligned} \tag{B.9}$$

$$\begin{aligned} pH_0 = {} & -\frac{k}{2}H_{-1} + \frac{k}{2}H_1 - \eta(k^2+\ell^2)H_0 + \frac{ikB_0}{2\eta}\left[\frac{1}{1+k^2+\ell^2-2\ell}\right]G_{-1} \\ & + \frac{ikB_0}{2\eta}\left[\frac{1}{1+k^2+\ell^2+2\ell}\right]G_1 + \frac{i\ell B_0}{k^2+\ell^2}G_0 \end{aligned} \tag{B.10}$$

For $n = \pm 1$ we have

$$pG_1 = \frac{k}{2}[\frac{1}{\ell^2+k^2} - 1]G_0 - \nu(1+2\ell+\ell^2+k^2)G_1 + \frac{ikB_0}{2\eta}(k^2+\ell^2-1)H_0 + iB_0(1+3\ell)H_1 \tag{B.11}$$

$$pG_{-1} = -\frac{k}{2}[\frac{1}{\ell^2+k^2} - 1]G_0 - \nu(1+2\ell+\ell^2+k^2)G_{-1} + \frac{ikB_0}{2\eta}(k^2+\ell^2-1)H_0 + iB_0(-1+3\ell)H_{-1} \tag{B.12}$$

$$pH_1 = -\frac{k}{2}H_0 - \eta H_1 - \eta 2\ell H_1 + iB_0(1-\ell-k^2+\ell^2)G_1 + \frac{ikB_0}{2\eta}(\frac{1}{\ell^2+k^2})G_0 \tag{B.13}$$

$$pH_{-1} = \frac{k}{2}H_0 - \eta H_{-1} + \eta 2\ell H_{-1} + iB_0(1-\ell-k^2+\ell^2)G_{-1} + \frac{ikB_0}{2\eta}(\frac{1}{k^2+\ell^2})G_0 \tag{B.14}$$

Then approximating some complex terms we have received from introducing small Floquet wavenumber ℓ into equations (B.10 - B.9), with $\ell = O(k),\ \ell,\ k \to 0$:

$$\frac{-k^2-\ell^2 \pm 2\ell}{1+k^2+\ell^2 \pm 2\ell} \simeq \pm 2\ell - (k^2 - 3\ell^2) + ..., \tag{B.15}$$

$$\pm 2\ell + \ell^2 + k^2 \simeq \pm 2\ell, \tag{B.16}$$

$$\frac{1}{1 \pm 2\ell + \ell^2 + k^2} \simeq \frac{1}{1 \pm 2\ell} \simeq 1 \mp 2\ell. \tag{B.17}$$

$$(\pm 1 + \ell)(1 \pm 2\ell + k^2 + \ell^2) \simeq \pm 1 + 3\ell \tag{B.18}$$

$$(1+\ell)(1 - 2\ell - \ell^2 - k^2 + 4\ell^2...) \simeq 1 - \ell - k^2 + \ell^2 \tag{B.19}$$

By using equations (B.9-B.14), and neglecting some smaller terms from equations [B.15 - B.19], we obtain:

$$\begin{aligned} pG_0 = k(k^2-3\ell^2)G_- + 2\ell k G_+ - \nu(k^2+\ell^2)G_0 + i\ell B_0(k^2+\ell^2)H_0 \\ + \frac{ikB_0}{\eta}(k^2+\ell^2)H_+ + \frac{ikB_0}{\eta}(2\ell)H_- \end{aligned} \tag{B.20}$$

$$pH_0 = kH_- - \eta(k^2+\ell^2)H_0 + \frac{i\ell B_0}{k^2+\ell^2}G_0 + \frac{ikB_0}{\eta}G_+ - \frac{ikB_0}{\eta}2\ell G_- \tag{B.21}$$

$$pG_1 = \frac{k}{2}\frac{1}{\ell^2+k^2}G_0 - \nu G_1 - 2\ell\nu G_1 - \frac{ikB_0}{2\eta}H_0 + iB_0(1+3\ell)H_1 \tag{B.22}$$

$$pG_{-1} = -\frac{k}{2}\frac{1}{\ell^2+k^2}G_0 - \nu G_{-1} + 2\ell\nu G_{-1} + iB_0(-1+3\ell)H_{-1} - \frac{ikB_0}{2\eta}H_0 \quad \text{(B.23)}$$

$$pH_1 = -\frac{k}{2}H_0 - \eta H_1 - \eta 2\ell H_1 + iB_0(1-\ell-k^2+\ell^2)G_1 + \frac{ikB_0}{2\eta}(\frac{1}{\ell^2+k^2})G_0 \quad \text{(B.24)}$$

$$pH_{-1} = \frac{k}{2}H_0 - \eta H_{-1} + \eta 2\ell H_{-1} + iB_0(1-\ell-k^2+\ell^2)G_1 + \frac{ikB_0}{2\eta}(\frac{1}{k^2+\ell^2})G_0 \quad \text{(B.25)}$$

By simplify the linear system [B.22 - B.25] and using the approximation equation (A.29), we then have:

$$pG_+ = -\nu G_+ - 2\ell\nu G_- - \frac{ikB_0}{2\eta}H_0 + iB_0 3\ell H_+ + iB_0 H_- \quad \text{(B.26)}$$

$$pG_- = \frac{k}{2}\frac{1}{\ell^2+k^2}G_0 - \nu G_- - 2\ell\nu G_+ + iB_0 3\ell H_- + iB_0 H_+ \quad \text{(B.27)}$$

$$pH_+ = -\eta H_+ - 2\ell\eta H_- + \frac{ikB_0}{2\eta}(\frac{1}{\ell^2+k^2})G_0 - iB\ell G_+ + iB_0 G_- \quad \text{(B.28)}$$

$$pH_- = -\frac{k}{2}H_0 - \eta H_- - 2\ell\eta H_+ - iB_0\ell G_- + iB_0 G_+$$

So we hold ℓ' and G_0' constant and the appropriate scale for obtaining useful results which is

$$G_0 = k^2 G_0', \qquad \tilde{B}_0 = B_0/\eta, \qquad B_0 = O(1), \qquad \ell = O(k) = k\ell'. \quad \text{(B.29)}$$

Then we have

$$\begin{aligned} pG_0' = k(1-3\ell'^2)G_- + 2\ell' G_+ - \nu k^2(1+\ell'^2)G_0' + ik\ell' B_0(1+\ell'^2)H_0 \\ + \frac{ikB_0}{\eta}(1+\ell'^2)H_+ + \frac{iB_0}{\eta}2\ell' H_- \end{aligned} \quad \text{(B.30)}$$

$$pH_0 = kH_- - \eta k^2(1+\ell'^2)H_0 + \frac{i\ell' B_0 k}{1+\ell'^2}G_0' + \frac{ikB_0}{\eta}G_+ - \frac{ikB_0}{\eta}2k\ell' G_-, \quad \text{(B.31)}$$

$$pG_+ = -\nu G_+ - 2k\ell'\nu G_- - \frac{ikB_0}{2\eta}H_0 + iB_0 3\ell' k H_+ + iB_0 H_- \quad \text{(B.32)}$$

$$pG_- = \frac{k}{2}\frac{1}{1+\ell'^2}G_0 - \nu G_- - 2k\ell'\nu G_+ + iB_0 3k\ell' H_- + iB_0 H_+ \quad \text{(B.33)}$$

$$pH_+ = -\eta H_+ - 2k\ell'\eta H_- - iB_0 k\ell' G_+ + iB_0 G_- + \frac{ikB_0}{2\eta}(\frac{1}{1+\ell'^2})G_0 \quad \text{(B.34)}$$

$$pH_- = -\frac{k}{2}H_0 - \eta H_- - 2\ell' k\eta H_+ - iB_0 k\ell' G_- + iB_0' G_+ \tag{B.35}$$

we write the system as $M\boldsymbol{v} = p\boldsymbol{v}$, with

$$M = \left(\begin{array}{ccc|ccc} -\nu k^2(1+\ell'^2) & k(1-3\ell'^2) & ik\tilde{B}_0(1+\ell'^2) & ik\ell' B_0(1+\ell'^2) & i\tilde{B}_0 2\ell' & 2\ell' \\ \frac{k}{2(1+\ell'^2)} & -\nu & iB_0 & 0 & iB_0 3k\ell' & -2k\ell'\nu \\ \frac{ik\tilde{B}_0}{2}(1+\ell'^2)^{-1} & iB_0 & -\eta & 0 & -2k\ell'\eta & -iB_0 k\ell' \\ \hline i\ell' B_0 k(1+\ell'^2)^{-1} & ik\tilde{B}_0 2k\ell' & 0 & -\eta k^2(1+\ell'^2) & k & ik\tilde{B}_0 \\ 0 & -iB_0 k\ell' & -2\ell' k\eta & -\frac{k}{2} & -\eta & iB_0 \\ 0 & -2k\ell'\nu & iB_0 3\ell' k & -\frac{ik\tilde{B}_0}{2} & iB_0 & -\nu \end{array}\right) \left(\begin{array}{c} G_0' \\ G_- \\ H_+ \\ H_0 \\ H_- \\ G_+ \end{array}\right), \tag{B.36}$$

We now write an expansion matrix $M = M_0 + kM_1 + \cdots$ (see section 5.5.2).

By expand the matrix $M = M_0 + kM_1 + ...$,

$$M_0 = \left(\begin{array}{ccc|ccc} 0 & 0 & 0 & 0 & 2\ell' i\tilde{B}_0 & 2\ell' \\ 0 & -\nu & iB_0 & 0 & 0 & 0 \\ 0 & iB_0 & -\eta & 0 & 0 & 0 \\ \hline 0 & 0 & 0 & 0 & 0 & 0 \\ 0 & 0 & 0 & 0 & -\eta & iB_0 \\ 0 & 0 & 0 & 0 & iB_0 & -\nu \end{array}\right), \tag{B.37}$$

and

$$M_1 = \left(\begin{array}{ccc|ccc} 0 & 1-3\ell'^2 & i\tilde{B}_0(1+\ell'^2) & iB_0\ell'(1+\ell'^2) & 0 & 0 \\ \frac{1}{2}(1+\ell'^2)^{-1} & 0 & 0 & 0 & iB_0 3\ell' & -2\ell'\nu \\ \frac{1}{2}i\tilde{B}_0(1+\ell'^2)^{-1} & 0 & 0 & 0 & -2\ell'\eta & -iB_0\ell' \\ \hline iB_0\ell'(1+\ell'^2)^{-1} & 0 & 0 & 0 & 1 & i\tilde{B}_0 \\ 0 & -iB_0\ell' & -2\ell'\eta & -\frac{1}{2} & 0 & 0 \\ 0 & -2\ell'\nu & iB_0 3\ell' & -\frac{1}{2}i\tilde{B}_0 & 0 & 0 \end{array}\right), \tag{B.38}$$

Figure B.1 shows that the matrix M_0 involving coupling between the flow G_0 and undamped waves G_+, H_- and between the terms H_-, G_+ and G_-, H_+, where the

Alfvén waves drive each other.

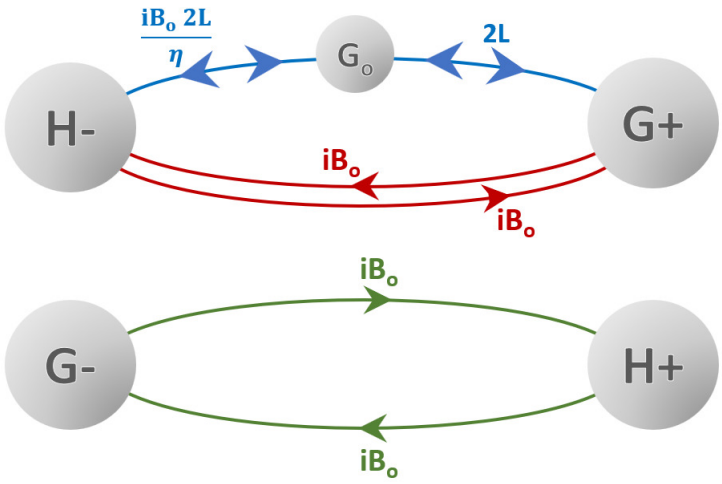

Figure B.1: Schematic of the matrix M_0

Figure B.2 shows that the matrix M_1 involving couplings between the terms (H_-, G_+) and the terms (G_-, H_+), Also there are coupling terms between the flow G_0 and the wave H_+.

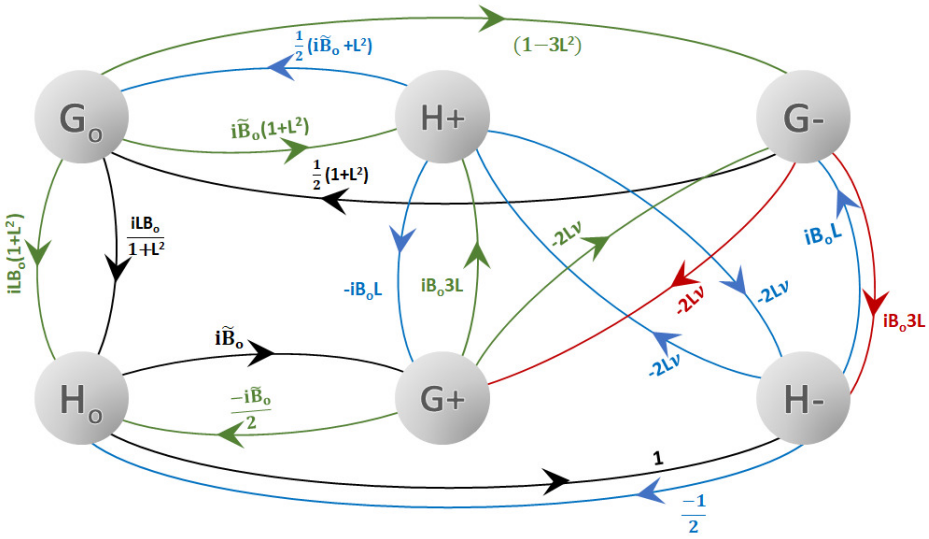

Figure B.2: Schematic of the matrix M_1, we set $\tilde{B}_0 = \frac{B_0}{\eta}$

We now calculate p. The matrix M_0 has now lost the attractive block structure present in the earlier expansion as a consequence of the scaling of ℓ. Then, M_0 has

double zero eigenvalues p_0 with the right eigenvectors

$$\boldsymbol{v}_0 = \begin{pmatrix} a & 0 & 0 & b & 0 & 0 \end{pmatrix}^T = a \begin{pmatrix} 1 & 0 & 0 & 0 & 0 & 0 \end{pmatrix}^T + b \begin{pmatrix} 0 & 0 & 0 & 1 & 0 & 0 \end{pmatrix}^T \tag{B.39}$$

$$\boldsymbol{v}_0 = a\ \boldsymbol{v}_{01} + b\ \boldsymbol{v}_{02}$$

However if we try

$$\boldsymbol{w}_{01} = \begin{pmatrix} 1 & 0 & 0 & 0 & 0 & 0 \end{pmatrix}, \quad \boldsymbol{w}_{02} = \begin{pmatrix} 0 & 0 & 0 & 1 & 0 & 0 \end{pmatrix} \tag{B.40}$$

we have $M_0 \boldsymbol{w}_{02} = 0$, but $M_0 \boldsymbol{w}_{01} \neq 0$

$$\boldsymbol{w}_{01} M_0 = \begin{pmatrix} 0 & 0 & 0 & 0 & 2\ell' \tilde{B}_0 & 2\ell' \end{pmatrix} \tag{B.41}$$

In order to fix this, look for $\boldsymbol{w}_{01}$ of the form

$$\boldsymbol{w}_{01} = \begin{pmatrix} 1 & 0 & 0 & 0 & c & d \end{pmatrix}$$

and multiply by the lower block of B.37, we obtain

$$\boldsymbol{w}_{01} M_0 = \begin{pmatrix} 0 & 0 & 0 & 0 & 2\ell' i\tilde{B}_0 - \eta c + i B_0 d, 2\ell' + i B_0 c - \nu d \end{pmatrix} \tag{B.42}$$

So we need to set

$$\begin{pmatrix} -\eta & i B_0 \\ i B_0 & -\nu \end{pmatrix}^{-1} \begin{pmatrix} c \\ d \end{pmatrix} = -2\ell' \begin{pmatrix} i\tilde{B}_0 \\ 1 \end{pmatrix} \tag{B.43}$$

So we invert this Matrix

$$\begin{pmatrix} c \\ d \end{pmatrix} = \Delta \begin{pmatrix} -\nu & -i B_0 \\ -i B_0 & -\eta \end{pmatrix} (-2\ell') \begin{pmatrix} i\tilde{B}_0 \\ 1 \end{pmatrix} \tag{B.44}$$

for convenience we set $\Delta^{-1} = \eta\nu + B_0^2$

$$\begin{pmatrix} c \\ d \end{pmatrix} = 2\ell'\Delta \begin{pmatrix} i\tilde{B}_0\nu + iB_0 \\ -B_0\tilde{B}_0 + \eta \end{pmatrix}, \tag{B.45}$$

Thus, by taking $\tilde{B}_0 = \frac{B_0}{\eta}$ the left eigenvectors are

$$\boldsymbol{w}_0 = c \begin{pmatrix} 1 & 0 & 0 & 0 & 2\ell'\Delta i B_0 \frac{\nu+\eta}{\eta} & 2\ell'\Delta \frac{\eta^2 - B_0^2}{\eta} \end{pmatrix} + d \begin{pmatrix} 0 & 0 & 0 & 1 & 0 & 0 \end{pmatrix} \tag{B.46}$$

$$\boldsymbol{w}_0 = c\, \boldsymbol{w}_{01} + d\, \boldsymbol{w}_{02}$$

Generally, we cannot predict the structure of the mode, so we set $\boldsymbol{v}_0 = a\boldsymbol{v}_{01} + b\boldsymbol{v}_{02}$ & need to find a and b.

Now, looking at the first order equation (3.60), namely $p_1\boldsymbol{v}_0 = (M_0 - p_0)\boldsymbol{v}_1 + M_1\boldsymbol{v}_0$ with $p_0 = 0$, we can apply either of the two vectors on the left, we obtain

$$(M_0 - p_0)\boldsymbol{v}_{01} = 0, \quad (M_0 - p_0)\boldsymbol{v}_{02} = 0 \tag{B.47}$$

$$\boldsymbol{w}_{01}(M_0 - p_0) = 0, \quad \boldsymbol{w}_{02}(M_0 - p_0) = 0 \tag{B.48}$$

Where $\boldsymbol{v}_{01}, \boldsymbol{v}_{02}$ are the eigenvectors on the right and $\boldsymbol{w}_{01}, \boldsymbol{w}_{02}$ are the eigenvectors on the left:

$$\boldsymbol{w}_{01}\boldsymbol{v}_{01} = 1 \qquad \boldsymbol{w}_{02}\boldsymbol{v}_{02} = 1, \quad \boldsymbol{w}_{01}\boldsymbol{v}_{02} = 0 \qquad \boldsymbol{w}_{02}\boldsymbol{v}_{01} = 0 \tag{B.49}$$

Multiplying by $\boldsymbol{v}_1$ on the LHS we find:

$$(M_0 - p_0)\boldsymbol{v}_1 = -(M_1 - p_1)(a\boldsymbol{v}_{01} + b\boldsymbol{v}_{02}) \tag{B.50}$$

Multiplying by $\boldsymbol{w}_{01}$ in the LHS we find:

$$0 = \boldsymbol{w}_{01}(M_0 - p_0)\boldsymbol{v}_1 = -\boldsymbol{w}_{01}(M_1 - p_1)(a\boldsymbol{v}_{01} + b\boldsymbol{v}_{02}) \tag{B.51}$$

$$0 = \boldsymbol{w}_{02}(M_0 - p_0)\boldsymbol{v}_1 = \boldsymbol{w}_{02}(M_1 - p_1)(a\boldsymbol{v}_{01} + b\boldsymbol{v}_{02}) \tag{B.52}$$

So we have

$$\begin{pmatrix} \boldsymbol{w}_{01}(M_1 - p_1)\boldsymbol{v}_{01} & \boldsymbol{w}_{01}(M_1 - p_1)\boldsymbol{v}_{02} \\ \boldsymbol{w}_{02}(M_1 - p_1)\boldsymbol{v}_{01} & \boldsymbol{w}_{02}(M_1 - p_1)\boldsymbol{v}_{02} \end{pmatrix} \begin{pmatrix} a \\ b \end{pmatrix} = 0 \tag{B.53}$$

So we calculate the entries of this matrix & set the determinant to zero

$$A = \begin{pmatrix} w_{01}M_1v_{01} - p_1 & w_{01}M_1v_{02} \\ w_{02}M_1v_{01} & w_{02}M_1v_{02} - p_1 \end{pmatrix} \tag{B.54}$$

By using the equations (B.49), we calculate each index in matrix (B.54) separately:

$$\boldsymbol{w}_{01}M_1\boldsymbol{v}_{01} = \boldsymbol{w}_{01}M_1 \begin{pmatrix} 1 & 0 & 0 & 0 & 0 & 0 \end{pmatrix}^T = \boldsymbol{w}_{01} \begin{pmatrix} 0 \\ \frac{1}{2(1+\ell'^2)} \\ \frac{1}{2}i\tilde{B}_0(1+\ell'^2) \\ i\ell' B_0 \frac{1}{1+\ell'^2} \\ 0 \\ 0 \end{pmatrix} = 0 \tag{B.55}$$

$$\boldsymbol{w}_0 2 M_1 \boldsymbol{v}_0 1 = \boldsymbol{w}_0 2 \begin{pmatrix} 0 \\ \frac{1}{2(1+\ell'^2)} \\ \frac{1}{2}i\tilde{B}_0(1+\ell'^2) \\ i\ell' B_0 \frac{1}{1+\ell'^2} \\ 0 \\ 0 \end{pmatrix} = \frac{i\ell' B_0}{1+\ell'^2} \tag{B.56}$$

$$\boldsymbol{w}_{01}M_1\boldsymbol{v}_{02} = \boldsymbol{w}_{01} \begin{pmatrix} i\ell' B_0(1+\ell'^2) \\ 0 \\ 0 \\ 0 \\ -\frac{i\tilde{B}_0}{2} \\ -\frac{1}{2} \end{pmatrix} = i\ell' B_0(1+\ell'^2) - \frac{iB_0\ell'}{\Delta}(2 + \frac{\nu}{\eta} - \frac{B_0^2}{\eta^2}) \tag{B.57}$$

$$\boldsymbol{w}_{02} M_1 \boldsymbol{v}_{02} = \boldsymbol{w}_{02} \begin{pmatrix} i\ell' B_0(1+\ell'^2) \\ 0 \\ 0 \\ 0 \\ -\frac{i\tilde{B}_0}{2} \\ -\frac{1}{2} \end{pmatrix} = 0 \tag{B.58}$$

which gives :

$$\boldsymbol{w}_{01} M_1 \boldsymbol{v}_{01} = 0, \qquad \boldsymbol{w}_{02} M_1 \boldsymbol{v}_{02} = 0 \tag{B.59}$$

$$\boldsymbol{w}_{02} M_1 \boldsymbol{v}_{01} = \frac{i\ell' B_0}{1+\ell'^2}, \qquad \boldsymbol{w}_{01} M_1 \boldsymbol{v}_{02} = i\ell' B_0(1+\ell'^2) - \frac{iB_0\ell'}{\triangle}(2 + \frac{\nu}{\eta} - \frac{B_0^2}{\eta^2}) \tag{B.60}$$

Substituting the equations from (B.59 - B.60) into the equation B.54, so the matrix A becomes:

$$\begin{pmatrix} -p_1 & \boldsymbol{w}_{01} M_1 \boldsymbol{v}_{02} \\ \boldsymbol{w}_{02} M_1 \boldsymbol{v}_{01} & -p_1 \end{pmatrix} \begin{pmatrix} a \\ b \end{pmatrix} = 0$$

For non-trivial solutions of a, b we require the determinant of the square matrix to zero From the determinant of the matrix A, we obtain:

$$p_1^2 - (\boldsymbol{w}_{01} M_1 \boldsymbol{v}_{02})(\boldsymbol{w}_{02} M_1 \boldsymbol{v}_{01}) = 0, \qquad p_1 = \sqrt{(\boldsymbol{w}_{01} M_1 \boldsymbol{v}_{02})(\boldsymbol{w}_{02} M_1 \boldsymbol{v}_{01})} \tag{B.61}$$

yielding

$$p_1 = \sqrt{\frac{i\ell' B_0}{1+\ell'^2}\left[iB_0\ell'(1+\ell'^2) - \frac{iB_0\ell'}{\Delta}(2 + \frac{\nu}{\eta} - \frac{B_0^2}{\eta^2})\right]} \tag{B.62}$$

Using the scale $\ell' = \ell/k$ and Δ we find the growth rate as

$$p_1 = \sqrt{\frac{ik^2\ell B_0}{1+\frac{\ell^2}{k^2}}\left[ik\ell B_0(1+\frac{\ell^2}{k^2}) - \frac{iB_0 k\ell}{\nu\eta + B_0^2}(2 + \frac{\nu}{\eta} - \frac{B_0^2}{\eta^2})\right]} \tag{B.63}$$

$$p = p_1 k + \cdots = \pm B_0 \ell \left[\frac{k^2}{\ell^2 + k^2} \frac{\nu\eta + 2\eta^2 - B_0^2}{\eta^2(\nu\eta + B_0^2)} - 1\right]^{1/2} + ... \tag{B.64}$$

For instability at general points in the (ν, B_0) plane, we need the first term

of the equation (5.8) to be positive for some values of k, ℓ. This amounts to the condition,

$$B_0^2 = \frac{\nu^2(P^2 + 2P - \nu^2)}{P(\nu^2 + P^2)}\,. \tag{B.65}$$

We maximise B_0^2 over ν^2 we obtain :

$$2B_0\frac{\partial B_0}{\partial \nu} = \frac{2\nu}{P}\frac{P^2 + 2P - \nu^2}{\nu^2 + P^2} + \frac{\nu^2}{P}\left[\frac{-2\nu(\nu^2 + P^2) - 2\nu(P^2 + 2P - \nu^2)}{(\nu^2 + P^2)^2}\right] \tag{B.66}$$

$$2B_0\frac{\partial B_0}{\partial \nu} = \frac{\nu}{P}\frac{2(P^2 + 2P - \nu^2)(\nu^2 + P^2) - 4\nu^2(P^2 + P)}{(\nu^2 + P^2)^2} \tag{B.67}$$

we take the numerator to zero and for simplification, we set $x = \nu^2$

$$2(P^2 + 2P - \nu^2)(\nu^2 + P^2) = 4\nu^2(P^2 + P) \tag{B.68}$$

$$-(\nu^2)^2 + \nu^2(-2P^2) + (P^4 + 2P^3) = 0 \tag{B.69}$$

and then

$$-x^2 - 2P^2x + (P^4 + 2P^3) = 0 \tag{B.70}$$

$$x = \frac{2P^2 \pm \sqrt{4P^4 + 4(P^4 + 2P^3)}}{-2} \tag{B.71}$$

$$x = \frac{2P^2 \pm \sqrt{4P^4 + 4P^4 + 8P^3}}{-2} \tag{B.72}$$

The maximum occurs at

$$\nu^2 = -P^2 \pm \sqrt{2P^3(P + 1)} \tag{B.73}$$

We keep up the discussion in the main part of the chapter in section 5.5.2

C. Derivation of growth rate for general angle γ and $\ell = 0$

In order to avoid complexity in the system, we rewrite the equations (5.14-5.15) with the symbols: $s = \sin\gamma, \quad c = \cos\gamma$, we obtain:

$$\begin{aligned} pG_n = &\left[\frac{k}{2}\frac{1}{(n-1)^2+k^2} - \frac{k}{2}\right] G_{n-1} - \left[\frac{k}{2}\frac{1}{(n+1)^2+k^2} - \frac{k}{2}\right] G_{n+1} - \nu(k^2+n^2)G_n \\ &+ \frac{ikB_0s}{2\eta}(k^2+(n-1)^2-1)H_{n-1} + \frac{ikB_0s}{2\eta}(k^2+(n+1)^2-1)H_{n+1} \\ &+ (ikB_0c + inB_0s)(k^2+n^2)H_n, \end{aligned} \tag{C.1}$$

$$\begin{aligned} pH_n = &-\frac{k}{2}H_{n-1} + \frac{k}{2}H_{n+1} - \eta(k^2+n^2)H_n + \frac{ikB_0s}{2\eta}\frac{1}{(n-1)^2+k^2}G_{n-1} \\ &+ \frac{ikB_0s}{2\eta}\frac{1}{(n+1)^2+k^2}G_{n+1} + \frac{inB_0s}{k^2+n^2}G_n + \frac{ikB_0c}{k^2+n^2}G_n, \end{aligned} \tag{C.2}$$

We reduce the general linear equations in terms of $G_0, H_0, G_{\pm1}, H_{\pm1}$ and dropping any terms involving $G_{\pm2}, H_{\pm2}$, then we rewrite the equations in term of $G_\pm, H_\pm$ defined in equation (A.29). For $n = 0$ we have

$$pG_0 = \frac{k}{2}[\frac{1}{1+k^2}-1]G_{-1} - \frac{k}{2}[\frac{1}{1+k^2}-1]G_1 - \nu k^2 G_0 + \frac{ikB_0sk^2}{2\eta}H_{-1} + \frac{ikB_0sk^2}{2\eta}H_1 + ikB_0ck^2H_0 \tag{C.3}$$

$$pH_0 = -\frac{k}{2}H_{-1} + \frac{k}{2}H_1 - \eta k^2 H_0 + \frac{ikB_0s}{2\eta}[\frac{1}{1+k^2}]G_{-1} + \frac{ikB_0s}{2\eta}[\frac{1}{1+k^2}]G_1 + ikB_0ck^{-2}G_0 \tag{C.4}$$

and for $n = \pm1$ we find

$$pG_1 = \frac{k}{2}[\frac{1}{k^2} - 1]G_0 - \nu(1+k^2)G_1 - \frac{ikB_0s}{2\eta}(-1+k^2)H_0 + (ikB_0c + iB_0s)(1+k^2)H_1 \tag{C.5}$$

$$pH_1 = -\frac{k}{2}H_0 - \eta(1+k^2)H_1 + \frac{iB_0s}{1+k^2}G_1 + \frac{ikB_0sk^{-2}}{2\eta}G_0 + \frac{ikB_0c}{1+k^2}G_1 \tag{C.6}$$

$$pG_{-1} = -\frac{k}{2}(\frac{1}{k^2}-1)G_0-\nu(1+k^2)G_{-1}+\frac{ikB_0s}{2\eta}(-1+k^2)H_0+(ikB_0c-iB_0s)(1+k^2)H_{-1} \tag{C.7}$$

$$pH_{-1} = \frac{k}{2}H_0 - \eta(1+k^2)H_{-1} - \frac{iB_0s}{1+k^2}G_{-1} + \frac{ikB_0sk^{-2}}{2\eta}G_0 + \frac{ikB_0c}{1+k^2}G_{-1} \tag{C.8}$$

Now $k \ll 1$ we approximate

$$1+k^2 \simeq 1 \qquad \frac{1}{1+k^2} \simeq 1 \qquad \frac{1}{1+k^2} - 1 = 1 - k^2 + k^4 .... - 1 \approx -k^2 \tag{C.9}$$

To gives

$$pG_0 = k^3G_- - \nu k^2G_0 + \frac{ikB_0k^2s}{\eta}H_+ + ikB_0ck^2H_0, \tag{C.10}$$

$$pH_0 = -\eta k^2H_0 + kH_- + \frac{ikB_0s}{\eta}G_+ + \frac{ikB_0c}{k^2}G_0, \tag{C.11}$$

$$pG_+ = -\nu G_+ - \frac{ikB_0s}{2\eta}H_0 + iB_0sH_- + ikB_0cH_+, \tag{C.12}$$

$$pH_+ = -\eta H_+ + \frac{ikB_0sk^{-2}}{2\eta}G_0 + iB_0sG_- + ikB_0cG_+, \tag{C.13}$$

$$pG_- = \frac{1}{2k}G_0 + ikB_0cH_- - \nu G_- + iB_0sH_+, \tag{C.14}$$

$$pH_- = -\eta H_- - \frac{k}{2}H_0 + iB_0sG_+ + ikB_0cG_-, \tag{C.15}$$

where $G_0 = k^2G_0'$ as used in previous calculations. Before expanding M in powers of k , for general field, we rescale $ckB_0 = c'B_0', \quad sB_0 = s'B_0'$ with B_0 fixed in the limit $k \to 0$. then $\frac{s}{c} = k\frac{s'}{c'} = O(k)$ which is the the limit of small γ.

$$pG_0' = kG_-' - \nu k^2G_0' + \frac{ikB_0's'}{\eta}H_+' + iB_0'c'H_0' \tag{C.16}$$

$$pH_0' = -\eta k^2H_0' + kH_-' + \frac{iks'B_0'}{\eta}G_+' + iB_0'c'G_0' \tag{C.17}$$

$$pG_+' = -\nu G_+' - \frac{iks'B_0'}{2\eta}H_0' + iB_0's'H_-' + ic'B_0'H_+' \tag{C.18}$$

$$pH_+' = -\eta H_+' + \frac{iks'B_0'}{2\eta}G_0' + iB_0's'G_-' + iB_0'c'G_+' \tag{C.19}$$

$$pG_-' = \frac{k}{2}G_0' + ic'B_0'H_-' - \nu G_-' + is'B_0'H_+' \tag{C.20}$$

$$pH_-' = -\eta H_-' - \frac{k}{2}H_0' + iB_0's'G_+' + iB_0'c'G_-' \tag{C.21}$$

We drop the primes and write the matrix M in the form $M\boldsymbol{v} = p\boldsymbol{v}$, then expanding M gives the matrices.

$$M = \left(\begin{array}{ccc|ccc} -\nu k^2 & iB_0c & 0 & \frac{ikB_0s}{\eta} & k & 0 \\ iB_0c & -\eta k^2 & \frac{ikB_0s}{\eta} & 0 & 0 & k \\ 0 & -\frac{ikB_0s}{2\eta} & -\nu & iB_0c & 0 & iB_0s \\ \hline \frac{ikB_0s}{2\eta} & 0 & iB_0c & -\eta & iB_0s & 0 \\ \frac{1}{2} & 0 & 0 & iB_0s & -\nu & iB_0c \\ 0 & -\frac{1}{2} & iB_0s & 0 & iB_0c & -\eta \end{array}\right)\left(\begin{array}{c} G_0 \\ H_0 \\ G_+ \\ H_+ \\ G_- \\ H_- \end{array}\right) \tag{C.22}$$

By expanding the matrix $M = M_0 + kM_1 + ...$,

$$M_0 = \left(\begin{array}{cc|cccc} 0 & iB_0c & 0 & 0 & 0 & 0 \\ iB_0c & 0 & 0 & 0 & 0 & 0 \\ \hline 0 & 0 & -\nu & iB_0c & 0 & iB_0s \\ 0 & 0 & iB_0c & -\eta & iB_0s & 0 \\ 0 & 0 & 0 & iB_0s & -\nu & iB_0c \\ 0 & 0 & iB_0s & 0 & iB_0c & -\eta \end{array}\right), \tag{C.23}$$

and

$$M_1 = \left(\begin{array}{ccc|ccc} 0 & 0 & 0 & \frac{iB_0s}{\eta} & 1 & 0 \\ 0 & 0 & \frac{iB_0s}{\eta} & 0 & 0 & 1 \\ 0 & -\frac{iB_0s}{2\eta} & 0 & 0 & 0 & 0 \\ \hline \frac{iB_0s}{2\eta} & 0 & 0 & 0 & 0 & 0 \\ \frac{1}{2} & 0 & 0 & 0 & 0 & 0 \\ 0 & -\frac{1}{2} & 0 & 0 & 0 & 0 \end{array}\right), \tag{C.24}$$

and

$$M_2 = \left(\begin{array}{ccc|ccc} -\nu & 0 & 0 & 0 & 0 & 0 \\ 0 & -\eta & 0 & 0 & 0 & 0 \\ 0 & 0 & -\nu & 0 & 0 & 0 \\ \hline 0 & 0 & 0 & -\eta & 0 & 0 \\ 0 & 0 & 0 & 0 & -\nu & 0 \\ 0 & 0 & 0 & 0 & 0 & -\eta \end{array}\right) \tag{C.25}$$

For an approximate growth rate $\mathrm{Re}\, p$, we use the expansion (3.58) and solve order by order. At leading order (3.59) we focus on the eigenvalues $p_0 = \pm iB_0$ of M_0, corresponding to large scale undamped Alfvén waves, without loss of generality, and take

$$p_0 = iB_0 c, \qquad \boldsymbol{v}_0 = (1,1,0,0,0,0)^T, \quad \boldsymbol{w}_0 = (1,1,0,0,0,0) \tag{C.26}$$

Here $\boldsymbol{w}_0$ is the left eigenvectors as usual, with $\boldsymbol{w}_0(M_0 - p_0 I) = 0$ and $\boldsymbol{w}_0\boldsymbol{v}_0 = 2$. Moving to the first order, from equation (3.64) we rapidly find:

$$M_1\boldsymbol{v}_0 = \left(0, 0, \frac{-iB_0 s}{2\eta}, \frac{iB_0 s}{2\eta}, \frac{1}{2}, \frac{-1}{2}\right)^T, \quad p_1 = 0 \tag{C.27}$$

$$\boldsymbol{w}_0 M_1 = \left(0, 0, \frac{iB_0 s}{\eta}, \frac{iB_0 s}{\eta}, 1, 1\right) \tag{C.28}$$

To find a solution we clearly need only invert the 4×4 lower right block of $(M_0 - p_0)$ from the matrix (C.23), which gives

$$\boldsymbol{v}_1 = -\left(\begin{array}{cc|cc} -(\nu + iB_0 c) & iB_0 c & 0 & iB_0 s \\ iB_0 c & -(\eta + iB_0 c) & iB_0 s & 0 \\ \hline 0 & iB_0 s & -(\nu + iB_0 c) & iB_0 c \\ iB_0 s & 0 & iB_0 c & -(\eta + iB_0 c) \end{array}\right)^{-1} \left(\begin{array}{c} -\frac{iB_0 s}{2\eta} \\ \frac{iB_0 s}{2\eta} \\ \frac{1}{2} \\ -\frac{1}{2} \end{array}\right) \tag{C.29}$$

This gives

$$\boldsymbol{v}_1 = \begin{pmatrix} \frac{iB_0 s}{2\eta} \\ -\frac{iB_0 s}{2\eta} \\ -\frac{1}{2} \\ \frac{1}{2} \end{pmatrix} \tag{C.30}$$

We then calculate p_2 from equation (3.65), the second correction to p_0 is given by

$$p_2 = -\frac{\boldsymbol{w}_0 M_1 (M_0 - p_0)^{-1} M_1 \boldsymbol{v}_0}{\boldsymbol{w}_0 \boldsymbol{v}_0} + \frac{\boldsymbol{w}_0 M_2 \boldsymbol{v}_0}{\boldsymbol{w}_0 \boldsymbol{v}_0}, \tag{C.31}$$

We compute the remaining calculations using the Maple framework (details in subsection C.0.1). We choose the symbols α, β instead of the terms $(ikB_0 c, iB_0 s)$ where $c = \cos\gamma, s = \sin\gamma$. We set $c = 1, s = 0$, referring to the vertical field, whereas for the $s = 1, c = 0.$ referring to the horizontal field. Thus, we are able to prove the agreement mathematically.

$$p_2 = \frac{1}{4\eta^2} \frac{(\eta - \beta)(\nu - \eta)(\beta + \eta)[(\nu + \alpha)\eta + \alpha\nu - \beta^2]}{[(\nu + \alpha)\eta + \nu\alpha - 2\alpha\beta - \beta^2][(\nu + \alpha)\eta + \nu\alpha + 2\alpha\beta - \beta^2]} - 0.5(\nu + \eta)k^2 \tag{C.32}$$

We simplify equation (C.32) and we obtain:

$$p_2 k^2 = \frac{1}{4\eta^2} \frac{(\eta - \nu)(\eta^2 - \beta^2)[\nu\eta + (\nu + \eta)\alpha - \beta^2]k^2}{[\nu\eta + (\nu + \eta)\alpha - \beta^2 - 2\alpha\beta][\nu\eta + (\nu + \eta)\alpha - \beta^2 + 2\alpha\beta]} - \frac{1}{2}(\nu + \eta)k^2 \tag{C.33}$$

$$p_2 k^2 = \frac{k^2}{4\eta^2} \frac{(\eta - \nu)(\eta^2 - \beta^2)[\nu\eta + (\nu + \eta)\alpha - \beta^2]}{[\nu\eta + (\nu + \eta)\alpha - \beta^2]^2 - 4\alpha^2\beta^2} - \frac{1}{2}(\nu + \eta)k^2 \tag{C.34}$$

This is the form for α, β, we check this form by using the Maple framework we get back to the vertical field case by setting $\beta = 0$, and $\alpha = ikB_0$, first $\beta = 0$ gives:

$$p_2 k^2 = \frac{k^2}{4} \frac{(\eta - \nu)[\nu\eta + (\nu + \eta)\alpha]}{[\nu\eta + (\nu + \eta)\alpha]^2} - \frac{1}{2}(\nu + \eta)k^2 \tag{C.35}$$

simplifying

$$p_2 k^2 = \frac{k^2}{4} \frac{(\eta - \nu)}{(\nu\eta + (\nu + \eta)\alpha)} - \frac{1}{2}(\nu + \eta)k^2 \tag{C.36}$$

By taking over a common denominator, and setting $\alpha = ikB_0$

$$p_2 k^2 = \frac{k^2}{4}\frac{(\eta-\nu)[\nu\eta-(\nu+\eta)ikB_0]}{\nu^2\eta^2+(\nu+\eta)^2k^2B_0^2} - \frac{1}{2}(\nu+\eta)k^2 \tag{C.37}$$

by taking a real part in the growth rate

$$\mathrm{Re}\, p_2 k^2 = \frac{1}{4}\frac{\nu\eta(\eta-\nu)k^2}{\nu^2\eta^2+(\nu+\eta)^2k^2B_0^2} - \frac{1}{2}(\nu+\eta)k^2 \tag{C.38}$$

We have obtained a similar formula of vertical growth rate, (3.100) in chapter 3. The critical case is when the numerator is zero which gives the equation (3.109). Details are in the vertical field section 3.7.1.

Now we try something similar for general γ but avoid too much work. First, we set $\alpha = ickB_0,\ \beta = isB_0$ in equation (C.32), and we again undo the scalings we find:

$$p_2 k^2 = \frac{k^2}{4\eta^2}\frac{(\eta-\nu)(\eta^2+s^2B_0^2)[\nu\eta+(\nu+\eta)ickB_0+s^2B_0^2]}{[\nu\eta+(\nu+\eta)ickB_0+s^2B_0^2]^2-4s^2c^2k^2B_0^4} - \frac{1}{2}(\nu+\eta)k^2 \tag{C.39}$$

By combining over a common denominator, we obtain

$$p_2 k^2 = \frac{k^2}{4\eta^2}\frac{(\eta-\nu)(\eta^2+s^2B_0^2)[\nu\eta+(\nu+\eta)ickB_0+s^2B_0^2]-2\eta^2(\nu+\eta)[(\nu\eta+(\nu+\eta)ickB_0+s^2B_0^2)^2}{[(\nu\eta+(\nu+\eta)ickB_0+s^2B_0^2)^2-4s^2c^2k^2B_0^4]} \tag{C.40}$$

Now we set everything with $k = 0$ set to zero, we find:

$$p_2 k^2 = \frac{k^2}{4\eta}\frac{[(\eta-\nu)(\eta^2+s^2B^2)(\nu\eta+s^2B^2)-2\eta^2(\nu+\eta)(\nu\eta+s^2B^2)^2]}{(\nu\eta+s^2B^2)^2} \tag{C.41}$$

This form is real, we don't need to take the real part, by setting the top numerator of the equation (C.41) to zero and finding the instability threshold.

$$(\eta-\nu)(\eta^2+s^2B_0^2)(\nu\eta+s^2B_0^2) = 2\eta^2(\nu+\eta)(\nu\eta+s^2B_0^2)^2 \tag{C.42}$$

or

$$(\eta-\nu)(\eta^2+s^2B_0^2) = 2\eta^2(\nu+\eta)(\nu\eta+s^2B_0^2) \tag{C.43}$$

Further checking if we set $s = 0$ we get back to the previous case, equation (C.38). By substituting the Prandtl number with expression $\eta = \nu/P$ into equation (C.42), we obtain:

$$\nu(\frac{1}{P} - 1)(\frac{\nu^2}{P^2} + s^2 B_0^2) = \frac{2\nu^2}{P^2}\nu(1 + \frac{1}{P})(\frac{\nu^2}{P} + s^2 B_0^2) \tag{C.44}$$

or

$$\nu P(1 - P)(\nu^2 + P^2 s^2 B_0^2) = 2\nu^3(1 + P)(\nu^2 + P s^2 B_0^2) \tag{C.45}$$

$$P(1 - P)(\nu^2 + P^2 s^2 B_0^2) = 2\nu^2(1 + P)(\nu^2 + P s^2 B_0^2) \tag{C.46}$$

It can be written as:

$$2(1 + P)\nu^4 + [2(1 + P)P s^2 B_0^2 - P(1 - P)]\nu^2 - P(1 - P)P^2 s^2 B_0^2 = 0 \tag{C.47}$$

By rearrangement of equation C.47, we obtain B_0^2 in terms of ν, P, which can be expressed as follows:

$$B_0^2 = \frac{2\nu^4(1 + P) - P(1 - P)\nu^2}{P(1 - P)s^2 P^2 - 2\nu^2(1 + P)P s^2} \tag{C.48}$$

C.0.1 Maple calculations

In this section, we have complicated calculations and we use the Maple framework to simplify. The instability growth rate of equation (C.32- C.37) is found by the Maple framework as follows:

$$A := \begin{bmatrix} -\nu - \alpha & \alpha & 0 & \beta \\ \alpha & -\eta - \alpha & \beta & 0 \\ 0 & \beta & -\nu - \alpha & \alpha \\ \beta & 0 & \alpha & -\eta - \alpha \end{bmatrix}$$

Figure C.1: Maple output- the matrix A from equation (C.29), we replace $\alpha = iB_0'c' = ikcB_0, \beta = iB_0's' = isB_0$.

By using the linear algebra package and the determinant of the matrix A we obtain:

$$-4\alpha^2\beta^2+\alpha^2\eta^2+2\alpha^2\eta\nu+\alpha^2\nu^2-2\alpha\beta^2\eta-2\alpha\beta^2\nu+2\alpha\eta^2\nu+2\alpha\eta\nu^2+\beta^4-2\beta^2\eta\nu+\eta^2\nu^2$$

Figure C.2: Maple output- the determinant of matrix A.

Then we take the inverse of the matrix A called "L=Matrix inverse (A)", which gives us a massive calculation that will not display here. Now we use equation (C.31) to find the p_2, we rewrite the $M_1\boldsymbol{v}_0$ from equation C.27 and $M_1\boldsymbol{w}_0$ from equation C.28

$$v_0 := \begin{bmatrix} \frac{\beta}{2\eta} \\ -\frac{\beta}{2\eta} \\ -\frac{1}{2} \\ \frac{1}{2} \end{bmatrix} \qquad w_0 := \begin{bmatrix} \frac{\beta}{\eta} & \frac{\beta}{\eta} & 1 & 1 \end{bmatrix}$$

(a) (b)

Figure C.3: Maple output. (a) $M_1\boldsymbol{v}_0$, (b) $M_1\boldsymbol{w}_0$.

The p_2 formula after simplification gives the vertical and horizontal expression:

$$p2 := -\frac{w_0 \cdot L \cdot v_0}{2}:$$

simplify(p2)

$$\frac{(\beta+\eta)(\nu-\eta)(\eta-\beta)\left((\alpha+\nu)\eta+\nu\alpha-\beta^2\right)}{4\eta^2\left((\alpha+\nu)\eta+(\nu+2\beta)\alpha-\beta^2\right)\left((\alpha+\nu)\eta+(\nu-2\beta)\alpha-\beta^2\right)}$$

Figure C.4: Maple output- p_2 for vertical and horizontal fields with α and β.

Now, we need to enter the values of $\alpha = iB_0'c' = ikB_0c$ and $\beta = iB_0's' = iB_0s$, and then calculate p_2 based on the values

> $\alpha := I \cdot B \cdot c$

$$\alpha := I(B \cdot c)$$

> $\beta := I \cdot B \cdot s$

$$\beta := I(B \cdot s)$$

> p2 :
> simplify(p2)

$$\frac{\left(\eta^2+(B\cdot s)^2\right)(\nu-\eta)\left((I\nu+I\eta)(B\cdot c)+\nu\eta+(B\cdot s)^2\right)}{8\left(\left(-2(B\cdot s)^2-\frac{(\eta+\nu)^2}{2}\right)(B\cdot c)^2+I\left(\nu\eta+(B\cdot s)^2\right)(\eta+\nu)(B\cdot c)+\frac{\left(\nu\eta+(B\cdot s)^2\right)^2}{2}\right)\eta^2}$$

Figure C.5: Maple output- p_2 for vertical and horizontal fields, similar to equation (C.39).

If we set $c = 0$ and $s = 1$ we get back to horizontal field calculations. We simplify the calculation and obtain the formula for both the flow branch and field branch.

```
> c := 0
                                   c := 0
> s := 1
                                   s := 1
> p2
```

$$-\frac{I\left(\frac{IB\left(B^2\eta+\eta^2\nu\right)}{\eta\left(-B^4-2B^2\eta\nu-\eta^2\nu^2\right)}+\frac{IB\left(B^2+\nu\eta\right)}{-B^4-2B^2\eta\nu-\eta^2\nu^2}\right)B}{4\eta}$$

$$+\frac{I\left(\frac{IB\nu\left(B^2+\nu\eta\right)}{\eta\left(-B^4-2B^2\eta\nu-\eta^2\nu^2\right)}+\frac{IB\left(B^2+\nu\eta\right)}{-B^4-2B^2\eta\nu-\eta^2\nu^2}\right)B}{4\eta}+\frac{B^2\eta+\eta^2\nu}{4\left(-B^4-2B^2\eta\nu-\eta^2\nu^2\right)}$$

$$-\frac{B^2\nu+\eta\nu^2}{4\left(-B^4-2B^2\eta\nu-\eta^2\nu^2\right)}$$

```
> simplify( (12) )
```

$$\frac{\left(B^2+\eta^2\right)(\nu-\eta)}{4\left(B^2+\nu\eta\right)\eta^2}$$

Figure C.6: Maple output- horizontal field

If we set $s = 0$ and $c' = k$ we get back to vertical field calculation

```
> s := 0
                                   s := 0
> c := k
                                   c := k
> p2
```

$$\frac{-(B\cdot k)^2\eta-(B\cdot k)^2\nu+I(B\cdot k)\eta^2+2I(B\cdot k)\eta\nu+\eta^2\nu}{4\left((B\cdot k)^2\eta^2+2(B\cdot k)^2\eta\nu+(B\cdot k)^2\nu^2-2I(B\cdot k)\eta^2\nu-2I(B\cdot k)\eta\nu^2-\eta^2\nu^2\right)}$$

$$-\frac{-(B\cdot k)^2\eta-(B\cdot k)^2\nu+2I(B\cdot k)\eta\nu+I(B\cdot k)\nu^2+\eta\nu^2}{4\left((B\cdot k)^2\eta^2+2(B\cdot k)^2\eta\nu+(B\cdot k)^2\nu^2-2I(B\cdot k)\eta^2\nu-2I(B\cdot k)\eta\nu^2-\eta^2\nu^2\right)}$$

```
> simplify( (16) )
```

$$\frac{(\nu-\eta)\left((I\nu+I\eta)(B\cdot k)+\nu\eta\right)}{-4(\eta+\nu)^2(B\cdot k)^2+8I\eta(\eta+\nu)\nu(B\cdot k)+4\eta^2\nu^2}$$

```
>
```

Figure C.7: Maple output- vertical field

We need to simplify the vertical field formula to see the agreement between the Maple formula (C.7) and vertical field formula (C.37)

$$p_2k^2=\frac{(\eta-\nu)(\nu\eta-(\eta+\nu)ikB_0)}{4(\nu^2\eta^2+(\eta+\nu)^2k^2B_0^2)} \tag{C.49}$$

We keep up the discussion in the main part of the chapter in section 5.7

Bibliography

H. Alfvén (1942). 'Existence of electromagnetic-hydrodynamic waves'. In: *Nature* 150.3805, pp. 405–406 (Cited on page 27).

A. Algatheem, A. Gilbert and A. S. Hillier (2023). 'Zonostrophic instabilities in magnetohydrodynamic Kolmogorov flow'. In: *Geophysical & Astrophysical Fluid Dynamics* 0.0, pp. 1–40. DOI: 10.1080/03091929.2023.2268817 (Cited on pages 62, 75, 148 and 244).

A. Alonso (1999). 'A mathematical justification of the low-frequency heterogeneous time-harmonic Maxwell equations'. In: *Mathematical Models and Methods in Applied Sciences* 9.03, pp. 475–489 (Cited on page 27).

N. J. Balmforth and Y.-N. Young (2002). 'Stratified Kolmogorov flow'. In: *Journal of Fluid Mechanics* 450, pp. 131–167 (Cited on page 22).

C. M. Bender and S. A. Orszag (1999). *Advanced mathematical methods for scientists and engineers I: Asymptotic methods and perturbation theory*. Vol. 1. Springer Science & Business Media (Cited on page 80).

L. C. Berselli (2021). *Three-dimensional Navier-Stokes equations for turbulence*. Academic Press (Cited on page 12).

G. Boffetta and R. E. Ecke (2012). 'Two-dimensional turbulence'. In: *Annual review of fluid mechanics* 44, pp. 427–451 (Cited on page 206).

S. Boldyrev and N. F. Loureiro (2018). 'Calculations in the theory of tearing instability'. In: *Journal of Physics: Conference Series*. Vol. 1100. 1. IOP Publishing, p. 012003 (Cited on page 219).

P. Bradshaw (1973). *Effects of streamline curvature on turbulent flow*. Tech. rep. Advisory group for aerospace research and development Paris (France) (Cited on page 207).

K. J. Burns, G. M. Vasil, J. S. Oishi, D. Lecoanet and B. P. Brown (Apr. 2020). 'Dedalus: A flexible framework for numerical simulations with spectral methods'. In: *Physical Review Research* 2.2, 023068, p. 023068. DOI: 10.1103/PhysRevResearch.2.023068. arXiv: 1905.10388 [astro-ph.IM] (Cited on pages 160, 161 and 162).

P. Bushby and J. Mason (2004). 'Understanding the solar dynamo'. In: *Astronomy & Geophysics* 45.4, pp. 4–7 (Cited on page 5).

S. Chandrasekhar (2013). *Hydrodynamic and hydromagnetic stability*. Courier Corporation (Cited on page 17).

A. Chechkin (1999). 'Negative magnetic viscosity in two dimensions'. In: *Journal of Experimental and Theoretical Physics* 89, pp. 677–688 (Cited on page 23).

Z. Chen, J. Huang, Z. Chen and J. Huang (2015). 'Fundamentals of Nonlinear Systems'. In: *Stabilization and Regulation of Nonlinear Systems: A Robust and Adaptive Approach*, pp. 15–65 (Cited on page 7).

S. Childress and A. D. Gilbert (1995). *Stretch, twist, fold: the fast dynamo*. Vol. 37. Springer Science & Business Media (Cited on page 3).

J. Christensen-Dalsgaard and M. J. Thompson (2007). *Observational results and issues concerning the tachocline* (Cited on page 7).

N. Coleman (2010). 'A Derivation of the Navier-Stokes Equations'. In: (Cited on page 12).

R. Dascaliuc and Z Grujić (2016). 'On energy cascades in the forced 3D Navier–Stokes equations'. In: *Journal of Nonlinear Science* 26, pp. 683–715 (Cited on page 250).

P. A. Davidson (2001). 'Dynamics at Moderate to High Magnetic Reynolds' Number'. In: *An Introduction to Magnetohydrodynamics*. Cambridge Texts in Applied Mathematics. Cambridge University Press, 159–221. DOI: 10.1017/CBO9780511626333.008 (Cited on page 96).

P. A. Davidson (2002). *An introduction to magnetohydrodynamics* (Cited on pages 27 and 31).

P. H. Diamond, S.-I. Itoh, K. Itoh and L. J. Silvers (2007). 'β-plane MHD turbulence and dissipation in the solar tachocline'. In: *The solar tachocline*, pp. 211–239 (Cited on pages 23 and 243).

P. G. Drazin (2002). *Introduction to hydrodynamic stability*. Vol. 32. Cambridge University Press (Cited on pages 17, 43 and 46).

P. G. Drazin and W. H. Reid (2004). *Hydrodynamic stability*. Cambridge University Press (Cited on pages 7, 9 and 19).

B. Dubrulle and U. Frisch (1991). 'Eddy viscosity of parity-invariant flow'. In: *Physical Review A* 43.10, p. 5355 (Cited on pages 22, 26 and 205).

S. Durston and A. D. Gilbert (2016). 'Transport and instability in driven two-dimensional magnetohydrodynamic flows'. In: *Journal of Fluid Mechanics* 799, pp. 541–578 (Cited on pages 23, 26, 106 and 244).

B. F. Farrell and P. J. Ioannou (2008). 'Formation of jets by baroclinic turbulence'. In: *Journal of the Atmospheric Sciences* 65.11, pp. 3353–3375 (Cited on page 23).

A. Fraser, I. Cresswell and P Garaud (2022). 'Non-ideal instabilities in sinusoidal shear flows with a streamwise magnetic field'. In: *Journal of Fluid Mechanics* 949, A43 (Cited on pages ii, 25, 38, 39, 62, 74, 75, 77, 80, 94, 162, 202, 244, 247, 248 and 249).

U Frisch, B Legras and B Villone (1996). 'Large-scale Kolmogorov flow on the beta-plane and resonant wave interactions'. In: *Physica D: Nonlinear Phenomena* 94.1-2, pp. 36–56 (Cited on pages 21, 22, 50, 81 and 243).

U. Frisch, B. Legras and B. Villone (Jan. 1996). 'Large-scale Kolmogorov flow on the beta-plane and resonant wave interactions'. In: *Physica D Nonlinear Phenomena* 94.1, pp. 36–56. DOI: 10.1016/0167-2789(95)00304-5 (Cited on page 75).

U. Frisch (1995). *Turbulence: The Legacy of A. N. Kolmogorov*. Cambridge University Press. DOI: 10.1017/CBO9781139170666 (Cited on page 176).

U. Frisch, P.-L. Sulem and M. Nelkin (1978). 'A simple dynamical model of intermittent fully developed turbulence'. In: *Journal of Fluid Mechanics* 87.4, pp. 719–736 (Cited on page 19).

B Galperin, S Sukoriansky, N Dikovskaya, P. Read, Y. Yamazaki and R. Wordsworth (2006). 'Anisotropic turbulence and zonal jets in rotating flows with a β-effect'. In: *Nonlinear Processes in Geophysics* 13.1, pp. 83–98 (Cited on page 23).

A. Gill (1974). 'The stability of planetary waves on an infinite beta-plane'. In: *Geophysical and Astrophysical Fluid Dynamics* 6.1, pp. 29–47 (Cited on page 50).

C Godreche and P Manneville (1998). 'Hydrodynamics and nonlinear instabilities'. In: *Oceanographic Literature Review* 9.45, p. 1723 (Cited on page 40).

D. Gough (2007). 'An introduction to the solar tachocline'. In: *The Solar Tachocline*. Ed. by D. W. Hughes, R. Rosner and N. O. Weiss. Cambridge University Press, 3–30. DOI: 10.1017/CBO9780511536243.002 (Cited on pages 4 and 6).

A. Hillier (2020). 'Ideal MHD instabilities, with a focus on the Rayleigh–Taylor and Kelvin–Helmholtz instabilities'. In: *Topics in Magnetohydrodynamic Topology, Reconnection and Stability Theory*, pp. 1–36 (Cited on pages 7 and 8).

A. Hillier and V. Polito (2018). 'Observations of the Kelvin–Helmholtz instability driven by dynamic motions in a solar prominence'. In: *The Astrophysical Journal Letters* 864.1, p. L10 (Cited on page 160).

D. W. Hughes and N. H. Brummell (2021). 'Double-diffusive magnetic layering'. In: *The Astrophysical Journal* 922.2, p. 195 (Cited on page 91).

D. Hughes, R Rosner and N. Weiss (2007). 'The Solar Tachocline Cambridge University Press'. In: *Cambridge, UK* (Cited on pages 2, 4, 5, 6 and 243).

C. Jones and P. Roberts (2000). 'The onset of magnetoconvection at large Prandtl number in a rotating layer II. Small magnetic diffusion'. In: *Geophysical & Astrophysical Fluid Dynamics* 93.3-4, pp. 173–226 (Cited on page 91).

S. E. Jones and A. D. Gilbert (2014). 'Dynamo action in the ABC flows using symmetries'. In: *Geophysical & Astrophysical Fluid Dynamics* 108.1, pp. 83–116 (Cited on page 131).

D. D. Joseph (1976). 'Global Stability and Uniqueness'. In: *Stability of Fluid Motions I*. Berlin, Heidelberg: Springer Berlin Heidelberg, pp. 7–24. DOI: 10.1007/978-3-642-80991-0_2. URL: https://doi.org/10.1007/978-3-642-80991-0_2 (Cited on pages 18 and 46).

E.-j. Kim (2007). 'Role of magnetic shear in flow shear suppression'. In: *Physics of Plasmas* 14.8, p. 084504 (Cited on page 23).

G. Klaassen and W. Peltier (1985). 'Evolution of finite amplitude Kelvin–Helmholtz billows in two spatial dimensions'. In: *Journal of Atmospheric Sciences* 42.12, pp. 1321–1339 (Cited on page 160).

S. Kobayashi, Ö. D. Gürcan and P. H. Diamond (2015). 'Direct identification of predator-prey dynamics in gyrokinetic simulations'. In: *Physics of Plasmas* 22.9 (Cited on page 228).

B Legras, B Villone and U Frisch (1999). 'Dispersive stabilization of the inverse cascade for the Kolmogorov flow'. In: *Physical review letters* 82.22, p. 4440 (Cited on pages 21, 176, 207 and 236).

N. Leprovost and E.-j. Kim (2009). 'Turbulent transport and dynamo in sheared magnetohydrodynamics turbulence with a nonuniform magnetic field'. In: *Physical Review E* 80.2, p. 026302 (Cited on page 23).

E. N. Lorenz (1972). 'Barotropic instability of Rossby wave motion'. In: *Journal of Atmospheric Sciences* 29.2, pp. 258–265 (Cited on page 50).

A. J. Manfroi and W. R. Young (Feb. 2002). 'Stability of β-plane Kolmogorov flow'. In: *Physica D Nonlinear Phenomena* 162.3-4, pp. 208–232. DOI: 10.1016/S0167-2789(01)00384-0 (Cited on pages i, 13, 19, 22, 34, 38, 39, 40, 50, 52, 53, 54, 55, 56, 58, 59, 61, 75, 81, 142, 242, 247 and 248).

L. D. Meshalkin and I. G. Sinai (1961). 'Investigation of the stability of a stationary solution of a system of equations for the plane movement of an incompressible viscous liquid'. In: *Journal of Applied Mathematics and Mechanics* 25, pp. 1700–1705 (Cited on pages i, 18, 26, 34, 35, 38, 40, 46, 47, 48, 53, 61, 62, 94, 105, 122, 159, 193, 194, 214, 215, 242 and 243).

M. S. Miesch (2005). 'Large-scale dynamics of the convection zone and tachocline'. In: *Living Reviews in Solar Physics* 2.1, pp. 1–139 (Cited on page 5).

H. K. Moffatt (1978). 'Field generation in electrically conducting fluids'. In: *Cambridge University Press, Cambridge, London, New York, Melbourne* 2, pp. 5–1 (Cited on page 27).

A. Nepomniashchii (1976). 'On stability of secondary flows of a viscous fluid in unbounded space'. In: *Prikladnaia Matematika i Mekhanika* 40, pp. 886–891 (Cited on page 19).

J. B. Parker and N. C. Constantinou (2019). 'Magnetic eddy viscosity of mean shear flows in two-dimensional magnetohydrodynamics'. In: *Physical Review Fluids* 4.8, p. 083701 (Cited on page 23).

M. E. Pessah (2010). 'Angular momentum transport in protoplanetary and black hole accretion disks: the role of parasitic modes in the saturation of MHD turbulence'. In: *The Astrophysical Journal* 716.2, p. 1012 (Cited on page 219).

F. Plunian and K.-H. Rädler (2002). 'Subharmonic dynamo action in the Roberts flow'. In: *Geophysical & Astrophysical Fluid Dynamics* 96.2, pp. 115–133 (Cited on page 168).

E. Priest (2014). *Magnetohydrodynamics of the Sun*. Cambridge University Press (Cited on pages 2, 3, 4 and 5).

P. B. Rhines (1975). 'Waves and turbulence on a β-plane'. In: *Journal of Fluid Mechanics* 69.3, pp. 417–443 (Cited on page 23).

Z. S. She (1987). 'Metastability and vortex pairing in the Kolmogorov flow'. In: *Physics Letters A* 124.3, pp. 161–164 (Cited on page 19).

G. I. Sivashinsky (1985). 'Weak turbulence in periodic flows'. In: *Physica D: Nonlinear Phenomena* 17.2, pp. 243–255 (Cited on pages 19, 22 and 250).

A. M. Soward, C. A. Jones, D. W. Hughes and N. O. Weiss (2005). *Fluid dynamics and dynamos in astrophysics and geophysics*. CRC Press (Cited on page 5).

S. Stanley (2014). 'Magnetic field generation in planets'. In: *Encyclopedia of the Solar System*. Elsevier, pp. 121–136 (Cited on page 3).

G. G. Stokes (1849). 'On the dynamical theory of diffraction'. In: *Transactions of the Cambridge Philosophical Society* 9, pp. 1–48 (Cited on page 11).

G. G. Stokes (1880). 'On the theories of the internal friction of fluids in motion, and of the equilibrium and motion of elastic solids'. In: *Transactions of the Cambridge Philosophical Society* 8 (Cited on page 11).

S. Tobias, K Dagon and J. Marston (2011). 'Astrophysical fluid dynamics via direct statistical simulation'. In: *The Astrophysical Journal* 727.2, p. 127 (Cited on page 248).

S. Tobias and N. Weiss (2007). 'The solar dynamo and the tachocline'. In: *The Solar Tachocline*. Ed. by D. W. Hughes, R. Rosner and N. O. Weiss. Cambridge University Press, 319–350. DOI: 10.1017/CBO9780511536243.014 (Cited on page 4).

S. M. Tobias, P. H. Diamond and D. W. Hughes (2007). 'β-plane magnetohydrodynamic turbulence in the solar tachocline'. In: *The Astrophysical Journal* 667.1, p. L113 (Cited on pages 23, 24, 25, 105 and 182).

G. K. Vallis (2017). *Atmospheric and oceanic fluid dynamics*. Cambridge University Press (Cited on pages 13 and 24).

G. M. Vasil (2015). 'On the magnetorotational instability and elastic buckling'. In: *Proceedings of the Royal Society A: Mathematical, Physical and Engineering Sciences* 471.2177, p. 20140699 (Cited on page 162).

G. P. Williams (1978). 'Planetary circulations: 1. Barotropic representation of Jovian and terrestrial turbulence'. In: *Journal of Atmospheric Sciences* 35.8, pp. 1399–1426 (Cited on page 23).